

277.2



National Library of Canada / Bibliothèque nationale du Canada

CANADIAN THESES ON MICROFICHE

THÈSES CANADIENNES SUR MICROFICHE

NAME OF AUTHOR / NOM DE L'AUTEUR: PETER GEORGE WRIGHT

TITLE OF THESIS / TITRE DE LA THÈSE: MID-INFRARED SPECTRA OF THE CLATHRATE HYDRATES OF TRIMETHYLENE OXIDE AND VIBRATIONAL SPECTRA OF THIOPHOSPHORYL CHLORIDE

UNIVERSITY / UNIVERSITÉ: ALBERTA

DEGREE FOR WHICH THESIS WAS PRESENTED / GRADE POUR LEQUEL CETTE THÈSE FUT PRÉSENTÉE: Ph D

YEAR THIS DEGREE CONFERRED / ANNÉE D'OBTENTION DE CE GRADE: 1976

NAME OF SUPERVISOR / NOM DU DIRECTEUR DE THÈSE: J. E. BERTIE

Permission is hereby granted to the NATIONAL LIBRARY OF CANADA to microfilm this thesis and to lend or sell copies of the film.

The author reserves other publication rights, and neither the thesis nor extensive extracts from it may be printed or otherwise reproduced without the author's written permission.

L'autorisation est, par la présente, accordée à la BIBLIOTHÈQUE NATIONALE DU CANADA de microfilmer cette thèse et de prêter ou de vendre des exemplaires du film.

L'auteur se réserve les autres droits de publication, ni la thèse ni de longs extraits de celle-ci ne doivent être imprimés ou autrement reproduits sans l'autorisation écrite de l'auteur.

DATED / DATE: 26<sup>th</sup> January 1976 SIGNED / SIGNÉ: Peter Gwinn

PERMANENT ADDRESS / RÉSIDENCE FIXE: 3W HIBBEN APARTMENTS, FACULTY ROAD, PRINCETON, NEW JERSEY, USA 08540

INFORMATION TO USERS

THIS DISSERTATION HAS BEEN  
MICROFILMED EXACTLY AS RECEIVED

This copy was produced from a microfiche copy of the original document. The quality of the copy is heavily dependent upon the quality of the original thesis submitted for microfilming. Every effort has been made to ensure the highest quality of reproduction possible.

PLEASE NOTE: Some pages may have indistinct print. Filmed as received.

Canadian Theses Division  
Cataloguing Branch  
National Library of Canada  
Ottawa, Canada K1A 0N4

AVIS AUX USAGERS

LA THESE A ETE MICROFILMEE  
TELLE QUE NOUS L'AVONS RECUE

Cette copie a été faite à partir d'une microfiche du document original. La qualité de la copie dépend grandement de la qualité de la thèse soumise pour le microfilmage. Nous avons tout fait pour assurer une qualité supérieure de reproduction.

NOTA BENE: La qualité d'impression de certaines pages peut laisser à désirer. Microfilmée telle que nous l'avons reçue.

Division des thèses canadiennes  
Direction du catalogage  
Bibliothèque nationale du Canada  
Ottawa, Canada K1A 0N4

THE UNIVERSITY OF ALBERTA

MID-INFRARED SPECTRA OF THE CLATHRATE HYDRATES OF  
TRIMETHYLENE OXIDE AND VIBRATIONAL SPECTRA OF  
THIOPHOSPHORYL CHLORIDE

(C)

BY

PETER GEORGE WRIGHT

A THESIS

SUBMITTED TO THE FACULTY OF GRADUATE STUDIES AND RESEARCH  
IN PARTIAL FULFILMENT OF THE REQUIREMENTS FOR THE DEGREE

OF

DOCTOR OF PHILOSOPHY

DEPARTMENT OF CHEMISTRY

EDMONTON, ALBERTA

SPRING 1976

THE UNIVERSITY OF ALBERTA  
FACULTY OF GRADUATE STUDIES AND RESEARCH

The undersigned certify that they have read, and recommend to the Faculty of Graduate Studies and Research, for acceptance, a thesis entitled

'MID-INFRARED SPECTRA OF THE CLATHRATE HYDRATES OF TRIMETHYLENE OXIDE AND VIBRATIONAL SPECTRA OF THIOPHOSPHORYL CHLORIDE'

submitted by PETER GEORGE WRIGHT in partial fulfilment of the requirements for the degree of Doctor of Philosophy.

*John E. Beut*  
.....  
Supervisor

*G. Howell*  
.....

*P. Kitarik*  
.....

*W. C. ...*  
.....

*W. ...*  
.....

*W. ...*  
.....  
External Examiner

Date: *January 16, 1976*

To Helen, Scott, Ivy and Reg.

## Abstract

The mid-infrared spectra have been recorded of the structure I and structure II clathrate hydrates of trimethylene oxide dispersed in mulling agents at 95°K and in potassium bromide pellets between 175 and 62°K. The assignment of the water absorption was made by comparison with that of other disordered water systems. The frequencies and half-widths of the water absorptions were related to the number, length and range of the O---O bonds. This was most successful for the  $\nu_{OD}$  (HDO) absorptions, for which an explanation was suggested for the differences between clathrate hydrates of polar and non-polar guest molecules.

The assignment of the guest absorptions of the two hydrates of trimethylene oxide was made by comparison with those of gaseous, liquid and solid trimethylene oxide. The differences between the frequencies of gaseous trimethylene oxide molecules and those trapped in the 14- and 16-hedral cages of the structure I and structure II hydrates, respectively, were interpreted, using ideas proposed by Pimentel and Charles, in terms of the magnitude of the interaction between the guest and the cage. These differences for the  $\alpha$ - and  $\beta$ -CH<sub>2</sub> vibrations of the structure I guest molecule were shown to support the previously proposed preferential orientation of the guest molecules in

the 14-hedral cages. The frequencies of the guest absorptions of ethylene oxide hydrate were also related to the guest-cage interaction. The temperature dependence of the frequencies, half-widths and peak heights of the water and guest absorptions of the structure I hydrate showed no effect of the proposed, parallel ordering of the guest dipoles at temperatures below about 100°K.

The infrared spectra of thiophosphoryl chloride in the gas phase and adsorbed thiophosphoryl chloride on polyethylene have been recorded between 200 and 1000  $\text{cm}^{-1}$ , together with the Raman spectra of liquid thiophosphoryl chloride between 150 and 1000  $\text{cm}^{-1}$ . The complicated absorption at 250  $\text{cm}^{-1}$  in the infrared spectrum of gaseous thiophosphoryl chloride has been assigned to the symmetric and antisymmetric Cl-P-Cl deformation vibrations of the various naturally occurring isotopic forms of the molecule. Also the symmetric and antisymmetric P-Cl stretching vibrations of various isotopic forms of the molecule have been assigned to absorptions in the 400 to 600  $\text{cm}^{-1}$  region of the infrared spectrum of the gas. A normal coordinate calculation was performed to aid the assignment of the spectrum.

## Preface

This thesis deals with two unrelated molecular systems. Chapters 1 to 5 are concerned with the vibrations of the two clathrate hydrates of trimethylene oxide, while Chapter 6 is concerned with the vibrations of thiophosphoryl chloride.



### Acknowledgements

I would like to express my gratitude to Dr. J. E. Bertie for his guidance and encouragement during the course of this work. I have enjoyed working for him. I would also like to thank the members, past and present, of Dr. Bertie's group for their interest, and in particular, Frances Bates and Steven Jacobs for making available to me unpublished results from their research. Particular thanks must go to the staff of the electronics and machine shops for their prompt and competent workmanship, and to Mr. Vernon Ball for all of his help with the figures.

I am very grateful to my wife, Helen, for her patience and understanding while this work was in progress, and for the many hours she spent on the formidable task of typing this manuscript. She did an excellent job. Also I would like to thank my parents for their encouragement through the years.

I gratefully acknowledge the financial support provided by the University of Alberta, the Province of Alberta, the Killam Estate and the National Research Council of Canada.

## Table of Contents

	Page
Abstract .....	v
Preface .....	vii
Acknowledgements .....	viii
List of Tables .....	xiii
List of Figures .....	xvi
<u>Chapter One. Introduction</u> .....	1
1.1 General .....	1
1.2 Vibrations of Encaged Species .....	1
1.3 Polymorphs of Ice and Clathrate Hydrates .....	15
1.3.1 Structures and Vibrations of the Ice Polymorphs .....	15
1.3.2 Structures and Vibrations of the Clathrate Hydrate Polymorphs .....	23
1.3.3 Physical Properties of the Clathrate Hydrates of Trimethylene Oxide .....	36
1.4 Vibrations of Trimethylene Oxide .....	45
1.5 Objectives of this Study .....	57
<u>Chapter Two. Experimental Techniques</u> .....	60
2.1 Chemicals .....	60
2.2 Hydrate Preparation .....	61
2.3 Hydrate Characterisation by Powder X-ray Diffraction .....	64
2.4 Mull Samples for Mid-Infrared Spectroscopy .....	66
2.5 Pellet Samples for Mid-Infrared Spectroscopy .....	70
2.5.1 Pellet Preparation .....	70
2.5.2 Liquid Helium Cryostat .....	76
2.5.3 Pellet Handling Procedure and Cryogenics .....	80

	Page
2.6 Mid-Infrared Instrumentation .....	84
<u>Chapter Three. Mid-Infrared Spectra of Structure I</u> <u>Trimethylene Oxide Hydrate</u> .....	86
3.1 General .....	86
3.2 Mid-Infrared Spectra of Structure I Trimethylene Oxide Hydrate in Mulls ...	92
3.2.1 General .....	92
3.2.2 Absorption by the Water Molecules .....	101
3.2.3 Absorption by the Trimethylene Oxide Molecules .....	106
3.3 Mid-Infrared Spectra of Structure I, Trimethylene Oxide Hydrate in Pellets .....	114
3.3.1 General .....	114
3.3.2 Absorption by the Water Molecules .....	145
3.3.3 Absorption by the Trimethylene Oxide Molecules .....	152
3.4 Powder X-ray Diffraction Pattern of Structure I Trimethylene Oxide Hydrate .....	155
<u>Chapter Four. Mid-Infrared Spectra of Structure II</u> <u>Trimethylene Oxide Hydrate</u> .....	160
4.1 General .....	160
4.2 Mid-Infrared Spectra of Structure II Trimethylene Oxide Hydrate in Mulls ...	162
4.2.1 Absorption by the Water Molecules .....	166
4.2.2 Absorption by the Trimethylene Oxide Molecules .....	174
4.3 Mid-Infrared Spectra of Structure II Trimethylene Oxide Hydrate in Pellets .....	179
4.4 Powder X-ray Diffraction Pattern of Structure II Trimethylene Oxide Deuterate .....	182

	Page
Chapter Five. <u>Discussion of the Mid-Infrared Spectra of Structure I and II Trimethylene Oxide Hydrates</u> .....	186
5.1 General .....	186
5.2 Absorption by the Water Molecules .....	186
5.3 Absorption by the Guest Molecules .....	210
5.3.1 General .....	210
5.3.2 Discussion of the Assignment of the Trimethylene Oxide Absorption .....	213
5.3.3 Vibrations of the Trimethylene Oxide Molecules .....	222
Chapter Six. <u>Vibrational Spectra of Thiophosphoryl Chloride</u> .....	237
6.1 Introduction .....	237
6.1.1 General Introduction .....	237
6.1.2 The Structure and Vibrations of Thiophosphoryl Chloride .....	237
6.1.3 Previous Studies of the Vibrations of Thiophosphoryl Chloride .....	242
6.1.4 Aims of this Study .....	246
6.2 Experimental Techniques .....	248
6.2.1 Sample Handling and Cells .....	248
6.2.2 Spectrophotometers .....	251
6.3 Results .....	255
6.3.1 General .....	255
6.3.2 Cl-P-Cl Deformation Vibrations .....	256
6.3.3 P-Cl Symmetric Stretching Vibration .....	260
6.3.4 Other Fundamental Vibrations .....	263
6.3.5 Impurities .....	265
6.4 Normal Coordinate Analysis .....	267
6.4.1 General .....	267
6.4.2 Theory of Normal Vibrations .....	267

	Page
6.4.3 Computer Programmes .....	269
6.4.4 Vibrational Coordinates and Force Field Developments .....	271
6.5 Discussion .....	288
6.5.1 Cl-PCl Deformation Vibrations .....	288
6.5.2 Other Fundamental Vibrations .....	297
References .....	302
Appendix I G Matrices .....	313
Appendix II Eigenfunctions .....	316
Appendix III Potential Energy Distributions .....	319

List of Tables

Table		Page
1.1	Experimental Frequency Shifts of the Hydrogen Halides in Matrices .....	8
1.2	Experimental Frequency Shifts of ClCN, SO <sub>2</sub> and HCN in Matrices .....	10
1.3	Experimental Frequency Shifts of HN <sub>3</sub> and NH <sub>3</sub> in Matrices .....	12
1.4	Carbon-Halogen Stretching Frequencies of Methyl Fluoride, Methyl Chloride and Methyl Bromide in the Gas Phase and as Guest Molecules in β-Quinol .....	14
1.5	Geometric Parameters of the Unit Cells and Cages of the Structure I and Structure II Clathrate Hydrates .....	25
1.6	Parameters of the Trimethylene Oxide-Water Phase Diagram .....	38
1.7	Representations formed by the Internal Coordinates of Trimethylene Oxide under the Point Group C <sub>2v</sub> .....	47
1.8	Assignment of the Infrared Spectrum of Trimethylene Oxide in the Gas, Liquid and Solid Phases .....	49
3.1	Frequencies of the Observed Features in the Mid-Infrared Spectra of Structure I Trimethylene Oxide Hydrate and Deuterate in Mulls at 95°K .....	97
3.2	Frequencies of the Observed Features in the Mid-Infrared Spectra of Structure I Trimethylene Oxide Hydrate and Deuterate in Potassium Bromide Pellets at 95°K .....	129
3.3	Temperature Dependence of the ν <sub>OD</sub> (D <sub>2</sub> O) and ν <sub>R</sub> (D <sub>2</sub> O) Bands in the Mid-Infrared Spectrum of Structure I Trimethylene Oxide Deuterate in Potassium Bromide Pellets .....	132
3.4	Temperature Dependence of the ν <sub>OH</sub> (HDO) and ν <sub>OD</sub> (HBO) Bands in the Mid-Infrared Spectra of Structure I Trimethylene Oxide Deuterate and Hydrate in Potassium Bromide Pellets .....	133

Table	Page
3.5	Temperature Dependence of Guest Features in the Mid-Infrared Spectrum of Structure I Trimethylene Oxide Hydrate in Potassium Bromide Pellets ..... 134
3.6	Temperature Dependence of Guest Features in the Mid-Infrared Spectrum of Structure I Trimethylene Oxide Deuterate in Potassium Bromide Pellets ..... 136
3.7	Powder X-ray Diffraction Pattern of Structure I Trimethylene Oxide Hydrate at $100 \pm 20^\circ\text{K}$ .... 157
3.8	Powder X-ray Diffraction Pattern of Trimethylene Oxide at $100 \pm 20^\circ\text{K}$ ..... 159
4.1	Frequencies of the Observed Features in the Mid-Infrared Spectra of Structure II Trimethylene Oxide Hydrate and Deuterate in Mulls at $95^\circ\text{K}$ ..... 167
4.2	Powder X-ray Diffraction Pattern of Structure II Trimethylene Oxide Deuterate at $100 \pm 20^\circ\text{K}$ ..... 184
5.1	Structural Data for Ices Ih, Ic, V, VI, Structure I Hydrates of Trimethylene Oxide, Ethylene Oxide and Cyclopropane and the Structure II Hydrate of Trimethylene Oxide at $100^\circ\text{K}$ ..... 190
5.2	Comparison of the Fundamental Frequencies of Trimethylene Oxide in the Spectra of Gaseous Trimethylene Oxide and Structures I and II Trimethylene Oxide Deuterate ..... 217
5.3	Comparison of the Fundamental Frequencies of Ethylene Oxide in the Spectra of Gaseous Ethylene Oxide and the Structure I Hydrate of Ethylene Oxide ..... 229
6.1	Approximate Description of the Fundamental Vibrations of Thiophosphoryl Chloride, Point Group $C_{3v}$ ..... 240
6.2	Approximate Description of the Fundamental Vibrations of Thiophosphoryl Chloride, Point Group $C_s$ ..... 241
6.3	Previous Assignments of the Fundamental Frequencies of Gaseous and Liquid Thiophosphoryl Chloride ..... 245

Table	Page
6.4 Principal Moments of Inertia for Thiophosphoryl Chloride .....	257
6.5 Internal Coordinates of Thiophosphoryl Chloride .....	273
6.6 Symmetry Coordinates for $^{32}\text{SP}^{35}\text{Cl}_3$ , $^{32}\text{SP}^{37}\text{Cl}_3$ and $^{34}\text{SP}^{35}\text{Cl}_3$ , Point Group, $C_{3v}$ .....	274
6.7 Symmetry Coordinates for $^{32}\text{SP}^{35}\text{Cl}_2^{37}\text{Cl}$ , $^{32}\text{SP}^{35}\text{Cl}^{37}\text{Cl}_2$ and $^{34}\text{SP}^{35}\text{Cl}_2^{37}\text{Cl}$ , Point Group $C_s$ .....	275
6.8 Force Field Development for Thiophosphoryl Chloride .....	277
6.9 Experimental Frequencies and Assignment for Gaseous $^{32}\text{SP}^{35}\text{Cl}_3$ , and Calculated Frequencies from Various Force Fields .....	278
6.10 Calculated Frequencies for Six Isotopic Forms of Thiophosphoryl Chloride from Force Field 5 .....	283
6.11 Calculated Frequencies for Six Isotopic Forms of Thiophosphoryl Chloride from the Final Force Field .....	284
6.12 Potential Energy Distribution between the Diagonal Elements of the Symmetrised Force Constant Matrix for $^{32}\text{SP}^{35}\text{Cl}_3$ .....	285
6.13 Potential Energy Distribution between the Diagonal Elements of the Symmetrised Force Constant Matrix for $^{32}\text{SP}^{35}\text{Cl}_2^{37}\text{Cl}$ .....	286
6.14 Calculated Frequencies for $^{32}\text{SP}^{35}\text{Cl}_3$ and $^{32}\text{SP}^{35}\text{Cl}_2^{37}\text{Cl}$ using Force Fields 2 and 6 .....	290
6.15 Assignment of the Fundamental Vibrations of Thiophosphoryl Chloride .....	301



## List of Figures

Figure		Page
1.1	Potential energy of interaction, $U_{BM}$ , between a polyatomic solute molecule and a matrix cage, and its first $U'_{BM}$ , and second $U''_{BM}$ , derivatives with respect to $r_{AB}$ .....	6
1.2	Cages of structure I (a, b) and structure II (c, d) clathrate hydrates viewed along the axes of highest symmetry .....	24
1.3	Phase diagram of the trimethylene oxide-water system .....	37
1.4	Molecular structure of trimethylene oxide ...	46
2.1	Low temperature infrared mull cell .....	67
2.2	Piston-cylinder pressure apparatus .....	71
2.3	Cold end of low temperature infrared pellet cell .....	77
2.4	Liquid helium cryostat and peripheral equipment .....	79
3.1	Mid-infrared mull spectra of TMO deuterate I (I), TMO deuterate II (II) and solid trimethylene oxide (TMO) at 95°K .....	90
3.2	Mid-infrared spectra of structure I trimethylene oxide hydrate dispersed in mulling agents at 95°K .....	93
3.3	Mid-infrared spectra of structure I trimethylene oxide deuterate dispersed in mulling agents at 95°K .....	94
3.4	Mid-infrared spectrum of structure I trimethylene oxide hydrate at 95°K composed from spectra of samples dispersed in different mulling agents .....	95
3.5	Mid-infrared spectrum of structure I trimethylene oxide deuterate at 95°K composed from spectra of samples dispersed in different mulling agents .....	96

Figure		Page
3.6	The $\nu_{OH}(H_2O)$ band of structure I trimethylene oxide hydrate and the $\nu_{OD}(D_2O)$ band of structure I trimethylene oxide deuterate dispersed in mulling agents at 95°K .....	102
3.7	The $\nu_R(D_2O)$ band of structure I trimethylene oxide deuterate dispersed in a mulling agent at 95°K .....	104
3.8	The $\nu_{OH}(HDO)$ and $\nu_{OD}(HDO)$ bands of structure I trimethylene oxide deuterate and hydrate dispersed in mulling agents at 95°K .....	107
3.9	Absorption by the C-H stretching vibrations of structure I trimethylene oxide deuterate dispersed in a mulling agent at 95°K .....	108
3.10	Absorption by $\nu_4/\nu_{14}$ , $\nu_{11}$ , $\nu_{16}$ and $\nu_{23}$ of structure I trimethylene oxide hydrate and $\nu_{21}$ , $\nu_{22}$ and $\nu_{12}$ of structure I trimethylene oxide deuterate dispersed in mulling agents at 95°K .....	110
3.11	Absorption by the ring vibrations of structure I trimethylene oxide deuterate as recorded from a good mull (curves A) and a poor mull (curves B) at 95°K .....	113
3.12	Mid-infrared spectra of pellets containing no sample (curve A) and structure I trimethylene oxide deuterate (curves B and C), with the potassium bromide used for the pellet of curve B being much drier than that used for curves A and C .....	120
3.13	Mid-infrared spectrum of structure I trimethylene oxide hydrate dispersed in a KBr pellet at 95°K .....	126
3.14	Mid-infrared spectrum of structure I trimethylene oxide deuterate dispersed in a KBr pellet at 95°K .....	127
3.15	The $\nu_{OD}(D_2O)$ and $\nu_R(D_2O)$ bands of structure I trimethylene oxide deuterate dispersed in a KBr pellet at 62, 80, 125 and 175°K .....	139

Figure	Page
3.16	The $\nu_{OH}$ (HDO) and $\nu_{OD}$ (HDO) bands of structure I trimethylene oxide deuterate and hydrate, respectively, dispersed in a KBr pellet at 62, 80, 125 and 175°K ..... 140
3.17	The guest bands of structure I trimethylene oxide hydrate dispersed in a KBr pellet at 62, 80, 125 and 175°K ..... 141
3.18	The C-H stretching bands of structure I trimethylene oxide deuterate dispersed in a KBr pellet at 62, 80, 125 and 175°K ..... 142
3.19	The non-ring bands of structure I trimethylene oxide deuterate dispersed in a KBr pellet at temperatures between 62 and 175°K ..... 143
3.20	The ring bands of structure I trimethylene oxide deuterate dispersed in a KBr pellet at 62, 80, 125 and 175°K ..... 144
4.1	The $\nu_7/\nu_{17}$ bands of uncontaminated structure I trimethylene oxide deuterate, structure II trimethylene oxide deuterate contaminated by structure I trimethylene oxide deuterate, and uncontaminated structure II trimethylene oxide deuterate, dispersed in a mulling agent at 95°K ..... 163
4.2	Mid-infrared spectra of structure II trimethylene oxide hydrate and deuterate at 95°K ..... 164
4.3	The $\nu_{OH}$ (H <sub>2</sub> O) band of structure II trimethylene oxide hydrate and the $\nu_{OD}$ (D <sub>2</sub> O) band of structure II trimethylene oxide deuterate dispersed in mulling agents at 95°K ..... 169
4.4	The $\nu_{OH}$ (HDO) band of structure II trimethylene oxide deuterate and the $\nu_{OD}$ (HDO) band of structure II trimethylene oxide hydrate dispersed in mulling agents at 95°K ..... 172
4.5	The C-H stretching bands of structure II trimethylene oxide deuterate dispersed in a mulling agent at 95°K ..... 176

Figure		Page
4.6	The ring bands of structure II trimethylene oxide deuterate dispersed in a mulling agent at 95°K .....	177
4.7	The $\nu_7/\nu_{17}$ and $\nu_6$ bands of: structure I trimethylene oxide deuterate in a mull; a KBr pellet made from structure II trimethylene oxide deuterate; structure II trimethylene oxide deuterate in a mull; all at 95°K .....	181
5.1	Graph of $\nu_{OD}$ (HDO) versus the O---O distance for ordered phases and cyclopropane hydrate or weighted mean O---O distance for the disordered phases .....	192
6.1	Molecular structure of thiophosphoryl chloride .....	239
6.2	Far-infrared gas cell .....	250
6.3	Infrared spectra of gaseous thiophosphoryl chloride and Raman spectra of liquid thiophosphoryl chloride between 235 and 265 $\text{cm}^{-1}$ at 25°C .....	258
6.4	Raman spectra of liquid thiophosphoryl chloride between 720 and 780 $\text{cm}^{-1}$ (upper box) and between 510 and 570 $\text{cm}^{-1}$ (lower box) at 25°C .....	261
6.5	Infrared spectrum between 410 and 450 $\text{cm}^{-1}$ of gaseous thiophosphoryl chloride (box A) and Raman spectrum between 420 and 435 $\text{cm}^{-1}$ of liquid thiophosphoryl chloride (box B) at 25°C .....	262
6.6	Infrared spectra between 750 and 790 $\text{cm}^{-1}$ (left upper box) and between 530 and 570 $\text{cm}^{-1}$ (right upper box) of gaseous thiophosphoryl chloride and Raman spectrum between 150 and 180 $\text{cm}^{-1}$ (lower box) of liquid thiophosphoryl chloride at 25°C .....	264

## Chapter One. Introduction

### 1.1 General

The first five chapters of this thesis are concerned with the vibrations of the clathrate hydrates of oxetane (hereafter called trimethylene oxide). In order to provide a theoretical framework within which the absorption by the encaged trimethylene oxide molecules may be interpreted, a general approach to the vibrations of encaged species is presented in Section 1.2. The clathrate hydrate lattices are formed by hydrogen-bonded, four-coordinated water molecules; as are the various phases of ice. The vibrations of the water lattices in the hydrates should, therefore, be similar to those of the ice phases. Thus the structures and vibrations of the polymorphs of ice as well as the clathrate hydrates are discussed in Section 1.3. The previous studies of the physical properties of the clathrate hydrates of trimethylene oxide are also presented in Section 1.3. A most probable assignment of the vibrational spectrum of gaseous, liquid and solid trimethylene oxide is deduced in Section 1.4 from a comparison of the previous studies. Finally, the objectives of this study are presented in Section 1.5.

### 1.2 Vibrations of Encaged Species

In order to approach the problem of the perturbation, by the cage, of the vibrational energy levels of an encaged

molecule, it is first necessary to identify the various interactions which may occur between a pair of molecules which are sufficiently far apart that electron exchange may be neglected (1). These interactions can be divided into static and dynamic effects.

The static effects can be subdivided (1) as follows: the electrostatic interaction of the permanent charge distributions of the two molecules, the inductive interaction of the permanent charge distribution of one molecule with the charge distribution induced in the other molecule, the dispersive interaction of the instantaneous charge distribution of one molecule with the instantaneous charge distribution induced in the other molecule, and the repulsive interaction of the charge distributions of the two molecules. The dynamic effects arise from the fluctuations in the interactions listed above during the normal vibrations of the two molecules.

Barnes (1) has performed detailed calculations of the differences between the fundamental frequencies of vibration of gaseous diatomic molecules and those of diatomic molecules engaged in low temperature matrices. The individual vibrational frequency shifts due to the inductive, dispersive and repulsive interactions were summed to give the total calculated shift for the four hydrogen halides in matrices of neon, argon, krypton, xenon, methane, tetrafluoromethane, sulphur hexafluoride, nitrogen, carbon dioxide and carbon

monoxide. The shifts calculated for the attractive interactions were negative. These shifts are  $\Delta\nu_{ind}$  due to the inductive interaction and  $\Delta\nu_{dis}$  due to the dispersive interaction, where  $\Delta\nu$  is defined as the difference between the frequency of the encaged molecule and that of the gaseous molecule in  $\text{cm}^{-1}$  units. For hydrogen fluoride,  $\Delta\nu_{ind}$  was about half of  $\Delta\nu_{dis}$ , whereas for hydrogen iodide  $\Delta\nu_{ind}$  was about 0.1 percent of  $\Delta\nu_{dis}$ . The shifts calculated for the repulsive interactions,  $\Delta\nu_{rep}$ , were positive, and were of the same order of magnitude as  $\Delta\nu_{dis}$ , except for hydrogen fluoride for which they usually had the same magnitude as  $\Delta\nu_{ind}$ . As the ratio of the size of the solute molecule to that of the cage increased, so did  $\Delta\nu_{rep}$ , as would be expected. Comparison of the total calculated shifts with those available from experiment showed that there was reasonable agreement for the matrices which produced approximately spherical cages, however the agreement was poor for the non-spherical cages of the nitrogen, carbon dioxide and carbon monoxide matrices.

More qualitative ideas have been successfully applied to systems which cannot be explained, at present, by detailed calculations. Buckingham (2) has considered the shifts of the vibrational frequencies of diatomic, solute molecules due to the interaction with a liquid solvent. He assumed that the interaction energy could be expanded as a power series in the dimensionless displacement coordinate,

$(r - r_e)/r_e$ , of the solute molecule, where  $r_e$  is the equilibrium bond length and  $r - r_e$  is the displacement from equilibrium. Then, by treating this interaction, and the anharmonic terms in the potential energy function of the free, solute molecule, as small perturbations to the harmonic potential of the free molecule, an expression for the vibrational frequency shift,  $\Delta\nu$ , was obtained. Buckingham obtained the expression for the fundamental frequency shift,

$$\Delta\nu = \frac{B_e}{hc\omega_e} \left[ U'' - \frac{3A}{\omega_e} U' \right],$$

where  $\Delta\nu$  is defined above,  $B_e$  is the equilibrium rotational constant in  $\text{cm}^{-1}$  units,  $\omega_e$  is the 'classical' frequency of the harmonic oscillator in  $\text{cm}^{-1}$  units,  $U'$  and  $U''$  are, respectively, the first and second derivatives of the interaction energy with respect to the dimensionless displacement coordinate, averaged over all solvent configurations,  $A$  is an anharmonicity constant expressed in  $\text{cm}^{-1}$  units,  $h$  is Planck's constant and  $c$  is the speed of light. This expression relates the frequency shift to the interaction energy, but in order to obtain the magnitude of  $\Delta\nu$ , it is necessary to have a detailed knowledge of the interaction energy. By substituting,

$$B_e = \frac{h}{8\pi^2 \mu c r_e^2} \text{ and } \omega_e = \frac{1}{2\pi c} \left( \frac{k}{\mu} \right)^{1/2}$$

into Buckingham's expression for  $\Delta\nu$ , Pimentel and Charles (3)



obtained,

$$\Delta\nu = \frac{1}{4\pi c r_e^2 \sqrt{\mu k}} \left[ U'' - \frac{3A}{\omega_e} U' \right]$$

where  $r_e$  is the equilibrium bond length,  $\mu$  is the reduced mass and  $k$  is the harmonic force constant.

Pimentel and Charles (3) were able to interpret the  $\Delta\nu$  values of polyatomic solute molecules trapped in low temperature matrices in terms of this expression. The sign of  $\Delta\nu$  is determined by the expression inside the brackets, whereas the magnitude of  $\Delta\nu$  is inversely proportional to the square root of the force constant. Pimentel and Charles related the sign of  $\Delta\nu$  to the degree of freedom experienced by the solute molecule in the cage, using the ideas illustrated in Fig. 1.1. They considered only the displacement of the internal coordinate  $r_{AB}$  of the solute molecule ABCD and assumed the matrix cage molecules M to be fixed rigidly in position. Fig. 1.1 shows the potential energy of interaction of atoms B and M,  $U_{BM}$ , as a function of the distance  $r_{PM}$  or  $r_{AB}$ , distance AM being assumed to be constant. It also shows the corresponding curves for the first  $U'_{BM}$ , and second,  $U''_{BM}$ , derivatives of  $U_{BM}$  with respect to  $r_{AB}$ . Pimentel and Charles noted that if atom B is lodged at a distance greater than  $r_1$  from atom M, both  $U'_{BM}$  and  $U''_{BM}$  are negative and, since the anharmonicity constant A is negative,  $\Delta\nu$  must be negative; in this case, they described the internal coordinate  $r_{AB}$  as being in a

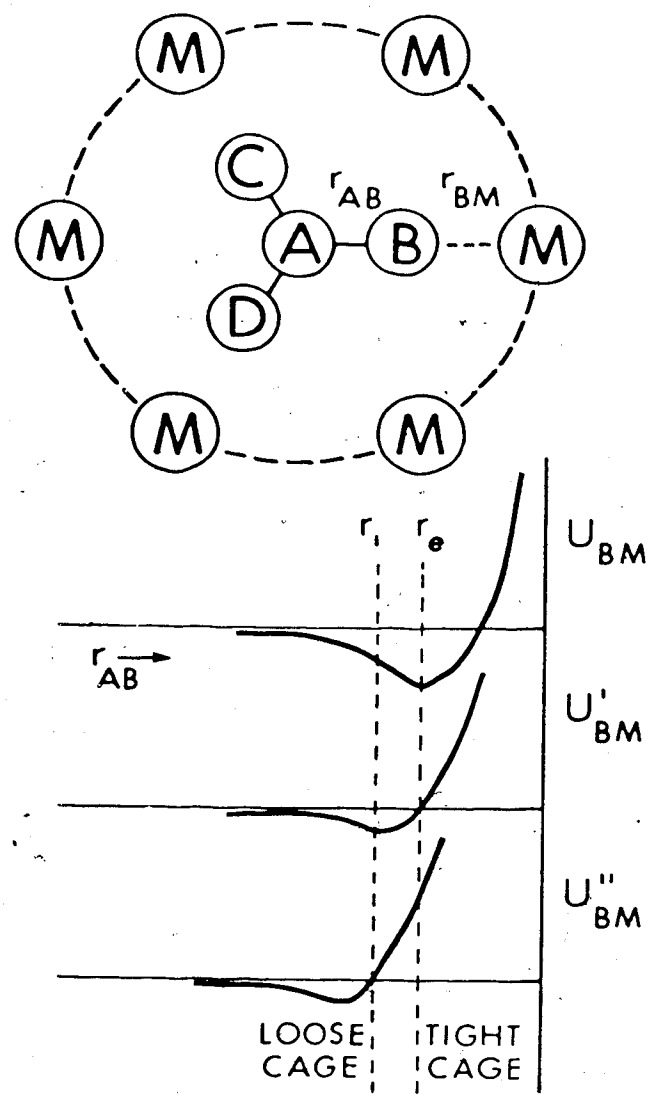


Fig. 1.1. Potential energy of interaction,  $U_{BM}$ , between a polyatomic solute molecule and a matrix cage, and its first  $U'_{BM}$  and second,  $U''_{BM}$  derivatives with respect to  $r_{AB}$ .

loose cage environment. Conversely, if atom B is lodged at a distance less than  $r_0$  from atom M, both  $U'_{BM}$  and  $U''_{BM}$  are positive and  $\Delta v$  must be positive; Pimentel and Charles described the coordinate  $r_{AB}$  as being in a tight cage environment in this case. Clearly, the sign of  $\Delta v$  for  $r_0 < r_{BM} < r_1$  is determined by the relative magnitudes of  $U'_{BM}$  and  $U''_{BM}$  and no generalisations can be made.

The experimental values of  $\Delta v$  for the four hydrogen halides in low temperature matrices (1) are listed in Table 1.1. For every matrix, the value of  $\Delta v$  becomes progressively more positive as the size of the solute molecule increases. This is completely consistent with Pimentel and Charles' arguments, since the H-X stretching vibration must experience a progressively tighter cage environment as the size of HX increases for a given matrix. Apparently the inverse dependence of  $\Delta v$  on the square root of the force constant does not affect the trend. Also the values of  $\Delta v$  for a given hydrogen halide in the four inert gas matrices become progressively more negative as the size of the inert gas atom, and thus the size of the substitutional site, increases, which is consistent with the progressively looser cage environment experienced by the vibration.

Pimentel and Charles (3) reviewed the experimental values of  $\Delta v$  for the various vibrations of polyatomic molecules in low temperature matrices that were available to them in 1962. They found that, in general, stretching

Table 1.1

Experimental Frequency Shifts<sup>a, b</sup> of  
the Hydrogen Halides in Matrices<sup>c</sup>

Matrix	$\Delta\nu$ (HF)	$\Delta\nu$ (HCl)	$\Delta\nu$ (HBr)	$\Delta\nu$ (HI)
Ne	- 8.8	+14.5	-	-
Ar	-40.9	-15.1	+ 0.9	+16
Kr	-39.5	-30.6	-16.7	-6.6
Xe	-58.9	+43.8	-	-
CH <sub>4</sub>	-	-38.2 <sup>d</sup>	-25.7	-8.8
CF <sub>4</sub>	-	-18.0	-	-
SF <sub>6</sub>	-	-20.8	-19.9	+2
N <sub>2</sub>	-81.1	-31.7	-12.8	+7.6
CO <sub>2</sub>	-	-42.7	-	+30.0
CO	-	-79.5	-53.9	-22 <sup>d</sup>

a) In cm<sup>-1</sup>

b) Frequency shift =  $\Delta\nu = \nu_{\text{matrix}} - \nu_{\text{gas}}$

c) Taken from reference 1.

d) Derived from the value for the deuterium halide.

9

vibrations exhibited negative values of  $\Delta\nu$  whereas bending vibrations exhibited positive values. They rationalised this trend by arguing that the lowest energy position of the solute molecule would be a compromise between optimum distances at some points of contact with the cage and less than optimum distances at other points; and that the normal coordinates with low force constants, the bending coordinates, would be more tolerant of tight cage environments than those with high force constants, the stretching coordinates.

Murchison and Overend (4) pointed out that the frequency shifts of the fundamental vibrations of the matrix isolated, triatomic molecule  $^{35}\text{Cl}^{12}\text{C}^{14}\text{N}$  can be understood in terms of the arguments of Pimentel and Charles. Data obtained from other workers (5, 6) for other matrix isolated, triatomic molecules,  $^{32}\text{S}^{16}\text{O}_2$  and HCN, can also be understood in this way. The experimental  $\Delta\nu$  values are listed in Table 1.2. In every case the  $\Delta\nu$  value for the bending vibration is more positive than the  $\Delta\nu$  values for the stretching vibrations, in agreement with the trend noted by Pimentel and Charles (3). It can also be seen that the  $\nu_3$  and  $\nu_1$  modes of ClCN experience a looser cage environment in argon than in neon, as would be expected, although the bending mode,  $\nu_2$ , is apparently slightly more restricted in argon than in neon. The frequency shifts for HCN in different matrices are difficult to evaluate (1) because the cages in  $\text{N}_2$  and CO are not approximately spherical.

Table 1.2

Experimental Frequency Shifts<sup>a, b</sup> of<sup>35</sup>Cl<sup>12</sup>C<sup>14</sup>N, <sup>32</sup>S<sup>16</sup>O<sub>2</sub> and HCN in Matrices<sup>c</sup>(i) <sup>35</sup>Cl<sup>12</sup>C<sup>14</sup>N

Mode	$\nu_3$ (a.str.)	$\nu_1$ (s.str.)	$\nu_2$ (bend)
$\nu_{\text{gas}}$	2215.6	714.0	378.6
Matrix			
Ne	+0.8	+5.6	+5.9
Ar	-6.9	+3.7	+7.2

(ii) <sup>32</sup>S<sup>16</sup>O<sub>2</sub>

Mode	$\nu_3$ (a.str.)	$\nu_1$ (s.str.)	$\nu_2$ (bend)
$\nu_{\text{gas}}$	1361.8	1151.4	517.7
Matrix			
Kr	-10.9	-1.6	+1.3

(iii) HCN

Mode	$\nu_3$ (a.str.)	$\nu_1$ (s.str.)	$\nu_2$ (bend)
$\nu_{\text{gas}}$	3311	2097	712
Matrix			
Ar	-8	-4	+8
N <sub>2</sub>	-23	0	+29 <sup>d</sup>
CO	-50	+7	+38 <sup>d</sup>

a) In cm<sup>-1</sup>.b) Frequency shift =  $\nu_{\text{matrix}} - \nu_{\text{gas}}$ .c) Taken from reference 4 (ClCN), 5 (SO<sub>2</sub>) and 6 (HCN).

d) Average of doublet frequencies.

Pimentel and Charles' (3) experimental  $\Delta\nu$  values for two tetra-atomic molecules,  $\text{HN}_3$  and  $\text{NH}_3$ , in a number of matrices are listed in Table 1.3. For every case in Table 1.3, the  $\Delta\nu$  value of the lowest frequency vibration is more positive than that for the highest frequency vibration. Also the  $\Delta\nu$  values for all of the vibrations listed for  $\text{HN}_3$  in xenon matrices are more negative than the corresponding  $\Delta\nu$  values for argon matrices, as would be expected. However, it is not clear why the  $\Delta\nu$  values for the  $\nu_2$ ,  $\nu_3$ , and  $\nu_4$  vibrations of  $\text{HN}_3$  in a krypton matrix are more positive than the corresponding values in an argon matrix.

In summary it can be said that Pimentel and Charles' ideas apply rather well, and that a molecule trapped in a tight cage environment in inert gas matrices generally has higher vibrational frequencies than when it is trapped in a loose cage environment. Further the highest frequency vibration usually has a larger negative shift than the lowest frequency vibration, however, the shifts of the intermediate vibrations are sometimes contrary to those expected.

Before concluding this section on the vibrations of encaged species, it is of interest to mention some work on the vibrations of molecules trapped in the cages formed by  $\beta$ -quinol. Palin and Powell (7) showed that when hydroquinone crystallises in its  $\beta$ -quinol form, an open structure is formed, which contains cages large enough to accommodate guest molecules. The cages are formed by two groups of six

Table 1.3

Experimental Frequency Shifts<sup>a, b</sup> of  
 $\text{HN}_3$  and  $\text{NH}_3$  in Matrices<sup>c</sup>

(i)  $\text{HN}_3$ 

Mode	$\nu_1$ (NH str.)	$\nu_2$ (NNN a.str.)	$\nu_3$ (NNN s.str.)	$\nu_4$ (NNN bend)
$\nu_{\text{gas}}$	3335.6	2140.4	1269.0	1152.5

Matrix

Ar	-12	-2	-5	-6
Kr	-15	0	-3	-4
Xe	-37	-8	-6	-7
$\text{N}_2$	-13	+8	+3	+15
CO	-41	-	+15	+25
$\text{CO}_2$	-31	+26	+18	+35

(ii)  $\text{NH}_3$ 

Mode	$\nu_3$ (NH a.str.)	$\nu_1$ (NH s.str.)	$\nu_2$ (s. bend)
$\nu_{\text{gas}}$	3443.7	3336.2	950.0

Matrix

$\text{N}_2$	-4	-4	+20
--------------	----	----	-----

a) In  $\text{cm}^{-1}$ b) Frequency shift =  $\nu_{\text{matrix}} - \nu_{\text{gas}}$ 

c) Taken from reference 3.



oxygen atoms bonded together to form hexagonal rings, which constitute two opposite, parallel faces of the cage, while the remaining faces are formed by six benzene rings inclined at angles of  $45^\circ$  with respect to the plane of the hexagons (8). The free diameter of the cage, that is, after taking account of the van der Waals radii of the atoms of the cage, is about  $4.2 \text{ \AA}$  (8). Child (8) noted that the geometry of the cage is such that the force field within it is not precisely spherical and that the guest molecules  $\text{SO}_2$  and  $\text{CO}_2$  preferentially orient their long axes parallel to a line joining the centers of the hexagons.

Davies and co-workers (9) studied the Raman spectra of the  $\beta$ -quinol clathrates of methyl fluoride, methyl chloride and methyl bromide, and their frequencies for the carbon-halogen stretching vibrations of the engaged molecules are given in Table 1.4 together with the gas phase values. If the values for the largest percent occupancy are considered first, it is seen that  $\Delta\nu$  becomes progressively more positive as the size of the guest molecule increases. The carbon-halogen stretching vibration must experience a progressively tighter cage environment as the size of the guest molecule increases and so the observed trend for the  $\Delta\nu$  values is consistent with a prediction based on the ideas of Pimentel and Charles (3). It should be remembered that the magnitudes of the  $\Delta\nu$  values are inversely proportional to the force constant of the vibration, however, this

Table 1.4

Carbon-Halogen Stretching Frequencies<sup>a</sup>  
 of Methyl Fluoride, Methyl Chloride and  
 Methyl Bromide in the Gas Phase and as  
 Guest Molecules in  $\beta$ -Quinol<sup>b</sup>

Molecule	Percent <sup>c</sup> Occupancy	$\nu_{\text{guest}}$	$\nu_{\text{gas}}$	$\Delta\nu^d$
CH <sub>3</sub> F	62	1022	1049	-27
CH <sub>3</sub> Cl	70 23	734	733	+ 1
		737		+ 4
CH <sub>3</sub> Br	59 28 18	621	610	+11
		623		+13
		626		+16

a) In  $\text{cm}^{-1}$ .

b) Taken from reference 9.

c) Values of the percentage of cages occupied.

d)  $\Delta\nu = \nu_{\text{guest}} - \nu_{\text{gas}}$ .

does not affect the observed trend.

Also it is seen that for a given guest molecule, the value of  $\Delta v$  becomes more positive as the percentage of occupied cages decreases. Davies et al (9) argued that, for the case of methyl bromide, the host lattice is undistorted when only 18 percent of the cages are occupied and, consequently, the guest molecules experience tight cage environments, whereas when 59 percent of the cages are occupied, the resulting distortion of the host lattice gives the guest molecule more freedom in the cage, which results in a more negative value of  $\Delta v$ .

Thus it appears that the loose cage - tight cage ideas of Pimentel and Charles (3) may be useful for rationalising the  $\Delta v$  values of guest molecules in more complex host lattices than the low temperature matrices.

### 1.3 Polymorphs of Ice and Clathrate Hydrates

#### 1.3.1 Structures and Vibrations of the Ice Polymorphs

Kamb (10) has reviewed the structures of the ice polymorphs and several reviews of their vibrations are available (11 - 16), so no attempt will be made here to give a comprehensive coverage of these subjects. Instead, sufficient background material will be presented to introduce the discussion of the vibrations of the host lattices of the clathrate hydrates of carbon dioxide.

At present there are three polymorphic phases of crystalline ice known (10, 17). The oxygen atoms of the

water molecules in all of the ice polymorphs are four-coordinated and lie essentially on regular lattice sites, however the orientation of the water molecules, that is the positions of the hydrogen atoms, may be completely ordered, partially ordered or completely disordered. Completely disordered in this context is always qualified by: subject to very short range correlation between the positions of the hydrogen atoms. Ices II, VIII and IX are essentially completely ordered, ices V and VI' are partially ordered and ices Ih, Ic, III, VI, VII and, probably, IV are completely disordered (10, 17). Ice also exists in a vitreous phase in which neither the hydrogen nor the oxygen atoms are ordered and which, like all glasses, can be considered to resemble a liquid which has been supercooled to the point of rigidity. Vitreous ice will not be considered further in this thesis.

The infrared spectra of the ice polymorphs (see below) were recorded on samples held at about 100°K. The translational vibrations of the water molecules will be considered first, since their absorption is the most completely understood. These vibrations occur in the region below  $360\text{ cm}^{-1}$  in all of the phases studied (18 - 20), and the isotopic frequency shifts confirm that the observed absorptions are due to essentially pure translational vibrations. Whalley and Bertie (21) proposed that the absorption by the translational lattice vibrations consists of two components, the order-

allowed and the disorder-allowed absorptions. The order-allowed absorption is a result of the term  $\left(\frac{\partial \mu}{\partial Q}\right)_{\text{ave}}^2$  which is the square of the average over the crystal of the dipole moment derivatives with respect to diffraction-equivalent (displacements of diffraction-equivalent sets of molecules. The disorder-allowed absorption is a result of the term  $\left(\frac{\partial \mu}{\partial Q}\right)_{\text{dis}}^2$  which is derived from the difference between the actual value of the dipole moment derivative with respect to a displacement of a given molecule and the average value over the crystal for the equivalent displacements of the diffraction-equivalent set of molecules to which the molecule belongs (21).

For the ordered phases,  $\left(\frac{\partial \mu}{\partial Q}\right)_{\text{ave}}^2$  is non-zero whereas  $\left(\frac{\partial \mu}{\partial Q}\right)_{\text{dis}}^2$  vanishes. The selection rules based on the first term require that the value of the wave vector of the vibration

---

be essentially zero, because of the law of conservation of momentum, so a small number of narrow bands is expected, as were seen in the far-infrared spectra of the ordered ices

II and IX (19). Bertie et al were able to assign the observed bands to vibrations allowed under the symmetry of the unit cell (22).

For the disordered ice phases,  $\left(\frac{\partial \mu}{\partial Q}\right)_{\text{ave}}^2$  is expected, and found, to be essentially zero, whereas  $\left(\frac{\partial \mu}{\partial Q}\right)_{\text{dis}}^2$  has a non-zero value (21). The absorption due to non-zero values of  $\left(\frac{\partial \mu}{\partial Q}\right)_{\text{dis}}^2$  arises inherently from the disorder, or lack of symmetry, in the lattice, and hence there are no selection rules to limit the values of the wave vectors of

the vibrations which absorb radiation by this mechanism. Thus all of the vibrations are formally infrared active. Hence, the absorption by the disordered ice phases is expected (21) to resemble the density of vibrational states curve (23) and, in fact, Bertie and Whalley (18) were able to show that the density of vibrational states curve deduced from the spectrum agreed rather well with that deduced from incoherent, inelastic neutron scattering studies (24 - 26).

The absorption by the rotational vibrations,  $\nu_R$ , of the water molecules extends between 400 and 1050  $\text{cm}^{-1}$  for  $\text{H}_2\text{O}$  phases and between 350 and 900  $\text{cm}^{-1}$  for  $\text{D}_2\text{O}$  phases, for all of the ice phases that have been studied (20, 27, 28). The  $\nu_R(\text{H}_2\text{O})$  and  $\nu_R(\text{D}_2\text{O})$  bands of the disordered ices Ih and Ic (27) are broad with only poorly defined features, whereas the corresponding bands for the ordered ices II and IX (28, ice IX is referred to as ice III in the reference) exhibit sharp features superimposed on a broad absorption. These sharp features are broader and less intense in samples which contain a few percent of HDO molecules, and this led Bertie and Whalley (28) to argue that they are due to the unit-cell-group-allowed fundamental transitions, since the disorder introduced into the lattice by the HDO molecules is expected to relax the zero-wave-vector selection rule, thereby weakening and broadening the sharp, order-allowed features.

The extreme breadth of the  $\nu_R$  bands in the disordered ice phases can be understood in general terms to arise from

the density of rotational vibrational states curve, since all of the vibrations are infrared active because of the disorder (15). No more detailed understanding of these bands exists at present, but it is probable that other factors contribute to the breadth, since the  $\nu_R$  bands in ices II and IX are also exceedingly broad, with the above-mentioned sharp features superimposed on them, and broad absorption is not expected for the ordered phases. The breadth is presumably due to large anharmonic effects (28) and, if this is the case, a similar contribution from this source should exist for the disordered ices.

Broad, featureless absorptions in the range 1600 to 1700  $\text{cm}^{-1}$  for  $\text{H}_2\text{O}$  phases and 1200 to 1250  $\text{cm}^{-1}$  for  $\text{D}_2\text{O}$  phases of all of the ices studied (20, 27, 28) are assigned to the H-O-H or D-O-D bending vibration,  $\nu_2$ , superimposed on the first overtone of the rotational vibrations,  $2\nu_R$ . Absorptions in the range 2150 to 2300  $\text{cm}^{-1}$  for  $\text{H}_2\text{O}$  phases and 1600 to 1700  $\text{cm}^{-1}$  for  $\text{D}_2\text{O}$  phases are assigned to the second overtone of the rotational vibrations,  $3\nu_R$ , and the combination band,  $\nu_2 + \nu_R$ . These bands are equally broad in the ordered and disordered ice phases, presumably due to anharmonic effects in the ordered phases, and no further understanding of their origin is known.

A discussion of the O-H and O-D stretching bands of the ice phases can be most usefully approached by first considering the absorption by the stretching vibration involving

the isotopically dilute atom of an HDO molecule surrounded by either  $\text{H}_2\text{O}$  or  $\text{D}_2\text{O}$  molecules. The difference in frequency between this vibration and those of the surrounding water molecules is large enough to ensure that it does not interact dynamically with the vibrations of the surrounding water molecules. Therefore, the absorption by  $\nu_{\text{OH}}(\text{HDO})$  of HDO molecules surrounded by  $\text{D}_2\text{O}$  molecules, or by  $\nu_{\text{OD}}(\text{HDO})$  of HDO molecules surrounded by  $\text{H}_2\text{O}$  molecules, only reflects the static field effects (29). These absorptions (and vibrations) are usually called the isolated O-H or O-D stretching bands (and vibrations), and are simply designated the  $\nu_{\text{OH}}(\text{HDO})$  or  $\nu_{\text{OD}}(\text{HDO})$  bands (and vibrations).

Bertie and Whalley (27) observed single, featureless bands with half-widths of 50 and 30  $\text{cm}^{-1}$  for the  $\nu_{\text{OH}}(\text{HDO})$  and  $\nu_{\text{OD}}(\text{HDO})$  bands of ice Ih, respectively, whereas the corresponding bands of the ordered ices II and IX (28) showed several sharp features, each with a half-width of about 5  $\text{cm}^{-1}$ . They (27) were able to interpret the multiplet absorption of the ordered ices in terms of the number of non-equivalent O-O bonds in these structures. The larger half-widths of the  $\nu_{\text{OH}}(\text{HDO})$  and  $\nu_{\text{OD}}(\text{HDO})$  bands of ice Ih, compared to those of ice II and IX, were explained by Bertie and Whalley in the following way. The disorder in the hydrogen atom positions in ice Ih requires the positions of the oxygen atoms to be slightly disordered, thereby producing a small range of O-O bond lengths for each set of



diffraction-equivalent bonds. This, in turn, produces a small range of absorption frequencies for the isolated O-H and O-D stretching vibrations of ice Ih, thereby producing broader bands than those seen for the ordered ices.

It should be noted that the exact half-widths of the  $\nu_{\text{OH}}$  (HDO) and  $\nu_{\text{OD}}$  (HDO) bands of ice Ih appear to depend on the method used to prepare the infrared samples. When ice is milled with isopentane (27) or liquid propane, propylene or Freon 13 (30), the half-widths are about 50 and 30  $\text{cm}^{-1}$ . For infrared samples prepared by condensing water onto a plate held at 173°K, and cooling it to 100°K (31), Bertie *et al* reported that the  $\nu_{\text{OH}}$  (HDO) band had a half-width of about 25  $\text{cm}^{-1}$ . For samples prepared by freezing a capillary film of water, Ford and Falk (32) reported that the  $\nu_{\text{OD}}$  (HDO) band had a half-width of 18  $\text{cm}^{-1}$  at -173°C.

The very broad bands exhibited by all of the  $\text{H}_2\text{O}$  phases at about 3200  $\text{cm}^{-1}$  and by all of the  $\text{D}_2\text{O}$  phases at about 2400  $\text{cm}^{-1}$  are due to the O-H stretching vibration,  $\nu_{\text{OH}}$  ( $\text{H}_2\text{O}$ ), and the O-D stretching vibration,  $\nu_{\text{OD}}$  ( $\text{D}_2\text{O}$ ), respectively (20, 27, 28). Early workers (29, 33, 34) assigned the features observed on the  $\nu_{\text{OH}}$  ( $\text{H}_2\text{O}$ ) band of ice Ih to crystal vibrations derived from the symmetric,  $\nu_1$ , and antisymmetric,  $\nu_3$ , O-H stretching vibrations and the first overtone,  $2\nu_2$ , of the bending vibration, of isolated water molecules. Bertie and Whalley (27) have pointed out that this assign-

ment is suspect. They argued that the intramolecular  $\nu_1$  vibrations couple in the crystal to produce a broad band of vibrational frequencies, and that the same occurs for the  $\nu_3$  vibrations. Further, since the crystal has no symmetry and the frequencies derived from  $\nu_1$  probably overlap with those derived from  $\nu_3$ , they argued that there is nothing to prevent  $\nu_1$  and  $\nu_3$  vibrations from coupling to produce mixed vibrations. Such a scheme is capable of producing a band with several features upon it, and five features were identified on the  $\nu_{OD}$  ( $D_2O$ ) band (27) of ice Ih. Therefore, Bertie and Whalley argued that there is no need to invoke  $2\nu_2$  to explain one of the features, and that the absorption should be attributed to a broad density of vibrational states curve multiplied by an intensity distribution function, neither of which need be a smooth function of frequency. These same considerations apply to the stretching bands of the other disordered ice phases.

The absorptions by  $\nu_{OH}$  ( $H_2O$ ) and  $\nu_{OD}$  ( $D_2O$ ) of the ordered forms of ice are just as broad as those by the disordered forms, although there is slightly more detail near the top of the bands. The breadth is presumably due to anharmonic effects (28), so it is possible that even a knowledge of the density of states curve of the disordered ices will not be sufficient to give a detailed understanding of the  $\nu_{OH}$  ( $H_2O$ ) and  $\nu_{OD}$  ( $D_2O$ ) bands.

In summary it can be said that the absorption by the

translational vibrations of the ice polymorphs is well understood, in contrast to the much poorer understanding of the absorption by the other vibrations.

### 1.3.2 Structures and Vibrations of the Clathrate Hydrate Polymorphs

Clathrate hydrates are a class of solids in which a wide variety of small molecules occupy almost spherical holes in ice-like lattices formed by hydrogen-bonded water molecules (35). The majority of the clathrate hydrates studied up to the present time conform to one of two structural types called structure I and structure II.

The single-crystal X-ray diffraction study by McMullan and Jeffrey (36) of the structure I hydrate of ethylene oxide at  $-25^{\circ}\text{C}$ , provides the most detailed knowledge available of the positions of the oxygen atoms in structure I hydrates. The oxygen atoms of structure II hydrates were similarly defined by the X-ray diffraction study of a single crystal of the double hydrate of tetrahydrofuran and hydrogen sulphide at  $-20^{\circ}\text{C}$  by Mak and McMullan (37).

The four types of cages found in the structure I and structure II hydrates are shown in Fig. 1.2, as viewed along the axes of highest symmetry (38), and some geometric parameters associated with the unit cells and cages are listed in Table 1.5 (39). Only the oxygen atoms are shown in Fig. 1.2, and each atom is bonded to four other atoms, although the fourth bonds are directed outwards from the

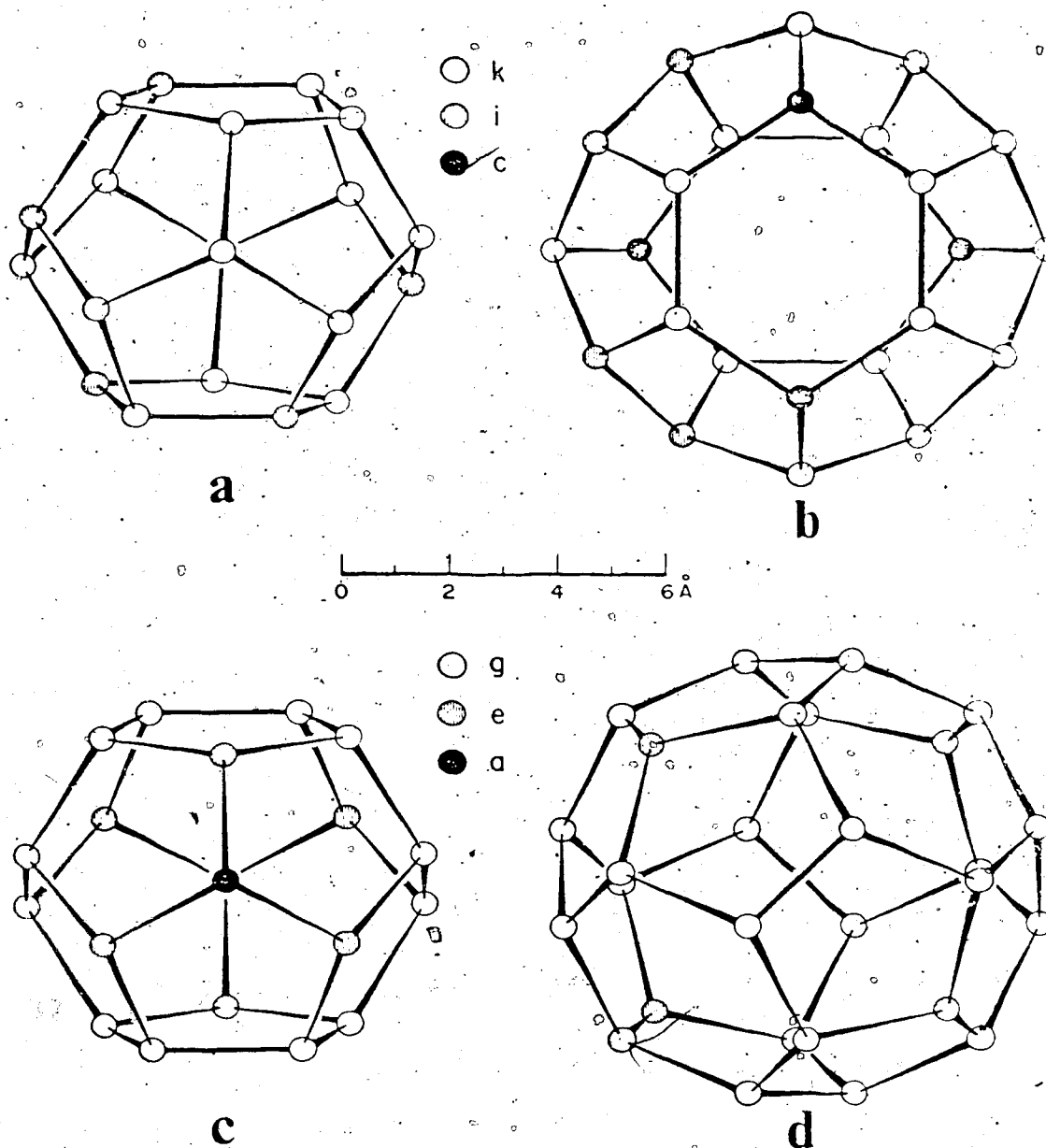


Fig. 1.2. Cages of structure I (a, b) and structure II (c, d) clathrate hydrates viewed along the axes of highest symmetry. Literal identification of the sites follows the notation of The International Tables for X-ray Crystallography. Reproduced from reference 38.

Table 1.5

Geometric Parameters of the Unit Cells  
and Cages of the Structure I and  
Structure II Clathrate Hydrates<sup>a, b</sup>

Parameter	Structure I <sup>c</sup>	Structure II <sup>c</sup>
Space group, cell parameter	Pm3n, 12.03 Å	Fd3m, 17.31 Å
Number of H <sub>2</sub> O molecules	46	136
Non-equivalent O sites	6 (c), 16 (i), 24 (k)	8 (a), 32 (e), 96 (g)
Oxygen site symmetry	$\bar{4}2m$ , 3m, m	$\bar{4}3m$ , 3m, m
Departure of O-O-O		
angle from tetrahedral:		
Average at O site	1.2°, 1.2°, 5.1°	0°, 2.1°, 3.6°
Average in structure	3.7°	3.0°
Average O-O length	2.793 Å	2.790 Å
Large cages:		
Number, symmetry	6, $\bar{4}2m$	8, $\bar{4}3m$
Oxygen sites	4 (c), 8 (i), 8 (k), 4 (k)	4 (e), 12 (g), 12 (g)
Distance to center (Å)	4.25, 4.47, 4.06, 4.645	4.729, 4.715, 4.635
Average cage radius	4.33 Å	4.683 Å
Small cages:		
Number, symmetry	2, m3	16, $\bar{3}m$
Oxygen sites	8 (i), 12 (k)	2 (a), 6 (e), 12 (g)
Distance to center (Å)	3.83, 3.96	3.748, 3.845, 3.956
Average cage radius	3.91 Å	3.902 Å

a) Taken from reference 39.

b) The structure I parameters are for ethylene oxide hydrate at -25°C; the structure II parameters are for the tetrahydrofuran-hydrogen sulphide hydrate at -20°C.

c) The symmetry symbols follow the notation of The International Tables for X-ray Crystallography.

cages and are not shown (40). The smaller cages in the two structures (Fig. 1.2, a and c) are essentially the same, with twelve five-sided faces; they are pentagonal dodecahedra and, in the literature on clathrate hydrates, this is abbreviated to 12-hedra. The large structure I cage (Fig. 1.2, b) consists of twelve pentagonal faces and two parallel hexagonal faces. It is a tetrakaidecahedron, which is usually abbreviated to 14-hedron. The  $\bar{4}$  axis of the cage is defined by the line joining the centers of the two hexagons. The variation in the radius of this cage is 14 percent (38), and it can be considered as an oblate spheroid with its shorter axis defined by the  $\bar{4}$  axis of the cage. The large structure II cage has tetrahedral symmetry (Fig. 1.2, d) and consists of twelve pentagonal faces and four hexagonal faces. It is a hexakaidecahedron, which is usually abbreviated to 16-hedron. The variation in the radius of this cage is only 2 percent (38), so it approximates a sphere. The free diameters, that is the diameters after allowing for the van der Waals radii of the water molecules, are about 5.0, 5.8 and 6.6 Å for the 12-, 14- and 16-hedral cages respectively (39).

The dielectric properties of the many structure I and structure II hydrates that have been studied (41) clearly indicate that the positions of the hydrogen atoms are disordered, as was found for the disordered polymorphs of ice (Section 1.3.1). In fact, the tetrahedral diffraction

symmetry of the (a) sites of the oxygen atoms in the small structure II cages is clearly incompatible with the water molecules, whose maximum symmetry is  $C_{2v}$ , being ordered on these sites (38).

Guest molecules may be accommodated by any of the four cages shown in Fig. 1.2. Essentially the only criteria for occupancy are that the guest molecule must be small enough to fit in the cage and must not react with water. In general, guest molecules with van der Waals diameters of 5.5 Å or less form structure I hydrates, whereas those with van der Waals diameters of greater than 5.5 Å form structure II hydrates, although there are exceptions to these rules. Generally, the larger cages of the two structures are fully occupied, whereas the occupancy of the smaller cages is only appreciable if the van der Waals diameter of the guest molecule is about 5.2 Å or less. For example, ethylene oxide has a largest van der Waals diameter of 5.2 Å (42), and, under equilibrium conditions, it forms a structure I hydrate with the 14-hedral cages fully occupied and about 20 to 40 percent of the 12-hedral cages occupied (36, 43), whereas cyclopropane has a van der Waals diameter of 5.4 Å (42) and forms a structure I hydrate with the large cages fully occupied and the small ones empty. Tetrahydrofuran has a largest van der Waals diameter of 5.9 Å (42) and it forms a structure II hydrate with the 16-hedral cages fully occupied, while the 12-hedral cages may be empty (44, 45) or, in the

double hydrate (37) may be 46 percent occupied by hydrogen sulphide molecules.

There have been very few studies of the infrared spectra of well characterised samples of clathrate hydrates. The far-infrared spectra of characterised samples of ethylene oxide hydrate (43), cyclopropane hydrate (46), hexamethylenetetramine hydrate (47) and tetrahydrofuran hydrate (44) have been reported, as have the mid-infrared spectra of ethylene oxide hydrate (48) and hexamethylenetetramine hydrate (49). The above studies of the vibrations of the clathrate hydrates will be briefly reviewed, with the exception of those of hexamethylenetetramine hydrate, which forms a quite different structure from those previously discussed, and is not pertinent to the subject matter of this thesis.

Bertie and Othen (43) have studied the far-infrared spectrum between  $360$  and  $20\text{ cm}^{-1}$  of the structure I hydrate of ethylene oxide at  $100^\circ\text{K}$ . Continuous, broad absorption was observed, and that above  $100\text{ cm}^{-1}$  was similar to the absorption by ice Ih in the same region (18). From the isotopic frequency shift, this absorption was assigned to the translational vibrations of the water lattice, and the fact that only broad absorption was observed, confirmed the orientational disorder of the water molecules in this structure I hydrate. Theoretical considerations (21 and Section 1.3.1) indicate that the absorption may be the



superposition of nine sharp features, due to the transitions allowed under the factor group of the diffraction space group, on a broad absorption, resulting from the transitions activated by the disorder. Since no sharp features were seen, it was argued that the observed absorption was entirely disorder-allowed, and approximated the density of states curve multiplied by an intensity distribution function, which is approximately proportional to the square of the frequency (21, 43).

Bertie and Othen (43) noted that there appears to be an empirical correlation between the frequencies of strong absorption and the number, length and distribution of hydrogen bonds for the orientationally disordered polymorphs of ice. They pointed out (48) that in ethylene oxide hydrate at 100°K, 52 percent of the hydrogen bonds are 2.75 Å long, 26 percent are 2.79 Å long and the remainder are either 2.74 or 2.82 Å long, compared to the single hydrogen bond length in ice Ih of about 2.75 Å at 100°K. The far-infrared spectrum of ice Ih contains a fairly sharp peak at 229.2  $\text{cm}^{-1}$  (18), which can be related to the single type of hydrogen bond of length 2.75 Å. The strongest feature in the far-infrared spectrum of ethylene oxide hydrate is at 229.6  $\text{cm}^{-1}$  (43), so this can be related to the 52 percent of the hydrogen bonds of length 2.75 Å in the hydrate. The hydrate absorbs more strongly to high frequency of the band maximum than ice, so Bertie and Othen (43) related this broadening to the

9 percent of the 2.74 Å bonds in the structure. The frequency maxima in the far-infrared spectra of ices V (19) and VI (20) are at 200 and 187  $\text{cm}^{-1}$  respectively, and Bertie and Othen (43) noted that they could be related to the weighted mean hydrogen bond lengths of 2.797 and 2.813 Å in the two structures. Features are also observed at 185 and 210  $\text{cm}^{-1}$  in the spectrum of the hydrate and these were related to the 26 percent of 2.79 Å bonds and the 13 percent of 2.82 Å bonds in the hydrate.

The absorption by the intermolecular vibrations of the encaged ethylene oxide molecules was expected below 100  $\text{cm}^{-1}$ , and a broad plateau was observed between 100 and 50  $\text{cm}^{-1}$  (43). After the predicted absorption by the translational water vibrations was subtracted, a broad band remained, extending to low frequency of about 100  $\text{cm}^{-1}$  with its maximum at about 50  $\text{cm}^{-1}$ . This band and, therefore, the plateau in the spectrum, were tentatively assigned to the intermolecular vibrations of the ethylene oxide molecules.

Bertie et al (46) have studied the far-infrared spectrum between 360 and 20  $\text{cm}^{-1}$  of the structure I hydrate of cyclopropane at 100°K. The absorption below 100  $\text{cm}^{-1}$  decreased rapidly with decreasing frequency, in contrast to the plateau observed between 100 and 50  $\text{cm}^{-1}$  for ethylene oxide hydrate. Thus the tentative assignment (43) of the plateau to the intermolecular vibrations of encaged ethylene oxide molecules was confirmed. The absorption above 100  $\text{cm}^{-1}$  by

cyclopropane hydrate was almost identical to that by ethylene oxide hydrate (43), except that it was shifted to low frequency by about 2 percent. Bertie et al (46) attributed this shift to the longer lattice parameter and, therefore, hydrogen bonds in cyclopropane hydrate.

The far-infrared spectrum between 70 and  $7\text{ cm}^{-1}$  of the structure II hydrate of tetrahydrofuran between 80 and  $17^\circ\text{K}$  has been obtained by Klug and Whalley (44). They observed two absorptions with half-widths of about  $15\text{ cm}^{-1}$ , centered at 25 and  $38\text{ cm}^{-1}$  at  $17^\circ\text{K}$ , superimposed on broad absorption. They assigned these bands to the rotational oscillations of the encaged tetrahydrofuran molecule about the principal axis perpendicular to the plane of the molecule and about the axis in the plane of the molecule perpendicular to the dipolar axis, respectively; the force constants calculated for these oscillations were 450 and  $600\text{ ferg rad}^{-2}$  respectively. From the integrated absorptivity of the two bands, they obtained a value of 1.63 Debyes for the dipole moment of tetrahydrofuran, which is close to the gas phase and solution values. They were able to calculate a contribution to the low frequency refractive index of 0.105 from the absorptivity, using the Kramers-Kronig relationship, and this agrees well with the 0.11 value calculated from dielectric measurements (50).

Klug and Whalley (44) deduced from the temperature dependence of the absorption bands that the bands must

remain quite broad at  $0^{\circ}\text{K}$ , unless a major change in the temperature dependence occurs below  $17^{\circ}\text{K}$ . They argued that this means that the breadth at  $17^{\circ}\text{K}$  is mainly due to a variation in the force constant from cage to cage. They stated that this variation in the force constant can arise from the following factors: tetrahydrofuran molecules occupy a number of non-equivalent potential minima in otherwise equivalent cages; the variation from cage to cage of the van der Waals, repulsive and electrostatic forces caused by the disorder in the orientations of the water molecules; the coupling of the vibrations of neighbouring tetrahydrofuran molecules; and, finally, anharmonicity. They noted that the first and last effects are temperature dependent whereas the others are essentially temperature independent.

Klug and Whalley (44) showed that the intermolecular coupling and electrostatic contributions to the breadth are extremely small for this hydrate. They had no direct evidence on whether the occupancy of non-equivalent potential minima contributes significantly to the breadth of the bands at  $17^{\circ}\text{K}$  but, if it does, the breadth should be reduced by this amount at  $0^{\circ}\text{K}$ . They argued that anharmonicity cannot influence the breadth of the bands at  $0^{\circ}\text{K}$ , and that the van der Waals forces should be almost independent of the orientations of the water molecules, because they depend on the polarizabilities of the molecules and it is known (51) that the polarizability of a water molecule is almost

isotropic. Thus van der Waals forces were not expected to vary greatly from cage to cage or, consequently, to make a major contribution to the breadth. Klug and Whalley argued that the repulsive forces between the hydrogen atoms of the water molecules and those of tetrahydrofuran do depend on the orientational disorder of the water molecules, and therefore are probably the main source of the breadth of the bands.

The breadth of the bands greatly increased as the temperature was raised, and Klug and Whalley suggested this could be due to the following effects: the limited life-time of the excited vibrational states due to transitions to lower states, and interaction with lattice vibrations; the limited life-time due to reorientation of the molecules; and the increasing occupancy of higher potential minima which would have different force constants. It can be noted that the first effect is what was previously referred to by these authors as anharmonicity. They showed that the contribution to the half-width from reorientation is negligible, even at 80°K, and concluded that the temperature dependent broadening is due to the other effects.

Finally, no absorption by the pseudorotation vibration of the molecule, which is observed in gas phase spectra (52), were seen in the spectra of the clathrate hydrate (44). Klug and Whalley concluded that either the pseudorotation is quenched in the cage or that the bands are too weak to

be observed, because either they are intrinsically weak or they are broadened by interaction with the cage.

The only mid-infrared study of well characterized samples of a clathrate hydrate which has one of the two common structural types is that, between 4000 and 360  $\text{cm}^{-1}$ , of the structure I hydrate of ethylene oxide at 100°K by Bertie and Othen (48). The absorption due to the water was extremely similar to the mid-infrared absorption by ice Ih (27). The general assignment and the discussion of the breadth of the bands given in Section 1.3.1 applies equally well to the spectrum of the hydrate, and need not be repeated.

Bertie and Othen (48) interpreted the fact that the frequencies of maximum absorption in the  $\nu_{\text{OH}}(\text{H}_2\text{O})$  and  $\nu_{\text{OD}}(\text{D}_2\text{O})$  bands of the hydrate are the same as those of ice Ih at 100°K (27) as indicating that this frequency in the hydrate is determined by the absorption by the 52 percent of the bonds which are 2.75 Å long. The features at the top of the hydrate bands are broader than those on the ice bands, and they attributed this to the influence of the other bonds in the hydrate.

Bertie and Othen (48) noted that the featureless breadth of the  $\nu_{\text{OH}}(\text{HDO})$  and  $\nu_{\text{OD}}(\text{HDO})$  bands, which have half-widths of about 125 and 80  $\text{cm}^{-1}$  respectively, provided further evidence of the orientational disorder of the water molecules in the clathrate structure. They (48) presented a plot of

the frequencies of the  $\nu_{OD}$  (HDO) bands of ices Ih, Ic, II, V, VI, and IX and ethylene oxide hydrate against the O-O distances in the ordered phases and against the weighted mean O-O distances in the disordered phases. The data were found to fit two straight lines of slopes 510 and 910  $\text{cm}^{-1}\text{\AA}^{-1}$  for the ordered and disordered phases, respectively; however one point for the ordered ice phase, IX, fell on the line for the disordered phases. The point for ethylene oxide hydrate fell close to the line for the disordered ice phases. Bertie and Othen (48) argued that, since only a single band was seen for each disordered phase, the half-widths of the  $\nu_{OD}$  (HDO) bands should reflect the range of crystallographically non-equivalent bond lengths in these phases. They were able to obtain an approximate correlation between the half-widths and the weighted mean deviations from the weighted mean of the hydrogen bond lengths in the disordered phases.

The absorption by the encaged ethylene oxide molecules was, in general, readily assigned by comparison with the absorptions of gaseous and liquid ethylene oxide. Bertie and Othen (48) noted that the strongest ethylene oxide absorption, at  $870\text{ cm}^{-1}$ , in the spectrum of the deuterate is reduced to an inflection point on the  $\nu_R(\text{H}_2\text{O})$  band in the spectrum of the hydrate. They attributed this effect to transition dipole-transition dipole coupling between the guest and host vibrations. The most notable feature of

the ethylene oxide absorptions was the fact that the absorption due to the ring breathing mode is split into a doublet separated by  $2\text{ cm}^{-1}$ . Bertie and Othen remarked that the possible causes of this effect are intermolecular coupling between neighbouring ethylene oxide molecules, the presence of two preferred orientations for the guest molecule in the 14-hedral cages, and a difference in frequency of the ring breathing mode of an ethylene oxide molecule in the 12- and 14-hedral cages. They concluded that the most likely reason for the splitting is the presence of two preferred orientations of the ethylene oxide molecule in the 14-hedral cages.

### 1.3.3 Physical Properties of the Clathrate Hydrates of Trimethylene Oxide

Rosso and Carbonnel (53) derived the phase diagram for the trimethylene oxide-water system by thermal analysis, and it is shown in Fig. 1.3. The four solid phases are ice Ih, solid trimethylene oxide, the structure I hydrate of trimethylene oxide (hereafter called TMO hydrate I) and the structure II hydrate of trimethylene oxide (hereafter called TMO hydrate II). All of the parameters of the phase diagram are listed in Table 1.6. The liquidus and solidus associated with the metastable eutectic,  $E_1$ , are indicated as dashed lines in Fig. 1.3, and the associated solid phases, which are not shown in Fig. 1.3, are TMO hydrate and solid TMO.



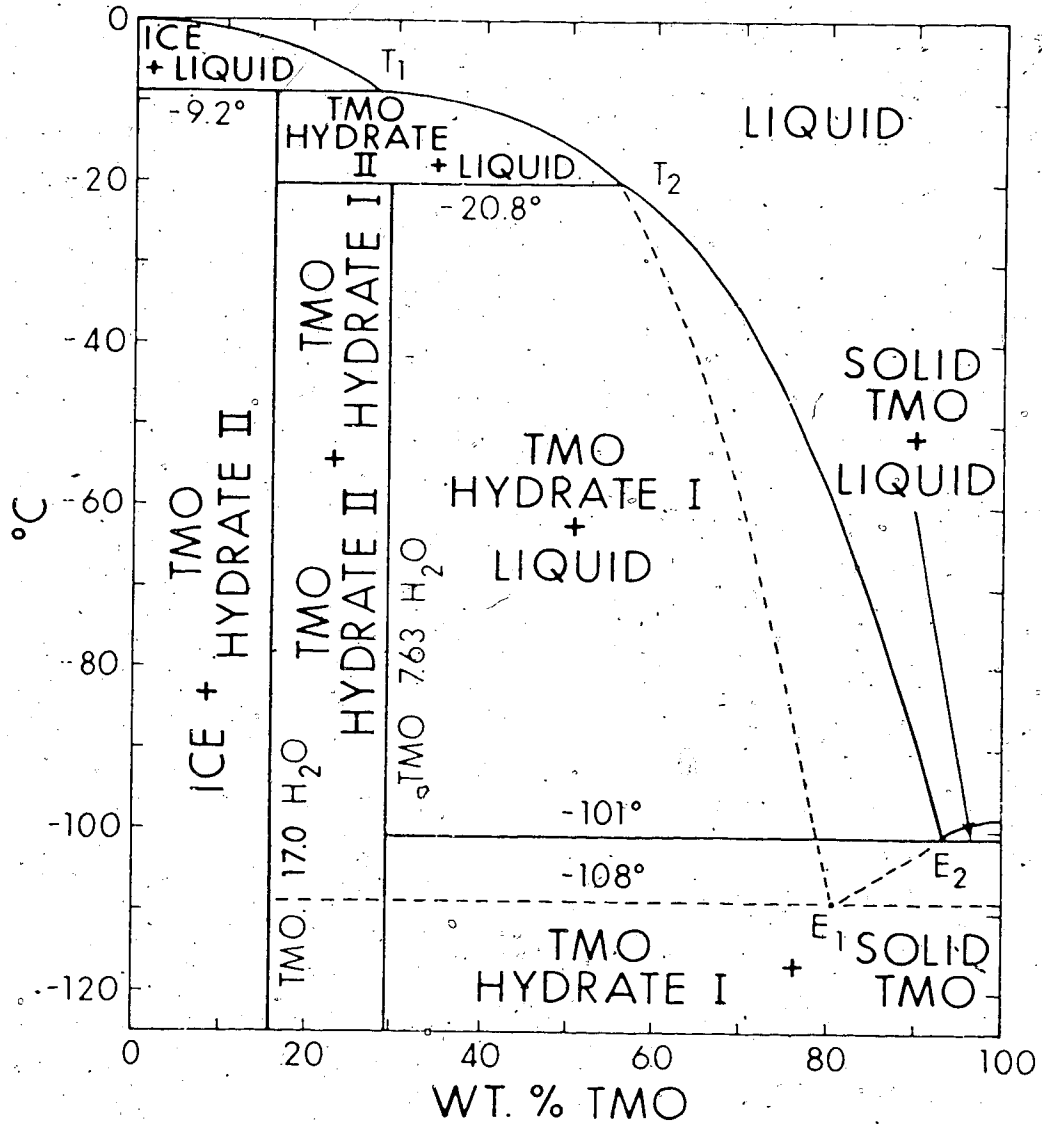


Fig. 1.3: Phase diagram of the trimethylene oxide-water system. The solid phases associated with the metastable eutectic (dashed lines) are TMO hydrate II and solid TMO (not shown).

Table 1.6

Parameters of the Trimethylene  
Oxide-Water Phase Diagram<sup>a</sup>

	Temp. (°C)	Composition <sup>b</sup>	Equilibrium
Peritectic T <sub>1</sub>	9.2	27.9	ice + liquid (T <sub>1</sub> ) ⇌ TMO hydrate II
Peritectic T <sub>2</sub>	-20.8	53.8	TMO hydrate II + liquid (T <sub>2</sub> ) ⇌ TMO hydrate I
Eutectic E <sub>2</sub>	-101	93.1	liquid (E <sub>2</sub> ) ⇌ TMO hydrate I + solid TMO
Eutectic E <sub>1</sub> (metastable)	-108	81	liquid (E <sub>1</sub> ) ⇌ TMO hydrate II + solid TMO

a) Taken from reference 53.

b) As weight percent of trimethylene oxide.

The phase diagram is most efficiently described by considering the cooling of a solution of trimethylene oxide in water, for example a solution with the structure I composition of TMO.7.63 H<sub>2</sub>O. At about -10°C, the liquidus T<sub>1</sub>T<sub>2</sub> (Fig. 1.3) is encountered, which results in the formation of some TMO hydrate II and a corresponding increase in the concentration of trimethylene oxide in the liquid. Further cooling results in more encounters with the T<sub>1</sub>T<sub>2</sub> liquidus and the formation of more TMO hydrate II. When the peritectic point T<sub>2</sub> is reached, there is an equilibrium between an aqueous solution of composition 53.8 weight percent of trimethylene oxide, TMO hydrate II and TMO hydrate I. Further cooling down the liquidus T<sub>2</sub>E<sub>2</sub> results in the formation of TMO hydrate I. At the eutectic point, E<sub>2</sub>, there is an equilibrium between an aqueous solution of composition 93.1 weight percent of trimethylene oxide, TMO hydrate I and solid trimethylene oxide. Thus the completely solidified mixture below -101°C contains TMO hydrate II, TMO hydrate I and solid trimethylene oxide.

Powder X-ray diffraction photographs confirmed that the two hydrates have the well known structures I and II, and gave the cubic unit cell parameter as 12.02 ± 0.05 Å at -130°C and 12.15 ± 0.02 Å at -30°C for TMO hydrate I (54), and 17.095 ± 0.006 Å at -138°C for TMO hydrate II (55).

Ross and Carbonell (53) reported the composition of TMO hydrate I to be TMO.6.5 H<sub>2</sub>O or 7.1 TMO.46 H<sub>2</sub>O. This

corresponds to full occupancy of the large cages and 55 percent occupancy of the small cages. Davidson et al (45, 54) concluded that the composition is TMO.7.63 H<sub>2</sub>O or 6 TMO.46 H<sub>2</sub>O, which corresponds to full occupancy of the large cages and zero occupancy of the small cages. The largest van der Waals diameter of trimethylene oxide is 6.2 Å, so it is too large to fit in the small cage (Section 1.3.2) and therefore, following Davidson, TMO.7.63 H<sub>2</sub>O is believed to be correct and is used in the phase diagram (Fig. 1.3) and elsewhere in this thesis. Rosso and Carbonnel (53) reported the composition of TMO hydrate II to be TMO.17 H<sub>2</sub>O, which corresponds to full occupancy of the large cages and zero occupancy of the small cages; it was assumed that this value is correct. The results of all of the preparations of TMO hydrate I and II in this work (Chapter 2) supported the adopted compositions for the two hydrates. It should be noted that trimethylene oxide and cyclopropane are the only molecules known to form hydrates of both structures. They are among the largest molecules that form structure I hydrates and the smallest that form structure II hydrates.

Davidson et al have studied the dielectric relaxation of the water molecules of TMO hydrate I (45) between 118 and 248°K and of TMO hydrate II (56) between 4 and 250°K. It was found that the water molecules of TMO hydrate I relax about twenty times faster than those of TMO hydrate II at

about 170°K. The values for the Arrhenius activation energies are 5.8 and 7.0 kcal mole<sup>-1</sup> for TMO hydrate I and TMO hydrate II respectively.

Davidson et al have studied the dielectric relaxation of the guest molecules of TMO hydrate I (54) and TMO hydrate II (56) between 1.8 and 200°K. Of particular interest, is the behaviour of the limiting low and high frequency permittivities associated with the dispersion due to the reorientation of the guest molecule,  $\epsilon_{02}$  and  $\epsilon_{\infty 2}$  respectively. At temperatures such that the measuring frequency is far below the frequency of reorientation,  $\epsilon_{02}$  is measured and usually increases slightly with decreasing temperature (56). As the reorientation frequency passes through the measuring frequency with decreasing temperature, the measured permittivity drops to  $\epsilon_{\infty 2}$ , which then remains essentially constant as the temperature is decreased further. This behaviour was found by Davidson et al (56) for TMO hydrate II. For TMO hydrate I, however, Davidson et al (54) found that  $\epsilon_{02}$  decreased sharply from about 13 to 5 between about 150 and 80°K, even though the reorientation frequency was well above the measuring frequency at these temperatures. A further decrease in the permittivity as the reorientation frequency passed through the measuring frequency was observed at lower temperatures. Davidson et al (54) attributed the decrease in  $\epsilon_{02}$  between 150 and 80°K to a transition involving the parallel ordering of the

dipoles of nearest neighbour trimethylene oxide molecules.

Davidson et al (54) also studied the reorientation of the guest molecules directly, at temperatures below 80°K, by measuring the frequency of maximum dielectric absorption (or loss) at various temperatures. They found the Arrhenius activation energies for the reorientation of the trimethylene oxide dipoles to be 2.1 and 0.41 kcal mole<sup>-1</sup> for TMO hydrate I below the ordering transition (54) and TMO hydrate II (56) respectively. Thus it is clear that a trimethylene oxide molecule experiences much more freedom in the 16-hedral structure II cages than in the 14-hedral structure I cages. This is also indicated by the temperatures at which the guest molecule reorientation rate is 1 kHz, which were found (54, 56) to be 51.5 and 12.1°K for TMO hydrate I and TMO hydrate II respectively.

Davidson et al (54) also noted that for samples of TMO hydrate I which had been quenched through the transition region by immersion in liquid nitrogen, the amplitudes of the dispersion ( $\epsilon_{02} - \epsilon_{\infty 2}$ ) and loss decreased with time to an equilibrium value, whereas samples cooled slowly through the transition region yielded values which did not greatly exceed the equilibrium values. This is the only example of time dependent behaviour found in a clathrate hydrate (54).

Davidson et al (54) also measured the proton magnetic resonance absorption by the trimethylene oxide molecules of TMO deuterate I as a function of temperature between 250

and 1.8°K. Their plot of the proton second moment against temperature shows a rise from 0.31 Gauss<sup>2</sup> at 243°K to the rigid lattice value of 13.4 Gauss<sup>2</sup> at 5°K, with a plateau region between 95 and 70°K. This is in contrast to a similar plot for TMO deuterate II (57, 58) which shows the normal temperature dependence, which is a rise from a low value to a high value with decreasing temperature, with no plateau region (57). Thus the plateau region of the structure I plot is clearly associated with the transition deduced from the permittivity measurements.

Davidson et al (54) suggested that, during the ordering transition, the guest dipoles align along the  $\bar{4}$  axis of the 14-hedral cages (Section 1.3.2) and that this is potentially possible as long as the guest-water interactions favour, or at least permit, it. They (54) performed a calculation of the van der Waals and repulsive interactions between the water molecules of the 14-hedral cage and the trimethylene oxide molecule using the Lennard-Jones 6-12 potential, and concluded that the most stable configurations are those with the dipolar axis of the trimethylene oxide molecule collinear with the  $\bar{4}$  axis of the cage, together with the displacement of the trimethylene oxide molecule from the center of the cage such that its oxygen atom approaches the center of the hexagonal ring (Fig. 1.2). They found that the potential energy varied as the molecule rotated about the  $\bar{4}$  axis of the cage, passing through 6 minima during a

360° rotation. The minima occurred when the plane of the trimethylene oxide ring nearly coincided with the planes through the cage center which contain pairs of opposite water molecules of the hexagonal ring (Fig. 1.2). The barriers to rotation between the six potential minima were calculated to be less than 1 kcal mole<sup>-1</sup>, and the energy of the different minima were the same to within 0.05 kcal mole<sup>-1</sup>. Davidson et al (54) calculated that the displacement of the trimethylene oxide molecule placed the guest dipole, treated as a point dipole, about 1.2 Å from the cage center. They (54) calculated the interaction energy between this dipole and the average, dipolar, electrostatic field of the water molecules to be about 1 kcal mole<sup>-1</sup> higher at this position than at the cage center, and concluded that there is a statistical tendency for the dipolar fields to counteract the displacement favoured by the van der Waals interactions.

Davidson et al (54) pointed out that the interactions between the guest dipoles favour parallel ordering of nearest neighbour guest dipoles. Further, the most stable configuration of the lattice is that in which neighbouring guest dipoles point in the same sense along chains, extending in the x, y and z directions, with the sense alternating between adjacent chains. They (54) calculated an energy of -0.72 kcal mole<sup>-1</sup> for this completely ordered state with respect to the state with random orientations, which



they stated corresponds to an ordering transition temperature of about 360°K. They concluded that it is not surprising that the perturbing effects of the fields of the water molecules cause the temperature of the transition to be lowered to about 105°K. They were, thus, able to provide some justification for their interpretation of the experimental results, but their calculations were based on simple models and are clearly approximate.

There are no other published data on the hydrates of trimethylene oxide.

#### 1.4 Vibrations of Trimethylene Oxide

The trimethylene oxide molecule is shown in Fig. 1.4. It contains ten atoms and therefore has 24 fundamental intramolecular vibrations. It can be considered to belong to the point group  $C_{2v}$  (see below), so its normal vibrations form a basis to the representation:

$$8A_1 + 4A_2 + 6B_1 + 6B_2 .$$

The  $A_1$ ,  $B_1$ , and  $B_2$  vibrations are infrared active and all of the vibrations are Raman active. The representations formed by the internal coordinates are shown in Table 1.7. The ring vibrations can be defined in terms of five in-plane internal coordinates and one out-of-plane internal coordinate.

The  $B_2$  ring vibration,  $\nu_{24}$ , which is usually called the ring puckering vibration, has been studied extensively by far-infrared (59 - 64), Raman (63, 65, 66)

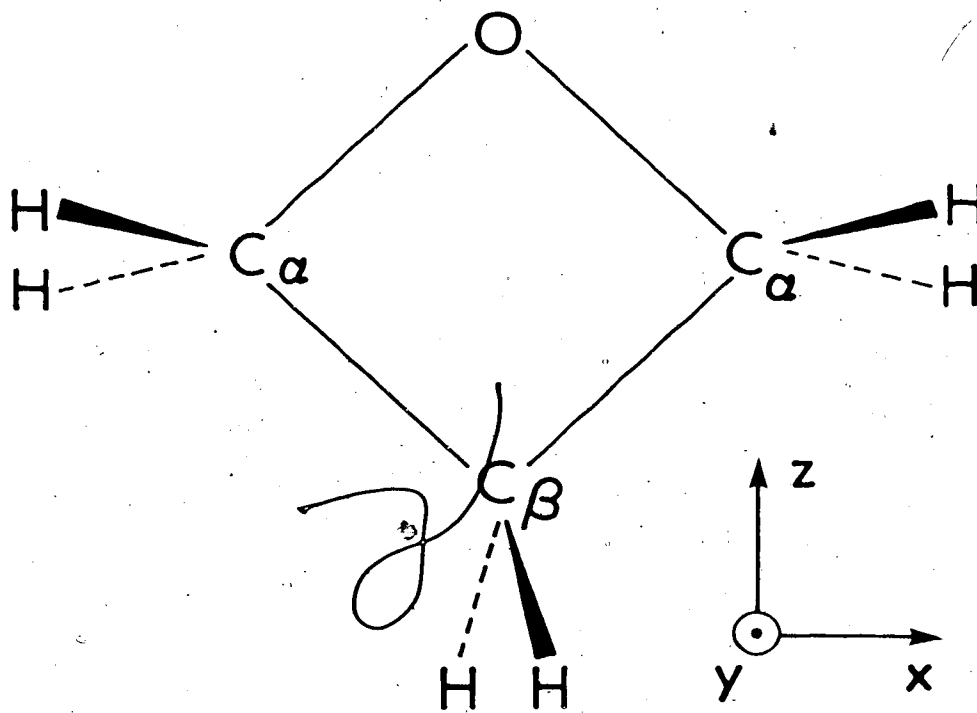


Fig. 1.4. Molecular structure of trimethylene oxide. The plane  $zx$  defines the plane of the ring. The hydrogen atoms bonded to each carbon atom, which should be eclipsed, have been offset for clarity.

Table 1.7

Representations formed by the  
Internal Coordinates of Trimethylene  
Oxide under the Point Group  $C_{2v}$

C-H stretching	$2A_1 + A_2 + B_1 + 2B_2$
CH <sub>2</sub> deformation	$2A_1 + B_1$
CH <sub>2</sub> wag	$A_1 + 2B_1$
CH <sub>2</sub> twist	$2A_2 + B_2$
CH <sub>2</sub> rock	$A_2 + 2B_2$
Ring vibration	$3A_1 + 2B_1 + B_2$
	<hr/>
	$8A_1 + 4A_2 + 6B_1 + 6B_2$

and microwave (67 - 69) spectroscopy. Since this work is not directly related to the subject matter of this thesis, only a brief summary of the results will be given. The potential function governing the ring puckering vibration of trimethylene oxide contains a barrier at the planar configuration of  $15.1 \text{ cm}^{-1}$  (63). The ground state vibrational energy level lies  $12.2 \text{ cm}^{-1}$  above the top of the barrier (63), and thus trimethylene oxide can be considered to be planar, and its point group is  $C_{2v}$ .

The mid-infrared and Raman spectra of the various phases of trimethylene oxide have been studied by a number of workers (70 - 80). Only certain of the more recent studies (74, 76, 78 - 80) will be considered, since the work in references 75 and 77 has been repeated in references 78 - 80 and the larger volume of information and the higher resolution available to Wiëser et al. (78 - 80) make their results more reliable. The results are summarised in Table 1.8, together with what is considered the best assignment of the infrared spectra of gaseous, liquid and solid trimethylene oxide. The axis system (Fig. 1.4) adopted in this work and in references 74 and 76 results in in-plane vibrations of  $B_1$  symmetry and out-of-plane vibrations of  $B_2$  symmetry; however that adopted in references 78 to 80 interchanges the x and y axes (Fig. 1.4) and results in in-plane vibrations of  $B_2$  symmetry and out-of-plane vibrations of  $B_1$  symmetry. The numbering and symmetry of the modes referred

Table 1.6

Assignment of the Infrared Spectrum of Trimethylene Oxide in the Gas, Liquid and Solid Phases<sup>a, b</sup>

Sym. C	No. C	Description	Gas			Liquid, c			Solid, e		
			Lafferty	Wieser	Best	Lafferty	Le Brant	Best	Le Brant	Wieser	Best
A <sub>1</sub>	1	β-CH <sub>2</sub> sym. str.	2958	2979.0 <sup>f</sup>	2979.0 <sup>f</sup>	2971	2971	2971	2961	2977.0	2977.0
	2	α-CH <sub>2</sub> sym. str.	2889	2893.9	2893.9	2877	2877	2877	2882	2892.6	2892.6
	3	α-CH <sub>2</sub> def.	1511	1505.0 <sup>f</sup>	1505.0 <sup>f</sup>	1495 <sup>g</sup>	-	-	1505.2	-	1505.2
	4	β-CH <sub>2</sub> def.	1452	1452.0	1452.0	1451	1452	1452	1452.8	-	1452.8
	5	α-CH <sub>2</sub> wag	1343	-	1343	1336	1338	1336	1342	-	1342
	6	ring breathing	1030	-	1030	1028	1028	1028	1028.6	-	1028.6
	7	ring def.	1008	-	1008	980	981	981	967	-	967
	8	ring def.	908	-	908	893	899	899	904.8	-	904.8
A <sub>2</sub>	9	α-CH <sub>2</sub> asym. str.	-	2940 <sup>g</sup>	2940 <sup>g</sup>	-	29347	29347	~2939	-	~2939
	10	α-CH <sub>2</sub> twist	-	-	-	1280	1283	1283	1288.2	-	1288.2
	11	β-CH <sub>2</sub> twist	-	-	-	-	-	-	1394.2	-	1394.2
	12	α-CH <sub>2</sub> rock	-	-	-	-	830	830	827.8	-	827.8
B <sub>1</sub> (B <sub>2</sub> )	13 (19)	α-CH <sub>2</sub> sym. str.	2892	2887.1	2887.1	<	2877	2877	2885.5	2885.0	2885.0
	14 (20)	α-CH <sub>2</sub> def.	1463	~1480	~1480	-	-	-	1467.8	-	1467.8
	15 (21)	α-CH <sub>2</sub> wag	-	-	-	-	1356	1356	1353	-	1353
	16 (22)	β-CH <sub>2</sub> wag	1230	-	1230	1229	1231	1231	1231.6	-	1231.6
	17 (23)	ring def.	999	-	999	980	981	981	961	-	961
	18 (24)	ring def.	940	-	940	920	924	924	927.3	-	927.3

Sym. <sup>c</sup>	No. C	Description	Gas			Liquid <sup>d, e</sup>			Solid <sup>e</sup>		
			Lafferty	Wieser	Best	Lafferty	Le Brumant	Best	Le Brumant	Wieser	Best
	19 (13)	$\beta$ -CH <sub>2</sub> asym. str.	3006	3006.0	3006.0	-	3001	3001	2999	2998.7	2998.7
	20 (14)	$\alpha$ -CH <sub>2</sub> asym. str.	2938	2957.3	2957.3	-	2934	2934	2951.5	2956	2956
B <sub>2</sub> (B <sub>1</sub> )	21 (15)	$\alpha$ -CH <sub>2</sub> twist	1136	-	1136	1134	1134	1134	1137.4	-	1137.4
	22 (16)	$\alpha$ -CH <sub>2</sub> rock	839	-	839	-	-	-	843.6	-	843.6
	23 (17)	$\beta$ -CH <sub>2</sub> rock	7847	-	7847	730	725	725	730.8	-	730.8
	24 (18)	ring puckering	90	53.5	53.5	-	-	-	-	-	-

- a) Frequencies in cm<sup>-1</sup>
- b) Lafferty refers to reference 74; Le Brumant refers to reference 76; Wieser (gas) refers to references 78 and 80, and Wieser (solid) refers to reference 80.
- c) Bracketed entries refer to the axis system in which the plane yz defines the plane of the ring.
- d) Lafferty did not assign the spectrum.
- e) Le Brumant did not assign the C-H stretching region.
- f) Frequency taken from Raman spectrum of gas in references 79 and 80.
- g) Estimated from its series of  $\Delta\nu_p = i$  combinations in the infrared spectrum of gaseous  $\beta$ -d<sub>2</sub> trimethylene oxide.
- h) Uncertain since it was not seen by Le Brumant.

to in references 78 to 80 have been changed in accordance with the axis system adopted in this work (Fig. 1.4). For convenience the correspondence between the two systems is shown in Table 1.8.

Lafferty (74) and Wieser and co-workers (78 - 80) have studied the mid-infrared spectrum of gaseous trimethylene oxide. Wieser et al (78 - 80) have obtained the C-H stretching and  $\text{CH}_2$  deformation regions of the spectrum of normal ( $\bar{n}$ ),  $\alpha\text{-d}_2$ ,  $\beta\text{-d}_2$  and  $\alpha$ ,  $\alpha'\text{-d}_4$  trimethylene oxide and they were able to assign the fundamental vibrations as well as the progressions of the combination bands with the ring puckering mode. Lafferty (74) also studied these regions, however, the larger volume of data available to Wieser et al (78 - 80) and their far more complete analysis of this data, makes their assignment more reliable, so only their results will be discussed.

The moments of inertia of n-trimethylene oxide are such that the infrared vibration-rotation bands for the  $A_1$ ,  $B_1$  and  $B_2$  vibrations are of types (81) A, B and C respectively (74). A C-type band was observed (80) near  $3006\text{ cm}^{-1}$  in the infrared spectra of  $\bar{n}$ ,  $\alpha\text{-d}_2$  and  $\alpha$ ,  $\alpha'\text{-d}_4$  trimethylene oxide, whereas it was not observed in the spectrum of  $\beta\text{-d}_2$  trimethylene oxide. This band was thus assigned to the  $\beta\text{-CH}_2$  antisymmetric stretch,  $\nu_{19}(B_2)$ . The  $\beta\text{-CH}_2$  symmetric stretch,  $\nu_1(A_1)$ , was not observed in the infrared spectrum, however a sharp, intense, polarized line

in the Raman spectrum (80) of the gas at  $2979.0 \text{ cm}^{-1}$  was assigned to this vibration. Wieser *et al* (80) noted that the frequency of this mode appears to have been raised slightly by a Fermi resonance interaction with the first overtone of the  $\beta\text{-CH}_2$  deformation mode,  $\nu_4(A_1)$  at  $1452 \text{ cm}^{-1}$ . The prominent C-type band at  $2957.3 \text{ cm}^{-1}$  was assigned to the  $\alpha\text{-CH}_2$  antisymmetric stretch,  $\nu_{20}(B_2)$ , since it was not observed in the spectrum of  $\alpha, \alpha'\text{-d}_4$  trimethylene oxide. This band is shifted to high frequency by Fermi resonance between the  $\nu_{20} = 1$  level of  $\nu_{20}(B_2)$  and the combination level  $\nu_2 = 1 \nu_{24} = 1$  involving the  $\alpha\text{-CH}_2$  symmetric stretch  $\nu_2(A_1)$  and the ring puckering mode  $\nu_{24}(B_2)$  (75, 80). The combination band was assigned at  $2929.2 \text{ cm}^{-1}$ . An estimate of  $2938.3 \text{ cm}^{-1}$  was made of the frequency of the  $\nu_{20}(B_2)$  fundamental unperturbed by Fermi resonance, since a distinct C-type band was observed at this frequency and assigned to the hot transitions  $\nu_{20}(B_2) + n\nu_{24}(B_2) - n\nu_{24}^0(B_2)$  with  $n \geq 1$ . A corresponding band was observed at this frequency in the Raman spectrum of the gas under perpendicular polarization. The  $\alpha\text{-CH}_2$  symmetric stretch,  $\nu_2(A_1)$ , was unambiguously assigned to the A-type band at  $2893.9 \text{ cm}^{-1}$  by virtue of the intense, polarized Raman band at  $2894.7 \text{ cm}^{-1}$  and its pronounced infrared sequence based on the ring puckering mode. The  $\alpha\text{-CH}_2$  symmetric stretch,  $\nu_{13}(B_1)$ , was assigned to the Q gap of the B-type band at  $2887.1 \text{ cm}^{-1}$ . The remaining C-H stretching vibration,  $\nu_9(A_2)$ , the  $\alpha\text{-CH}_2$  anti-



symmetric stretch has an infrared inactive fundamental but the combination transitions  $\nu_9 + (n \pm 1)\nu_{24} - n\nu_{24}$  are infrared active. The frequency of the fundamental was estimated to be about  $2940 \text{ cm}^{-1}$  from the series of combination bands observed in the spectrum of  $\beta$ - $d_2$  trimethylene oxide (80).

The infrared and Raman spectra of gaseous  $n$ ,  $\alpha$ - $d_2$ ,  $\beta$ - $d_2$  and  $\alpha$ ,  $\alpha'$ - $d_4$  trimethylene oxide in the  $\text{CH}_2$  deformation region have been studied by Wieser *et al* (78, 79). The  $\alpha$ - $\text{CH}_2$  deformation,  $\nu_3^{\sigma}(\text{A}_1)$ , was not observed in the infrared spectrum (78) of  $n$ -trimethylene oxide, however a distinct Raman band was observed at  $1505.0 \text{ cm}^{-1}$  (79) and assigned to this vibration. The second  $\alpha$ - $\text{CH}_2$  deformation,  $\nu_{14}(\text{B}_1)$ , was not observed in the infrared or Raman spectra (78, 79), however it was tentatively assigned to a band gap at  $1479 \text{ cm}^{-1}$  in the infrared spectrum of  $\beta$ - $d_2$  trimethylene oxide (78), and in a later paper (80) it was assigned near  $1480 \text{ cm}^{-1}$  in  $n$ -trimethylene oxide on the basis of unpublished results. The  $\beta$ - $\text{CH}_2$  deformation,  $\nu_4(\text{A}_1)$ , was assigned to a band at  $1452.0 \text{ cm}^{-1}$  in the infrared spectrum, by an examination of its infrared active combination bands with the ring puckering mode.

The remaining discussion of the assignment of the infrared spectrum of gaseous trimethylene oxide is based upon the unpublished study by Lafferty (74). Lafferty obtained the infrared spectra of gaseous and liquid

n- and d<sub>6</sub>-trimethylene oxide, and with the aid of the unpublished Raman spectrum of the liquid obtained by Rea (74), he assigned the infrared spectrum of the gas.

Lafferty's analysis of the complicated infrared spectrum of the gas was far less detailed than that of Wieser *et al.*, so, in general, the assigned frequencies for the gas must be considered less certain. Use will also be made of the infrared and Raman spectra of the liquid (presumably at room temperature) and the solid (10°K for infrared, 85°K for Raman) published by Le Brumant (76).

The  $\alpha$ -CH<sub>2</sub> wag,  $\nu_5(A_1)$ , was confidently assigned by Lafferty to the A-type band at 1343 cm<sup>-1</sup>, which corresponds to a polarized (73) band in the Raman spectrum of the liquid at 1339 cm<sup>-1</sup>. No absorption due to the other  $\alpha$ -CH<sub>2</sub> wag,  $\nu_{15}(B_1)$ , was observed in the infrared spectrum of the gas, however, a weak Raman band occurred at 1285 cm<sup>-1</sup>, which Lafferty assigned to this vibration. Le Brumant (76) observed a medium intensity band at 1353 cm<sup>-1</sup> in the infrared spectrum of solid trimethylene oxide at 10°K, which he assigned to  $\nu_{15}(B_1)$  and a band at 1288.2 cm<sup>-1</sup> which he assigned to the  $\alpha$ -CH<sub>2</sub> twist,  $\nu_{10}(A_2)$ . The correct assignment is unclear, so the most recent one (76) has been used. The  $\beta$ -CH<sub>2</sub> wag,  $\nu_{16}(B_1)$ , was assigned to the strong B-type band in the infrared spectrum of the gas at 1230 cm<sup>-1</sup> (74).

The only CH<sub>2</sub> twisting vibration which is formally active in the infrared spectrum is the  $\alpha$ -CH<sub>2</sub> twist,  $\nu_{21}(B_2)$ .

This was assigned (74) to the C-type band at  $1136 \text{ cm}^{-1}$ , which corresponds to a band in the Raman spectrum of the liquid at the same frequency. The  $\beta\text{-CH}_2$  twist,  $\nu_{11}(\text{A}_2)$ , was assigned to a band at  $1194.2 \text{ cm}^{-1}$  in the infrared spectrum of the solid (76) and to bands at 1184 and  $1195 \text{ cm}^{-1}$  in the Raman spectra of the liquid and the solid, respectively (76).

Lafferty (74) assigned the sharp Q branch at  $839 \text{ cm}^{-1}$  in the infrared spectrum of the gas to the  $\alpha\text{-CH}_2$  rock,  $\nu_{22}(\text{B}_2)$ . The corresponding band was observed at  $825 \text{ cm}^{-1}$  in the Raman spectrum of the liquid (74). The assignment of the  $\beta\text{-CH}_2$  rock,  $\nu_{23}(\text{B}_2)$ , is uncertain. Lafferty (74) assigned this vibration to a band at  $784 \text{ cm}^{-1}$  in the infrared spectrum of the gas, however, only very weak bands were found in this region of the infrared and Raman spectra of the liquid (74, 76) and solid (76). Le Brumant (76) assigned a medium intensity band at  $730.8 \text{ cm}^{-1}$  in the infrared spectrum of the solid to this mode. It is surprising that the frequency of this mode differs by about  $50 \text{ cm}^{-1}$  between the two phases, and so the correct assignment is unclear. The  $\alpha\text{-CH}_2$  rock,  $\nu_{12}(\text{A}_2)$ , was assigned (76) to a band at  $827.8 \text{ cm}^{-1}$  in the infrared spectrum of the solid.

Lafferty (74) assigned the strong, polarized band at  $1028 \text{ cm}^{-1}$  in the Raman spectrum of the liquid to the ring breathing mode,  $\nu_6(\text{A}_1)$ . The Q branch of this mode was obscured in the infrared spectrum of the gas by the strong

absorption at about  $1000\text{ cm}^{-1}$ , although a poorly defined shoulder was seen at about  $1030\text{ cm}^{-1}$  and assigned to  $\nu_6(A_1)$  (74). Thus the exact frequency of this mode in the infrared spectrum of the gas is uncertain.

The ring deformation modes,  $\nu_7(A_1)$  and  $\nu_{17}(B_1)$ , are both expected to contribute to the very intense absorption centered at about  $1000\text{ cm}^{-1}$  in the infrared spectrum of the gas. However the complicated structure on the top of this band makes a precise assignment difficult. Lafferty assigned the strong peak at  $1008\text{ cm}^{-1}$  to  $\nu_7(A_1)$  and the Q gap at  $999\text{ cm}^{-1}$  to  $\nu_{17}(B_1)$ . The exact frequencies of these vibrations in the gas must be considered as uncertain. The ring deformation  $\nu_{18}(B_1)$  was assigned to the distorted Q gap at  $940\text{ cm}^{-1}$  in the infrared spectrum of the gas. The exact frequency of this mode is probably slightly uncertain. There is no uncertainty associated with the frequency of the ring deformation  $\nu_8(A_1)$ , which was assigned to the A-type band at  $908\text{ cm}^{-1}$  in the infrared spectrum of the gas (74). The remaining ring deformation is the ring puckering mode,  $\nu_{24}(B_2)$ , which was assigned (63) to the band at  $53.5\text{ cm}^{-1}$  in the far-infrared spectrum of the gas.

The frequencies quoted by Lafferty (74) for the features in the infrared spectrum of the gas agree to within  $1\text{ cm}^{-1}$  with unpublished results obtained in this laboratory.

### 1.5 Objectives of this Study

The objectives of this study can be divided into those involving the vibrations of the water molecules and those involving the vibrations of the trimethylene oxide molecules.

#### A. Vibrations of the Water Molecules.

(i) To further investigate the behaviour of water molecules in solids formed from hydrogen-bonded water.

The mid-infrared absorption by the disordered water molecules of the structure I hydrate of ethylene oxide and the disordered phases of ice was known when this work was started (Section 1.3), so one objective was to compare it with the mid-infrared absorption by the disordered water molecules of the hydrates of trimethylene oxide to see to what extent the absorption depends on the structure. In particular, a comparison of the absorption by the water molecules of the structure I hydrates of trimethylene oxide and ethylene oxide was expected to indicate the effect that the size of the guest molecule has on the water vibrations, since the dipole moment of trimethylene oxide is approximately equal to that of ethylene oxide, whereas its van der Waals diameter is considerably larger than that of ethylene oxide. Further, the mid-infrared absorption by the water molecules of a structure II hydrate had not been previously investigated, so it was of interest to obtain ~~this information for the structure II hydrate of trimethy-~~lene oxide and compare it to that of the structure I hydrates.

It was also thought that a comparison of the water absorption by the structure I and structure II hydrates of trimethylene oxide might provide evidence of the differences between the interactions of the guest and water molecules for the 14- and 16-hedral cages.

(ii) To investigate the temperature dependence of the water absorption of a clathrate hydrate.

It is certain that hot bands contribute to the water absorption bands of the clathrate hydrates and the ice polymorphs at 100°K, so a study of the temperature dependence of these bands was expected to provide evidence of the extent of this contribution. Evidence was also sought on whether the order-disorder transition proposed by Davidson (54) has any detectable effect on the water lattice.

#### B. Vibrations of the Trimethylene Oxide Molecules

(i) To record the vibrational frequencies of the guest molecules of the structure I and II hydrates of trimethylene oxide.

It was thought that a comparison of the vibrational frequencies of trimethylene oxide molecules trapped in 14- and 16-hedral cages might provide information about the guest-host interactions in the two cages. Further information on guest-host interactions was sought from a comparison of the vibrational frequency shifts, relative to the gas phase values, of trimethylene oxide and ethylene oxide molecules trapped in the 14-hedral cages.

(ii) To seek further evidence on the proposed preferential orientation of guest molecules in the 14-hedral cages.

Davidson (54) has suggested that the trimethylene oxide molecules are preferentially oriented in the 14-hedral cages of the structure I hydrate, and Bertie and Othen (48) have suggested that preferential orientation of the ethylene oxide molecules in the 14-hedral cages of ethylene oxide hydrate may account for the doublet observed for the ring breathing mode in the mid-infrared spectrum. Thus it was of interest to see whether evidence of preferred orientations could be obtained from the mid-infrared spectrum of the structure I hydrate of trimethylene oxide.

(iii) To record the temperature dependence of the guest absorption of a clathrate hydrate.

Generally, the temperature dependence of the guest absorption of a clathrate hydrate should provide evidence concerning the anharmonic contributions to the bands, the effect of changes in the reorientation rate of the guest molecules, and effects due to the temperature dependence of the guest-host interactions. It was of particular interest in the case of the structure I hydrate of trimethylene oxide, since Davidson (54) had obtained evidence that the guest dipoles align in a parallel fashion along the  $\bar{4}$  axes of the 14-hedral cages when the hydrate is cooled below 105°K, so further evidence of this transition was sought from the vibrational spectrum.

## Chapter Two. Experimental Techniques

### 2.1 Chemicals

Reagent grade trimethylene oxide was initially obtained from K & K Laboratories, and water from the Aldrich Chemical Company. Gas-liquid chromatography, using a 20' x 4mm, 10% DEGS on chromasorb w column, and  $^1\text{H}$  n.m.r. spectroscopy were used to determine the purity of the K & K sample. The chromatograms showed the presence of two impurities, both more volatile than trimethylene oxide, amounting to a total of 0.2%. No impurities were detected in the  $^1\text{H}$  n.m.r. spectrum. A 10 ml sample of the K & K product was separated into three fractions by evaporation on a vacuum line. An infrared spectrum of a mull, in liquid propane (Section 2.4), of a solidified portion of the least volatile fraction was compared to the infrared spectrum of a mull of the solidified commercial product, and no differences were observed. Thus the commercial K & K product was used without further purification. The infrared spectrum of a mull, in liquid propane, of the solidified Aldrich sample, however, contained two weak bands, at  $703\text{ cm}^{-1}$  and  $985\text{ cm}^{-1}$ , not present in the spectrum of the K & K sample. Fractional distillation of the material failed to remove these bands from its spectrum, and therefore the use of the Aldrich product was discontinued.

The water used in the hydrate preparations was obtained from the distilled water supply in the laboratory. For deuterate preparations, deuterium oxide supplied by Columbia



Organic Chemicals was used. This was shown to have an isotopic purity of  $99.7 \pm 0.1\%$  by comparison of the area of its p.m.r. peak with a series of areas obtained from deuterium oxide samples of known hydrogen concentration.

The 'infrared quality' cesium iodide and potassium bromide, for making pellets, was used as supplied by The Harshaw Chemical Company.

## 2.2 Hydrate Preparation

Inspection of the phase diagram for the trimethylene oxide - water system, shown in Fig. 1.3, reveals the existence of two different structural types of clathrate hydrate, namely TMO hydrate I and TMO hydrate II. It is not possible to make pure samples of either of these hydrates by simply making a solution of the appropriate composition and cooling it slowly, due to the two peritectic points,  $T_1$  and  $T_2$ . For instance, in the case of TMO hydrate I, slowly lowering the temperature of a solution of molar composition  $6 \text{ C}_3\text{H}_6 \cdot 0.46 \text{ H}_2\text{O}$  would initially cause the precipitation of TMO hydrate II, followed by TMO hydrate I. Similarly, in the case of TMO hydrate II, the first solid to precipitate would be ice.

The preparation of TMO hydrate I was attempted by four different methods:

(i) A 60 weight percent solution of trimethylene oxide in water was made in a glass vessel, and degassed on a vacuum line. It was cooled to  $-78^\circ\text{C}$  in a solid carbon dioxide-methanol bath, and subsequently held at  $-35^\circ\text{C}$  for four days in a Neslab LT-9 low temperature bath. The glass cell was

then suspended near the top of an uninsulated metal can containing boiling liquid nitrogen. After opening the cell in the dry nitrogen atmosphere within the can, the solution was poured through a #100 sieve. The solid was transferred from the sieve to a pre-cooled stainless steel mortar resting on a platform inside the can. A pre-cooled stainless steel pestle was used to grind the sample to a fine powder. This sample was then transferred to a cold, screw-top, glass vial which was placed inside a second, larger, screw-top vial containing liquid nitrogen. A length of piano wire was attached to the lid of the larger vial, to allow it to be suspended from the neck of a five liter dewar for storage. All operations inside the can were carried out using long tweezers and spatulas, which had been previously cooled in the liquid nitrogen.

(ii) A degassed, 60 weight percent solution of trimethylene oxide in water was held at  $-35^{\circ}\text{C}$  in a 1,2-dichloroethane slush for one hour. The cell was then opened to a vacuum line to pump off the excess trimethylene oxide. The pressure, as measured by a mercury U-tube manometer, of the excess trimethylene oxide at  $-35^{\circ}\text{C}$ , was 8 Torr. The crust which formed on the surface during pumping, was broken up by a magnetic stirring rod. The pressure dropped to below 1 Torr after the cell had been pumped for 2 hours, and it was assumed that this was the vapour pressure of trimethylene oxide above the hydrate. The solid sample was broken into small pieces using a pre-cooled metal spike, and then removed from the cell,

ground and stored in liquid nitrogen by the previously outlined method.

(iii) A sample of molar composition  $6 \text{ C}_3\text{H}_6\text{O} \cdot 0.46 \text{ H}_2\text{O}$  was prepared in the following way. A single beam balance was used to accurately weigh 2.0 gm of trimethylene oxide, and this was transferred to a mortar in a can containing liquid nitrogen, using a syringe. Then 4.74 gm of boiled, distilled water were placed in a second mortar. The contents of each mortar were finely ground, and then the powders were mixed and reground. This sample was placed in a glass clathrate cell, consisting of a glass test tube coupled to a stopcock by a ground glass joint, and then packed down firmly using a plug of glass wool. The cell was very carefully evacuated and then transferred to the Neslab LT-9 low temperature bath and held at  $-27^\circ\text{C}$  for four days, at which time the sample was reground and stored in liquid nitrogen.

(iv) A sample of molar composition  $6 \text{ C}_3\text{H}_6\text{O} \cdot 0.46 \text{ H}_2\text{O}$  was made by separately degassing 2.0 gm of trimethylene oxide and 4.74 gm of  $\text{H}_2\text{O}$  and then vacuum distilling them into a clathrate cell cooled in liquid nitrogen. The cell was then allowed to warm to room temperature, producing a solution of trimethylene oxide in water of exactly the TMO hydrate I composition. This was rapidly cooled to  $-196^\circ\text{C}$  in liquid nitrogen, and then transferred to a low temperature bath, and held at  $-27^\circ\text{C}$ , for about two weeks. The sample was ground in the usual manner and stored in liquid nitrogen.

The hydrate produced by method (i) was found to contain

excess trimethylene oxide. In the samples produced by methods (ii) and (iii), some TMO hydrate II was formed together with the TMO hydrate I. However, method (iv) produced a pure sample of TMO hydrate I, as determined by powder X-ray diffraction results (see Section 2.3). Method (iv) was, therefore, adopted as the standard method for making TMO hydrate I. TMO deuterate I samples were made by the same method and using the same temperatures.

A variation on method (iv) was used to make TMO hydrate II. After degassing 1.0 gm of trimethylene oxide and 5.28 gm of  $H_2O$ , they were vacuum distilled into a clathrate cell, producing a solution of the correct composition,  $C_3H_6 \cdot 0.17 H_2O$ , for TMO hydrate II. This solution was rapidly cooled in liquid nitrogen, and then held at  $-18^\circ C$  for about two weeks. The samples were subsequently ground and stored.

### 2.3 Hydrate Characterisation by Powder X-ray Diffraction

Powder X-ray diffraction was used to characterise each hydrate preparation. A brass table was placed inside an uninsulated metal can, which was filled with liquid nitrogen to just below the top of the table. A metal mortar, and a brass block containing a small hole, were placed on the table. A 0.5 mm quartz capillary tube, with a wide neck, sat inside the hole. The top of the can was covered with plexi-glas, and the apparatus was left for half-an-hour to cool. At this time, the sample vial was lowered into the can, and the screw top was removed with pre-cooled tweezers. A small amount of the sample was placed in the mortar, using

a cold spatula. A small volume of ice-free liquid nitrogen was added to the mortar to exclude the possibility of thermal decomposition during grinding. The sample was ground for about half-an-hour. Then a small portion was placed on a spatula, in which a hole had been drilled. The hole was aligned with the top of the capillary tube, and the sample was pushed into the tube and firmly packed down, using a fine glass rod. When the tube was full, a bakelite support, containing a smear of oil, was placed over the end of the capillary tube. As soon as the oil had solidified, fixing the tube to the support, a small metal pot, with an insulated handle, containing liquid nitrogen was lowered into the can. The bakelite support containing the capillary tube was held under the liquid nitrogen in the metal pot with a pair of tweezers, and was then transferred to a goniometer head on the X-ray camera. A stream of cold nitrogen gas, produced by boiling liquid nitrogen, was transferred through a dewar tube to cool the sample on the goniometer head. A cone of warm nitrogen gas, co-axial with the cold nitrogen stream, prevented ice from forming on the capillary tube.

The X-ray beam was produced by an Enraf - Nonius Diffractis 601 generator. Filtered copper  $K_{\alpha}$  radiation, wavelength 1.5418 Å, was used to obtain the powder photographs. The camera was a Jarrell - Ash precession camera, which was used as a flat-plate powder camera. An iron-constantan thermocouple placed near the capillary tube indicated a temperature of

-140  $\pm$  20°C. However a thermocouple inserted into the capillary tube through the bakelite support indicated a temperature of -170  $\pm$  10°C, which is clearly a better estimate of the sample temperature. The sample to film distance was calibrated by measuring the powder diffraction pattern of ice Ih(82), and was found to be within the range 59.7  $\pm$  0.2 mm.

#### 2.4 Mull Samples for Mid-Infrared Spectroscopy

The cell used to contain the mull samples is shown in Fig. 2.1. It is made of stainless steel except for a copper sample holder, and it was constructed in the Chemistry Department Machine Shop. The inner part, consisting of the liquid nitrogen-reservoir A, and the sample holder B, fits inside the outer jacket C, which contains the cesium iodide windows D. When fully assembled, the cell was evacuated to a pressure of about  $10^{-2}$  Torr via the valve E, and the vacuum was sealed at the junction of the two parts by the concentric, Buna N rubber O-rings F. The seal between the outer jacket and the windows is achieved by two further Buna N O-rings G. The temperature of the sample may be varied over a small range by using the two heaters H. The temperatures at the top and bottom of the sample holder were monitored by two iron-constantan thermocouples, each inserted in a hole in the sample holder, and held in place by Wakefield thermal compound No. 122. The sample, contained between two cesium iodide windows, was fixed firmly in position by a spring attached to a copper ring, which was screwed to the sample holder.

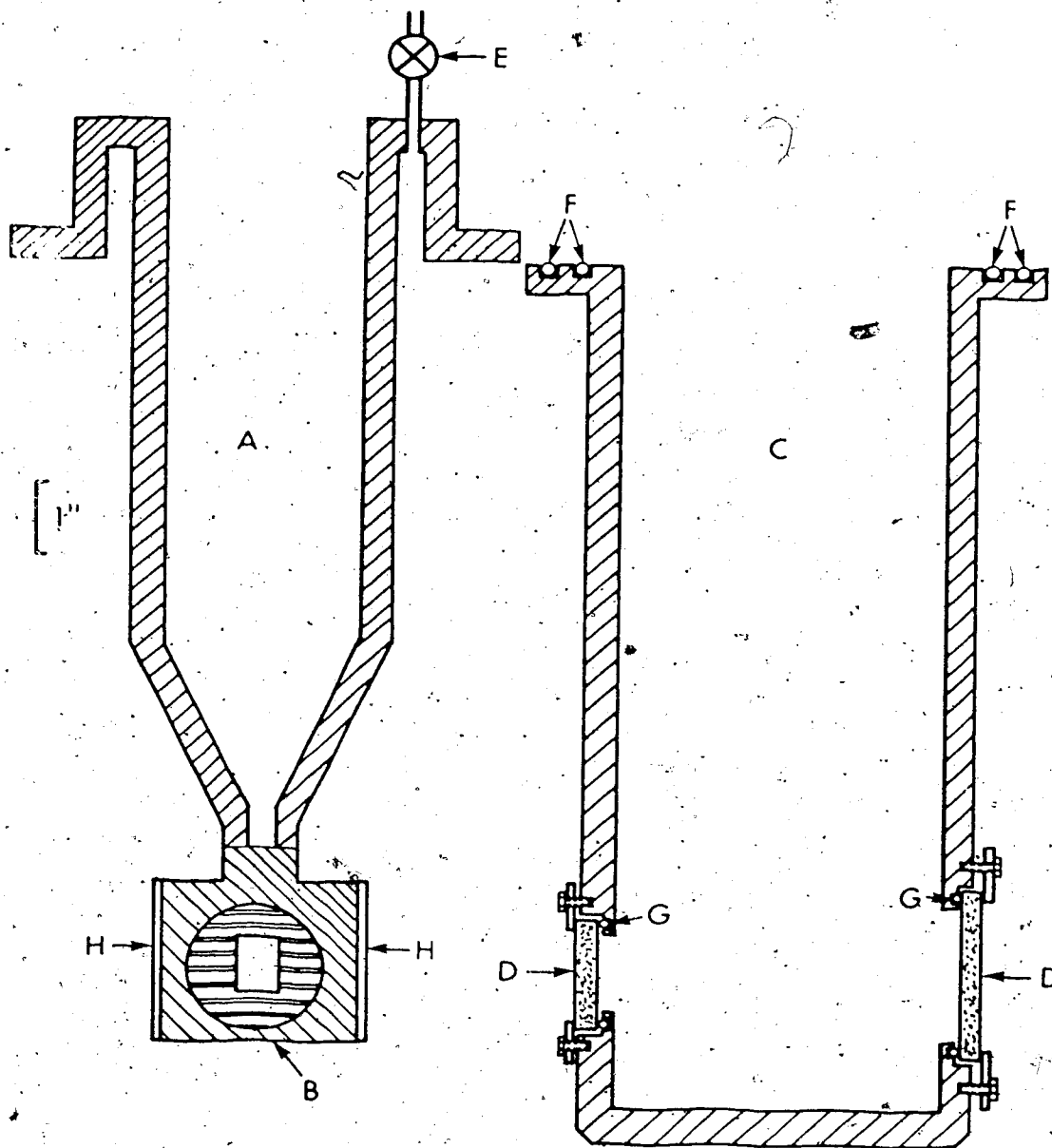


Fig. 2.1. Low temperature infrared mull cell: A, liquid nitrogen reservoir; B, sample holder; C, outer jacket; D, windows; E, valve; F, O-rings; G, O-rings; H, heater.

The low temperature mulling technique employed here was developed by Bertie and Whalley (83). All operations were carried out inside an uninsulated metal can to which a rectangular side arm had been attached. A section of the can had been removed to allow passage between the can and the side arm. A rectangular brass table was placed inside the can. At the front of the table, there were four circular wells. A stainless steel mortar was placed in one of the two larger wells. A small circular metal platform, which was attached to a rod held by a retort stand in the side arm, was positioned on the left-hand side of the table. The copper ring, with attached spring, was placed on the right-hand side of the table. The inner part of the low temperature cell rested on the back of the table, with the flange out of the can. Two pieces of plexi-glas, cut to fit snugly around the inner cell, were attached to each other and to the can, by masking tape. A rectangular piece of plexi-glas was used to cover the side arm. Thus only the front half of the can was left open to allow access for working. Heating tape was wrapped around the inner cell just below the flange. The glass ball joint attached to the valve at the top of the cell was connected to a vacuum line by a length of rubber pressure tubing. Outside the can, the outer jacket was slowly flushed with dry nitrogen gas. At this stage the apparatus was ready to be cooled.

The can was filled with liquid nitrogen to just below the surface of the table, and was left to cool for about



half-an-hour. From this point onwards, all operations were carried out wearing rubber gloves and using pre-cooled tweezers or spatulas. The sample container was removed from storage and placed on the table. The inner sample vial was then lowered into a well at the front of the table, and a small amount of the sample was transferred to the mortar. The steel pestle was cooled to liquid nitrogen temperature and, after half-filling the mortar with ice-free liquid nitrogen, the sample was ground for half-an-hour. During this time further additions of liquid nitrogen to the mortar were necessary.

Towards the end of the grinding procedure, two cesium iodide windows were placed in the can; one on the circular metal platform and the other on the copper ring. After they had been allowed to cool for about fifteen minutes, some finely powdered sample was sprinkled onto the window resting on the platform. A large vial was then cooled in the liquid nitrogen, and placed in the middle of the table. Mulling agent was condensed into this vial, by cooling the glass pipette at the end of the delivery tube attached to the gas cylinder. Propane, trifluorochloromethane and propylene were the three mulling agents used during this study. A few drops of liquid mulling agent were placed over the sample on the window, and the second window was put on top. A small indentation in the middle of this window allowed the mull to be smeared uniformly, by rubbing one window over the other with a pair of pointed tweezers. The steel platform was

then released from the retort stand and carried to the cell, where the windows were tipped into the sample holder by a pair of tweezers. The copper spring was placed against the windows, and screwed into place by a long screw driver, inserted through a hole in the side of the can.

At this point, the outer jacket of the cell, previously flushed with dry nitrogen gas, was laid in the side arm of the can. The heating tape was removed, and a small amount of liquid nitrogen was added to the reservoir of the inner cell. The plexi-glas covers were dismantled, and the inner cell was very quickly inserted into the outer jacket and evacuated. The complete cell was then removed from the side arm, filled with liquid nitrogen and thoroughly evacuated, and the remaining sample was returned to the storage dewar. The cell was then ready to be transferred to the sample compartment of the spectrophotometer where it was continuously evacuated while the spectra were recorded.

## 2.5 Pellet Samples for Mid-Infrared Spectroscopy

### 2.5.1 Pellet Preparation

The pellet samples were made by mixing the hydrate and powdered potassium bromide or cesium iodide at about 77°K, placing the mixture into a piston-cylinder pressure apparatus at about 77°K, and pressurising it to 2.5 Kbar at 230°K.

The piston-cylinder pressure apparatus used to prepare the pellets is shown in Fig. 2.2. The sample S was held between the faces of the two pistons, A and B, which were inserted into the cylinder C. The retaining block D supported this

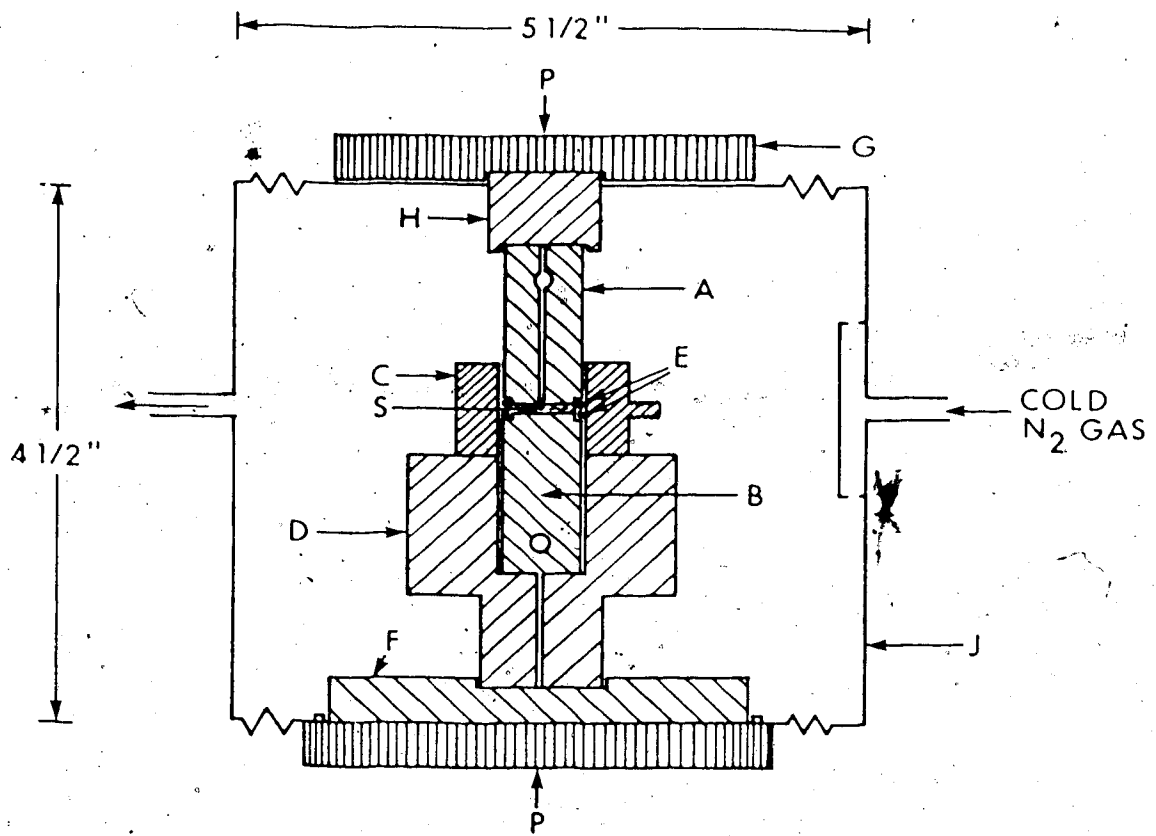


Fig. 2.2. Piston-cylinder pressure apparatus: A and B, pistons; C, cylinder; D, retaining block; E, back-up rings; F and G, pressure distributing blocks; H, spacer; J, container; P, pressure.

whole assembly. A brass back-up ring E was seated in a groove on each piston face, to prevent the sample from extruding into the 0.001" clearance between the cylinder and the pistons. The fine hole drilled through the length of the top piston A ends 0.05" from the face, and it was used to house the thermocouple which recorded the temperature of the sample during pressurisation. The large diametrical hole through each piston facilitated the removal of the pistons at low temperature after the pellet had been made. The container J is a circular stainless steel pot with a lid. Variation of the voltage across a 200 watt pencil heater, immersed in liquid nitrogen, allowed the rate of flow of cold nitrogen gas to be controlled. A curved metal shield, covering the gas-entrance side arm, dispersed the cold gas inside the pot. The blocks F and G serve to distribute the pressure, and the block H is merely a spacer. The arrows P represent the application of pressure by a standard 100 ton press.

The pistons A and B and the blocks D, F, G and H were made of Vascomax 350, 18% nickel maraging steel, heat treated to 54 Rockwell C. Once the pellet sample had been made, the cylinder served as a sample holder and was screwed directly into the cryo-tip of a liquid helium cryostat. When the cryostat was assembled and evacuated, the sample was cooled in part by thermal conduction through the cylinder. The cylinder therefore had to be a reasonable heat conductor at low temperatures, as well as being strong enough to withstand the pressure applied to form the pellet. Two percent

beryllium-copper was chosen as a suitable material for the cylinder.

The remainder of this section describes in detail the procedure developed in this work for making the pellets. This procedure resulted from about twenty-five trials in which the pellet thickness, the pressure, and the time of pressurisation were varied. This procedure produced 0.35 mm thick pellets which only minimally attenuated mid-infrared radiation, and did not produce interference fringes in the spectra.

In the earlier experimental work, 0.40 gm of cesium iodide or 0.28 gm of potassium bromide were accurately weighed in a small glass vial. This was then quickly placed inside a glass tube which was evacuated overnight at a pressure of about 0.001 Torr. In the more recent experiments, 0.28 gm of potassium bromide were placed directly in a smaller glass tube, which was then evacuated to a pressure of about  $10^{-5}$  Torr and heated to about 175°C in a covered heating mantle, while pumping for two days.

The apparatus shown in Fig. 2.2 was assembled in the uninsulated steel can containing liquid nitrogen. The steel pot containing the bottom block F was placed in the side arm of the can, together with the top steel block G. Two mortars were placed in wells at the front of the brass table (Section 2.4) inside the can, and the retaining block D containing the lower piston B and supporting the cylinder C was placed in a third well in the middle of the table. The spacer H was placed at the back of the table. Plexi-glas

covers were put over the side arm and the back half of the can. Then the can was filled with liquid nitrogen to just below the surface of the table and left to cool for half-an-hour. During this time, a small amount of water was syringed into the hole in the top piston A and a copper-constantan thermocouple was inserted. The piston was then placed on the spacer H with the thermocouple leads protruding from the can. The water quickly froze, securing the thermocouple tip inside the piston.

When the contents of the can were cold, the evacuated tube containing the pelleting agent, (KBr or CsI), was filled with dry nitrogen and quickly placed on the table in the can, together with the vial containing the hydrate sample. A small amount of the hydrate was ground in one of the mortars, as described in Section 2.4. At this point, the pelleting agent was very carefully emptied from the glass tube into the mortar, using two pairs of tweezers. Essentially complete transfer was assured by gently tapping the tube against the side of the mortar. A few grains of the powdered hydrate were added to the pelleting agent, and the powders were mixed thoroughly by grinding them for five minutes. The mixture was then totally transferred to the cylinder C. The mixture was evenly distributed inside the cylinder, first by a spatula, and then by shaking the retaining block while holding it by metal pincers inserted into diametrically opposed holes. The same metal pincers were then hooked into the diametrical hole in the top piston, which was then inserted into the

cylinder. Some liquid nitrogen was poured into the steel pot in the side arm, the metal pincers were again hooked into the hole in the retaining block, and the piston-cylinder assembly was placed into the steel pot. It was possible to stay within the dry nitrogen atmosphere of the can throughout this transfer. The spacer block, which is notched to accommodate the thermocouple, was placed on top of the upper piston, the lid of the pot was put in place and, finally, the top steel block G was added.

The complete cell (Fig. 2.2) was rapidly transferred to the insulated platten of the 100 ton press. An insulated rubber transfer tube from a 50 liter dewar of liquid nitrogen was attached to the entrance side arm of the pot, and fifty volts was applied to the pencil heater in the dewar to produce a stream of cold, dry nitrogen gas. The thermocouple leads were attached to the terminals of a strip chart recorder, the reference thermocouple was placed in an ice-water bath, and the temperature of the sample was allowed to rise to  $-40^{\circ}\text{C}$ . When a steady temperature had been achieved, 300 bars pressure was applied to the sample for 30 minutes, and then the pressure was released for 5 minutes. A pressure of 2500 bars was then applied for 75 minutes and subsequently released for 5 minutes. This latter combination was repeated twice. Liquid nitrogen was then added through the exit tube of the pot, which was then quickly transferred back to the side arm of the can.

The cylinder containing the sample was then ready to be placed in the infrared cell. The cell used for all of the work with pellet samples was a liquid helium optical cell. This cell, together with its associated cryogenic equipment, is briefly described in the next section.

#### 2.5.2 Liquid Helium Cryostat

The liquid helium cryostat used in this work was a Model LP-3-110 Liquid Transfer Heli-Tran Refrigerator, purchased from Air Products and Chemicals Inc., Allentown, Pennsylvania. The liquid helium cryostat consists of a cold end and a vacuum shroud, collectively called the optical cell, a flexible transfer tube, and a standard 25 or 50 liter liquid helium dewar.

A schematic view of the cold end is shown in Fig. 2.3. The liquid helium flows into the cold end from the transfer tube in two parts, the tip flow, which cools the sample holder by passing through the needle valve and is then warmed and vented, and the heat shield flow, which cools the heat shield in the transfer tube and is directed back through the tube from the cold end to increase the efficiency of the heat shield cooling. The ratio of tip flow, which controls the temperature of the sample, to heat shield flow, can be regulated by adjustment of the needle valve, using the screw near the top of the cold end. The sample temperature is further controlled by varying the voltage applied to the control heater. This is a 20 watt non-inductive heater which requires a 30 volt maximum, 60 Hz power supply. Three temperature sensing devices



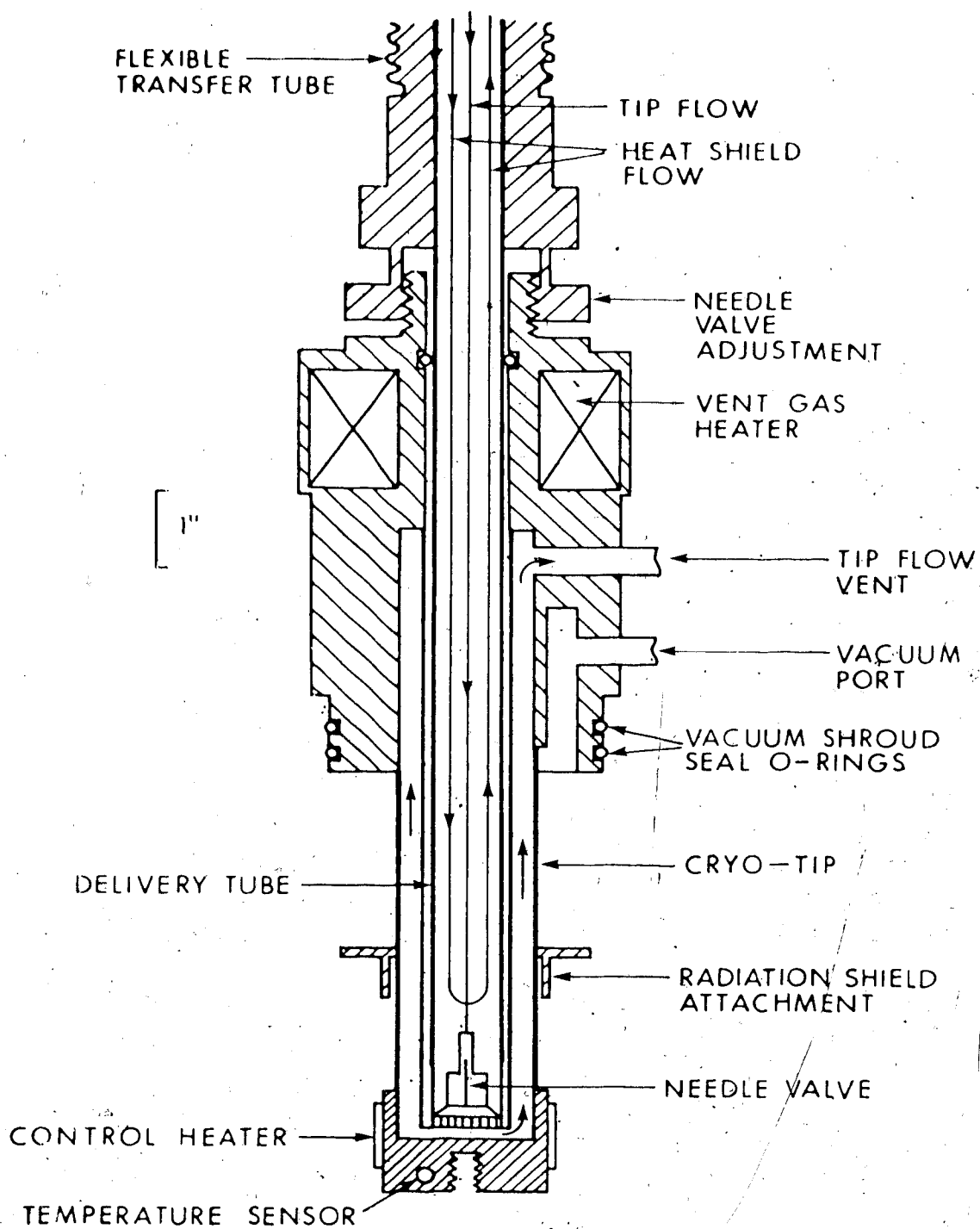


Fig. 2.3. Cold end of low temperature infrared pellet cell.

inserted into the end of the cryo-tip cover the range 2 to 300°K. A germanium resistance sensor is useful between 2°K and 100°K, a platinum resistance sensor covers the range 20°K to 300°K, and a chromel vs. gold -0.07 atomic % iron thermocouple has approximately the same useful range as the platinum sensor.

The sample holder screws into the end of the cryo-tip, with good thermal contact being provided by an indium gasket. A radiation shield is placed over the sample holder, and screwed onto the cryo-tip. The vacuum shroud contains two cesium iodide windows, and is placed over the radiation shield during operation, forming a vacuum tight seal with the cold end, through the O-rings. The end of the cryo-tip and the radiation shield connection are made of OFHC copper. The remainder of the cold end, and the vacuum shroud, is made of non-magnetic stainless steel, except for the tip flow vent which is brass.

A schematic view of the cryostat and peripheral equipment is shown in Fig. 2.4. The liquid helium dewar A is connected to the optical cell B by the flexible transfer line C. A positive pressure of helium gas inside the liquid helium dewar is supplied by the helium gas cylinder D through the dewar pressurisation connection. This pressure is measured by the gauge G, and is regulated by valves on the cylinder and by safety vent valves on the transfer tube and on the dewar itself. The pressure in the dewar must not exceed 5 psig, for fear of cracking the dewar and a consequent

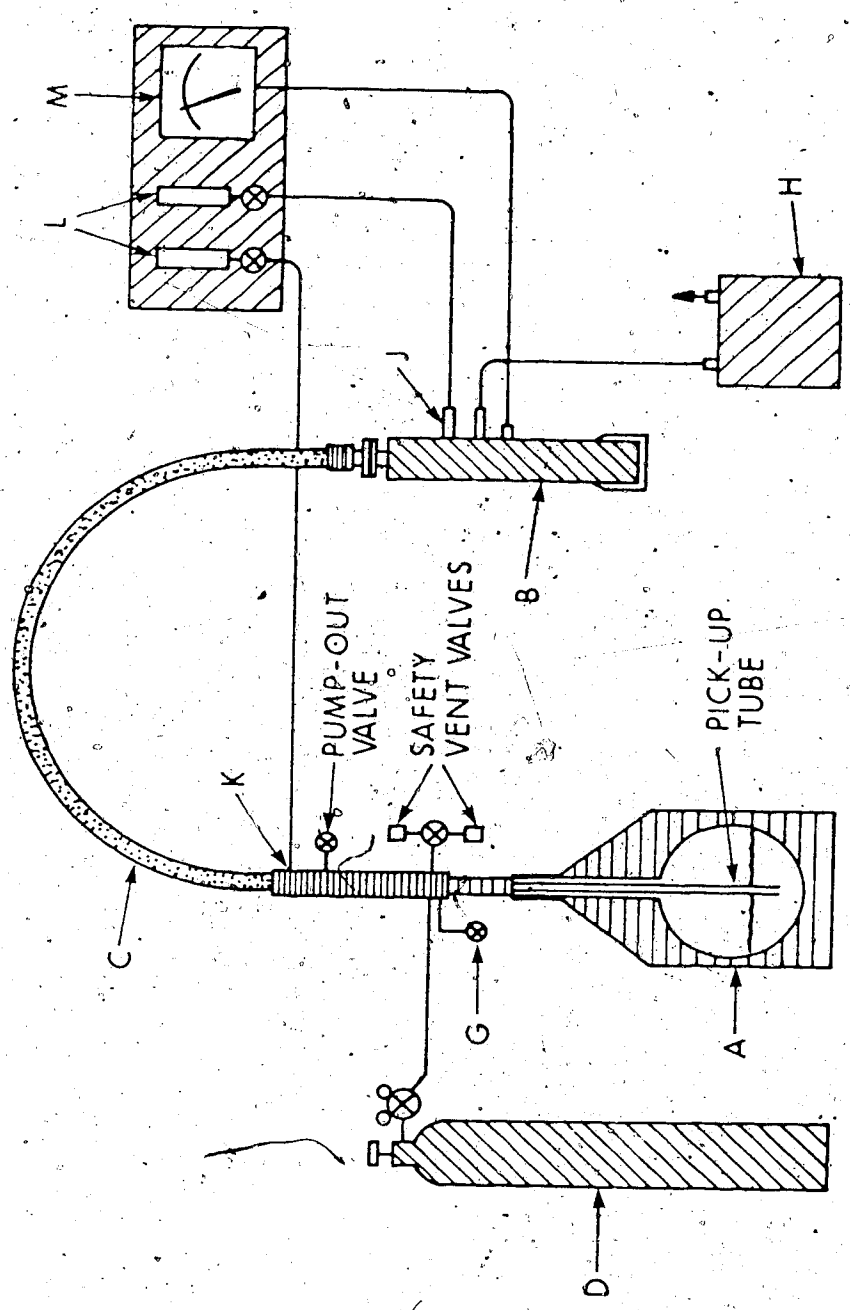


Fig. 2.4. Liquid helium cryostat and peripheral equipment: A, dewar; B, optical cell; C, transfer line; D, gas cylinder; G, gauge; H, pump; J, tip-flow vent; K, heat shield vent; L, flow meters; M, temperature controller.

explosion. The pump H evacuates the vacuum shroud to the required pressure. The helium gas flows from the tip flow vent J, and the heat shield vent K, into the two flow meters L. The leads from the temperature sensors and control heater are attached to the temperature controller M. This is a Model 5301 Temperature Controller purchased from Artronix Instrumentation, St. Louis, Missouri, which will, if required, automatically adjust the voltage applied to the control heater to give a temperature stability of  $0.01^{\circ}\text{K}$ . The vacuum jacket in the flexible transfer line was evacuated through its pump-out valve to a pressure of less than  $10^{-5}$  Torr before each time it was used.

The description of the apparatus is now complete. The procedure for placing the pellet samples in the optical cell, while keeping them cold and free from ice, and the coupling of the optical cell to the other cryogenic equipment, is described in the next section.

### 2.5.3 Pellet Handling Procedure and Cryogenics

The procedure for coupling the sample holder, that is the cylinder C (Fig. 2.2) containing the pellet, to the cold end and attaching the vacuum shroud will be described first.

The uninsulated can containing a table, which is described in Section 2.5.1, was used for this procedure. The cold end was suspended vertically inside the can from a retort stand, with the O-rings of the vacuum shroud seal just above the top of the can. Two cylindrical brass holders, which were designed to hold the radiation shield and the sample holder,

were placed on brass pivots screwed to the table. The radiation shield was placed in the appropriate holder and prevented from rotating inside the holder by polyethylene screws. The vacuum port on the cold end was attached to a vacuum line by rubber pressure tubing. A plexi-glas cover was placed over the back half of the can. This cover contained a slot to allow the cold end to be easily moved between the two brass holders. The can was then filled to just below the surface of the table with liquid nitrogen, and allowed to cool for 30 minutes.

The steel pot, containing the sample in the pressure apparatus cooled with liquid nitrogen (Section 2.5.1), was then transferred from the 100 ton press to the side arm of the can. The retaining block, containing the pistons and sample holder, was placed in a well in the table inside the can. The metal pincers were inserted in the hole in the top piston, and gently raised to remove the piston and leave the pellet intact in the sample holder. A long stainless steel rod was screwed onto the sample holder from the side arm of the can and, with the help of a pair of tongs, the sample holder was lifted free of the bottom piston. Great care was required during this operation in order not to dislodge the fragile pellet from the sample holder. The sample holder was then placed in the cylindrical brass holder, whose inner shape prevented the sample holder from rotating inside it, and the long steel rod was removed.

The end of the cryo-tip was placed over the thread on the sample holder, and the cylindrical brass holder was rotated to screw the sample holder firmly onto the cryo-tip, compressing the indium gasket. The sample holder was then lifted clear of the cylindrical brass holder, the cold end was moved across the table, and the cryo-tip plus sample was placed inside the radiation shield. This was screwed into place by rotating its holder. The polyethylene screws clamping the radiation shield were loosened and the radiation shield was removed from its holder. The vacuum shroud, which had been flushed with dry nitrogen gas, was placed in the side arm. The cold end was quickly mated with the vacuum shroud to complete the assembly of the optical cell containing the pellet sample. The cell was then evacuated and removed from the can. Liquid nitrogen was poured into the central tube of the cold end to maintain a sample temperature of below  $100^{\circ}\text{K}$ .

The final stage of the assembly of the cryostat was to connect the flexible transfer tube from the dewar of liquid helium to the cold end. The pick-up tube at the end of the transfer tube was slowly inserted into the liquid helium dewar, allowing five minutes for the helium gas to flush out the air in the transfer line. The pick-up tube was then completely inserted into the dewar, and secured to it by a rubber connector. The dewar was then pressurised from the gas cylinder to 5 psig, and the line from the heat shield vent tube was connected to one of the flow meters. The tube which

delivers the liquid helium to the cold end was placed in a glass cylinder, and the mouth of the cylinder was plugged with cotton wool. The temperature of the gas emerging from the delivery tube was monitored continuously with a thermocouple.

At first, the rate of flow through the heat shield was very erratic. However, over a period of 35 minutes, it stabilised and rose to a value of about 7 litres of gas per minute. At this point, the temperature of the gas emerging from the delivery tube started to drop below room temperature. The optical cell was then removed from the vacuum line, and placed close to the delivery tube. As the temperature of the gas emerging from the delivery tube approached 100°K, the thermocouple was removed from the glass cylinder, and the remaining liquid nitrogen was emptied from the optical cell. The glass cylinder was then removed from around the delivery tube and the tube was inserted into the optical cell as quickly as possible. The tube from the second flow meter was attached to the tip flow vent of the optical cell to ensure that the needle valve had not been blocked by ice during the coupling. The pressure in the dewar was decreased to 2½ psig at this point.

The cell was then secured in the sample compartment of the spectrophotometer, and the tip and heat shield flows were adjusted to give the desired temperature. If the sample was to be stored overnight, the gas flows were adjusted to give a temperature of about 200°K, and a strip chart recorder

was used to record any temperature variation during the night. The vacuum shroud could be continuously evacuated overnight, although usually this was not done.

### 2.6 Mid-Infrared Instrumentation

Mid-infrared spectra between 200 and 4000  $\text{cm}^{-1}$  were recorded on a Beckman IR-12 spectrophotometer. A variety of operating conditions were used. However, the most common ones employed a slit programme which gave a resolution of about 4  $\text{cm}^{-1}$  between 200 and 650  $\text{cm}^{-1}$ , and 2  $\text{cm}^{-1}$  between 650 and 4000  $\text{cm}^{-1}$ . Full scans between 200 and 4000  $\text{cm}^{-1}$  were run at a scanning speed of 20  $\text{cm}^{-1}$ /minute. The variable scale expansion option on the instrument was often used. A fiducial marker was set to give a mark every 25  $\text{cm}^{-1}$  below 2000  $\text{cm}^{-1}$ , and every 50  $\text{cm}^{-1}$  above 2000  $\text{cm}^{-1}$ . In conjunction with other people in this laboratory, mainly Frances E. Bates, the frequencies at which these marks occurred were calibrated against gaseous water, ammonia, carbon dioxide, hydrogen cyanide, deuterium cyanide, methane, hydrogen chloride, deuterium chloride and hydrogen bromide (84). The accuracy of the frequencies of the fiducial marks is believed to be at least  $\pm 0.5 \text{ cm}^{-1}$  below 2000  $\text{cm}^{-1}$ , and  $\pm 1.0 \text{ cm}^{-1}$  above 2000  $\text{cm}^{-1}$ . All frequencies reported herein were measured with respect to the fiducial marks.

The low temperature cells were sealed in the sample compartment by plexi-glas covers and plasticine. The instrument was purged with either dry air, from a Puregas Model HR-211-112-9 dryer, or dry nitrogen gas, boiled from a liquid nitrogen



dewar and warmed to room temperature by passage through a copper coil.

Chapter Three. Mid-Infrared Spectra of Structure I  
Trimethylene Oxide Hydrate

3.1 General

In this chapter, the results of the study of the mid-infrared spectra of TMO hydrate I contained in mulls and pellets will be presented. The technique of recording the infrared spectra of hydrates dispersed in mulling agents is now well-established (48, 49), so these spectra show definitive evidence of the vibrations of TMO hydrate I at about 95°K. The technique of recording the infrared spectra of hydrates dispersed in pelleting agents was developed during this work so that the temperature dependence of the absorption could be studied. The validity of the results obtained from the pellets will be determined by comparison with those obtained from the mulls.

The first half of this chapter will deal with the mid-infrared spectra of mulls of TMO hydrate I. The reason for dispersing the hydrate in mulling agents with a refractive index comparable to that of the hydrate is to reduce the reflection and scattering of radiation to the point where the transmission spectrum is a good approximation to the absorption spectrum, even when the diameters of the hydrate particles approximate or

exceed the wavelength of the radiation. However it is necessary to thoroughly grind the hydrate and to keep the mulling agents liquid rather than solid. The physical state of the three mulling agents propane, propylene and Freon 13 was easily determined from their mid-infrared absorption bands and, if necessary, was corrected by heating the sample (Section 2.4).

No impurity bands were detected in the infrared spectrum of the trimethylene oxide (Section 2.1). However there are basically three other possible impurities in the spectroscopic samples: extrinsic ice deposited on the windows during the preparation of the mull sample, solid trimethylene oxide due to an excess of trimethylene oxide being present during the hydrate preparation, and TMO hydrate II due to either a solution of incorrect concentration being used for the sample preparation or insufficient time being allowed for annealing the sample.

A common impurity in hydrate samples is intrinsic ice, which is formed during the preparation of the hydrate because an excess of water is present. The powder X-ray diffraction photographs showed that this was not a problem in samples of TMO hydrate I, because the intense lines due to ice at  $2\theta$  values of  $22.7^\circ$ ,  $24.2^\circ$  and  $25.6^\circ$  (Cu  $K_\alpha$  radiation) were not observed.

This is to be expected because care was taken to prepare the solutions with the correct stoichiometry and any excess water would have formed TMO hydrate II (see Fig. 1.3), not ice.

The possibility of contamination by extrinsic ice is solely dependent on the care taken when preparing the infrared samples in the cold can (Section 2.4). Possible sources are the liquid nitrogen used to cool the sample during grinding, liquid nitrogen splashes on the cesium iodide windows during cooling, dislodgement of ice from the rim of the can and condensation of ice on the cesium iodide windows while mating the inner and outer parts of the liquid nitrogen cryostat (Fig. 2.1). Contamination from all of these sources was shown to have been essentially eliminated by the extremely low intensity of the broad absorption at  $3220 \text{ cm}^{-1}$  (Section 1.3.1) in the spectra of Freon 13 and of TMO deuterate I in Freon 13.

Contamination of the hydrate samples by solid trimethylene oxide was a rare occurrence because the amount of trimethylene oxide required for the hydrate preparation was accurately weighed on a single beam balance. Such contamination was readily determined by the presence of a line with a  $2\theta$  value of  $20.2^\circ$  (Cu  $K_\alpha$  radiation, Section 3.4) in the X-ray photograph of a contaminated hydrate sample. Also the peak frequencies of powdered trimethylene oxide in a propane mull were determined, so that careful measurement

of an infrared spectrum of a contaminated hydrate sample revealed the presence of solid trimethylene oxide, as shown in Fig. 3.1, boxes A, B and C.

In fact the most common contaminant of the TMO hydrate I samples was TMO hydrate II. This was expected from a consideration of the trimethylene oxide - water phase diagram (Fig. 1.3), which shows that on cooling a solution of the TMO hydrate I composition, the first solid to form is TMO hydrate II. In order to minimise the amount of TMO hydrate II formed, the solution was rapidly cooled from room temperature to 77°K. If any TMO hydrate II formed during this rapid cooling, a corresponding excess of trimethylene oxide remained, so the sample was annealed at -27°C for about two weeks to allow these two contaminants to react to form TMO hydrate I. Occasionally samples made by this method contained TMO hydrate II. This was easily identified by the presence of a line with a  $2\theta$  value of  $9.0^\circ$  (Cu  $K_\alpha$  radiation) in the X-ray photograph. This is one of the more intense diffraction lines of TMO hydrate II (Section 4.4), and its  $2\theta$  value is lower than any observed for TMO hydrate I, so it provides a sensitive test for contamination by TMO hydrate II. The infrared spectra of TMO hydrate I in mulls were found to be less sensitive to the presence of TMO hydrate II than the X-ray photographs. All of the infrared spectra reported in this chapter were recorded on TMO hydrate I samples, which

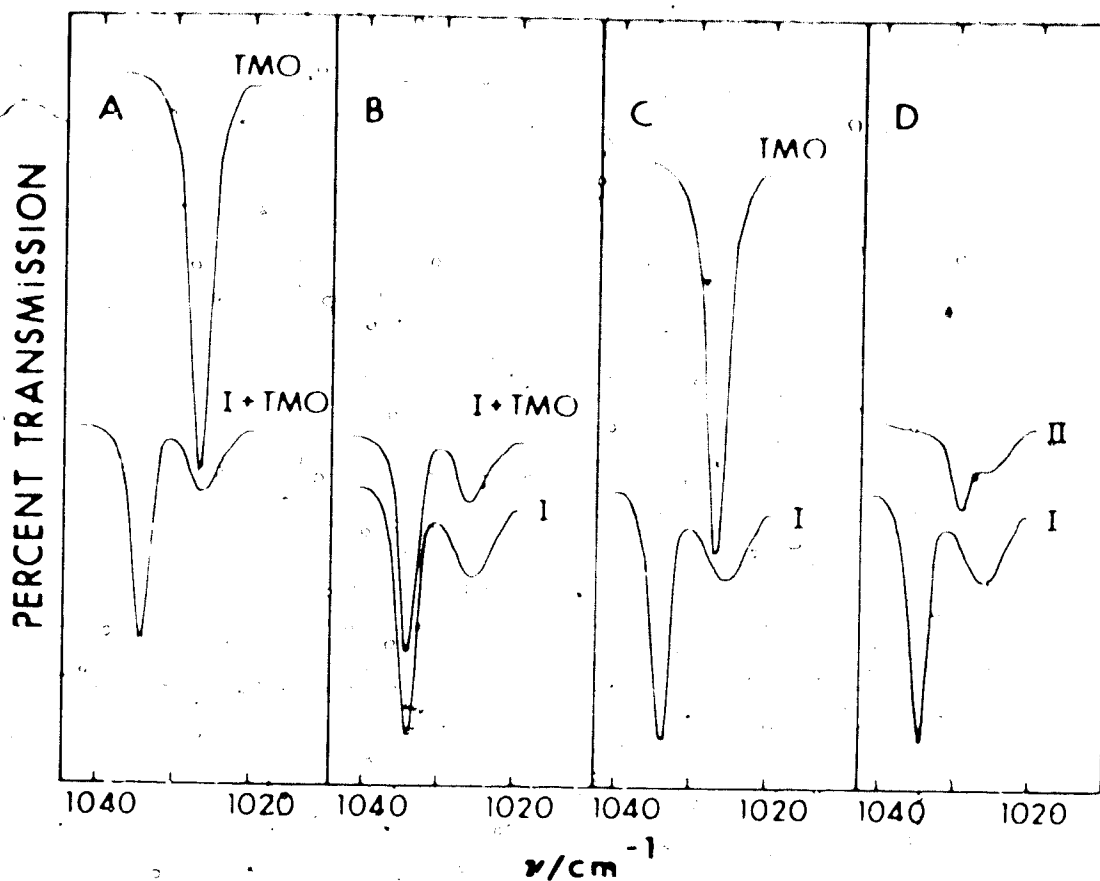


Fig. 3.1 Mid-infrared mull spectra of TMO deuterate I (I), TMO deuterate II (II) and solid trimethylene oxide (TMO) at  $95^{\circ}\text{K}$ . The maximum and minimum percent transmissions of each curve are: A- TMO, 73, 27, I + TMO, 71, 66; B- I + TMO, 71, 66, I, 59, 41; C- TMO, 73, 27, I, 59, 41; D- II, 86, 81, I, 59, 41.

were uncontaminated by TMO hydrate II as determined by X-ray diffraction.

Before presenting the spectra, it is convenient to discuss a band observed in the infrared spectra of the mulls at  $1025.2 \text{ cm}^{-1}$  which could not be attributed to TMO hydrate I, TMO hydrate II, ice or solid trimethylene oxide. This band was observed in all three mulling agents but its intensity relative to that of the hydrate absorption was highly variable even with the same mulling agent. Curves I in Fig. 3.1, boxes B, C, D, were taken from a spectrum in which the absorption at  $1025.2 \text{ cm}^{-1}$  was very strong. The absorption in the same region by TMO hydrate II (Fig. 3.1, box D, curve II), shows a peak at  $1028.5 \text{ cm}^{-1}$  superimposed on a broad band to slightly lower frequency. Thus the fundamental absorption at  $1028.5 \text{ cm}^{-1}$  of TMO hydrate II is clearly not responsible for the  $1025.2 \text{ cm}^{-1}$  band observed in the spectra of TMO hydrate I, and, in fact, the latter band also appears to be present in the spectra of TMO hydrate II. The absorption by powdered trimethylene oxide dispersed in liquid propane (Fig. 3.1 boxes A and C, curve TMO) at  $1026.1 \text{ cm}^{-1}$  is about  $1 \text{ cm}^{-1}$  to high frequency, and one-third of the half-width, of the band in question. Thus on this evidence alone, it is unlikely that the band at  $1025.2 \text{ cm}^{-1}$  is due to excess trimethylene oxide. This is confirmed in box B of Fig. 3.1, where it is seen that a slight excess of trimethylene oxide in a TMO hydrate I sample (curve I + TMO) results in an absorption at  $1026.0 \text{ cm}^{-1}$ ,  $0.8 \text{ cm}^{-1}$  to high frequency

of the uncontaminated TMO hydrate I sample (curve I). Box A of Fig. 3.1 shows the similarity in absorption of the powdered trimethylene oxide sample (curve TMO) and the TMO hydrate I sample contaminated by a slight excess of trimethylene oxide (curve I + TMO). The nature of the species which absorbs at  $1025.2 \text{ cm}^{-1}$  is unknown and this band will be ignored in the remainder of this thesis.

### 3.2 Mid-Infrared Spectra of Structure I Trimethylene Oxide Hydrate in Mulls

#### 3.2.1 General

Typical original spectra of TMO hydrate I and TMO deuterate I mulled with propane, propylene and Freon 13 at  $95^\circ\text{K}$  are shown in Figs. 3.2 and 3.3. The spectrum of each compound with the mulling agent absorption removed has been composed from spectra in each of the three mulling agents and is shown in Fig. 3.4 for TMO hydrate I and Fig. 3.5 for TMO deuterate I. The intensities of features which were taken from different original spectra were scaled so that the relative intensities shown in Figs. 3.4 and 3.5 are approximately correct. The original spectra (Figs. 3.2 and 3.3) were recorded at a resolution of better than  $5 \text{ cm}^{-1}$  between 300 and  $650 \text{ cm}^{-1}$ , and better than  $2.5 \text{ cm}^{-1}$  between 650 and  $4000 \text{ cm}^{-1}$ . The frequencies of the observed features and their estimated accuracy are listed in Table 3.1. All of the features, including the weak ones, were reproducible.



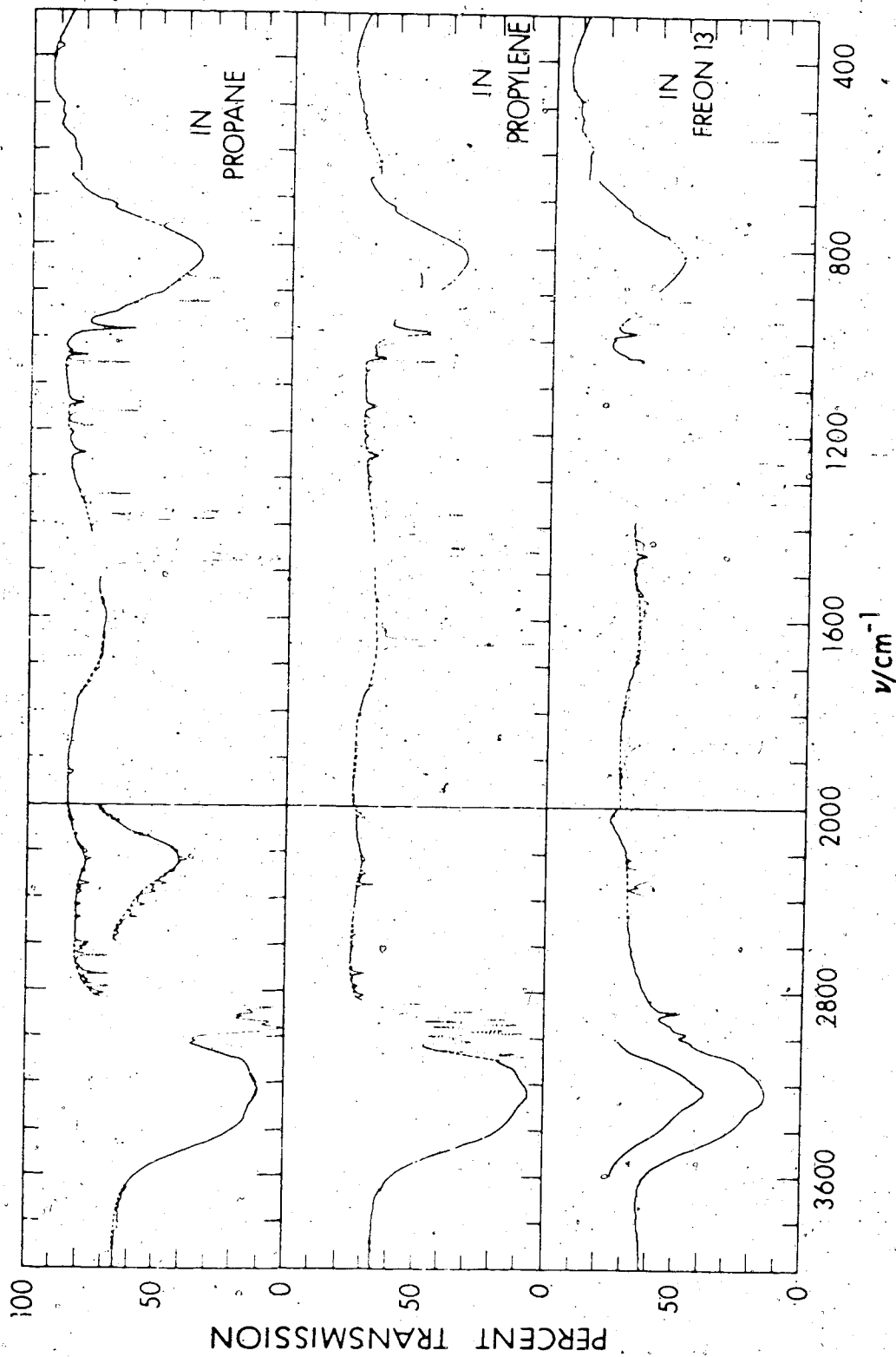


Fig. 3.2. Mid-infrared spectra of structure I trimethylene oxide hydrate dispersed in mulling agents at 95°K. The dotted lines indicate the absorptions of the mulling agents and the dashed lines indicate the absorption of the hydrate in these regions. The inserts have not been offset.

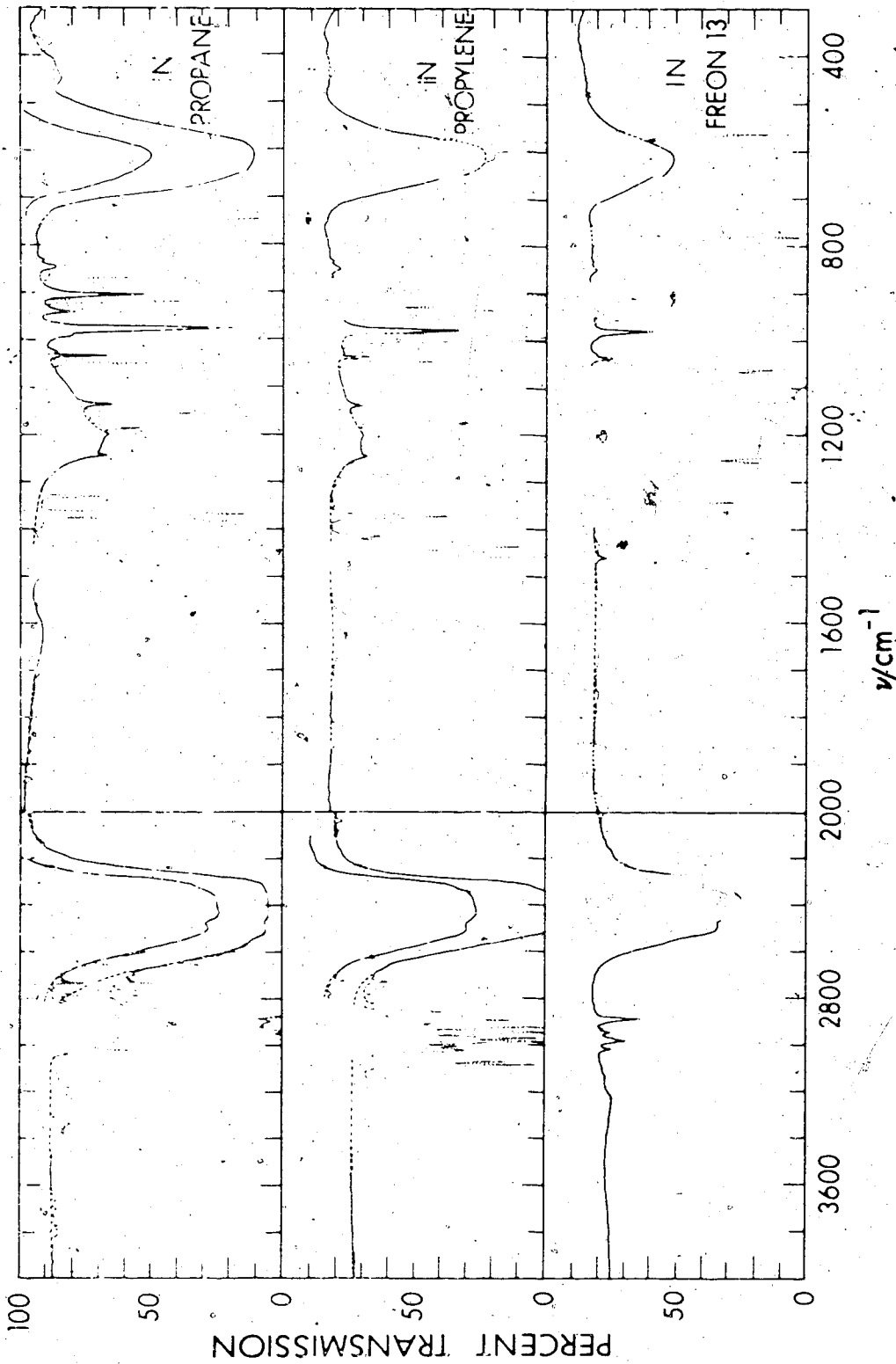


Fig. 3.3. Mid-infrared spectra of structure I trimethylene oxide deuterate dispersed in mulling agents at 95°K. The dotted lines indicate the absorptions of the mulling agents and the dashed lines indicate the absorption of the deuterate in these regions. The inserts have been raised by 10 percent transmission.

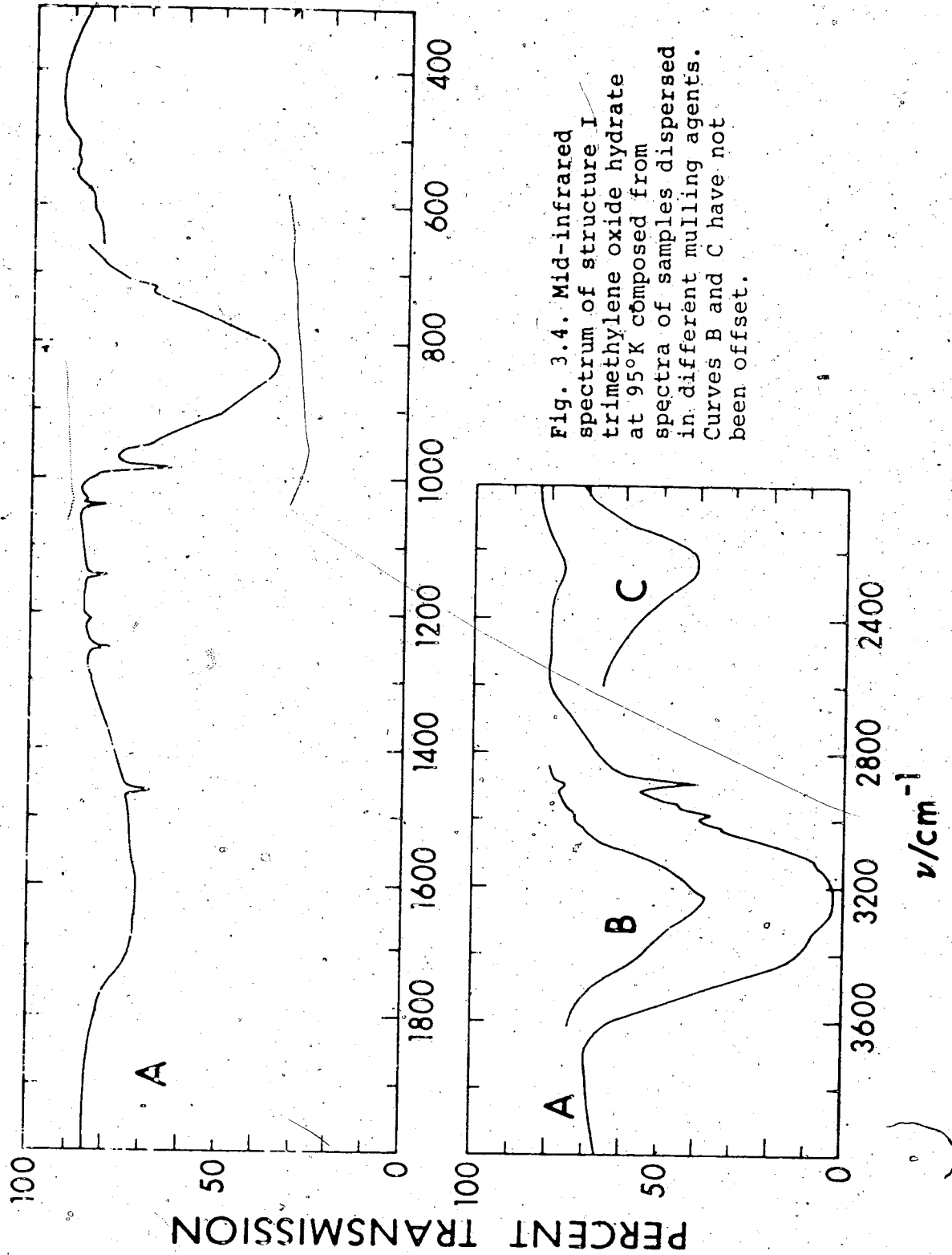


Fig. 3.4. Mid-infrared spectrum of structure I trimethylene oxide hydrate at 95°K composed from spectra of samples dispersed in different mulling agents. Curves B and C have not been offset.

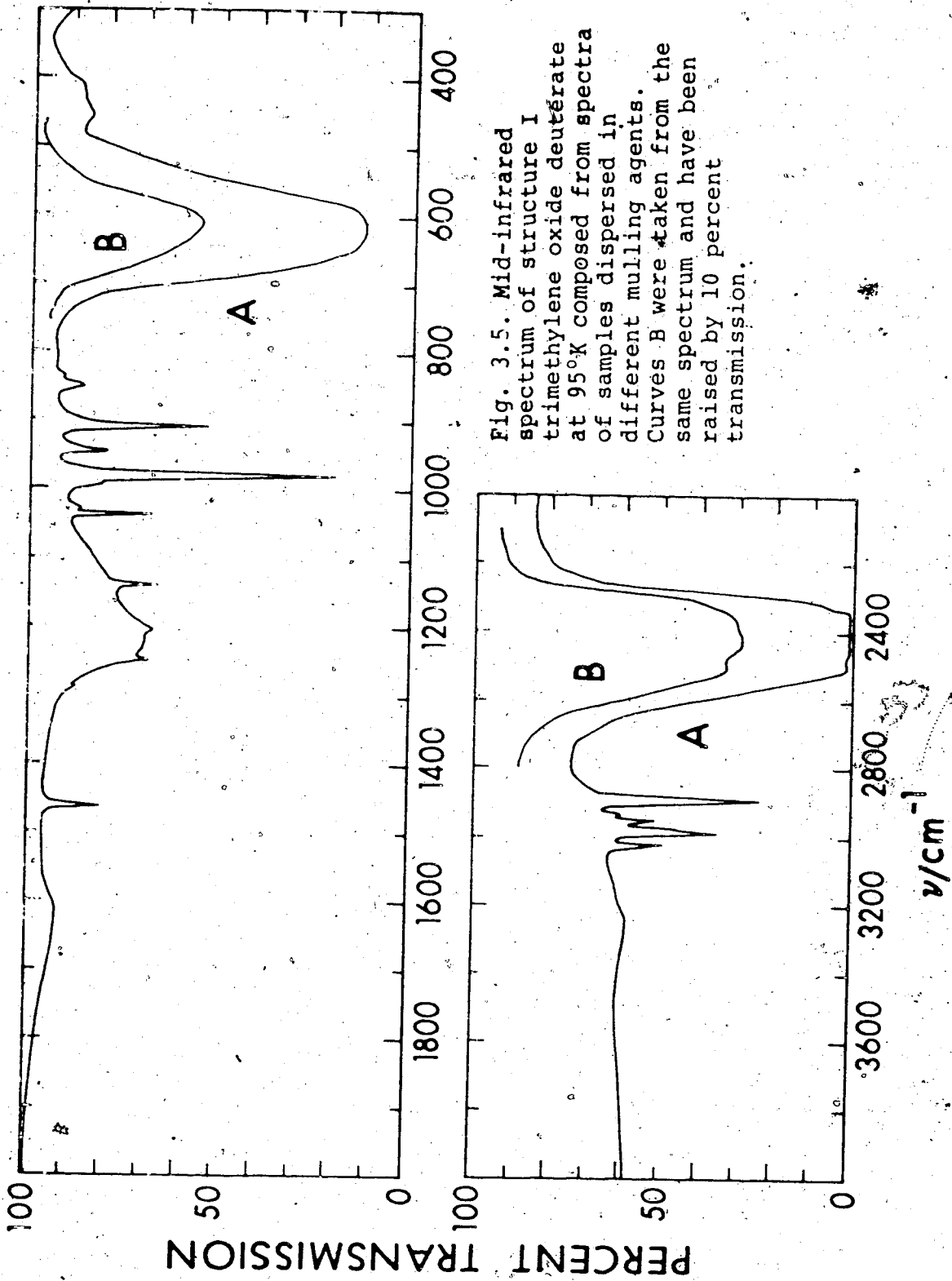


Fig. 3.5. Mid-infrared spectrum of structure I trimethylene oxide deutérate at 95°K composed from spectra of samples dispersed in different mulling agents. Curves B were taken from the same spectrum and have been raised by 10 percent transmission.

Table 3.1

Frequencies of the Observed Features  
in the Mid-Infrared Spectra of  
Structure I Trimethylene Oxide Hydrate  
and Deuterate in Mulls at 95°K<sup>a</sup>

TMO Hydrate I $\nu/\text{cm}^{-1}$	Assignment	TMO Deuterate I $\nu/\text{cm}^{-1}$	
~3335 sh	$\nu_{\text{OH}}(\text{H}_2\text{O})$	}	
3231 ±4 vs, br			
~3122 sh			
	$\nu_{\text{OH}}(\text{HDO})$	{ 3297 ±4 s, br	
		{ ~3237 sh	
3019 ±2 sh	$\nu_{19}(\text{TMO})$	3018.4 ±1 m	
2983 ±3 w	$\nu_1(\text{TMO})$	2984.9 ±1 s	
	2 x $\nu_{14}(\text{TMO})?$	2973 ±2 sh	
2946 ±3 sh	$\nu_{20}(\text{TMO})$	2946.1 ±1 m	
2930 ±5 sh	$\nu_9(\text{TMO})$	2930.9 ±1 mw	
2887 ±2 s	$\nu_{13}(\text{TMO})$	2887.7 ±1 s	
		2499 ±10 sh	
	$\nu_{\text{OD}}(\text{D}_2\text{O})$	}	
			{ 2428 ±4 vs, br
			{ ~2367 sh
		{ ~2303 sh	

TMO Hydrate I $\nu/\text{cm}^{-1}$	Assignment	TMO Deuterate I $\nu/\text{cm}^{-1}$
2439 $\pm 4$ s, br ~2414 sh	$\nu_{\text{OD}}$ (HDO)	
2235 $\pm 20$ m, br	$\left\{ \begin{array}{l} 3\nu_{\text{R}}(\text{H}_2\text{O}), \\ \nu_2(\text{H}_2\text{O}) + \nu_{\text{R}}(\text{H}_2\text{O}). \end{array} \right.$	
1650 $\pm 30$ m, br	$\nu_2(\text{H}_2\text{O})$	
	$\left\{ \begin{array}{l} 3\nu_{\text{R}}(\text{D}_2\text{O}), \\ \nu_2(\text{D}_2\text{O}) + \nu_{\text{R}}(\text{D}_2\text{O}) \end{array} \right.$	1630 $\pm 20$ w, br
1456.5 $\pm 1$ m	$\nu_4/\nu_{14}$ (TMO)	1457.5 $\pm 1$ m
1283 $\pm 2$ vw	$\nu_{10}$ (TMO)	1283 $\pm 2$ vw
1244.5 $\pm 0.5$ m	$\nu_{16}$ (TMO)	1244.8 $\pm 0.5$ mw
	$\nu_2(\text{D}_2\text{O})$	1225 $\pm 15$ m, br
1202.7 $\pm 1$ w	$\nu_{11}$ (TMO)	1201.4 $\pm 1$ w
1137.9 $\pm 0.5$ m	$\nu_{21}$ (TMO)	1137.3 $\pm 0.5$ m
1033.8 $\pm 0.5$ m	$\nu_6$ (TMO)	1033.6 $\pm 0.5$ m
991 $\pm 3$ sh		$\left\{ \begin{array}{l} 989 \pm 2 \text{ sh.} \\ 976.8 \pm 0.5 \text{ vs} \end{array} \right.$
978.1 $\pm 0.5$ s	$\nu_7/\nu_{17}$ (TMO)	
941 $\pm 5$ sh	$\nu_{18}$ (TMO)	940.9 $\pm 1$ m
900 $\pm 5$ sh	$\nu_8$ (TMO)	904.9 $\pm 0.5$ s
	$\nu_{22}$ (TMO)	846.0 $\pm 1$ mw
	$\nu_{12}$ (TMO)	831.2 $\pm 1$ w
819 $\pm 5$ vs, br	$\nu_{\text{R}}(\text{H}_2\text{O})$	
713.1 $\pm 1$ w	$\nu_{23}$ (TMO)	

TMO Hydrate I $\nu/\text{cm}^{-1}$	Assignment	TMO Deuterate I $\nu/\text{cm}^{-1}$
		~ 670 sh
	$\nu_R(\text{D}_2\text{O})$	611 $\pm$ 5 vs, br
		451 $\pm$ 5 mw
		420 $\pm$ 10 mw
		375 $\pm$ 10 w
615 $\pm$ 15 w, br	$\nu_R(\text{H}_2\text{O})$	
577 $\pm$ 10 w, br		
525 $\pm$ 5 w, br		
502 $\pm$ 5 w, br		

a) vs = very strong, s = strong, m = medium, mw = medium-weak, w = weak, vw = very weak, br = broad, sh = shoulder.

The temperature of the sample could not be measured accurately. However it was always necessary to heat propylene and Freon 13 mulls to melt the mulling agent, and sometimes this was also necessary for propane mulls. The melting points for propane, propylene and Freon 13 are 84, 88 and 92 K respectively, so the temperature was clearly in the range  $95 \pm 10$  K.

The interaction between the water and the trimethylene oxide molecules in the clathrate hydrate is weak compared to the strengths of the covalent bonds within each species and the hydrogen bonds between the water molecules (Chapter 1). Thus, in the first approximation, it is logical to consider the vibrations of the water molecules and the guest molecules separately. The absorption by the water molecules is readily identified since it is broad and occurs at approximately 30% lower frequencies in the spectra of the deuterate, while the absorption by the guest molecules is sharp and occurs at about the same frequency in the hydrate and deuterate. The assignment of the water absorption to specific vibrational modes follows from a comparison with the spectra of ice (Chapter 1) and ethylene oxide hydrate (Chapter 1). The assignment of the trimethylene oxide absorption to specific vibrational modes follows from previous studies of the spectra of gaseous trimethylene oxide (Chapter 1). These assignments are given in Table 3.1.



### 3.2.2 Absorption by the Water Molecules

The band due to  $\nu_{\text{OH}}(\text{H}_2\text{O})$  (see Section 1.3 for nomenclature) extends from about 2800 to 3600  $\text{cm}^{-1}$  as shown in Fig. 3.6. It has a peak frequency of 3231  $\text{cm}^{-1}$  with poorly defined shoulders at about 3335 and 3122  $\text{cm}^{-1}$ . The half-width of this band is about 300  $\text{cm}^{-1}$ . The five weak features between 2850 and 3050  $\text{cm}^{-1}$  (Fig. 3.6, Table 3.1) remain unchanged in frequency in the deuterate spectrum and must, therefore, be due to trimethylene oxide. The band due to  $\nu_{\text{OD}}(\text{D}_2\text{O})$  extends from about 2200 to 2700  $\text{cm}^{-1}$  (Fig. 3.6). The peak frequency is 2428  $\text{cm}^{-1}$  with a high frequency peak at 2499  $\text{cm}^{-1}$  and poorly defined low frequency shoulders at about 2367 and 2303  $\text{cm}^{-1}$ . This band has a half-width of about 250  $\text{cm}^{-1}$ . The ratio of the peak frequency of the  $\nu_{\text{OH}}(\text{H}_2\text{O})$  band to that of the  $\nu_{\text{OD}}(\text{D}_2\text{O})$  band is  $1.331 \pm 0.007$ .

The band due to  $\nu_2(\text{H}_2\text{O})$  is very broad and poorly defined in the spectra of the mulls (Fig. 3.4), since all three mulling agents absorb within this region. The band maximum is most clearly seen in the propane mull (Fig. 3.2) at a frequency of about 1650  $\text{cm}^{-1} \pm 30 \text{ cm}^{-1}$ . The corresponding band of the deuterate,  $\nu_2(\text{D}_2\text{O})$ , has its band maximum at 1225  $\text{cm}^{-1} \pm 15 \text{ cm}^{-1}$ , and extends over the region 1050 to 1300  $\text{cm}^{-1}$  (Fig. 3.5). The four sharp features at 1283, 1244.8, 1201.4 and 1137.3  $\text{cm}^{-1}$  observed on this band (Fig. 3.5) remain unshifted in the hydrate spectra and must be due to trimethylene oxide vibrations. The exact shape of

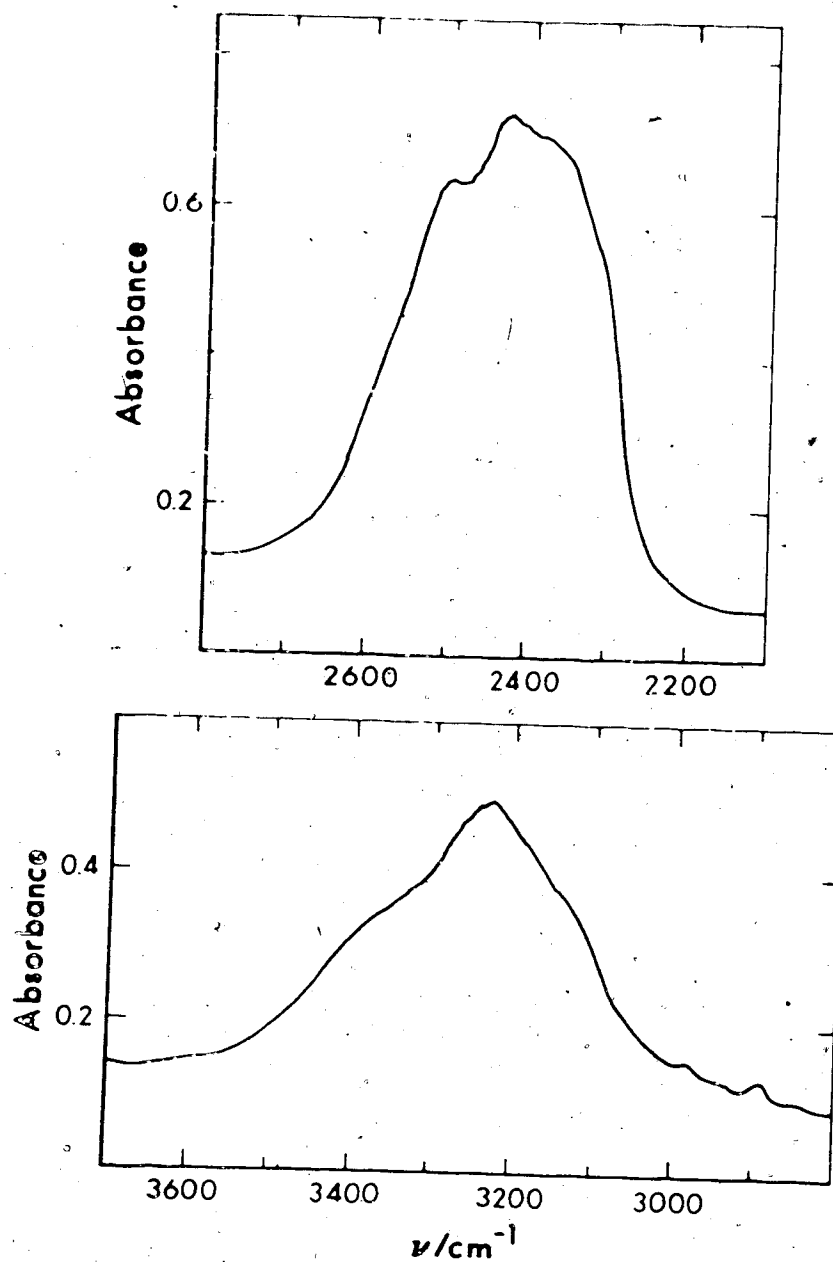


Fig. 3.6. The  $\nu_{OH}$  ( $\text{H}_2\text{O}$ ) band of structure I trimethylene oxide hydrate (lower box) and the  $\nu_{OD}$  ( $\text{D}_2\text{O}$ ) band of structure I trimethylene oxide deuterate (upper box) dispersed in mulling agents at  $95^\circ\text{K}$ .

this band is uncertain due to mulling agent and guest absorption, however the slope on the high frequency side appears to be much steeper than that on the low frequency side. The ratio of the peak frequencies of  $\nu_2(\text{H}_2\text{O})$  and  $\nu_2(\text{D}_2\text{O})$  is  $1.35 \pm 0.05$ .

The band due to  $\nu_R(\text{H}_2\text{O})$  extends from about 450 to  $1000 \text{ cm}^{-1}$  and is somewhat more complex than the water bands already described (Fig. 3.4). The maximum of the main band is at  $819 \pm 5 \text{ cm}^{-1}$ , and the half-width is  $160 \text{ cm}^{-1}$ . The sharp feature at  $978.1 \text{ cm}^{-1}$  and the shoulders at 991, 941 and  $900 \text{ cm}^{-1}$  are all clearly observed as bands at almost identical frequencies in the deuterate spectrum and are, thus, assigned to trimethylene oxide vibrations. The feature at  $713.1 \text{ cm}^{-1}$  is also assigned to trimethylene oxide although it was not observed in the spectrum of the deuterate, possibly because this frequency falls within the  $\nu_R(\text{D}_2\text{O})$  band (Fig. 3.5). The four broad, weak shoulders at about 615, 577, 525 and  $502 \text{ cm}^{-1}$  are believed to be genuine features of the  $\nu_R(\text{H}_2\text{O})$  band.

The corresponding band of the deuterate,  $\nu_R(\text{D}_2\text{O})$ , has its maximum at  $611 \pm 5 \text{ cm}^{-1}$  and a half-width of  $100 \text{ cm}^{-1}$  as shown in Fig. 3.7. This band is uncomplicated by trimethylene oxide or mulling agent absorption and clearly shows a very broad high frequency shoulder at about  $670 \text{ cm}^{-1}$ . The ratio of the peak frequencies of  $\nu_R(\text{H}_2\text{O})$  and  $\nu_R(\text{D}_2\text{O})$  is  $1.34 \pm 0.02$ . Using this ratio, the bands corresponding

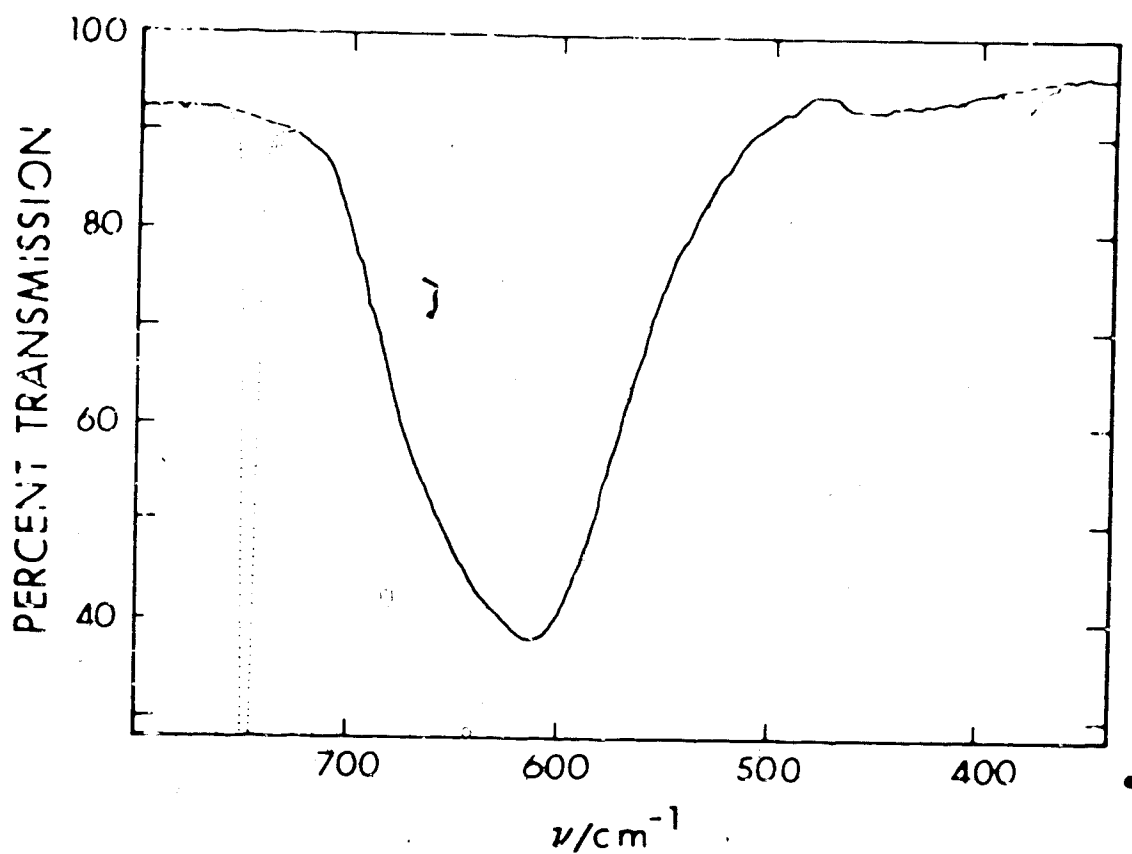


Fig. 3.7. The  $\nu_{\text{R}}(\text{D}_2\text{O})$  band of structure I trimethylene oxide deuterate dispersed in a mulling agent at 95°K. The dotted lines indicate the absorptions of the mulling agent and the dashed lines indicate the absorption of the deuterate in these regions.

to the four broad, weak, low frequency shoulders observed for  $\nu_R(\text{H}_2\text{O})$  would be expected at 458, 431, 392 and 375  $\text{cm}^{-1}$ , all  $\pm 8 \text{ cm}^{-1}$ , in the deuterate spectrum. In the propane mull of Fig. 3.3, two broad bands are observed at 451  $\pm 5 \text{ cm}^{-1}$  and 420  $\pm 10 \text{ cm}^{-1}$  which agree well with the predicted values. The region between 350  $\text{cm}^{-1}$  and 400  $\text{cm}^{-1}$  is obscured in the propane mull by propane absorption; however in the propylene mull (Fig. 3.3) a very weak broad band centered at about 375  $\text{cm}^{-1}$  is seen. The assignment of this band to a real feature of the  $\nu_R(\text{D}_2\text{O})$  band is tentative due to its broad, weak appearance. The band predicted at 392  $\text{cm}^{-1}$ , presumably, merged with the other bands (Fig. 3.5).

Overtone and combination bands of the fundamental water vibrations, discussed above, were also observed in the spectra. The second overtone  $3\nu_R(\text{H}_2\text{O})$  and the combination  $\nu_2(\text{H}_2\text{O}) + \nu_R(\text{H}_2\text{O})$  are both expected at about 2250  $\text{cm}^{-1}$  by comparison with the spectra of ice Ih (Chapter 1) and ethylene oxide hydrate (Chapter 1), and so the band observed at 2235  $\text{cm}^{-1}$  (Fig. 3.2) is assigned to these two modes. Similarly, the broad, weak band observed at about 1630  $\text{cm}^{-1}$  in the deuterate spectra (Fig. 3.3) is assigned to  $3\nu_R(\text{D}_2\text{O})$  and  $\nu_2(\text{D}_2\text{O}) + \nu_R(\text{D}_2\text{O})$ . The peak frequency isotope ratio for these bands is 1.37  $\pm 0.03$ .

The OH and OD stretching vibrations,  $\nu_{\text{OH}}(\text{HDO})$  and  $\nu_{\text{OD}}(\text{HDO})$ , of isolated HDO molecules, that is of HDO

molecules surrounded by  $\text{H}_2\text{O}$  or  $\text{D}_2\text{O}$  molecules, were studied in samples prepared from solutions of approximately 4 and 10 mole percent of HDO in  $\text{D}_2\text{O}$  and approximately 10 mole percent of HDO in  $\text{H}_2\text{O}$ . Although these water solutions were weighed quickly in air, undoubtedly some isotopic exchange occurred, and so the actual concentrations are probably about 6% and 12% HDO in  $\text{D}_2\text{O}$  and about 8% HDO in  $\text{H}_2\text{O}$ . For brevity, these hydrate samples will be referred to as 98%  $\text{D}_2\text{O}$ , 95%  $\text{D}_2\text{O}$  and 95%  $\text{H}_2\text{O}$  samples. The band due to  $\nu_{\text{OH}}$  (HDO) of a 95%  $\text{D}_2\text{O}$  sample has a peak frequency of  $3297 \pm 4 \text{ cm}^{-1}$  and a half-width of about  $155 \text{ cm}^{-1}$ , as shown in Fig. 3.8. This band also exhibits a poorly defined low frequency shoulder at about  $3237 \text{ cm}^{-1}$ . The corresponding band (not shown) from a 98%  $\text{D}_2\text{O}$  sample was identical except that the half-width was reduced to about  $125 \text{ cm}^{-1}$ . The band due to  $\nu_{\text{OD}}$  (HDO) (Fig. 3.8) of a 95%  $\text{H}_2\text{O}$  sample has a peak frequency of  $2439 \pm 4 \text{ cm}^{-1}$  and a half-width of about  $95 \text{ cm}^{-1}$ . This band also shows a very slight low frequency shoulder at about  $2414 \text{ cm}^{-1}$ . The ratio of the peak frequencies of  $\nu_{\text{OH}}$  (HDO) to  $\nu_{\text{OD}}$  (HDO) is  $1.35 \pm 0.01$ .

### 3.2.3 Absorption by the Trimethylene Oxide Molecules

The absorption in the C-H stretching region of TMO deuterate I is shown in Fig. 3.9. This region of the spectrum was studied using the mulling agent Freon 13, which does not absorb in this frequency range. The bands are seen clearly in the spectrum of the deuterate (Fig. 3.9), whereas in the spectrum of the hydrate (Fig. 3.6), they

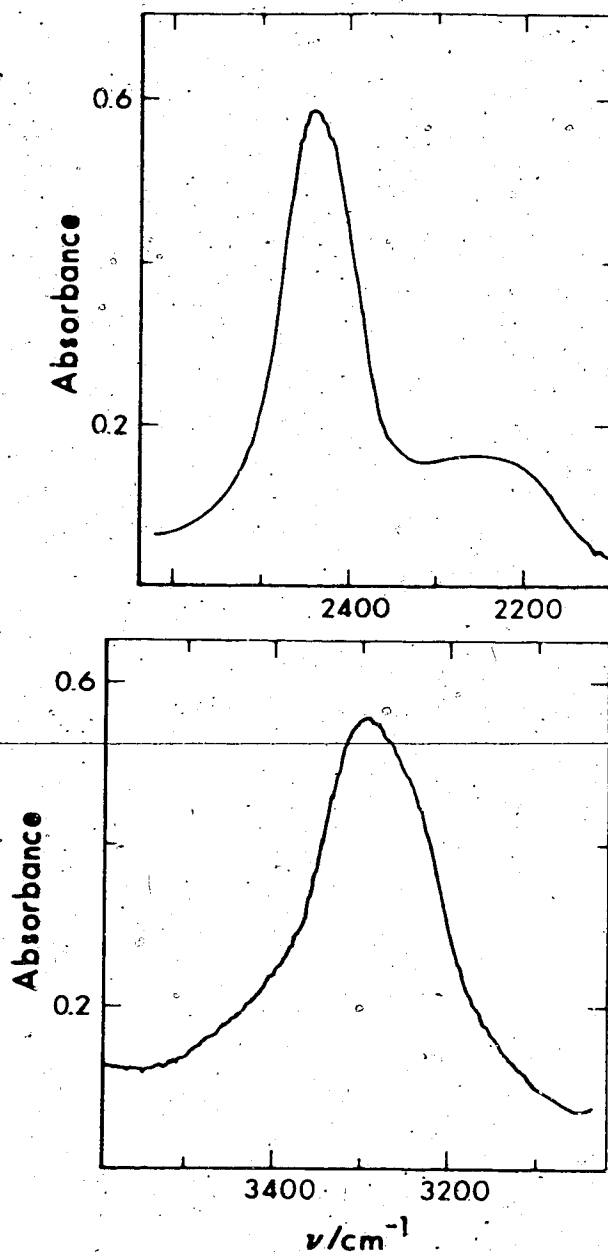


Fig. 3.8. The  $\nu_{OH}$  (HDO) band of structure I trimethylene oxide deuterate containing about 12 percent of HDO (lower box) and the  $\nu_{OD}$  (HDO) band of structure I trimethylene oxide hydrate containing about 8 percent of HDO (upper box) dispersed in mulling agents at 95°K. The broad band near 2225 wavenumbers is  $3\nu_R(H_2O)$  and  $\nu_2(H_2O) + \nu_R(H_2O)$ .

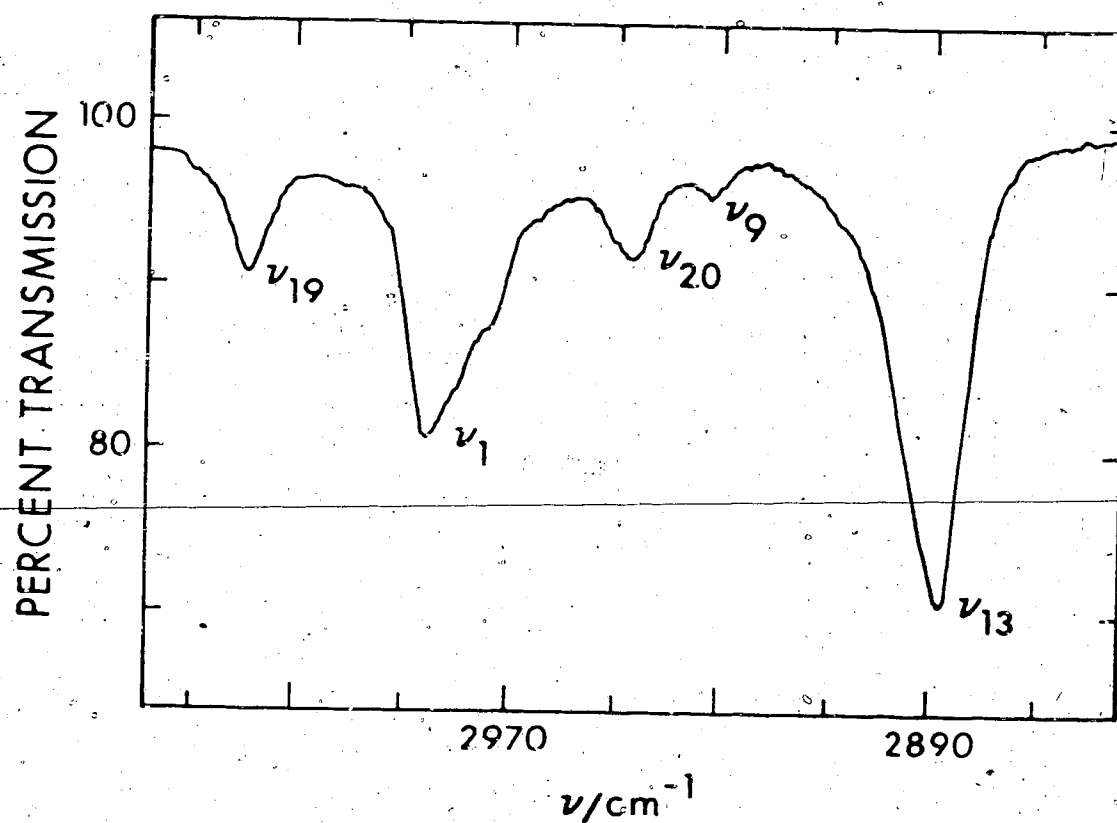



Fig. 3.9. Absorption by the C-H stretching vibrations of structure I trimethylene oxide deuterate dispersed in a mulling agent at 95°K.



are superimposed on the low frequency side of the very intense  $\nu_{\text{OH}}(\text{H}_2\text{O})$  band. The strong, broad absorption observed (Fig. 3.9) at  $2887.7 \text{ cm}^{-1}$  with a half-width of about  $15 \text{ cm}^{-1}$ ,  $\nu_{13}$ , is the third strongest guest absorption and it appears clearly at the same frequency in the hydrate spectrum. The absorption at  $2930.9 \text{ cm}^{-1}$ , due to  $\nu_9$ , is observed as a weak band in the deuterate spectrum and a poorly defined shoulder in the hydrate spectrum, as is the case with the slightly stronger absorption at  $2946.1 \text{ cm}^{-1}$ , due to  $\nu_{20}$ . The second strongest absorption in the C-H stretching region of the spectrum is seen at  $2984.9 \text{ cm}^{-1}$  in the deuterate spectrum with a shoulder at  $2973 \text{ cm}^{-1}$ . The peak, assigned to  $\nu_1$ , occurs at  $2983 \text{ cm}^{-1}$  in the hydrate spectrum but the low frequency shoulder is not observed. The highest frequency guest band, due to  $\nu_{19}$ , is observed as a medium intensity absorption at  $3018.4 \text{ cm}^{-1}$ , with a half-width of about  $8 \text{ cm}^{-1}$ , in the deuterate spectrum (Fig. 3.9), and as a shoulder at  $3019 \text{ cm}^{-1}$  in the hydrate spectrum (Figs. 3.4 and 3.6).

The bands due to the other C-H vibrations, namely the deformations, twists, wags and rocks are shown in Fig. 3.10. The bands due to  $\nu_{11}$ ,  $\nu_{16}$  and  $\nu_{23}$  are presented with a frequency scale of  $50 \text{ cm}^{-1}$  per inch whereas the remaining bands are presented with a frequency scale of  $20 \text{ cm}^{-1}$  per inch. The band due to  $\nu_4$  and  $\nu_{14}$  has been re-plotted at  $10 \text{ cm}^{-1}$  per inch from a spectrum recorded at  $50 \text{ cm}^{-1}$  per inch. The noise has been smoothed on the bands due to



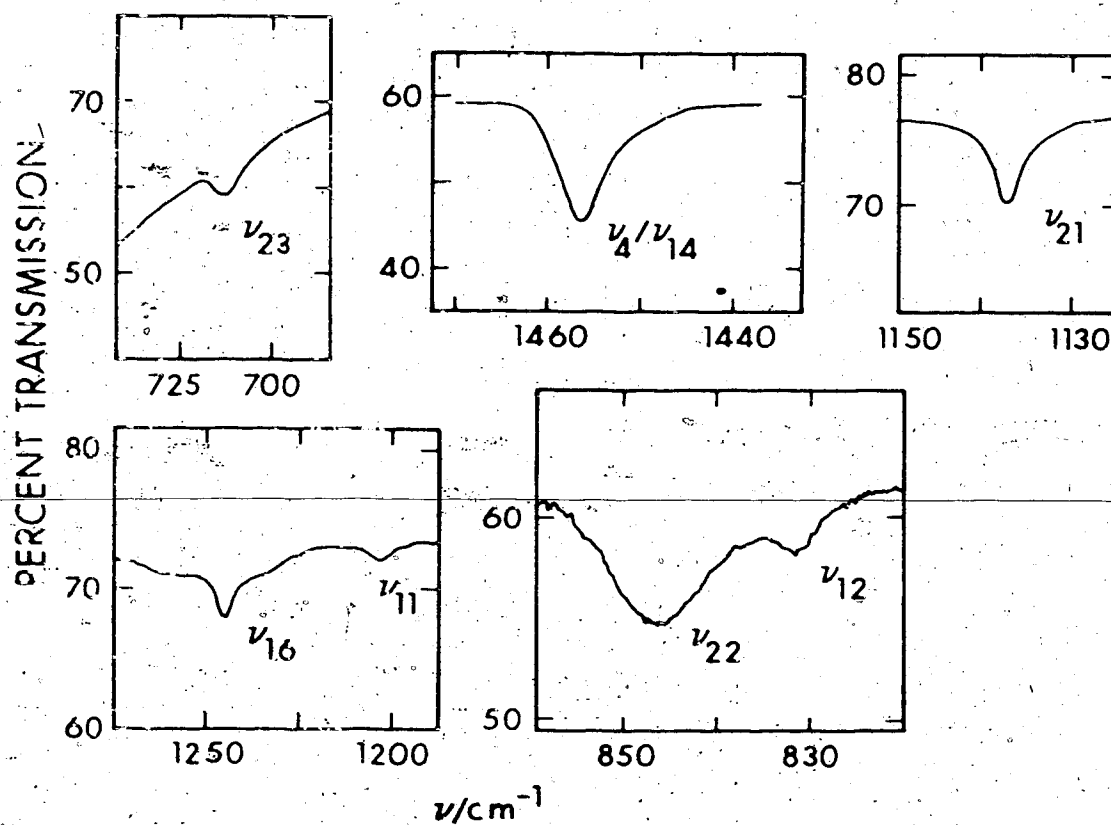


Fig. 3.10. Absorption by  $\nu_4/\nu_{14}$ ,  $\nu_{11}$ ,  $\nu_{16}$  and  $\nu_{23}$  of structure I trimethylene oxide hydrate and  $\nu_{21}$ ,  $\nu_{22}$  and  $\nu_{12}$  of structure I trimethylene oxide deuterate dispersed in mulling agents at  $95^\circ\text{K}$ .

$\nu_4$  and  $\nu_{14}$ ,  $\nu_{21}$  and  $\nu_{23}$ , and was of the magnitude shown for the other bands.

Both  $\nu_4$  and  $\nu_{14}$  are expected between 1400 and 1500  $\text{cm}^{-1}$ , so both are assigned to the only guest absorption observed in this region, at 1456.5  $\text{cm}^{-1}$  in the hydrate spectrum (Fig. 3.10) and 1457.5  $\text{cm}^{-1}$  in the deuterate spectrum. The half-widths of these bands are about 5  $\text{cm}^{-1}$ . A very weak guest absorption assigned to the  $\text{CH}_2$  twist,  $\nu_{10}$ , is observed at about 1283  $\text{cm}^{-1}$  in the hydrate spectra (Figs. 3.2 and 3.4) and the deuterate spectra (Figs. 3.3 and 3.5). It was, however, too weak to include in Fig. 3.10. A weak absorption due to  $\nu_{11}$  is observed at 1202.7  $\text{cm}^{-1}$  in the hydrate spectrum (Fig. 3.10) and at 1201.4  $\text{cm}^{-1}$  in the deuterate spectrum. The half-widths of these bands could not be measured reliably, but are about 6  $\text{cm}^{-1}$ . The absorption due to  $\nu_{16}$  in the spectrum of the hydrate is shown superimposed on a broad band in Fig. 3.10. This broad band is due to the liquid propylene mulling agent. The peak frequencies in the hydrate and deuterate spectra are almost identical at 1244.5 and 1244.8  $\text{cm}^{-1}$  respectively, and the half-width is 5.4  $\text{cm}^{-1}$ . The absorption due to  $\nu_{21}$  is seen at 1137.9  $\text{cm}^{-1}$  in the spectrum of the hydrate and at 1137.3  $\text{cm}^{-1}$  with a half-width of 3.1  $\text{cm}^{-1}$  in the spectrum of the deuterate (Fig. 3.10). Two broad, overlapping bands at 831.2 and 846.0  $\text{cm}^{-1}$  in the spectrum of the deuterate (Fig. 3.10) are assigned to  $\nu_{12}$  and  $\nu_{22}$  respectively. The half-width of the  $\nu_{22}$  band is 10  $\text{cm}^{-1}$ . The frequencies

of these two bands are close to the peak frequency of  $\nu_R(\text{H}_2\text{O})$  in the spectrum of the hydrate, and they were not observed. The remaining band in Fig. 3.10,  $\nu_{23}$ , is observed at  $713.1 \text{ cm}^{-1}$  in the spectrum of the hydrate and is absent in the spectrum of the deuterate, as noted in Section 3.2.2. Its half-width could not be reliably measured, but it is about  $8 \text{ cm}^{-1}$ .

The remaining guest bands are due to vibrations of the trimethylene oxide ring, and are shown in Fig. 3.11. The second strongest guest absorption is the band assigned to  $\nu_8$  which is observed at  $904.9 \text{ cm}^{-1}$  with a half-width of  $5.2 \text{ cm}^{-1}$  in the spectrum of the deuterate (Fig. 3.11). The contour of this band was particularly susceptible to the quality of the mull, and it varied between that shown in curve A for a good mull and that shown in curve B for a poor mull. This strong band is reduced to a shoulder at about  $900 \text{ cm}^{-1}$  in the spectrum of the hydrate (Fig. 3.4). A similar susceptibility to the quality of the mull was observed for the band at  $940.9 \text{ cm}^{-1}$ ,  $\nu_{18}$ , in the spectrum of the deuterate (Fig. 3.11). Curve A shows the contour obtained from a good mull, and curve B shows the one from a poor mull. The half-width for this band, measured from the spectrum of a good mull, was  $6.0 \text{ cm}^{-1}$ . The corresponding absorption of the hydrate is observed as a shoulder on the  $\nu_R(\text{H}_2\text{O})$  band at about  $941 \text{ cm}^{-1}$ . The strongest guest absorption is observed at  $978.1 \text{ cm}^{-1}$  in the spectrum of the

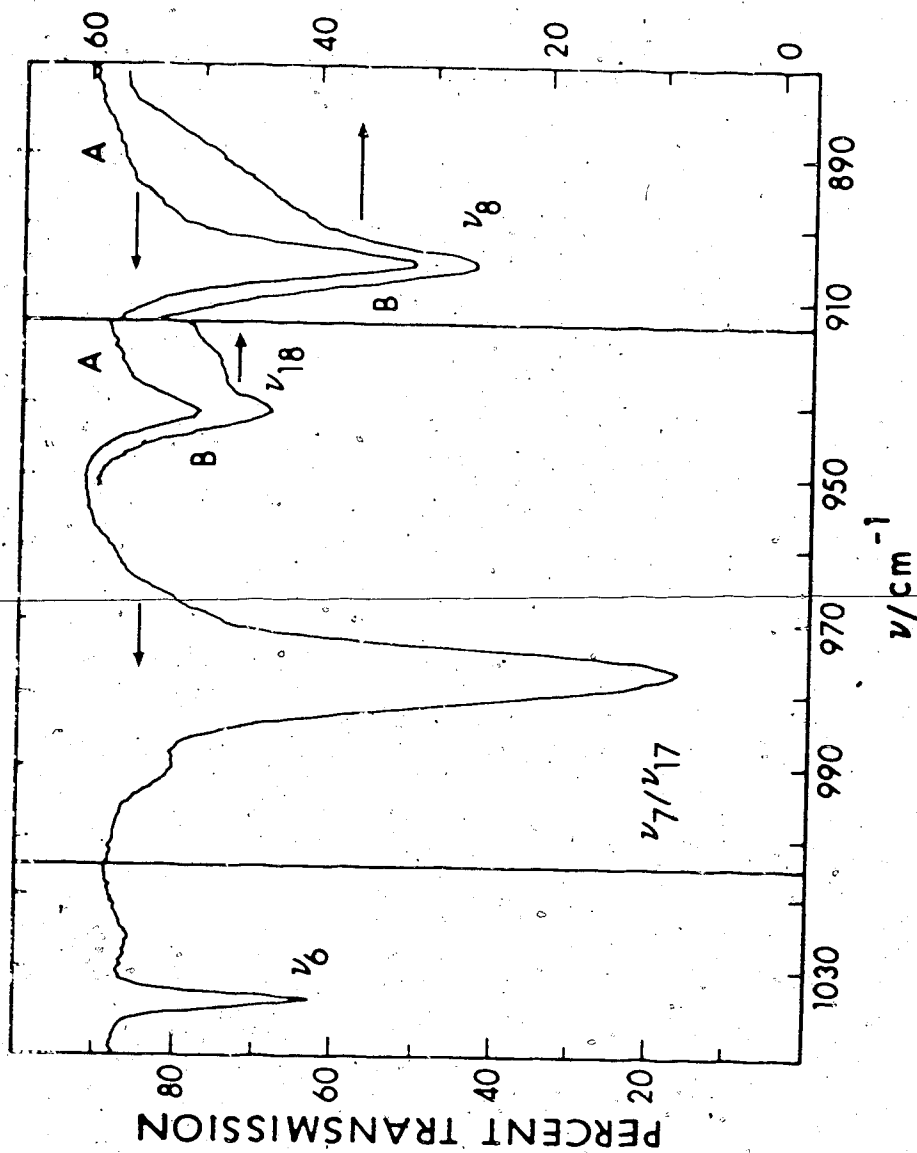


Fig. 3.11. Absorption by the ring vibrations of structure I trimethylene oxide deuterate as recorded from a good mull (curves A) and a poor mull (curves B) at 95°K. The arrows show the appropriate transmission scale.

hydrate and at  $976.8 \text{ cm}^{-1}$  in the spectrum of the deuterate (Fig. 3.11). A well defined shoulder is seen on the high frequency side of this band at about  $991 \text{ cm}^{-1}$  in the spectrum of the hydrate and about  $989 \text{ cm}^{-1}$  in the spectrum of the deuterate. There is also an indication of one, or possibly two, poorly defined shoulders to low frequency of the main band (Fig. 3.11). The half-width of this band is  $6.9 \text{ cm}^{-1}$  and the frequency difference of  $1.3 \text{ cm}^{-1}$  between the hydrate and deuterate is considered to be real. The two main features are assigned to  $\nu_7$  and  $\nu_{17}$ , and the specific assignment will be discussed in Chapter 5. Finally, the sharpest guest absorption, due to the ring breathing mode,  $\nu_6$ , is observed at  $1033.8 \text{ cm}^{-1}$  in the spectrum of the hydrate and  $1033.6 \text{ cm}^{-1}$  in the spectrum of the deuterate (Fig. 3.11), with a half-width of  $2.0 \text{ cm}^{-1}$ . The broad, weak absorption observed to low frequency of  $\nu_6$  in Fig. 3.11 has been discussed in Section 3.1.

The slight differences in the frequencies of corresponding trimethylene oxide absorptions of the hydrate and deuterate (Table 3.1), except in the one case noted above, are within experimental error and are, thus, not significant.

### 3.3 Mid-Infrared Spectra of Structure I Trimethylene Oxide Hydrate in Pellets

#### 3.3.1 General

In order to investigate the order-disorder transition in TMO hydrate I reported by Davidson et al (54), it was

necessary to vary the temperature of the spectroscopic sample between 75 and 135°K. The variation of the temperature of a sample dispersed in a mulling agent within this range results in three different physical phases of the spectroscopic sample: a mull with solid mulling agent, a mull with liquid mulling agent, and a dispersion in vacuum of the hydrate particles after the vaporization of the mulling agent. The consequent changes in the refractive index at the surface of the hydrate particles produce corresponding changes in the amount of light scattered by the sample, which in turn alter the apparent shapes of the absorption bands. These changes in band shape are sufficient to make the study of the temperature dependence of the bands impractical. It was for this reason that the temperature dependence of the mid-infrared spectrum of TMO hydrate I was studied using hydrate samples dispersed in an alkali halide pellet.

The use of pellets rather than mulls has the obvious added advantage that there are no uncertainties in the spectrum due to absorption by the mulling agent. However the uncertainty that can exist is whether the pressure applied during the formation of the pellet has changed the sample. Basically two methods were used to determine whether such a change had occurred. In the first method the spectrum of the pellet sample, at about 95°K, was compared with that of the mull sample (Section 3.2) to

determine if there were any differences which could be attributed to the pressure treatment. In the second method TMO hydrate I was subjected to a normal pellet pressurisation procedure without any pelletizing agent. The resulting pellet was ground and the X-ray diffraction photograph, and the infrared spectrum in a propane mull, of the resulting powdered sample were recorded. These results were then compared to those obtained from TMO hydrate I that had not been subjected to pressure. Both the X-ray photographs and the spectra of the second method showed that TMO hydrate I was unaffected by the pressure treatment, and this was confirmed by the comparison of the pellet and mull spectra of the first method. It should be emphasised that the most definitive criterion is the comparison of the pellet and mull spectra in method 1. This is because, for TMO hydrate II, method 2 indicated that no change in TMO hydrate II occurred under pressure, while method 1 showed that the pellet spectroscopic sample contained more hydrate I than hydrate II (Chapter 4).

Once it had been established that TMO hydrate I was unaffected by the pressure treatment, it was necessary to determine the factors which controlled the quality of the mid-infrared spectra of pellets. The temperature at which the pellet was made was determined by the facts that TMO hydrate I decomposes above  $-20.8^{\circ}\text{C}$  while potassium bromide and cesium iodide flow more effectively to form pellets



as the temperature is raised. A temperature of  $-40^{\circ}\text{C}$  was chosen. The thickness of the pellet was determined by numerous trials. It was found that pellets over 0.5 mm thick transmitted mid-infrared radiation very poorly, whereas pellets less than 0.3 mm thick transmitted very well but produced interference fringes in the spectra at the  $2.5\text{ cm}^{-1}$  resolution that was desired. This was most troublesome at frequencies below  $1000\text{ cm}^{-1}$ , and often disappeared at higher frequencies. However it was found that 0.35 mm thick pellets transmitted an acceptable level of mid-infrared radiation without causing interference fringes in the spectra, so this thickness was adopted. The pressurisation treatment is given in Section 2.5, and requires a pressure of 2500 bars. It was found that the use of less than 2500 bars reduced the light transmission of the pellet, however the specific combinations of pressure and time given in Section 2.5 are probably not critical.

One point which was critical was the amount of hydrate used in the pellet. It was found that using a very small amount of hydrate and employing the variable scale expansion option of the spectrophotometer gave much better spectra than were obtained with a larger amount of hydrate, since the latter resulted in unacceptably low background transmission in the spectra.

Ideally the refractive index of the hydrate and the pelleting agent should be equal, since in that case light

passing from one to the other would not be scattered. The effect of a difference in refractive index was observed by comparing the spectra of TMO hydrate I in potassium bromide and cesium iodide pellets. The average infrared refractive index of TMO hydrate I was calculated to be about 1.48 from the refractivities of ice and liquid triethylene oxide. The infrared refractive indices of potassium bromide and cesium iodide are close to their sodium-D line refractive indices, 1.56 and 1.79, respectively (85), and above  $500\text{ cm}^{-1}$  they are essentially constant since these compounds do not absorb in this region. The refractive index of the hydrate changes on passing through an absorption band (86), such that the value to high frequency of the band is less than the average value, and hence the difference between it and that of the pelleting agent is greater than the average value of the difference. The reverse is true on the low frequency side of absorption bands. Thus one expects more light scattering on the high frequency side of TMO hydrate I absorption bands than on the low frequency side for both potassium bromide and cesium iodide pellets, with the effect being more pronounced for cesium iodide pellets. This effect was clearly observed in the spectra. The distortion of the bands for cesium iodide pellets was quite severe, whereas the distortion for potassium bromide pellets was only noticeable for the stronger bands, for which the change in refractive index is larger than for the weaker bands. It was, therefore, decided to

use potassium bromide as the pelleting agent:

Another factor which was critical for obtaining the correct spectrum of TMO hydrate I from pellet samples was the dryness of the potassium bromide as the following facts and arguments show. Initially pellets were made with potassium bromide which had been pumped on a vacuum line overnight at room temperature and a pressure of about  $10^{-4}$  Torr. Part of the spectrum of such a pellet, containing no hydrate, which was made by the same technique used for making pellets containing hydrate, is shown in the lower box of Fig. 3.12 as curve A. It can be seen that the absorption due to the water molecules, centered at about  $3450 \text{ cm}^{-1}$ , is extremely weak. The same region of the spectrum of a pellet containing TMO deuterate I, made with potassium bromide which had been dried in the same way, is shown in Fig. 3.12, lower box, curve C. It is seen that there is a very strong absorption centered at about  $3300 \text{ cm}^{-1}$  which is not due to pure TMO deuterate I (Section 3.2). A broad absorption at this frequency is most probably due to the O-H stretching vibrations of hydrogen bonded water molecules. There are two possible sources of these hydrogen containing water molecules: extrinsic ice, and traces of residual water in the potassium bromide. The peak frequency of about  $3300 \text{ cm}^{-1}$ , compared to about  $3220 \text{ cm}^{-1}$  for that of ice Ih (27), eliminates extrinsic ice as the possible source and indeed, this is confirmed by curve A

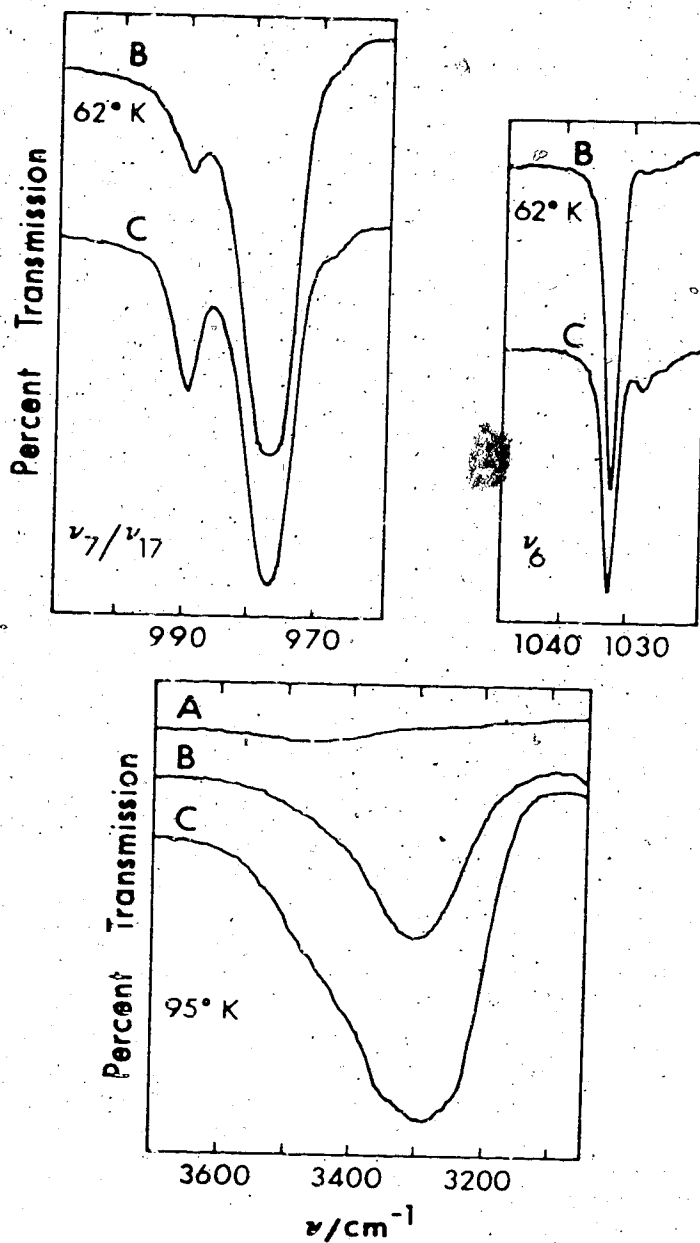


Fig. 3.12. Mid-infrared spectra of pellets containing no sample (curve A) and structure I trimethylene oxide deuterate (curves B and C). The potassium bromide used for the pellet of curve B was dried much more than that used for curves A and C. The maximum and minimum percent transmissions are: upper left box, B, 86, 17; C, 85, 25; upper right box, B, 81, 58; C, 92, 71; lower box, A, 55, 52; B, 57, 29; C, 69, 14.

of Fig. 3.12 which shows that extrinsic ice was not introduced in significant amounts into the pellet samples by the technique used. Thus it was concluded that the residual water in the potassium bromide must have been the source of the  $3300\text{ cm}^{-1}$  absorption by the pellet containing the deuterate, even though the pure potassium bromide pellet showed extremely weak water absorption.

The shift in the peak frequency and the enormous enhancement in intensity can be rationalised in the following way. It is shown in Fig. 3.8 that the band due to the isolated O-H stretching vibration,  $\nu_{\text{OH}}(\text{HDO})$ , in TMO deuterate I occurs at about  $3300\text{ cm}^{-1}$ . This suggests that the  $\text{H}_2\text{O}$  molecules in the potassium bromide exchanged with the  $\text{D}_2\text{O}$  molecules of the deuterate to produce HDO molecules in the host lattice of the deuterate, presumably during the pellet preparation at  $-40^\circ\text{C}$ . It is well known (87) that the O-H stretching vibrations of strongly hydrogen-bonded O-H groups absorb orders of magnitude more strongly than non-hydrogen-bonded O-H groups, and this undoubtedly explains the enormous intensity enhancement.

In addition to this isotopic exchange process, water in the potassium bromide can react with TMO deuterate I to form some TMO deuterate II. Evidence that this did, in fact, occur is shown by the absorption by  $\nu_6$  of trimethylene oxide (Fig. 3.12, curve C, upper box), which was taken from the same spectrum as curve C of the lower box.

The strong band at  $1033.5 \text{ cm}^{-1}$  is due to  $\nu_6$  of trimethylene oxide in TMO deuterate I (Section 3.2), while the weak band at  $1028.4 \text{ cm}^{-1}$  corresponds to the absorption by  $\nu_6$  in TMO deuterate II (Chapter 4, Fig. 4.6).

The proof that the residual water in the potassium bromide was the source of these effects, and the extent to which they were removed from the spectra to be presented is also shown in Fig. 3.12. Curves B were taken from a spectrum of a pellet, containing TMO deuterate I, which was made from potassium bromide which had been pumped on a vacuum line at a temperature of  $175^\circ\text{C}$  and a pressure of about  $10^{-5}$  Torr for two days. It can be seen that the intensity of the  $\nu_{\text{OH}}$  (HDO) band has been reduced considerably, and that the TMO deuterate II band at  $1028.4 \text{ cm}^{-1}$  has been essentially eliminated. Also shown in Fig. 3.12 is the absorption by  $\nu_7$  and  $\nu_{17}$ . Curves B and C were taken from the same spectra as the corresponding curves in the other boxes. TMO deuterate II absorbs strongly in this region at about  $990 \text{ cm}^{-1}$  (Chapter 4, Fig. 4.6) and the presence of some TMO deuterate II in the sample responsible for curve C is shown by the greater intensity of this band relative to that of the band at  $976.9 \text{ cm}^{-1}$  in curve C than in curve B. The residual intensity at about  $990 \text{ cm}^{-1}$  in curve B is, by comparison with the result for the  $\nu_6$  band, believed to be due to TMO deuterate I, which is known to absorb at this frequency (Section 3.2).

All of the spectra reported in this chapter were recorded on pellets which were made from potassium bromide which was at least as dry as that used for curves B in Fig. 3.12. Thus, slight residual contamination due to the water in the potassium bromide was present in the samples, but no influence of this contamination is observable in the spectra to be presented.

The fragility of the pellet samples prevented their temperatures from being measured by the insertion of a sensing device into the pellet, and so the temperature of the cryo-tip, into which was screwed the sample holder containing the pellet, was measured using the platinum resistance thermometer at sensor temperatures above 20°K. It was therefore necessary to obtain a correlation between the temperature of the pellet and that of the cryo-tip. This was achieved, in conjunction with Frances Bates and Allan Clement, by attempting to deposit various gases onto a transparent potassium bromide pellet. The success of the deposition attempt was determined by a visual inspection of the pellet. The temperature below which a particular gas will deposit was calculated from a knowledge of the pressure inside the cell and the vapour pressure of the compound. The gases used, and the references for their vapour pressures, are methane (88), krypton (88), xenon (88) and carbon dioxide (88). Temperature correlations were obtained with the cell evacuated to a pressure

of less than  $10^{-4}$  Torr, with a pressure of about  $10^{-1}$  Torr of air in the cell as a heat exchange gas and with a pressure of about  $10^{-1}$  Torr of helium gas in the cell as a heat exchange gas. It was found that with the cell evacuated to less than  $10^{-4}$  Torr, the temperature of the pellet did not drop below  $95 \pm 10^\circ\text{K}$ , even when the temperature of the cryo-tip was  $4^\circ\text{K}$ , as indicated by the fact that carbon dioxide would condense whereas xenon would not. It was also found that air was a more effective heat exchange gas than helium gas. With a pressure of  $10^{-1}$  Torr of air and a sensor temperature of  $50^\circ\text{K}$ , the temperature of the pellet was  $62 \pm 4^\circ\text{K}$ , whereas with  $10^{-1}$  Torr of helium gas in the cell, a cryo-tip temperature of about  $20^\circ\text{K}$  was required before the sample temperature reached  $62 \pm 4^\circ\text{K}$ , as determined by the fact that krypton condensed but methane did not. At sensor temperatures below  $45^\circ\text{K}$ , the air exchange gas was condensed on the cryo-tip, and consequently the sample temperature rose to  $95 \pm 10^\circ\text{K}$ .

The temperature effects observed in the infrared spectra were completely compatible with these correlations. The spectra obtained with about  $10^{-1}$  Torr of air inside the cell exhibited a reversal in the frequency and half-width trends of both the water and the guest bands after the temperature of the sensor dropped below  $45^\circ\text{K}$ . The resulting frequencies and half-widths were about the same as those obtained at a sensor temperature of  $100^\circ\text{K}$ . The spectra



obtained with a pressure of less than  $10^{-4}$  Torr in the cell exhibited the same frequencies and half-widths for all sensor temperatures below  $100^{\circ}\text{K}$ . Confirmation that these effects were due solely to a change in temperature and not due to a physical transformation taking place within the hydrate was obtained when, with a pressure of  $10^{-1}$  Torr of air in the cell, a similar reversal in the frequency and half-width trends was observed at sensor temperatures below  $45^{\circ}\text{K}$  for a potassium bromide pellet containing naphthalene.

All of the pellet spectra presented in this chapter were recorded using a cell containing about  $10^{-1}$  Torr of air. At sensor temperatures below  $45^{\circ}\text{K}$ , the sample temperature was taken to be  $95 \pm 10^{\circ}\text{K}$ , and at sensor temperatures of 50, 75, 85, 125, and  $175^{\circ}\text{K}$ , the sample temperature was taken to be  $62 \pm 4$ ,  $80 \pm 5$ ,  $90 \pm 5$ ,  $125 \pm 10$  and  $175 \pm 10^{\circ}\text{K}$ .

The infrared spectrum from 300 to  $4000\text{ cm}^{-1}$  of TMO hydrate I in a potassium bromide pellet at  $95 \pm 10^{\circ}\text{K}$  is shown in Fig. 3.13, and that for TMO deuterate I in a potassium bromide pellet at  $95 \pm 10^{\circ}\text{K}$  is shown in Fig. 3.14. The spectrum labelled A in Fig. 3.13 is of a sample of TMO hydrate I containing 10 mole percent of HDO, while the sample of curve B was made from normal water. The regions of curve A which are not included in curve B are identical in the normal and the isotopically substituted samples. Both the spectra labelled A and B in Fig. 3.14 were recorded

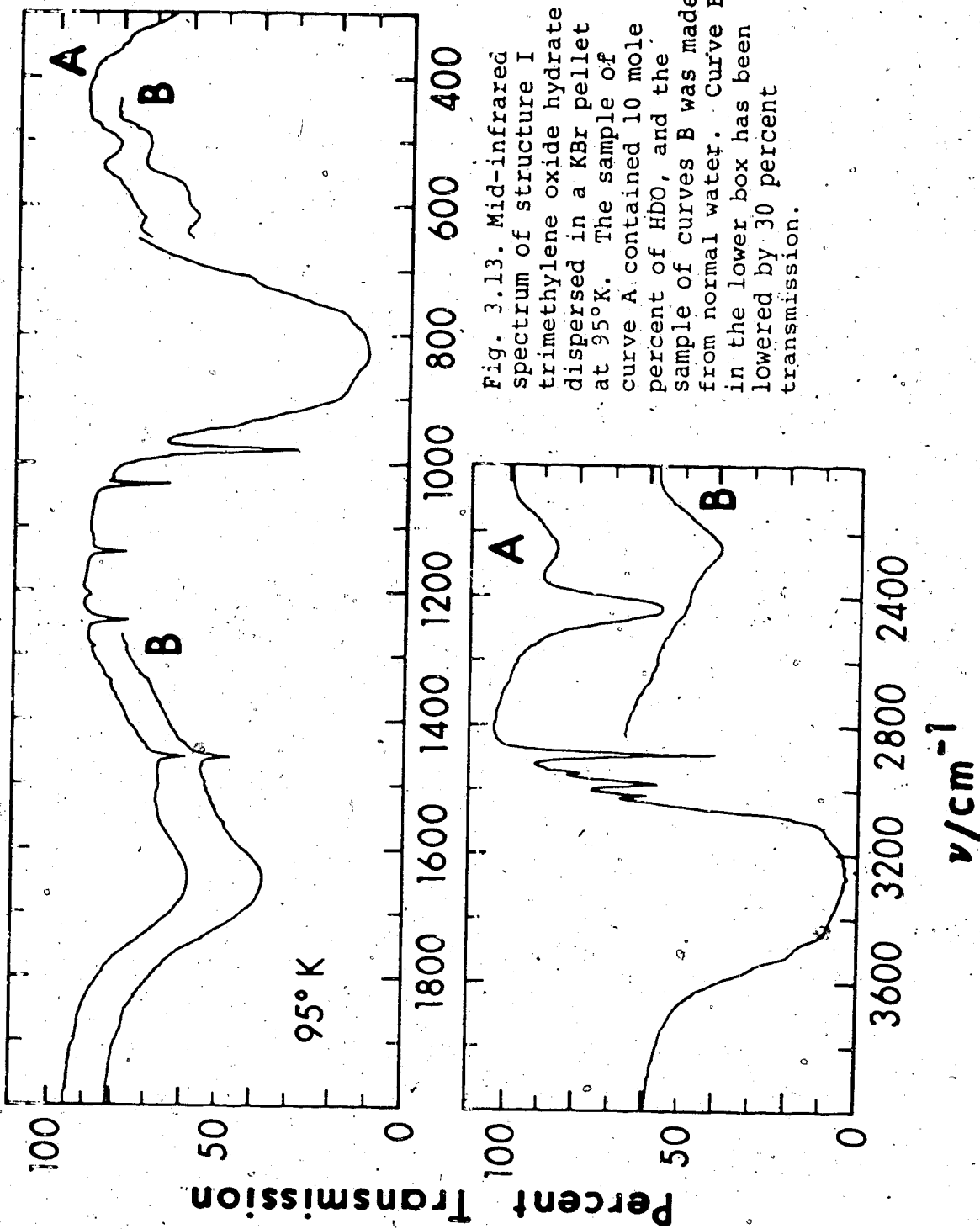


Fig. 3.13. Mid-infrared spectrum of structure I trimethylene oxide hydrate dispersed in a KBr pellet at 95°K. The sample of curve A contained 10 mole percent of H<sub>2</sub>O, and the sample of curves B was made from normal water. Curve B in the lower box has been lowered by 30 percent transmission.

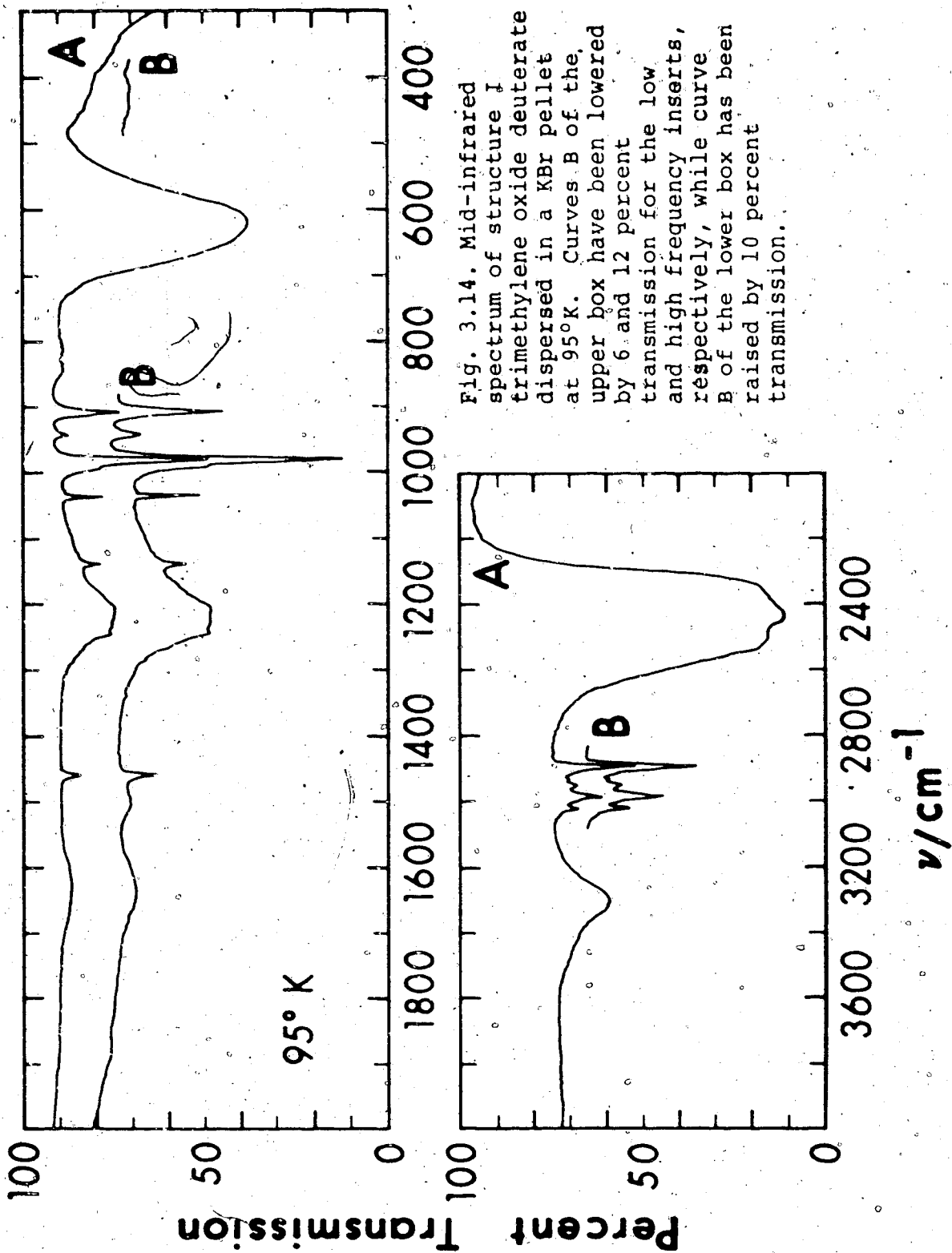


Fig. 3.14. Mid-infrared spectrum of structure I trimethylene oxide deuterate dispersed in a KBr pellet at 95°K. Curves B of the upper box have been lowered by 6 and 12 percent transmission for the low and high frequency inserts, respectively, while curve B of the lower box has been raised by 10 percent transmission.

for samples of TMO deuterate I made from 99.7%  $D_2O$ . However, as discussed earlier in this chapter, the incorporation of a small amount of HDO from the water in the potassium bromide was unavoidable, even for the most stringently dried pellet samples, and so these samples contained about 7 (curve A) and 12 (curve B) mole percent of HDO (Section 3.3.2).

The spectra shown in Figs. 3.13 and 3.14 were recorded at a resolution of better than  $5\text{ cm}^{-1}$  between 300 and  $650\text{ cm}^{-1}$ , and better than  $2.5\text{ cm}^{-1}$  between 650 and  $4000\text{ cm}^{-1}$ . The frequencies of the observed features at  $95 \pm 10^\circ\text{K}$  are listed in Table 3.2, with their estimated accuracy and the assignment. The temperature dependence between 175 and  $62^\circ\text{K}$  of the frequencies, half-widths and peak heights of the bands due to  $\nu_{OD}(D_2O)$ ,  $\nu_R(D_2O)$ ,  $\nu_{OH}(HDO)$ ,  $\nu_{OD}(HDO)$ , guest modes in TMO hydrate I, and guest modes in TMO deuterate I are listed in Tables 3.3 to 3.6 and are shown in Figs. 3.15 to 3.20 respectively.

The bands due to  $\nu_R(H_2O)$  and  $\nu_{OH}(H_2O)$  are not particularly well defined in Fig. 3.13, and were not observed well in pellets, for reasons given in the next section. Nevertheless, the spectra of TMO hydrate I and TMO deuterate I in mulls (Figs. 3.4 and 3.5, Table 3.1) and pellets (Figs. 3.13 and 3.14, Table 3.2) are sufficiently similar to leave no doubt that the sample did not change while being pressed into pellets. Special features of the pellet

Table 3.2

Frequencies of the Observed Features  
in the Mid-Infrared Spectra of  
Structure I Trimethylene Oxide Hydrate and  
Deuterate in Potassium Bromide Pellets at 95°K<sup>a</sup>

TMO Hydrate I $\nu/\text{cm}^{-1}$	Assignment	TMO Deuterate I $\nu/\text{cm}^{-1}$
~3438 sh	} $\nu_{\text{OH}}(\text{H}_2\text{O})$	
3263 ±20 vs, br		
~3122 sh		
	$\nu_{\text{OH}}(\text{HDO})$	3298 ±5 ms
3018 ±2 m	$\nu_{19}(\text{TMO})$	3017.1 ±1 m
2982 ±2 ms	$\nu_1(\text{TMO})$	2983.1 ±1 m
	2 x $\nu_{14}(\text{TMO})?$	2973 ±2 sh
2946 ±2 w	$\nu_{20}(\text{TMO})$	2948 ±2 w
2931 ±3 sh	$\nu_9(\text{TMO})$	2930 ±2 vw
2888 ±2 s	$\nu_{13}(\text{TMO})$	2889.0 ±1 s
	} $\nu_{\text{OD}}(\text{D}_2\text{O})$	~2494 sh
		2437 ±15 vs, br
		~2367 sh
		~2309 sh

TMO Hydrate I $\nu/\text{cm}^{-1}$	Assignment	TMO Deuterate I $\nu/\text{cm}^{-1}$
~2550 sh	$\nu_{\text{OD}}(\text{HDO})$	
~2432 sh	$\left\{ \begin{array}{l} 3\nu_{\text{R}}(\text{H}_2\text{O}), \\ \nu_2(\text{H}_2\text{O}) + \nu_{\text{R}}(\text{H}_2\text{O}) \end{array} \right. ?$	
2443 $\pm 5$ s, br		
~2425 sh	$\nu_{\text{OD}}(\text{HDO})$	
~2400 sh		
2248 $\pm 10$ m	$\left\{ \begin{array}{l} 3\nu_{\text{R}}(\text{H}_2\text{O}), \\ \nu_2(\text{H}_2\text{O}) + \nu_{\text{R}}(\text{H}_2\text{O}) \end{array} \right.$	
1645 $\pm 10$ s, br		$\nu_2(\text{H}_2\text{O})$
	$\left\{ \begin{array}{l} 3\nu_{\text{R}}(\text{D}_2\text{O}), \\ \nu_2(\text{D}_2\text{O}) + \nu_{\text{R}}(\text{D}_2\text{O}) \end{array} \right.$	1634 $\pm 10$ w
1500 $\pm 20$ vw		$\nu_2(\text{HDO})$
1456.4 $\pm 0.5$ m	$\nu_4/\nu_{14}(\text{TMO})$	1457.3 $\pm 0.5$ m
1339 $\pm 2$ vw	$\nu_5(\text{TMO})$	1340 $\pm 2$ vw
1283 $\pm 2$ vw	$\nu_{10}(\text{TMO})$	1283 $\pm 2$ vw
1244.0 $\pm 0.5$ m	$\nu_{16}(\text{TMO})$	1243.5 $\pm 1$ w
	$\nu_2(\text{D}_2\text{O})$	1225 $\pm 15$ ms
1203.1 $\pm 1$ w	$\nu_{11}(\text{TMO})$	1204 $\pm 4$ vw
1137.6 $\pm 0.5$ m	$\nu_{21}(\text{TMO})$	1136.9 $\pm 0.5$ m
1033.8 $\pm 0.5$ m	$\nu_6(\text{TMO})$	1033.5 $\pm 0.5$ m
990.3 $\pm 1$ sh	$\nu_7/\nu_{17}(\text{TMO})$	989.4 $\pm 1$ sh
979.5 $\pm 0.5$ s		978.1 $\pm 0.5$ vs
		968 $\pm 2$ sh

TMO Hydrate I $\nu/\text{cm}^{-1}$		Assignment	TMO Deuterate I $\nu/\text{cm}^{-1}$	
940 $\pm$ 5	sh	$\nu_{18}$ (TMO)	940.3 $\pm$ 1	m
901 $\pm$ 5	sh	$\nu_8$ (TMO)	905.2 $\pm$ 0.5	s
		$\nu_{22}$ (TMO)	844.0 $\pm$ 1	w
829 $\pm$ 5	vs, br	$\nu_R$ (H <sub>2</sub> O)		
716 $\pm$ 5	sh	$\nu_{23}$ (TMO)		
		$\nu_R$ (D <sub>2</sub> O)	~670	sh
			615 $\pm$ 5	vs, br
			445 $\pm$ 10	vw
			413 $\pm$ 10	vw
616 $\pm$ 5	vw	$\nu_R$ (H <sub>2</sub> O)		
577 $\pm$ 20	vw			
498 $\pm$ 15	w			

a) vs = very strong, s = strong, ms = medium-strong,  
 m = medium, w = weak, vw = very weak, br = broad,  
 sh = shoulder.

Table 3.3

Temperature Dependence of the  $\nu_{OD}$  ( $D_2O$ )  
and  $\nu_R$  ( $D_2O$ ) Bands in the Mid-Infrared  
Spectrum of Structure I Trimethylene Oxide  
Deuterate in Potassium Bromide Pellets<sup>a</sup>

T, °K	$\nu_R$ ( $D_2O$ )	$\Delta\nu_{1/2}$ <sup>b</sup>	Peak Height	$\nu_{OD}$ ( $D_2O$ )	$\Delta\nu_{1/2}$ <sup>b</sup>	Peak Height
125	613	115	0.310	2449	266	0.803
125	614	108	0.367	2440	260	0.870
95	615	105	0.386	2437	259	0.886
80	616	100	0.410	2434	258	0.918
62	617	99	0.427	2428	256	0.939

- a) The units are: °K for temperature,  $cm^{-1}$  for  $\nu$  and  $\Delta\nu_{1/2}$ , absorbance  $\left(\log_{10} \frac{I_0}{I}\right)$  for peak height.
- b)  $\Delta\nu_{1/2}$  is the full width of the peak at half height.



Table 3.4

Temperature Dependence of the  $\nu_{OH}$  (HDO) and  $\nu_{OD}$  (HDO) Bands in the Mid-Infrared Spectra of Structure I Trimethylene Oxide Dodecylate and Hydrate in Potassium Bromide Pellets<sup>a</sup>

Temp.	$\nu_{OH}$ (HDO)	$\Delta\nu_{1/2}$ <sup>b</sup>	Peak Height	$\nu_{OD}$ (HDO)	$\Delta\nu_{1/2}$ <sup>b</sup>	Peak Height
175	3311	163	0.207	2448	92	0.138
125	3302	159	0.230	2444	87	0.158
95	3298	150	0.241	2443	87	0.171
80	3298	150	0.254	2443	86	0.171
62	3309 3280	150	0.261	2442	85	0.179

a) The units are: °K for temperature,  $\text{cm}^{-1}$  for  $\nu$  and  $\Delta\nu_{1/2}$ , absorbance  $\left(\log_{10} \frac{I_0}{I}\right)$  for peak height.

b)  $\Delta\nu_{1/2}$  is the full width of the peak at half height.

Table 3.5

Temperature Dependence of Guest  
Features in the Mid-Infrared Spectrum  
of Structure I Trimethylene Oxide  
Hydrate<sup>a</sup> in Potassium Bromide Pellets

Temp.	$\nu_{7/\nu_{17}}$	$\Delta\nu_{\frac{1}{2}}^b$	Peak Height	$\nu_6$	$\Delta\nu_{\frac{1}{2}}^b$	Peak Height
175	981.0	10.1	0.236	1034.6	3.7	0.051
125	980.2	8.4	0.284	1034.2	3.3	0.079
95	979.5	7.6	0.339	1033.8	2.7	0.102
80	979.0	7.4	0.366	1033.6	2.7	0.109
62	978.5	7.3	0.374	1033.4	2.6	0.119

Temp.	$\nu_{21}$	$\Delta\nu_{\frac{1}{2}}^b$	Peak Height	$\nu_{16}$	$\Delta\nu_{\frac{1}{2}}^b$	Peak Height
175	1137.8	4.3	0.022	1241.1	9.5	0.020
125	1137.6	3.4	0.038	1243.1	6.8	0.036
95	1137.6	3.3	0.050	1244.0	5.7	0.057
80	1137.6	3.2	0.055	1244.3	4.9	0.065
62	1137.6	3.2	0.061	1244.8	4.4	0.081

Temp.	$\nu_4/\nu_{14}$	$\Delta\nu_{1/2}^b$	Peak Height
175	1456.2	6.2	0.025
125	1456.3	5.8	0.028
95	1456.4	4.9	0.040
80	1456.4	4.8	0.040
62	1456.5	4.6	0.047

a) The units are: °K for temperature,  $\text{cm}^{-1}$  for  $\nu$  and  $\Delta\nu_{1/2}$ ,  
absorbance  $\left(\log_{10} \frac{I_0}{I}\right)$  for peak height.

b)  $\Delta\nu_{1/2}$  is the full width of the peak at half height.

Table 3.6

Temperature Dependence of Guest Features in the  
Mid-Infrared Spectrum of Structure I Trimethylene  
Oxide Deuterate in Potassium Bromide Pellets<sup>a</sup>

Temp.	$\nu_8$	$\Delta\nu_{\frac{1}{2}}^b$	Peak Height	$\nu_{18}$	$\Delta\nu_{\frac{1}{2}}^b$	Peak Height
175	906.3	9.7	0.104	937.7	13	0.013
125	905.6	7.2	0.163	939.9	9.9	0.029
95	905.2	6.4	0.203	940.3	7.6	0.044
80	904.7	5.6	0.248	940.6	5.9	0.064
62	904.4	5.2	0.285	940.7	5.3	0.084

Temp.	$\nu_7/\nu_{17}$	$\Delta\nu_{\frac{1}{2}}^b$	Peak Height	$\nu_6$	$\Delta\nu_{\frac{1}{2}}^b$	Peak Height
175	979.8	11.8	0.419	1034.2	3.8	0.064
125	978.7	8.8	0.519	1033.8	3.2	0.093
95	978.1	7.9	0.622	1033.5	2.9	0.114
80	977.1	7.6	0.673	1033.2	2.6	0.135
62	976.9	7.6	0.695	1033.0	2.4	0.146

Temp.	$\nu_{21}$	$\Delta\nu_{\frac{1}{2}}^b$	Peak Height	$\nu_4/\nu_{14}$	$\Delta\nu_{\frac{1}{2}}^b$	Peak Height
175	1137.5	5.0	0.023	1456.8	5.9	0.030
125	1137.1	4.0	0.035	1457.1	5.0	0.043
95	1136.9	3.4	0.050	1457.3	4.7	0.053
80	1137.0	3.2	0.059	1457.4	4.5	0.064
62	1137.0	3.0	0.069	1457.6	4.4	0.072

Temp.	$\nu_{13}$	$\Delta\nu_{\frac{1}{2}}^b$	Peak Height	$\nu_{20}$	$\Delta\nu_{\frac{1}{2}}^b$	Peak Height
175	2891.8	16.0	0.101	2951	—	0.003
125	2890.0	15.0	0.134	2949	8.4	0.008
95	2889.0	14.2	0.151	2948	8.2	0.012
80	2887.4	12.8	0.197	2946	8.0	0.021
62	2886.2	12.8	0.216	2944	7.8	0.032

Temp.	$\nu_1$	$\Delta\nu_{\frac{1}{2}}^b$	Peak Height	$\nu_{19}$	$\Delta\nu_{\frac{1}{2}}^b$	Peak Height
175	2982.5	12.0	0.043	3018.3	13.0	0.013
125	2982.9	11.8	0.057	3017.9	9.4	0.020
95	2983.1	11.4	0.067	3017.1	9.0	0.023
80	2983.7	10.8	0.083	3016.9	7.0	0.032
62	2984.1	10.8	0.097	3016.3	7.0	0.037

Temp.	$\nu_{16}$	$\Delta\nu_{\frac{1}{2}}^b$	Peak Height	$\nu_{22}$	$\Delta\nu_{\frac{1}{2}}^b$	Peak Height
95	1243.5	—	—	844.0	—	—
90	1244.5	—	—	844.1	—	—
62	1245.1	4.4	—	844.9	10.7	—

a) The units are: °K for temperature,  $\text{cm}^{-1}$  for  $\nu$  and  $\Delta\nu_{\frac{1}{2}}$ , absorbance  $\left(\log_{10} \frac{I_0}{I}\right)$  for peak height.

b)  $\Delta\nu_{\frac{1}{2}}$  is the full width of the peak at half height.

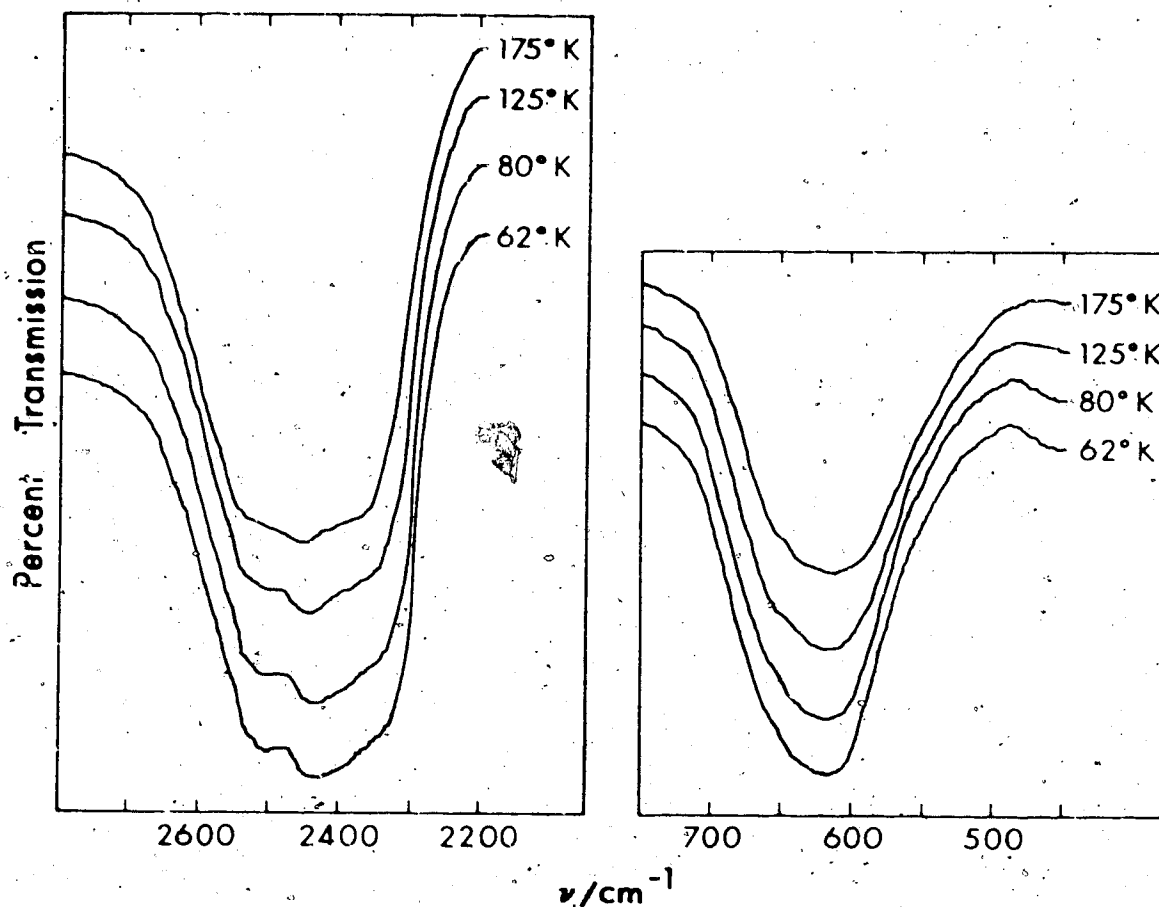


Fig. 3.15. The  $\nu_{OD}(D_2O)$  (left box) and  $\nu_R(D_2O)$  (right box) bands of structure I trimethylene oxide deuterate dispersed in a KBr pellet at 62, 80, 125 and 175°K. The maximum and minimum percent transmission of the 62°K band and the raised (in parenthesis) offset (in parenthesis) of the 80, 125 and 175°K bands are respectively: left box, 95, 10 (11, 24, 34); right box, 88, 33 (8, 16, 22).

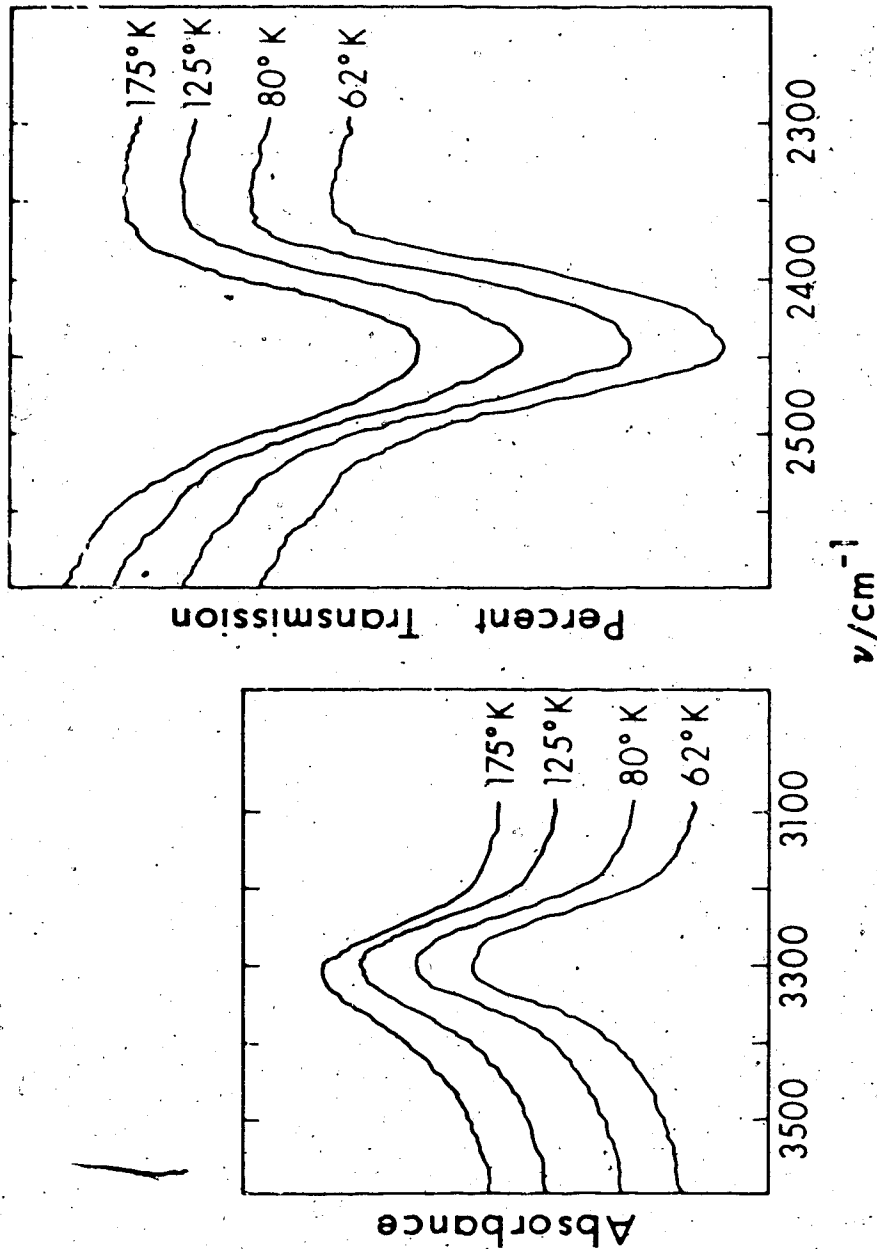


Fig. 3.16. The  $\nu_{OH}$  (HDO) (left box) and  $\nu_{OD}$  (D<sub>2</sub>O) (right box) bands of structure I tri-methylene oxide deuterate and hydrate, respectively, dispersed in a KBr pellet at 62, 80, 125 and 175°K. The maximum and minimum absorbance (left box) and percent transmission (right box) of the 62°K band and the raised offsets (in parenthesis) of the 80, 125 and 175°K bands are respectively: left box, 0.81, 0.54 (0.07, 0.17, 0.23); right box, 90, 59 (5, 10, 15).



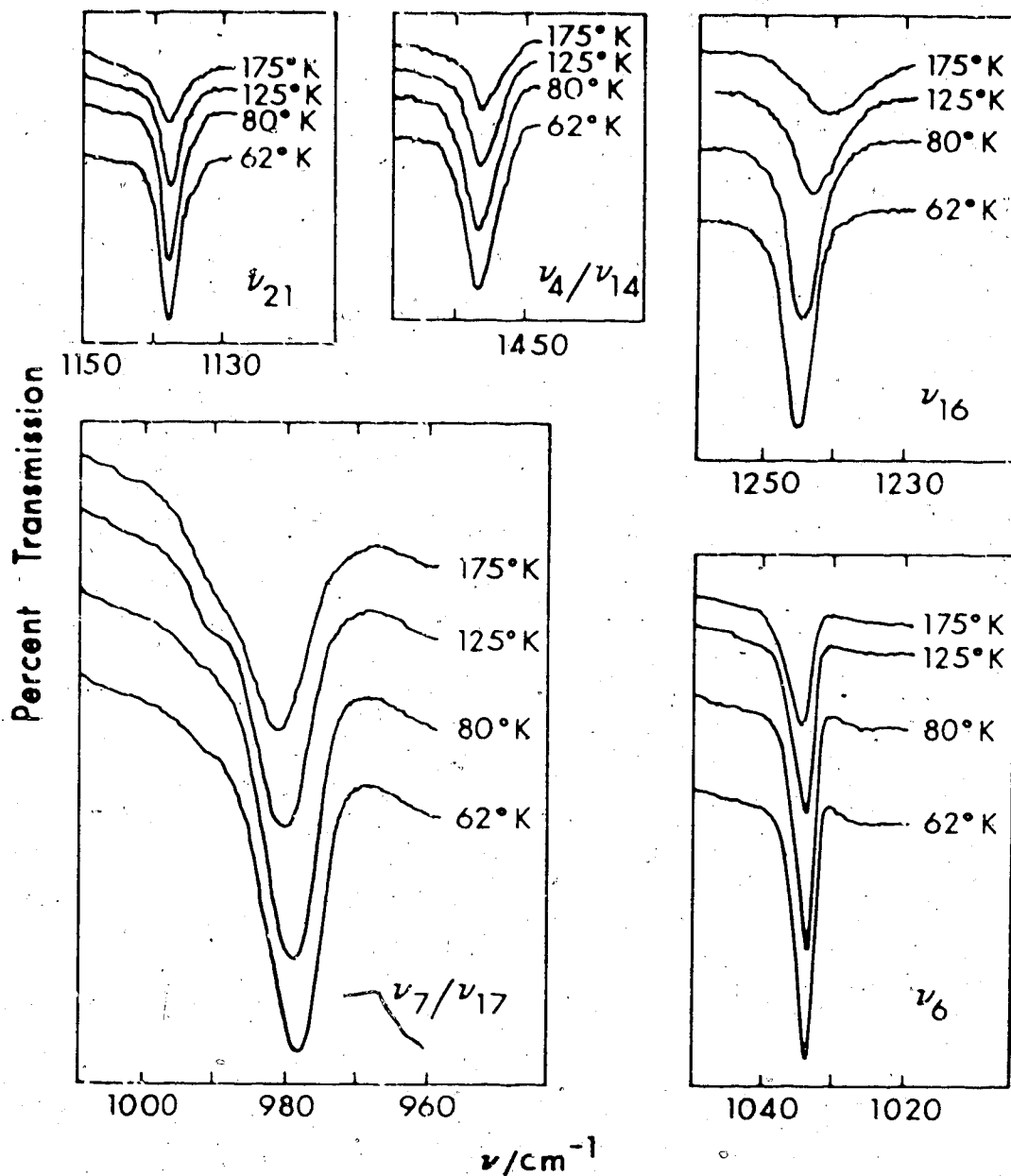


Fig. 3.17. The guest bands of structure I trimethylene oxide hydrate dispersed in a KBr pellet at 62, 80, 125 and 175°K. The maximum and minimum percent transmission of the 62°K bands and the raised offsets (in parenthesis) of the 80, 125 and 175°K bands are respectively:  $\nu_{21}$ , 82, 71 (3, 5, 7);  $\nu_4/\nu_{14}$ , 69, 56 (3, 4, 5);  $\nu_{16}$ , 83, 68 (5, 9, 13);  $\nu_7/\nu_{17}$ , 78, 28 (11, 23, 31);  $\nu_6$ , 82, 62 (7, 12, 15).

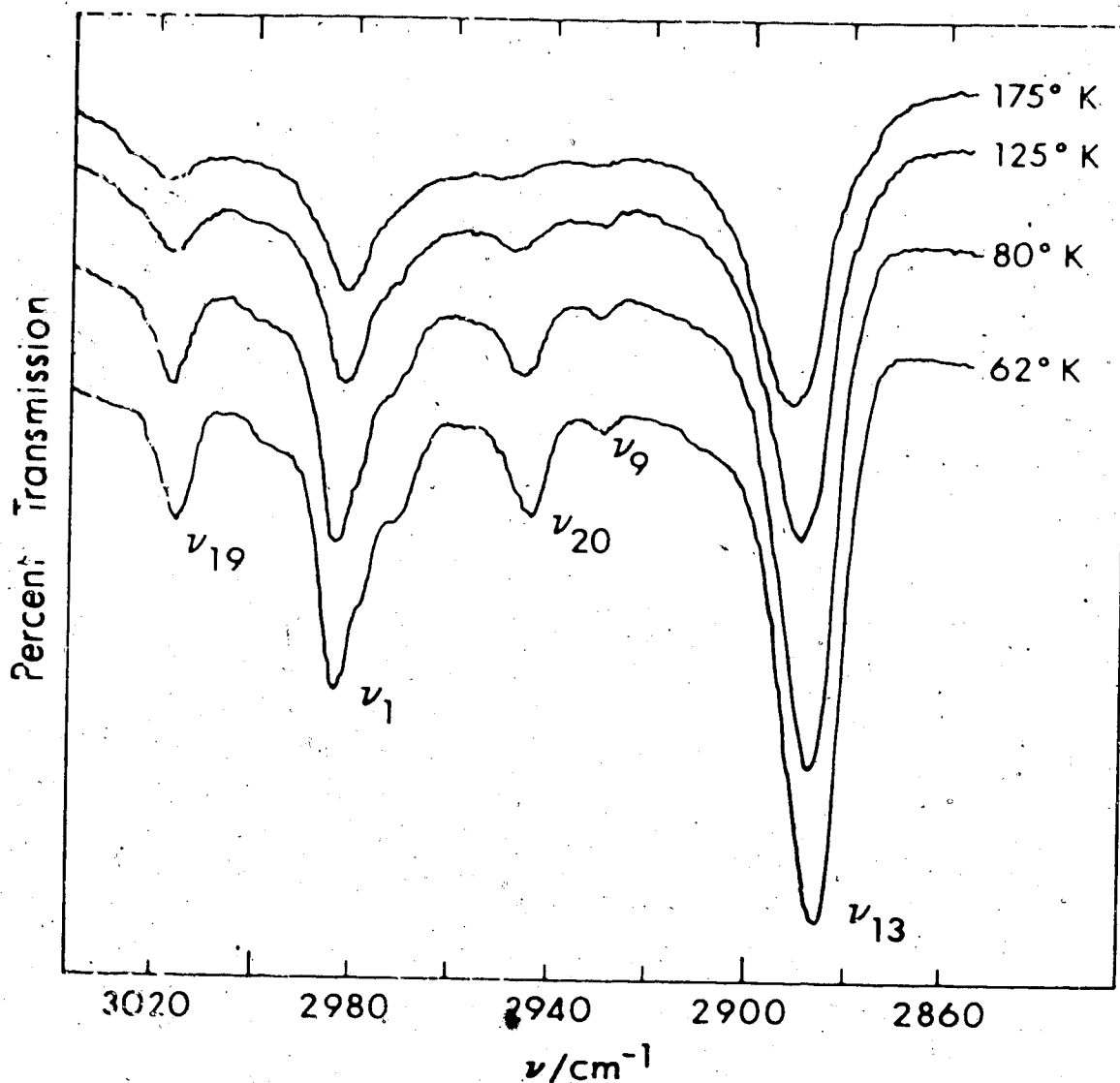


Fig. 3.18. The C-H stretching bands of structure I trimethylene oxide deuterate dispersed in a KBr pellet at 62, 80, 125 and 175°K. The maximum and minimum percent transmission at 62°K is 73 and 44, and the raised offsets at 80, 125 and 175°K are 16, 12 and 15 percent transmission respectively.

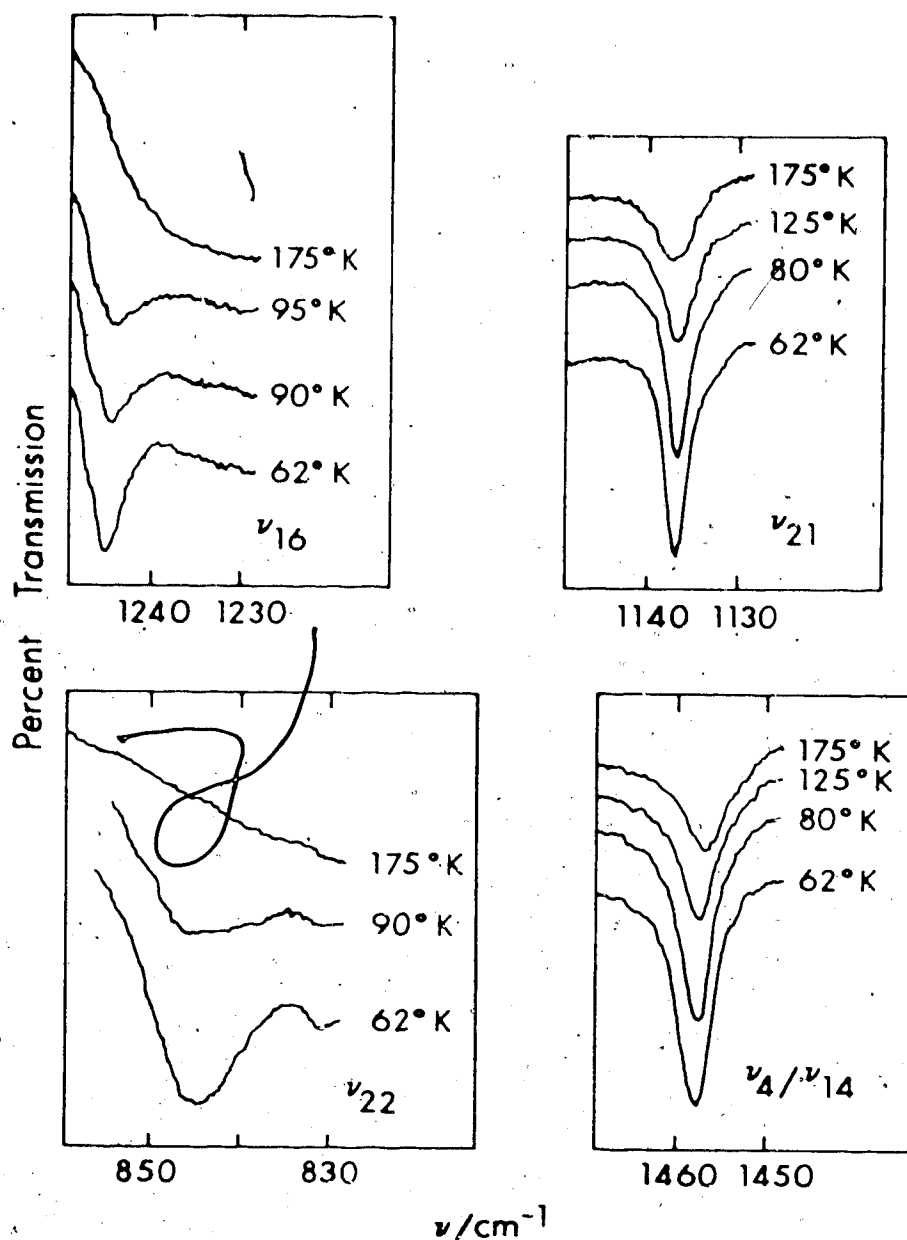


Fig. 3.19. The non-ring bands of structure I trimethylene oxide deuterate dispersed in a KBr pellet at temperatures between 62 and 175°K. The maximum and minimum percent transmission of the 62°K bands and the raised offsets (in parenthesis), in order of increasing temperature, for the bands at higher temperature are:  $\nu_{16}$ , 67, 59 (4, 9, 14);  $\nu_{21}$ , 73, 62 (3, 5, 6);  $\nu_{22}$ , 81, 71 (3, 7);  $\nu_4/\nu_{14}$ , 86, 72 (4, 7, 9).

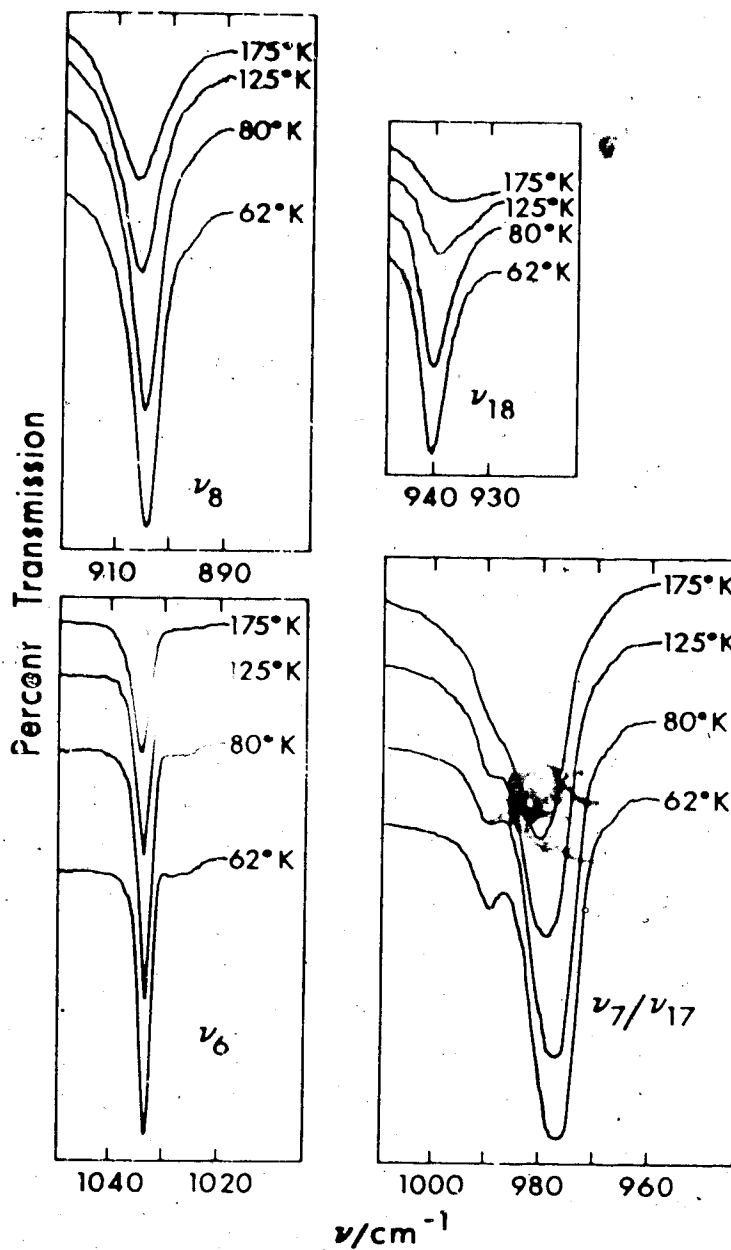


Fig. 3.20. The ring bands of structure I trimethylene oxide deuterate dispersed in a KBr pellet at 62, 80, 125 and 175°K. The maximum and minimum percent transmission of the 62°K bands and the raised offsets (in parenthesis) of the 80, 125 and 175°K bands are respectively:  $\nu_8$ , 87, 45 (12, 20, 24);  $\nu_{18}$ , 88, 73 (4, 8, 11);  $\nu_6$ , 82, 58 (10, 17, 22);  $\nu_7/\nu_{17}$ , 86, 17 (16, 33, 47).

spectra are discussed in the remainder of this chapter.

The spurious band at about  $1025\text{ cm}^{-1}$ , discussed in Section 3.1, was less evident in the pellet spectra than in the mull spectra. It has been ignored.

### 3.3.2 Absorption by the Water Molecules

In order to observe the features of the  $\nu_{\text{OH}}(\text{H}_2\text{O})$  band with the correct relative intensities, as shown in Fig. 3.6, and to observe the temperature dependence of the band, a pellet containing an extremely small amount of TMO hydrate I was prepared. The resulting spectrum clearly showed the presence of TMO hydrate II. This amount of TMO hydrate II, which resulted from the residual water in the potassium bromide (Section 3.3.1), was normally insignificant in comparison to the amount of TMO hydrate I present. Unfortunately this was not the case when such a small amount of hydrate was in the pellet. Therefore it was decided not to present a figure showing the temperature dependence of this band, which was, however, qualitatively similar to that of the  $\nu_{\text{OD}}(\text{D}_2\text{O})$  band (Fig. 3.15) in that the features were broad at  $62^\circ\text{K}$  and broadened further with increasing temperature. The frequencies reported in Table 3.2 for  $\nu_{\text{OH}}(\text{H}_2\text{O})$  were obtained from samples which absorbed too strongly to yield the correct relative intensities, but which gave consistent frequencies of the features.

The temperature dependence of the band due to  $\nu_{\text{OD}}(\text{D}_2\text{O})$  is shown in Fig. 3.15. The band changes from being fairly

symmetric with a peak frequency of about  $2449 \text{ cm}^{-1}$  and a half-width of about  $266 \text{ cm}^{-1}$  at  $175^\circ\text{K}$ , to being asymmetric with a well resolved high frequency shoulder, a peak frequency of about  $2428 \text{ cm}^{-1}$  and a half-width of about  $256 \text{ cm}^{-1}$  at  $62^\circ\text{K}$  (Table 3.3). The band at  $95^\circ\text{K}$  (Fig. 3.14) is essentially identical to that seen in the mull (Fig. 3.6) except that its peak frequency is  $9 \text{ cm}^{-1}$  higher (Tables 3.1 and 3.2). This shift is small, relative to the breadth of the peak and similar small, in this sense, shifts to high frequency were noted for many of the bands in the spectra of pellets (Tables 3.1 and 3.2). They are attributed to opposite reflection and scattering effects (Section 3.3.1) in the pellets than in the mulls, since the refractive indices of the mulling agents are between 1.29 and 1.38 (85) and are, thus, lower than that of the hydrate and much lower than that of potassium bromide (85). The frequencies of the high frequency shoulder and the two low frequency shoulders on the  $\nu_{\text{OD}}(\text{D}_2\text{O})$  band at  $95^\circ\text{K}$  (Table 3.2) agree well with those obtained from a mull (Table 3.1)

The broad band due to  $\nu_2(\text{H}_2\text{O})$  is shown in Fig. 3.13. It extends from  $1275$  to  $1950 \text{ cm}^{-1}$  and has a peak frequency of  $1645 \pm 10 \text{ cm}^{-1}$  and a half-width of about  $295 \text{ cm}^{-1}$  at  $95^\circ\text{K}$  (Table 3.2). A broad, weak shoulder is observed at about  $1890 \text{ cm}^{-1}$  (Fig. 3.13) which is also present in TMO deuterate I (Fig. 3.14). It is unlikely to be a guest absorption, because of its breadth, and the fact that it

occurs at the same frequency in both the hydrate and deuterate spectra makes its assignment to a real feature of the  $\nu_2(\text{H}_2\text{O})$  band impossible. The sharp absorption at  $1456.4 \text{ cm}^{-1}$  and the very weak bands at about  $1339$  and  $1283 \text{ cm}^{-1}$  (Fig. 3.13) are due to the guest. The exact contour and peak frequency of the  $\nu_2(\text{H}_2\text{O})$  band were not clearly defined by the mull spectra, and so the pellet spectra have provided additional information. The band due to  $\nu_2(\text{D}_2\text{O})$  in a pellet at  $95^\circ\text{K}$  (Fig. 3.14, Table 3.2) is essentially identical to that observed in the spectra of mulls (Fig. 3.5, Table 3.1). The temperature dependence of these bands was not studied.

The detailed study of the  $\nu_{\text{R}}(\text{H}_2\text{O})$  band (Fig. 3.13) in the pellets encountered the difficulty described above for the  $\nu_{\text{OH}}(\text{H}_2\text{O})$  band. Thus the details near the band maxima (Fig. 3.4) were not well defined in the spectra of the pellets, and the detailed temperature dependence of this band will not be given. However, the features near the peak of the band became less well defined as the temperature was raised to  $175^\circ\text{K}$ , so the top became smoother and more symmetrical. The band maximum is at  $829 \pm 5 \text{ cm}^{-1}$  at  $95^\circ\text{K}$  (Fig. 3.13),  $10 \text{ cm}^{-1}$  higher than in the spectra of mulls because of reflection and scattering effects (see above). The half-width at  $95^\circ\text{K}$  is  $175 \text{ cm}^{-1}$ , in good agreement with the value obtained from the mulls. The broad, weak features at  $616$  and  $577 \text{ cm}^{-1}$ , which were seen in the spectra

of the mulls (Fig. 3.4, Table 3.1), are confirmed in the spectra of the pellets (Fig. 3.13, Table 3.2), but the features at 530 and 502  $\text{cm}^{-1}$  (Fig. 3.4, Table 3.1) are replaced by a single broad band at  $498 \pm 15 \text{ cm}^{-1}$  (Fig. 3.13, Table 3.2).

The temperature dependence of the  $\nu_R(\text{D}_2\text{O})$  band is shown in Fig. 3.15. This broad band with a peak frequency of  $613 \text{ cm}^{-1}$  and a half-width of  $115 \text{ cm}^{-1}$  at  $175^\circ\text{K}$ , sharpens on cooling to  $62^\circ\text{K}$  to a band with a peak frequency of  $617 \text{ cm}^{-1}$  and a half-width of  $99 \text{ cm}^{-1}$  (Table 3.3). The presence of the high frequency shoulder at  $670 \text{ cm}^{-1}$  at  $95^\circ\text{K}$  (Figs. 3.7 and 3.14) was more evident at lower temperatures. Broad, weak features were seen in the spectra of mulls at 451, 420 and  $375 \text{ cm}^{-1}$  (Table 3.1). The first two are confirmed in the spectra of the pellets (Table 3.2; Fig. 3.14), but the third very weak one could not be clearly identified. This may be because this spectral region shows the effects of the changing refractive index of, and absorption by, the potassium bromide.

The broad band assigned to  $3\nu_R(\text{H}_2\text{O})$  and  $\nu_R(\text{H}_2\text{O}) + \nu_2(\text{H}_2\text{O})$  is rather better defined in the spectra of the pellets than in those of the mulls, because of the absence of the weak absorption by the mulling agents. The peak occurs at  $2248 \text{ cm}^{-1}$  (Fig. 3.13, curve B, Table 3.2),  $13 \text{ cm}^{-1}$  higher than in the spectra of the mulls, with a half-width of about  $300 \text{ cm}^{-1}$ . A definite, broad shoulder



is observed at about  $2432 \text{ cm}^{-1}$  with a second shoulder possibly at  $2620$  to  $2670 \text{ cm}^{-1}$ . The shoulder at about  $2432 \text{ cm}^{-1}$  coincides with the  $\nu_{\text{OD}}$  (HDO) band (Fig. 3.13, curve A, Table 3.2) within measurement error, but its intensity appears to be too great for it to arise from the 0.03 mole percent of HDO molecules in normal water. If it is a genuine feature of the overtone and combination band, it would be expected at about  $1770 \text{ cm}^{-1}$  in the spectrum of the deuterate. Unfortunately the overtone and combination band is very weak in the spectrum of the deuterate and it was not possible to obtain good spectra from a pellet which contained enough deuterate to yield a sufficiently intense band to enable the presence of a shoulder at  $1770 \text{ cm}^{-1}$  to be observed. Thus, the assignment of the shoulder at about  $2432 \text{ cm}^{-1}$  to a feature of the combination and overtone band must remain unproved. The band due to  $3\nu_{\text{R}}(\text{D}_2\text{O})$  and  $\nu_{\text{R}}(\text{D}_2\text{O}) + \nu_2(\text{D}_2\text{O})$  in the spectra of the deuterate in pellets is seen rather more clearly than in the spectra of mulls, at about  $1634 \text{ cm}^{-1}$  (Fig. 3.14, Table 3.2), with a half-width of about  $85 \text{ cm}^{-1}$ . The temperature dependence of these bands was not studied.

The temperature dependence of the band due to  $\nu_{\text{OH}}$  (HDO) is shown in Fig. 3.16. The symmetric band at  $175^\circ\text{K}$  with a peak frequency of  $3311 \text{ cm}^{-1}$  and a half-width of  $163 \text{ cm}^{-1}$  becomes a slightly asymmetric band at  $62^\circ\text{K}$  with a peak frequency of  $3309 \text{ cm}^{-1}$ , a shoulder at about  $3280 \text{ cm}^{-1}$ , and

a total half-width of  $150 \text{ cm}^{-1}$  (Table 3.4). Since this band arose from the residual water in the potassium bromide, it is necessary to compare it to the  $\nu_{\text{OH}}$  (HDO) band observed in the spectra of mulls, in order to obtain an estimate of the concentration of HDO molecules. Comparison of the peak height of this band in the spectra of pellets and mulls, relative to the peak height of the  $\nu_7/\nu_{17}$  guest band, showed that the molar concentration of HDO molecules in the sample used for Fig. 3.16 was 10%, and in the sample used for curves A and B of Fig. 3.14 were 7 and 12%, respectively. The peak frequency of this band in the pellet spectrum at  $95^\circ\text{K}$  (Table 3.2) is the same as that obtained from a mull (Table 3.1).

The temperature dependence of the band due to  $\nu_{\text{OD}}$  (HDO) is shown in Fig. 3.16. The featureless band at  $175^\circ\text{K}$  with a peak frequency of  $2448 \text{ cm}^{-1}$  and a half-width of  $92 \text{ cm}^{-1}$  becomes an asymmetric band at  $62^\circ\text{K}$  with a peak frequency of  $2442 \text{ cm}^{-1}$  and a half-width of  $85 \text{ cm}^{-1}$  (Table 3.4). Below  $125^\circ\text{K}$ , three shoulders become apparent: a high frequency shoulder at about  $2550 \text{ cm}^{-1}$ , a shoulder at about  $2425 \text{ cm}^{-1}$ , about  $18 \text{ cm}^{-1}$  to low frequency of the band maximum, and a very broad shoulder centered at about  $2400 \text{ cm}^{-1}$ . The frequency of the band maximum reported from the spectra of mulls (Table 3.1) is within  $4 \text{ cm}^{-1}$  of the one obtained from the pellet at  $95^\circ\text{K}$  (Table 3.2).

A comparison of the  $\nu_{\text{OH}}$  (HDO) band obtained from the

mulls (Fig. 3.8) with that from pellets (Fig. 3.16) shows that the distinct asymmetry of the band obtained from the mulls, due to the low frequency shoulder at about  $3237\text{ cm}^{-1}$ , is absent at all temperatures in the band obtained from the pellets. Also, this asymmetry is essentially absent in the  $\nu_{\text{OD}}$ (HDO) band obtained from the mulls (Fig. 3.8). Thus, it is probable that the low frequency shoulder on the  $\nu_{\text{OH}}$ (HDO) band obtained from the mulls is a result of reflection and scattering effects. Such effects have been previously noted (27) for the corresponding band of HDO ice. A shoulder at about  $3280\text{ cm}^{-1}$  is seen on the  $\nu_{\text{OH}}$ (HDO) band (Fig. 3.16) at  $62^\circ\text{K}$ , and this corresponds to the shoulder at about  $2425\text{ cm}^{-1}$  on the  $\nu_{\text{OD}}$ (HDO) band at temperatures below  $125^\circ\text{K}$  (Fig. 3.16). The latter shoulder could not be definitively identified in the spectra of mulls, but the spectrum (Fig. 3.8) is consistent with the existence of a shoulder at about this frequency. Finally, the very weak shoulder at about  $2550\text{ cm}^{-1}$  on the  $\nu_{\text{OD}}$ (HDO) band obtained from the pellets (Fig. 3.16) was not present on the  $\nu_{\text{OD}}$ (HDO) band in the spectra of the mulls (Fig. 3.8); and also a corresponding shoulder on the  $\nu_{\text{OH}}$ (HDO) band obtained from the pellets (Fig. 3.16) was absent. Thus, the assignment of this shoulder to a real feature of the band must remain tentative.

The only remaining absorption by water molecules is centered at  $1500\text{ cm}^{-1}$  in spectra of hydrate and deuterate

samples containing about 8 mole percent (Fig. 3.13, curve A) and about 12 mole percent (Fig. 3.14, curve B) of HDQ, and became weaker at lower HDO concentrations (Fig. 3.13, curve B; Fig. 3.14, curve A). It is assigned to  $\nu_2$ (HDO).

### 3.3.3 Absorption by the Trimethylene Oxide Molecules

The bands due to trimethylene oxide absorption in the spectra of TMO hydrate I in potassium bromide (Figs. 3.13, 3.14, 3.17 to 3.20) are essentially identical to those in the spectra of mulls (Figs. 3.4, 3.5, 3.9 to 3.11). An exception is that the C-H stretching bands of TMO hydrate I are resolved much more clearly in the spectra of pellets (Fig. 3.13) than in the spectra of mulls (Fig. 3.4). These bands are superimposed on the broad O-H stretching band, and it is believed that different reflection and scattering effects in the mulls and pellets are the source of this difference. A further exception is that the very weak band due to  $\nu_5$  at about  $1340\text{ cm}^{-1}$  in the spectra of pellets (Table 3.2, Figs. 3.13, 3.14) was not observed in the spectra of the mulls. The weak  $\nu_{12}$  band at  $831.2\text{ cm}^{-1}$  in the spectrum of the deuterate (Table 3.1, Figs. 3.5, 3.10) could not be clearly observed in the spectra of the pellets, because of overlapping, weak absorption by  $\nu_R$ (HDO). The frequencies of the guest absorption in the spectra of the pellets at  $95^\circ\text{K}$  (Table 3.2) are the same as in the spectra of the mulls (Table 3.1) within experimental error, with the exception of those of the very strong bands due to

$\nu_7/\nu_{17}$  at about  $978 \text{ cm}^{-1}$ , which are  $1.3$  to  $1.4 \text{ cm}^{-1}$  higher in the spectra of the pellets. As was discussed in Section 3.3.2 for the water absorption, this difference is undoubtedly due to reflection and scattering effects.

The frequencies of the guest absorption in pellets by the hydrate are the same as those by the deuterate at  $95^\circ\text{K}$  (Table 3.2) within experimental error, except for those of the strongest guest band, due to  $\nu_7/\nu_{17}$ , which differs by  $1.4 \text{ cm}^{-1}$ , with the hydrate band to high frequency. This band is superimposed on the high frequency tail of the  $\nu_R(\text{H}_2\text{O})$  band in the spectrum of the hydrate, and this is undoubtedly the cause of its higher frequency.

The temperature dependence of the medium and strong trimethylene oxide absorption bands of TMO hydrate I is shown in Fig. 3.17, and the frequencies, half-widths and peak heights are listed in Table 3.5. The temperature dependence of the absorption by the C-H stretching vibrations in the spectrum of the hydrate was not studied, and the other bands which are not included in Fig. 3.17 and Table 3.5 are either too weak to yield useful results or are shoulders which did not develop into peaks with decreasing temperature. The temperature dependence of all except the very weak guest bands of TMO deuterate I are shown in Figs. 3.18 to 3.20 and the parameters are listed in Table 3.6. The temperature dependence of the frequencies of the guest bands was determined by measuring the band at

at a temperature with respect to the same fiducial marker. When the bands were sharp and well defined, their frequencies could be measured in this way with a precision (reproducibility) of  $\pm 0.2 \text{ cm}^{-1}$  below  $2000 \text{ cm}^{-1}$  and  $\pm 0.4 \text{ cm}^{-1}$  above  $2000 \text{ cm}^{-1}$ . However the accuracy of the frequencies depends on the accuracy with which the frequency of the fiducial marker is known, and this is only  $\pm 0.5 \text{ cm}^{-1}$  below  $2000 \text{ cm}^{-1}$  and  $\pm 1 \text{ cm}^{-1}$  above  $2000 \text{ cm}^{-1}$ .

The first point to note is that no marked changes occur for any of the guest bands between 175 and  $62^\circ\text{K}$ . All of the bands become sharper and increase their peak heights upon cooling, and seven bands decrease their frequencies while five increase their frequencies on cooling. No clear signs of abnormal behaviour between 125 and  $75^\circ\text{K}$  are evident. Several shoulders become clearly evident in the spectra on cooling the samples towards  $62^\circ\text{K}$ . These may be seen at  $2912$ ,  $2973$ ,  $2978$  and  $3000 \text{ cm}^{-1}$  in Fig. 3.18, at  $1134 \text{ cm}^{-1}$  in Figs. 3.17 and 3.19, and at  $896$  and  $968 \text{ cm}^{-1}$  in Fig. 3.20. In all cases, their increased prominence at the lower temperatures appears to be a consequence simply of the decreased half-width of the neighbouring bands. Certain bands show slightly different temperature dependence in the spectra of the hydrate and deuterate. The frequencies of the bands due to  $\nu_4/\nu_{14}$  and  $\nu_{21}$  are essentially independent of temperature in the spectra of the hydrate, while that of  $\nu_{21}$  decreases slightly, and that

of  $\nu_4/\nu_{14}$  increases by  $0.8 \text{ cm}^{-1}$ , on cooling the deuterate from 175 to  $62^\circ\text{K}$ . More noticeably, the shoulder due to  $\nu_7/\nu_{17}$  at  $990 \text{ cm}^{-1}$  remains a shoulder as the hydrate is cooled to  $62^\circ\text{K}$  (Fig. 3.17), while it develops into a definite peak when the deuterate is cooled to  $62^\circ\text{K}$  (Fig. 3.20). The cause of these differences is undoubtedly the water absorption which underlies  $\nu_4/\nu_{14}$  and  $\nu_7/\nu_{17}$  in the spectrum of the hydrate and  $\nu_{21}$  in the spectrum of the deuterate (Figs. 3.13, 3.14). For the  $\nu_7/\nu_{17}$  band of the deuterate, the emergence of the peak at  $989.7 \text{ cm}^{-1}$  at  $62^\circ\text{K}$  from the shoulder observed at the higher temperatures (Fig. 3.20) appears to be solely a consequence of the smaller half-widths of the bands at the lower temperature.

The trends of the frequency changes with temperature for the bands due to  $\nu_{16}$  and  $\nu_{22}$  (Table 3.6) in the deuterate spectrum are considered to be reliable, although the absolute values of the frequencies at the higher temperatures are difficult to measure due to the broad, weak nature of these bands.

#### 3.4 Powder X-ray Diffraction Pattern of Structure I Trimethylene Oxide Hydrate

Powder X-ray diffraction photographs were taken of all samples of TMO hydrate I and TMO deuterate I to ensure that the correct phase had been obtained and to determine its purity. The two best photographs of different samples of TMO hydrate I were each measured twice to determine the diffraction parameters. The inside and outside diameter of each

diffraction circle was measured with an accuracy of  $\pm 0.1$  mm. This data was supplied to the programme POWDER, written in this laboratory by S. Sunder, which calculates the mean diameter of each circle, the corresponding  $2\theta$  value of the reflection and the interplanar spacing,  $d$ . Thus, four sets of  $2\theta$  and  $d$  values were obtained.

The  $2\theta$  and  $d$  values were indexed using the relationship for a cubic system,

$$\frac{h^2 + k^2 + l^2}{a^2} = \frac{1}{d^2}$$

where  $h$ ,  $k$  and  $l$  are the Miller indices,  $d$  is the value of the interplanar spacing and  $a$  is the unit cell parameter. An approximate value for the unit cell parameter, obtained during the indexing procedure, was refined for each set of data using the programme DREFINE (89). This programme accepts the indexed experimental  $2\theta$  values, the initial set of unit cell parameters and the wavelength of the X-ray radiation, and then refines these unit cell parameters by a least squares method until an optimum fit between the calculated and experimental  $2\theta$  values is obtained. Four values of the unit cell parameters were obtained in this way and averaged to yield the value  $11.95 \pm 0.02$  Å, where 0.02 Å indicates the range of the values obtained.

The powder X-ray diffraction pattern of TMO hydrate I at  $100 \pm 20^\circ\text{K}$  is given in Table 3.7. The calculated intensities (46) were determined from the structure factors of



Table 3.7

Powder X-ray Diffraction Pattern  
of Structure I Trimethylene Oxide  
Hydrate at 100 ± 20°K

Index	Calculated <sup>a</sup>	Calculated <sup>b, d</sup>	Calculated <sup>b, d</sup>	Observed <sup>c, d</sup>	Observed <sup>c, d</sup>	Observed
	Intensity	d Spacing (Å)	2θ (°)	2θ (°)	d Spacing (Å)	Intensity
110	14	8.450	10.47	10.51 (3)	8.42 (2)	47
200	2	5.975	14.83			
210	<0.01	5.344	16.59	16.63 (1)	5.331 (4)	4
211	10	4.879	18.18	18.19 (2)	4.878 (6)	12
220	5	4.225	21.03	21.00 (7)	4.23 (1)	6
310	12	3.779	23.54	23.56 (2)	3.776 (4)	25
222	49	3.450	25.83	25.81 (3)	3.452 (4)	63
320	54	3.314	26.90	26.90 (5)	3.315 (6)	74
321	100	3.194	27.94	27.96 (5)	3.191 (6)	100
400	9	2.987	29.91	29.88 (1)	2.990 (2)	14
410	23	2.898	30.85	30.86 (4)	2.897 (4)	22
411 } 330 }	11	2.817	31.77	31.80 (3)	2.814 (3)	12
420	0.7	2.672	33.54			
421	10	2.608	34.39	34.38 (4)	2.608 (3)	21
332	5	2.548	35.23	35.25 (8)	2.546 (6)	8
422	0.7	2.439	36.85			
430	2.5	2.390	37.63	37.58 (6)	2.391 (4)	6
510 } 431 }	2.3	2.344	38.41	38.43 (5)	2.342 (3)	5
520 } 432 }	8.6	2.219	40.66	40.64 (2)	2.220 (1)	17
521	1.2	2.182	41.38			
440	0.04	2.112	42.81			
433 } 530 }	28	2.049	44.19	44.16 (2)	2.051 (1)	29
531	8.3	2.020	44.87			
600 } 442 }	6.4	1.992	45.54	45.52 (3)	1.992 (1)	7
610	2.4	1.965	46.21			
611 } 532 }	13	1.939	46.87	46.83 (4)	1.940 (1)	12
620	3.0	1.889	48.16			
540 } 621 }	2.5	1.866	48.80			

a) Integrated intensity for flat-plate camera, calculated from  $I = [(1 + \cos^2 2\theta) / \sin^2 \theta \cos \theta] \cos 2\theta p F^2$ , where  $p$  is the multiplicity factor and  $F$  is the observed structure factor from (36).

b) Calculated from  $a = 11.95 \text{ \AA}$

c) The average of four measurements. The figure in parenthesis is the standard deviation in the last figure.

d) Cu K<sub>α</sub> radiation, wavelength = 1.5418 Å.

ethylene oxide hydrate at  $-25^{\circ}\text{C}$  (36), and the observed intensities were measured as peak heights on microdensitometer traces. The calculated  $2\theta$  and  $d$  values were obtained by supplying the programme 2THETA, written in this laboratory by R. J. Lamont, with the averaged unit cell parameter given above and the wavelength of the X-ray radiation. The observed  $2\theta$  and  $d$  values are averages of the four sets of values obtained from the photographs.

The powder X-ray diffraction pattern of TMO deuterate I was identical with that given in Table 3.7, within experimental error.

For comparison purposes, X-ray photographs of ice and solid trimethylene oxide at  $100 \pm 20^{\circ}\text{K}$  were also obtained. The diffraction pattern of ice is well known (82) and will not be reproduced here, but that of trimethylene oxide has not been reported previously. Thus, the  $2\theta$  and  $d$  values of the observed diffraction lines ( $\text{Cu K}\alpha$  radiation, wavelength  $1.5418 \text{ \AA}$ ) are presented in Table 3.8 for solid trimethylene oxide at  $100^{\circ}\text{K}$ . The unit cell size and the space group are not known, and no attempt was made to index the observed pattern.

Table 3.8

Powder X-ray Diffraction Pattern  
of Trimethylene Oxide at  $100 \pm 20^\circ\text{K}$

Observed <u>d Spacing (Å)<sup>b</sup></u>	Observed <u>2θ (°)<sup>b</sup></u>	Approximate Observed <u>Intensity<sup>a</sup></u>
1.938	46.892	w
1.979 (1)	45.86 (5)	w
2.010 (1)	45.12 (4)	w
2.120 (1)	42.64 (2)	w
2.160 (3)	41.82 (7)	w
2.188 (1)	41.26 (3)	m
2.407 (0)	37.35 (0)	w
2.627 (1)	34.13 (2)	m
3.000 (6)	29.78 (6)	m
3.174 (0)	28.11 (0)	m
3.554 (1)	25.054 (6)	s
3.912 (1)	22.734 (7)	m
4.387 (4)	20.24 (2)	s

- a) s = strong, m = medium, w = weak,  
 b) The d spacing and 2θ values are the averages of two measurements of one photograph. The figure in parenthesis is the deviation from the mean in the last figure quoted. Cu K<sub>α</sub> radiation, wavelength = 1.5418 Å, was used.

## Chapter Four. Mid-Infrared Spectra of Structure II

### Trimethylene Oxide Hydrate

#### 4.1 General

The results of the study of the mid-infrared spectra of TMO hydrate II will be presented in this chapter. The spectra obtained from samples dispersed in mulling agents are considered to be reliable since they were obtained using a well established technique (48, 49). In contrast, the spectra obtained from potassium bromide pellets containing TMO hydrate II are considered to be suspect from a comparison with the spectra of mulls, and therefore they will only be mentioned briefly in this chapter. The general comments of Section 3.1 concerning the mulling technique are equally applicable to the work presented in this chapter. The mid-infrared spectrum of TMO hydrate II was not studied in the same detail as the spectrum of TMO hydrate I; however the results presented here are believed to be accurate and attention will be drawn to any uncertainties that exist.

It was concluded in Section 2.1 that the level of impurities in the commercial trimethylene oxide that was used was insufficient to cause an observable effect in the spectra of the hydrate. The remaining possible sources of contamination are intrinsic ice, extrinsic ice, solid trimethylene oxide and TMO hydrate I.

Inspection of the trimethylene oxide-water phase diagram (Fig. 1.3) shows that during the preparation of TMO hydrate II (Section 2.2), ice is formed first, followed by a mixture of TMO hydrate II and TMO hydrate I. In order to remove this intrinsic ice, the samples were annealed at  $-18^{\circ}\text{C}$  for about two weeks to allow the ice to react with the TMO hydrate I, which is unstable at this temperature, to give TMO hydrate II. Further inspection of the phase diagram (Fig. 1.3) shows that a slight excess of water would result in intrinsic ice remaining after the annealing process. Although the trimethylene oxide and water were carefully weighed, the powder X-ray diffraction photographs revealed that a very small, constant amount of intrinsic ice was present in the TMO hydrate II samples. The concentration of the trimethylene oxide was increased for one sample to 1 TMO.16.4  $\text{H}_2\text{O}$ , however, this sample also contained intrinsic ice as well as some TMO hydrate I. The amount of intrinsic ice in the samples was extremely small judging by the intensity of the diffraction line, and it will be argued later that this ice had no effect on the spectra presented. Extrinsic ice was essentially eliminated by paying careful attention to technique as discussed in Chapter 3. The powder X-ray diffraction photographs and the infrared spectra indicated that solid trimethylene oxide was not present in any of the TMO hydrate II samples.

Contamination by TMO hydrate I was readily identified

in the powder X-ray diffraction photographs by its intense line with a  $2\theta$  value of  $10.5^\circ$  (Section 3.4). This contamination was also observed in the infrared spectra, and this is illustrated in Fig. 4.1 which shows the spectra between  $960$  and  $1010\text{ cm}^{-1}$  of uncontaminated TMO hydrate I (curve A), TMO hydrate II contaminated by TMO hydrate I (curve B) and uncontaminated TMO hydrate II (curve C). The weak low frequency band in curve C has a peak frequency of  $973.2\text{ cm}^{-1}$  whereas the strong band in curve A, which is the most intense guest band in the spectrum of TMO hydrate I (Chapter 3), has a peak frequency of  $976.8\text{ cm}^{-1}$ . This frequency difference of  $3.6\text{ cm}^{-1}$  provides strong evidence that the weak band in curve C is not due to TMO hydrate I. This is confirmed by the peak frequency of  $975.9\text{ cm}^{-1}$  for the weak band in curve B, as would be expected for a TMO hydrate II sample slightly contaminated by TMO hydrate I. All of the spectra to be presented in this chapter are of samples that were as pure as the one used for curve C of Fig. 4.1 and, thus, they show no observable effects of contamination by TMO hydrate I.

#### 4.2 Mid-Infrared Spectra of Structure II Trimethylene Oxide Hydrate in Mulls

The infrared spectra between  $300$  and  $4000\text{ cm}^{-1}$  of TMO hydrate II and TMO deuterate II at  $95 \pm 10^\circ\text{K}$  are shown in Fig. 4.2. The main spectrum in each case, labelled A, was obtained from the spectrum of a propane mull by

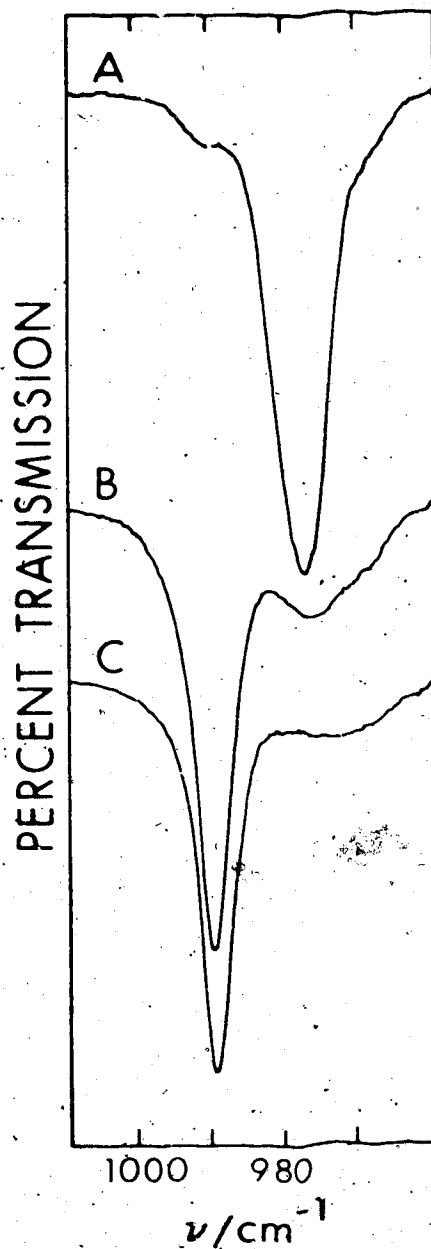


Fig. 4.1. The  $\nu_7/\nu_{17}$  bands of uncontaminated structure I trimethylene oxide deuterate (curve A), structure II trimethylene oxide deuterate contaminated by structure I trimethylene oxide deuterate (curve B), and uncontaminated structure II trimethylene oxide deuterate (curve C), dispersed in a mulling agent at 95°K. The maximum and minimum percent transmission of each curve are: A, 90, 20; B, 80, 32; C, 89, 50.

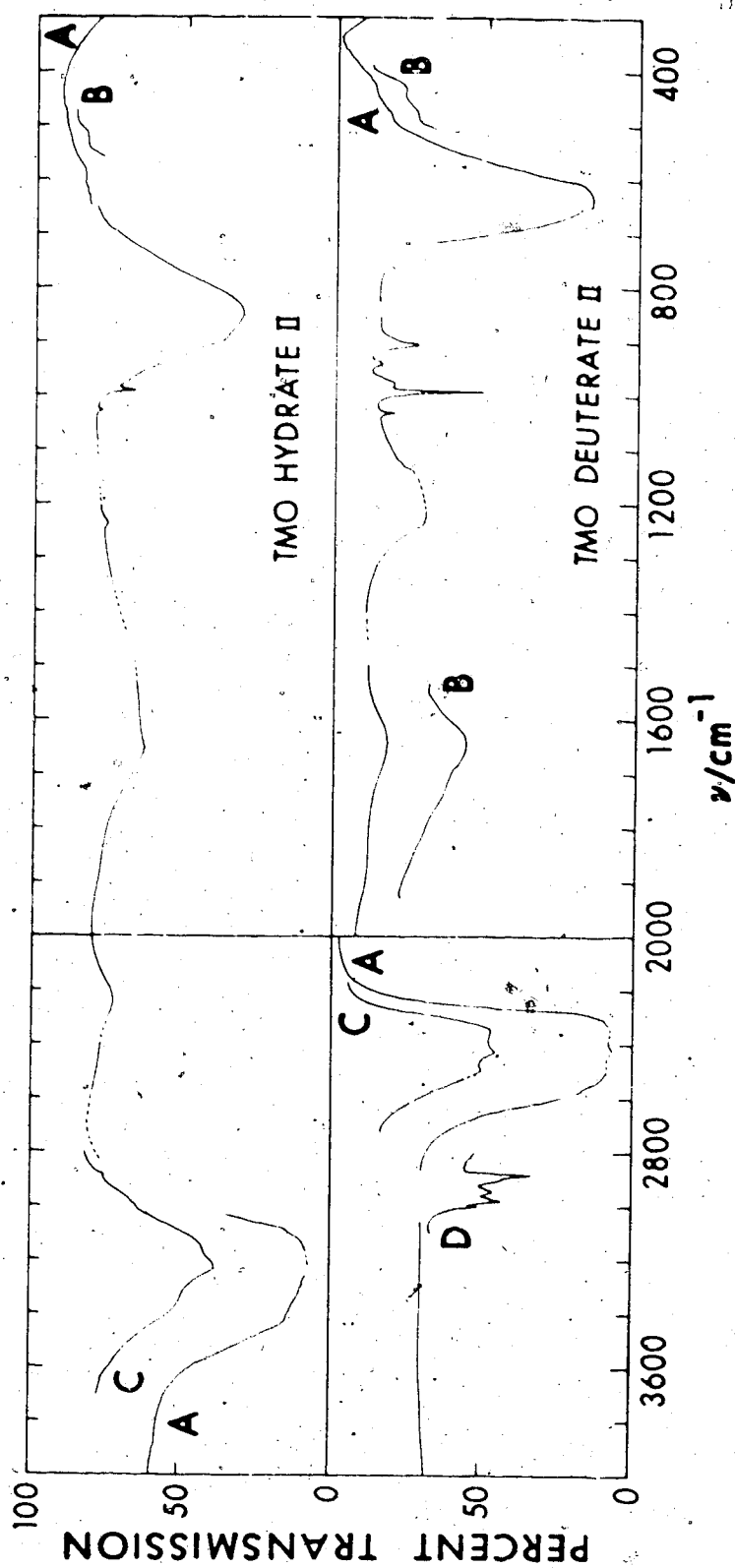


Fig. 4.2. Mid-infrared spectra of structure II trimethylene oxide hydrate. (upper box) and deuterate (lower box) at 95°K. The different curves and lines are described in the text. Curves B and C of the upper box have been lowered by 12 percent transmission. In the lower box, the low and high frequency curves B have been raised by 5 percent and lowered by 20 percent transmission, respectively; curves C and D have been raised by 12 percent and lowered by 5 percent transmission, respectively.



removing the peaks due to liquid propane. Curves B and C for TMO hydrate II were taken from spectra of a large amount of sample mullied with propylene and a very small amount of sample mullied with Freon 13, respectively. For TMO deuterate II, curves B, C and D were taken from spectra of the following samples: curve B, a propane mull; curve C, a very small amount of deuterate mullied with propylene; curve D, a Freon 13 mull containing about the same amount of deuterate as the mull used for curve A. The dashed lines indicate that, after inspection of spectra of propane, propylene and Freon 13 mulls, the spectrum of the sample is believed to approximate the dashed contour although that region of the spectrum used for curve A was obscured by the propane absorption. Dotted lines indicate that the corresponding region of the spectrum is uncertain due to the masking of weak guest bands, which are expected in these regions, by the propane absorption. For the regions above  $2800\text{ cm}^{-1}$ , spectra of Freon 13 mulls gave the absorption by the samples, as indicated by the additional curves. Composite spectra, such as were presented in Section 3.2.1, have not been made, because insufficient spectra were taken to assure that the composite spectra would have the desired degree of reliability.

The spectra shown in Fig. 4.2 were recorded at a resolution of better than  $5\text{ cm}^{-1}$  between  $300$  and  $650\text{ cm}^{-1}$ , and better than  $2.5\text{ cm}^{-1}$  between  $650$  and  $4000\text{ cm}^{-1}$ . The

frequencies of the observed features, and their estimated accuracy, are listed in Table 4.1 together with the assignment of the features. The temperature of the samples, as discussed in Section 3.2, was  $95 \pm 10^\circ\text{K}$ .

#### 4.2.1 Absorption by the Water Molecules

The band due to  $\nu_{\text{OH}}(\text{H}_2\text{O})$  is shown in detail in Fig. 4.3 and extends from 2800 to  $3700 \text{ cm}^{-1}$ . It has a peak frequency of  $3224 \text{ cm}^{-1}$  with a well defined high frequency shoulder at  $3335 \text{ cm}^{-1}$  and a more poorly defined low frequency shoulder at about  $3116 \text{ cm}^{-1}$ . The half-width of this band is about  $100 \text{ cm}^{-1}$ . The band due to  $\nu_{\text{OD}}(\text{D}_2\text{O})$  (Fig. 4.3) extends from 2100 to  $2800 \text{ cm}^{-1}$ . Three maxima are clearly seen at 2488, 2423 and  $2343 \text{ cm}^{-1}$ . There is a very broad low frequency shoulder at about  $2285 \text{ cm}^{-1}$ . The half-width of the overall band is about  $285 \text{ cm}^{-1}$ . The ratio of the peak frequency of  $\nu_{\text{OH}}(\text{H}_2\text{O})$  to the peak frequency of  $\nu_{\text{OD}}(\text{D}_2\text{O})$  is  $1.331 \pm 0.005$ .

The broad band due to  $\nu_2(\text{H}_2\text{O})$  was poorly defined in this work (Fig. 4.2). It extends from about 1200 to  $1900 \text{ cm}^{-1}$  and has a peak frequency of about  $1650 \text{ cm}^{-1}$ . The band due to  $\nu_2(\text{D}_2\text{O})$  extends from about 1050 to  $1400 \text{ cm}^{-1}$ . The details near the band maximum were not well defined in this work, so the peak frequency is only approximately known. However, the band appears to slope steeply on the high frequency side and gradually on the low frequency side, as is the case for  $\nu_2(\text{H}_2\text{O})$ , and such a contour would place the band maximum at about  $1225 \text{ cm}^{-1}$ . The ratio of the

Table 4.1

Frequencies of the Observed Features  
in the Mid-Infrared Spectra of  
Structure II Trimethylene Oxide  
Hydrate and Deuterate in Mulls at 95°K<sup>a</sup>

TMO Hydrate II $\nu/\text{cm}^{-1}$	Assignment	TMO Deuterate II $\nu/\text{cm}^{-1}$
~3335 sh	} $\nu_{\text{OH}}(\text{H}_2\text{O})$	
3224 ±4 vs, br		
~3116 sh		
	$\nu_{\text{OH}}(\text{HDO})$	3274 ±5 s, br
2995 ±5 sh	$\nu_{19}(\text{TMO})$	2997.3 ±1 m
2966 ±10 sh	$\nu_{18}(\text{TMO})$	2976.9 ±1 m
-----	2 x $\nu_{14}(\text{TMO})?$	2968 ±2 sh
		2950 ±3 sh
2935 ±10 sh	$\nu_{20}(\text{TMO})$	2943 ±2 m
-----	$\nu_9(\text{TMO})?$	2930 ±3 sh
-----	$\nu_2(\text{TMO})$	2895 ±5 sh
2879 ±2 w	$\nu_{13}(\text{TMO})$	2881.2 ±1 s
		2488 ±10 vs
	} $\nu_{\text{OD}}(\text{D}_2\text{O})$	2423 ±3 vs
		2343 ±10 vs
		~2285 sh

TMO Hydrate II $\nu/\text{cm}^{-1}$	Assignment	TMO Deuterate II $\nu/\text{cm}^{-1}$
2419 $\pm 5$ s, br	$\nu_{\text{OD}}(\text{HDO})$	
2241 $\pm 30$ m, br	$\left\{ \begin{array}{l} 3\nu_{\text{R}}(\text{H}_2\text{O}), \\ \nu_2(\text{H}_2\text{O}) + \nu_{\text{R}}(\text{H}_2\text{O}) \end{array} \right.$	
$\sim 1650$ m, br		$\nu_2(\text{H}_2\text{O})$
	$\left\{ \begin{array}{l} 3\nu_{\text{R}}(\text{D}_2\text{O}), \\ \nu_2(\text{D}_2\text{O}) + \nu_{\text{R}}(\text{D}_2\text{O}) \end{array} \right.$	1642 $\pm 15$ mw, br
1234 $\pm 10$ w		$\nu_{16}(\text{TMO})$
	$\nu_2(\text{D}_2\text{O})$	$\sim 1225$ m, br
1138 $\pm 4^b$	$\nu_{21}(\text{TMO})$	1137 $\pm 5$ sh
1029 $\pm 2$ mw	$\nu_6(\text{TMO})$	1028.1 $\pm 0.5$ mw
990.9 $\pm 1$ m	$\nu_7/\nu_{17}(\text{TMO})$	$\left\{ \begin{array}{l} 989.5 \pm 0.5 \text{ s} \\ 973.2 \pm 1 \text{ mw} \end{array} \right.$
974 $\pm 5$ sh		
938 $\pm 10$ sh	$\nu_{18}(\text{TMO})$	937 $\pm 5$ mw
900 $\pm 5$ sh	$\nu_8(\text{TMO})$	903.1 $\pm 0.5$ m
844 vs, br	$\nu_{\text{R}}(\text{H}_2\text{O})$	
580 0 mw		
519 $\pm 10$ w		
	$\nu_{\text{R}}(\text{D}_2\text{O})$	$\left\{ \begin{array}{l} 632 \pm 5 \text{ vs, br} \\ 476 \pm 10 \text{ w} \\ 430 \pm 10 \text{ w} \end{array} \right.$

a) vs = very strong, s = strong, m = medium, mw = medium-weak, w = weak, br = broad, sh = shoulder.

b) Observed as a shoulder on absorption by the mulling agent.

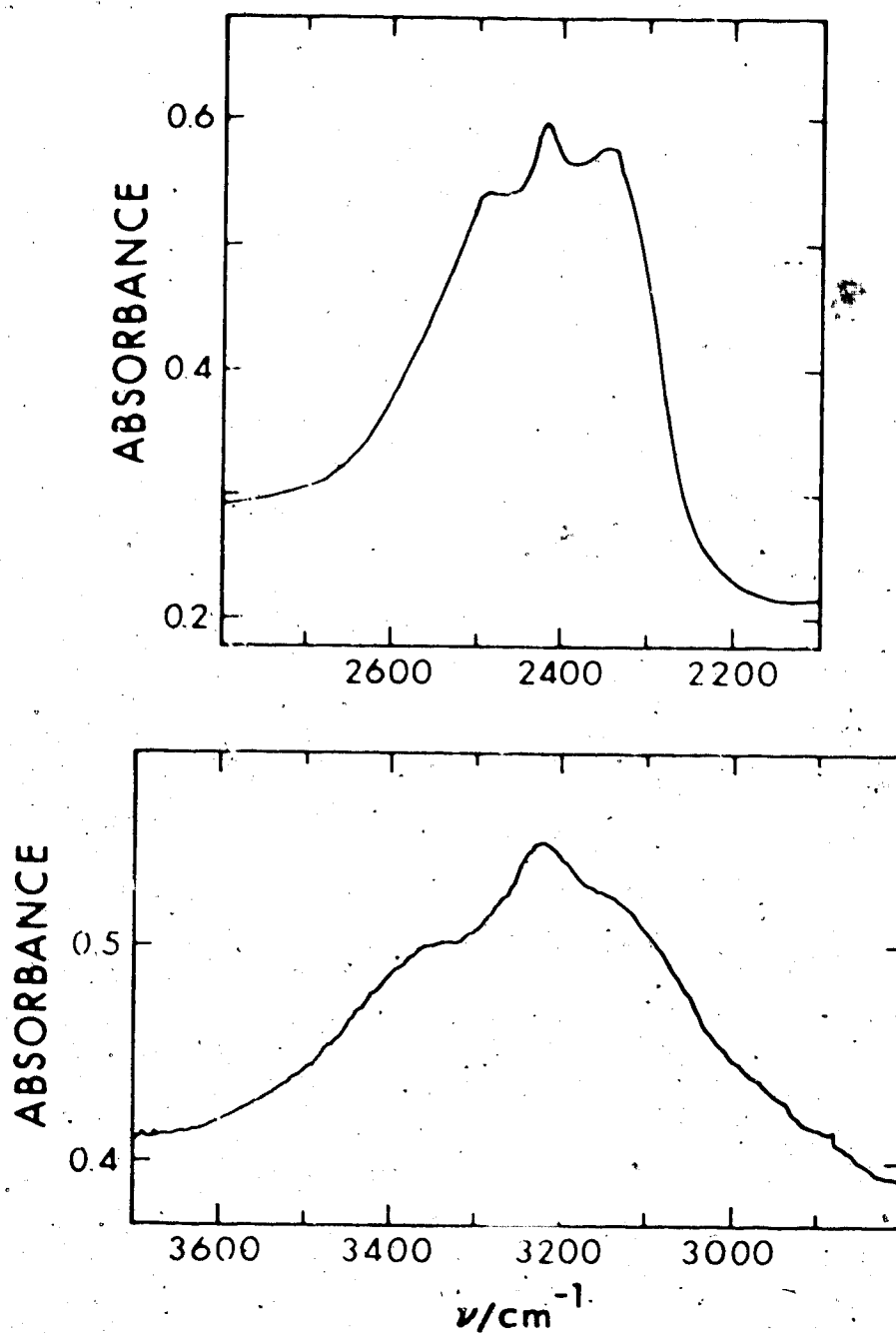


Fig. 4.3. The  $\nu_{OH}$  ( $\text{H}_2\text{O}$ ) band of structure II trimethylene oxide hydrate (lower box) and the  $\nu_{OD}$  ( $\text{D}_2\text{O}$ ) band of structure II trimethylene oxide deuterate (upper box) dispersed in mulling agents at 95°K.

peak frequencies of  $\nu_2(\text{H}_2\text{O})$  and  $\nu_2(\text{D}_2\text{O})$  is about 1.35.

The band due to  $\nu_R(\text{H}_2\text{O})$  extends from about 500 to 1050  $\text{cm}^{-1}$  (Fig. 4.2). The maximum of the main band is at 844  $\text{cm}^{-1}$  and it has a half-width of about 150  $\text{cm}^{-1}$ . Two broad, low frequency bands are observed at about 580 and 519  $\text{cm}^{-1}$ . The band due to  $\nu_R(\text{D}_2\text{O})$  (Fig. 4.2) shows a composite structure similar to that of  $\nu_R(\text{H}_2\text{O})$ , with a main band at 632  $\text{cm}^{-1}$  and two weak bands at 476 and 430  $\text{cm}^{-1}$ . The half-width of the main band is about 100  $\text{cm}^{-1}$ . If the two weak bands at 476 and 430  $\text{cm}^{-1}$  correspond to those at 580 and 519  $\text{cm}^{-1}$  in the spectrum of the hydrate, the isotopic frequency ratios are 1.22 and 1.21, respectively; these are significantly lower than the isotopic ratio of the frequencies of the main maxima of the  $\nu_R$  bands, which is 1.34. These isotopic frequency ratios are large enough to confirm the assignment of the weak features to  $\nu_R$  vibrations, but are sufficiently different from the expected value of about 1.34 to cast doubt on the above correspondence.

The overtone and combination band assigned to  $3\nu_R(\text{H}_2\text{O})$  and  $\nu_R(\text{H}_2\text{O}) + \nu_2(\text{H}_2\text{O})$  in the spectrum of the hydrate (Fig. 4.2) was poorly defined in this work, however, the corresponding band in the spectrum of the deuterate (Fig. 4.2) was rather better defined. The hydrate band extends from 2000 to 2700  $\text{cm}^{-1}$ , and has a peak frequency of about 2241  $\text{cm}^{-1}$ . The band appears asymmetric with a sharp low

frequency slope and a gradual high frequency slope. The corresponding band in the spectrum of the deuterate has a peak frequency of  $1642 \text{ cm}^{-1}$ , extends from about  $1500$  to  $2000 \text{ cm}^{-1}$ , and shows the same asymmetry exhibited by the hydrate band. The isotopic frequency ratio for this band is about 1.36.

The O-H and O-D stretching vibrations of isolated HDO molecules were studied in samples prepared from mixtures of 2 mole percent of  $\text{H}_2\text{O}$  in  $\text{D}_2\text{O}$  and 5 mole percent of  $\text{D}_2\text{O}$  in  $\text{H}_2\text{O}$ . The slight isotopic exchange expected to occur during the preparation of the samples should have resulted in both solutions containing about 5 mole percent of HDO. The band due to  $\nu_{\text{OH}}(\text{HDO})$  is shown in Fig. 4.4. It has a peak frequency of  $3274 \text{ cm}^{-1}$  and a half-width of about  $75 \text{ cm}^{-1}$ . The band due to  $\nu_{\text{OD}}(\text{HDO})$  (Fig. 4.4) has a peak frequency of  $2419 \text{ cm}^{-1}$  and a half-width of about  $75 \text{ cm}^{-1}$ . The broad band to low frequency of the  $\nu_{\text{OD}}(\text{HDO})$  band in Fig. 4.4 is the overtone and combination band discussed earlier.

It was mentioned earlier (Section 4.1) that an extremely small amount of intrinsic ice was present in the samples of TMO hydrate II and TMO deuterate II. It has been found in previous studies (48, 49) that small amounts of ice impurity can have a profound effect upon certain regions of the spectra of clathrate hydrates and deuterates. This is of particular concern to the present study, since the

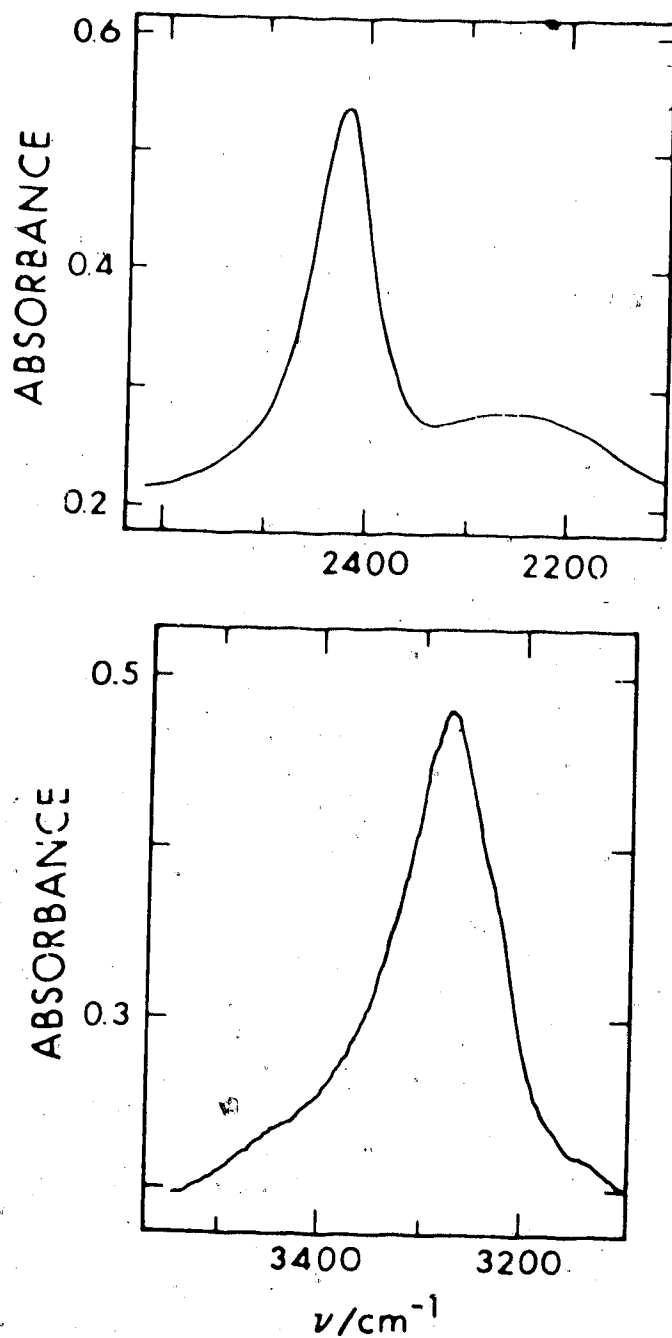


Fig. 4.4. The  $\nu_{OH}(HDO)$  band of structure II trimethylene oxide deuterate (lower box) and the  $\nu_{OD}(HDO)$  band of structure II trimethylene oxide hydrate (upper box), both containing about 5 percent of HDO, dispersed in muflite agents at 95°K.



frequencies of all of the bands due to the water vibrations essentially coincide with those of ice Ih (27). For the following reasons, it is believed that the ice impurity was present in sufficiently small concentrations to have no observable effect on the spectra presented.

Small amounts of intrinsic ice impurity in samples of hexamethylenetetramine hydrate and deuterate which contained 10 mole percent of HDO were clearly identified by the presence of the  $\nu_{OH}$ (HDO) and  $\nu_{OD}$ (HDO) bands of ice Ih at 3277 and 2420  $\text{cm}^{-1}$  (49). These bands were clearly visible at ice concentrations that were too low to affect the bands of  $\text{H}_2\text{O}$  and  $\text{D}_2\text{O}$  at all (49). During the study of the mid-infrared spectra of the structure I ethylene oxide hydrate and deuterate (48), it was found that the tops of the  $\nu_{OH}$ (HDO) and  $\nu_{OD}$ (HDO) bands became pointed and their half-widths decreased markedly when small amounts of intrinsic ice were present. Again, this was clearly seen at ice concentrations that were too low to affect the bands due to  $\text{H}_2\text{O}$  and  $\text{D}_2\text{O}$ . Unpublished work by Frances E. Bates on the structure II hydrates of cyclopropane and tetrahydrofuran provides further evidence of the effect of intrinsic ice impurity. The samples of tetrahydrofuran hydrate contained no intrinsic ice whereas those of cyclopropane hydrate II contained significant amounts of intrinsic ice, as determined by powder X-ray diffraction. The frequencies of the  $\nu_{OD}$ (HDO) bands of both hydrates are

close to that of HDO ice. The effect of the ice is to sharpen the top of the  $\nu_{OD}$  (HDO) band of cyclopropane hydrate II and reduce its half-width to about  $44 \text{ cm}^{-1}$ , compared to the  $\nu_{OD}$  (HDO) band of tetrahydrofuran hydrate, which has a half-width of about  $75 \text{ cm}^{-1}$ .

Comparison of the contours of the  $\nu_{OD}$  (HDO) bands of tetrahydrofuran hydrate, which contains no ice, and TMO hydrate II, shows that they are very similar, and the half-width of both bands is  $75 \text{ cm}^{-1}$ . There was no sharpening at the top of the  $\nu_{OD}$  (HDO) band of TMO hydrate II relative to that of tetrahydrofuran hydrate. Thus it is concluded that the extremely small amount of ice in the TMO hydrate II samples had no observable effect on the  $\nu_{OD}$  (HDO) band. As stated above, the HDO bands have been found to be the most sensitive bands in the spectra of clathrate hydrates and deuterates to the presence of intrinsic ice impurity, so it is argued that the other bands due to water vibrations in the spectra of TMO hydrate II are also unaffected. This conclusion is supported by the contour of the  $\nu_{OD}$  ( $D_2O$ ) band (Fig. 4.3) of TMO deuterate II, which is distinctly different from that of ice Ih (27).

#### 4.2.2 Absorption by the Trimethylene Oxide Molecules

The bands due to the C-H stretching vibrations in TMO hydrate II are shown in Fig. 4.3 as weak shoulders on the low frequency side of the  $\nu_{OH}$  ( $H_2O$ ) band. They are seen more clearly at essentially the same frequencies

(Table 4.1) in the spectra of TMO deuterate II, as shown in Fig. 4.5. The highest frequency guest band,  $\nu_{19}$ , has a peak frequency of  $2997.3 \text{ cm}^{-1}$  and a half-width of about  $7 \text{ cm}^{-1}$ . The band due to  $\nu_{11}$  is at  $2976.9 \text{ cm}^{-1}$  (Fig. 4.5) and has a low frequency shoulder at about  $2968 \text{ cm}^{-1}$ . The overall half-width of this band is about  $11 \text{ cm}^{-1}$ . The band at  $2943 \text{ cm}^{-1}$ , due to  $\nu_{20}$ , has a high frequency shoulder at  $2950 \text{ cm}^{-1}$ , and a low frequency shoulder at  $2930 \text{ cm}^{-1}$ , which is very tentatively assigned to  $\nu_9$ . The overall half-width of this band is about  $14 \text{ cm}^{-1}$ . The second strongest guest band,  $\nu_{13}$ , has a peak frequency of  $2881.2 \text{ cm}^{-1}$  and a broad high frequency shoulder at about  $2895 \text{ cm}^{-1}$  (Fig. 4.5), assigned to  $\nu_2$ . The half-width of this band, after approximately subtracting the absorption due to  $\nu_2$ , is  $15 \text{ cm}^{-1}$ .

The weak band at about  $1234 \text{ cm}^{-1}$ ,  $\nu_{16}$ , in the spectrum of the hydrate is not present in the spectrum of the deuterate, undoubtedly due to the presence of  $\nu_2(\text{D}_2\text{O})$  (Fig. 4.2). The shoulder at about  $1137 \text{ cm}^{-1}$ ,  $\nu_{21}$ , in the deuterate spectrum (Fig. 4.2) was also observed, as a shoulder at  $1138 \text{ cm}^{-1}$ , superimposed on mulling agent absorption in the hydrate spectrum. It has been omitted from the hydrate spectrum (Fig. 4.2), because its true shape and relative intensity are unclear.

The three strongest guest bands below  $2000 \text{ cm}^{-1}$  in the spectra of TMO deuterate II are shown in Fig. 4.6. The band due to  $\nu_6$  has a peak frequency of  $1029 \text{ cm}^{-1}$  in the hydrate spectrum (Fig. 4.2) and  $1028.1 \text{ cm}^{-1}$  in the deuterate

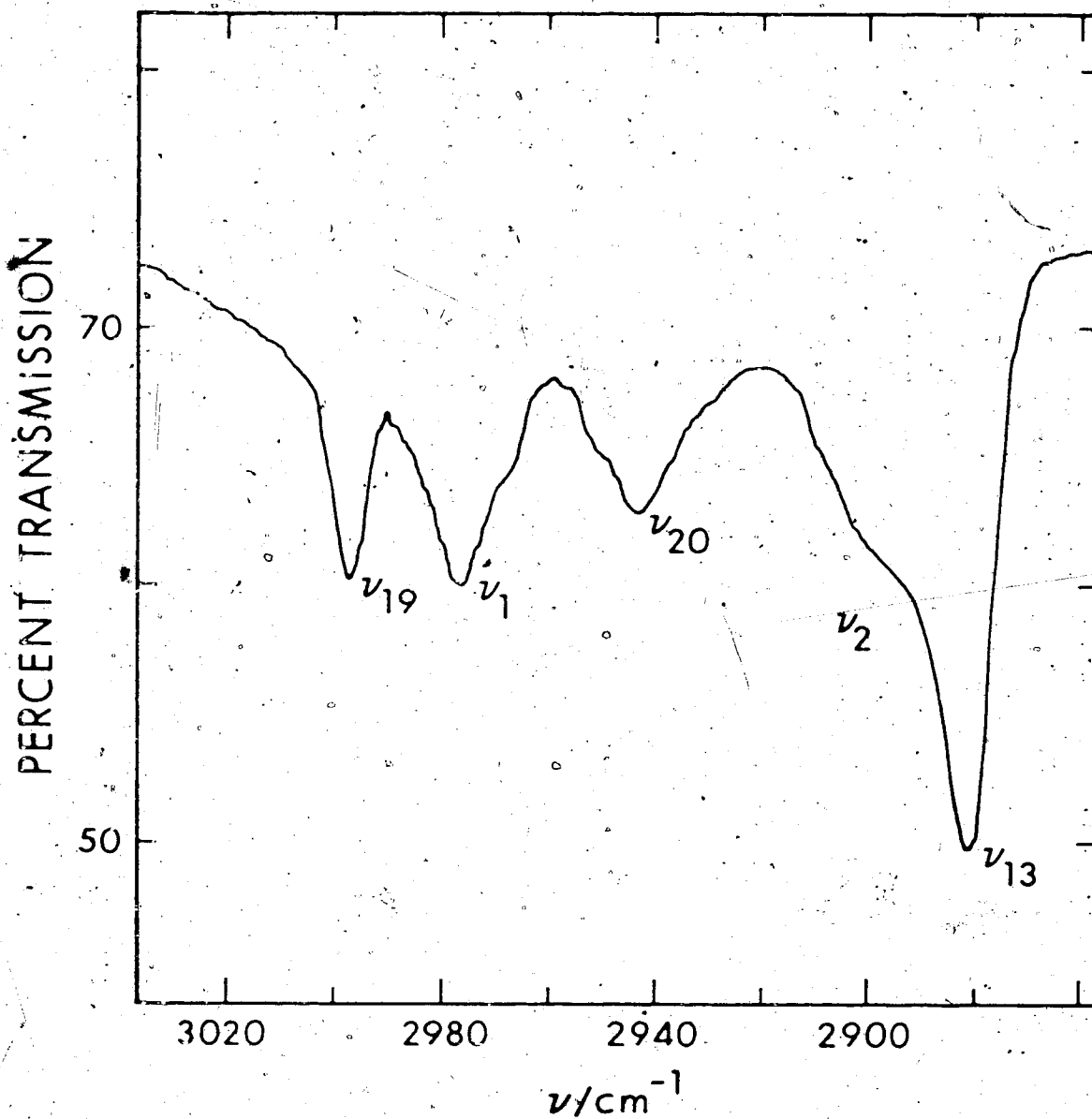


Fig. 4.5. The C-H stretching bands of structure II trimethylene oxide deuterate dispersed in a mulling agent at 95°K.

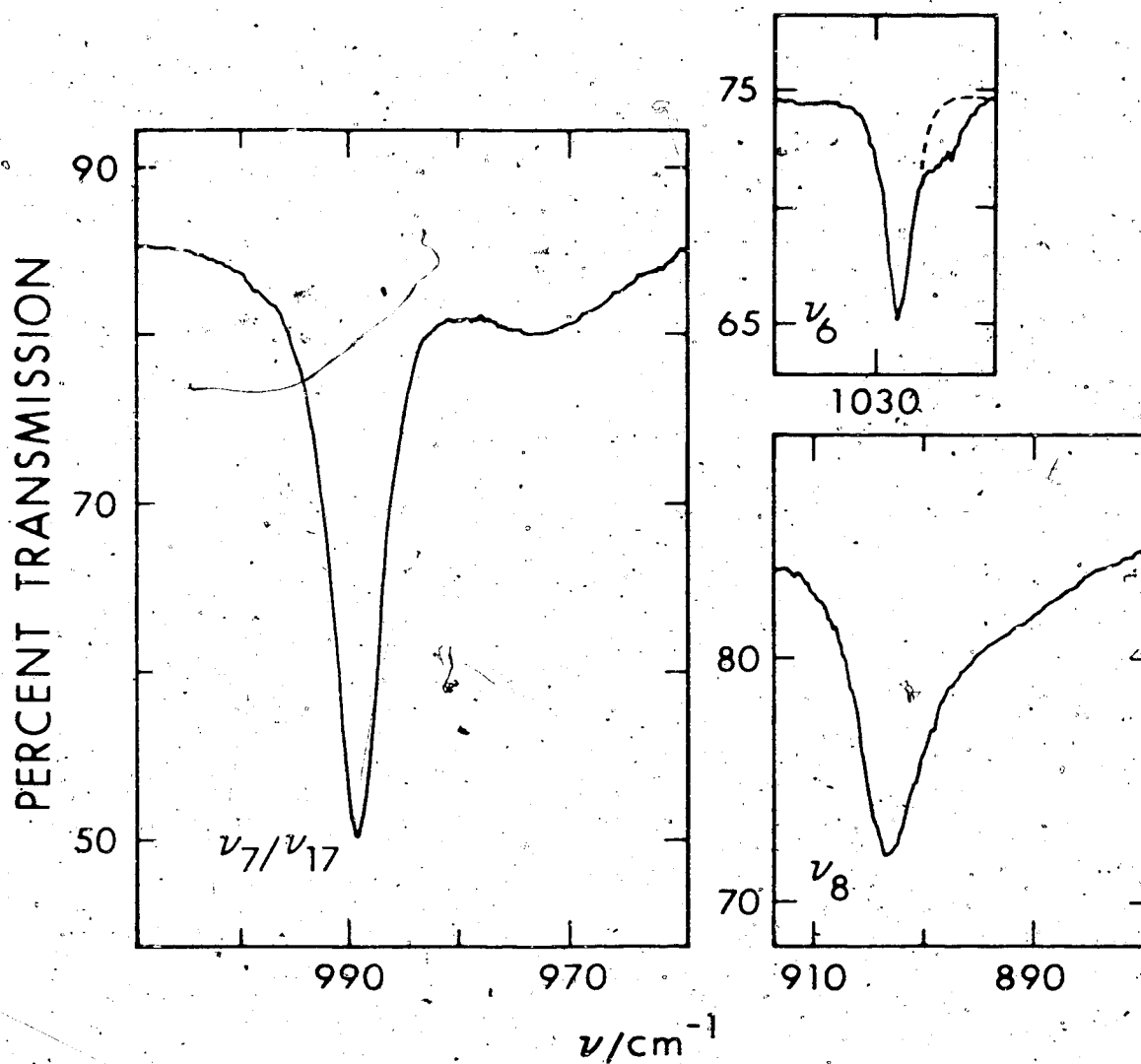


Fig. 4.6. The ring bands of structure II trimethylene oxide deuterate dispersed in a mulling agent at 95°K. The dashed line approximates the true contour of the  $\nu_6$  band.

spectrum (Fig. 4.6). The spurious absorption at about  $1025\text{ cm}^{-1}$  has already been discussed in Section 3.1 and the dashed line in Fig. 4.6 is believed to be a good approximation to the contour of the  $\nu_6$  band after this spurious absorption has been removed. The band due to  $\nu_6$  is the sharpest guest band in the spectrum, with a half-width of  $3\text{ cm}^{-1}$  (Fig. 4.6). The strongest guest band,  $\nu_7/\nu_{17}$ , is at  $989.5\text{ cm}^{-1}$  in the deuterate spectrum (Fig. 4.6) and at  $990.9\text{ cm}^{-1}$  in the hydrate spectrum (Fig. 4.2). The frequency difference is marginally significant. The half-width of this band in the spectrum of the deuterate is  $4.5\text{ cm}^{-1}$ . The broad band,  $\nu_7/\nu_{17}$ , located at  $973.2\text{ cm}^{-1}$  (Fig. 4.6) in the deuterate spectrum occurs as a shoulder at about  $974\text{ cm}^{-1}$  (Fig. 4.2), in the hydrate spectrum. The specific assignment of these two absorptions will be discussed in Chapter 5. The absorption by  $\nu_{18}$  appeared only as a poorly defined shoulder at  $938\text{ cm}^{-1}$  in the spectrum of the hydrate, and was partially obscured by propane absorption in the spectrum of the deuterate (Fig. 4.2). The frequency of this band is, therefore, only poorly known (Table 4.1), and its half-width is unknown. The only remaining guest band,  $\nu_8$ , observed during this study is clearly seen at  $903.1\text{ cm}^{-1}$  in the spectrum of the deuterate (Fig. 4.6). The half-width of this band is  $8.6\text{ cm}^{-1}$ , however the low frequency tail, which is due to reflection effects, probably affects the half-width. This strong band

is present as a shoulder at about  $900\text{ cm}^{-1}$  in the hydrate spectrum (Fig. 4.2):

The bands due to  $\nu_4$ ,  $\nu_{14}$ ,  $\nu_{10}$ ,  $\nu_{11}$ ,  $\nu_{22}$ ,  $\nu_{12}$  and  $\nu_{23}$ , which were observed in the spectra of the structure I hydrate, were not observed in the spectra of TMO hydrate II and deuterate II. This was undoubtedly because of their inherently weak nature, although it is possible that the band due to  $\nu_4/\nu_{14}$  might have been observed if spectra of Freon 13 mulls containing a very large amount of hydrate sample had been recorded. The only guest feature that was seen in the spectra of the structure II hydrate that was not seen in the spectra of the structure I hydrate was the shoulder at  $2895\text{ cm}^{-1}$  (Fig. 4.5) assigned to  $\nu_2$ . The reason that this feature was not seen in the spectra of the structure I hydrate was undoubtedly due to the presence of the very strong  $\nu_{13}$  fundamental, which was only  $7\text{ cm}^{-1}$  to low frequency of  $\nu_2$  in the spectrum of TMO deuterate I, whereas it was  $14\text{ cm}^{-1}$  to low frequency of  $\nu_2$  in the spectrum of TMO deuterate II.

#### 4.3 Mid-Infrared Spectra of Structure II Trimethylene Oxide Hydrate in Pellets

TMO hydrate II and TMO deuterate II were pressed into potassium bromide pellets by the method described in Section 2.5. Comparison of the mid-infrared spectra of these pellets with the spectra of TMO hydrate and deuterate I showed that substantial conversion to TMO hydrate I and

TMO deuterate I had taken place. Clear evidence of this conversion is shown in Fig. 4.7. For the case of  $\nu_7/\nu_{17}$ , the middle curve, labelled I + II, was obtained from a potassium bromide pellet at 95°K prepared from TMO deuterate II, the top curve was obtained from a mull of TMO deuterate I at 95°K, and the bottom curve was obtained from a mull of TMO deuterate II at 95°K. Comparison of these curves clearly shows that the pellet from which the middle curve was obtained, contained a mixture of TMO deuterate I and TMO deuterate II. The high frequency bands of the middle and bottom curves both occur at  $989.5 \text{ cm}^{-1}$ , and the low frequency bands of the middle and top curves occur at  $978.1$  and  $976.8 \text{ cm}^{-1}$  respectively. This small difference in frequency is due to the difference in the refractive index of the mulling agent and the pelleting agent. (Tables 3.1 and 3.2).

Further evidence of this conversion was supplied by the band due to  $\nu_6$ . This band in the three spectra from which the  $\nu_7/\nu_{17}$  bands were taken is shown in Fig. 4.7, where they are presented in the same order as the  $\nu_7/\nu_{17}$  bands. The dashed lines exclude the spurious  $1025 \text{ cm}^{-1}$  absorption. The conversion of the sample from which the middle curve was obtained to TMO deuterate I is even more clearly indicated by the  $\nu_6$  bands than by the  $\nu_7/\nu_{17}$  bands. The high frequency band in the middle curve and the band in the top curve both occur at  $1033.6 \text{ cm}^{-1}$ . The low



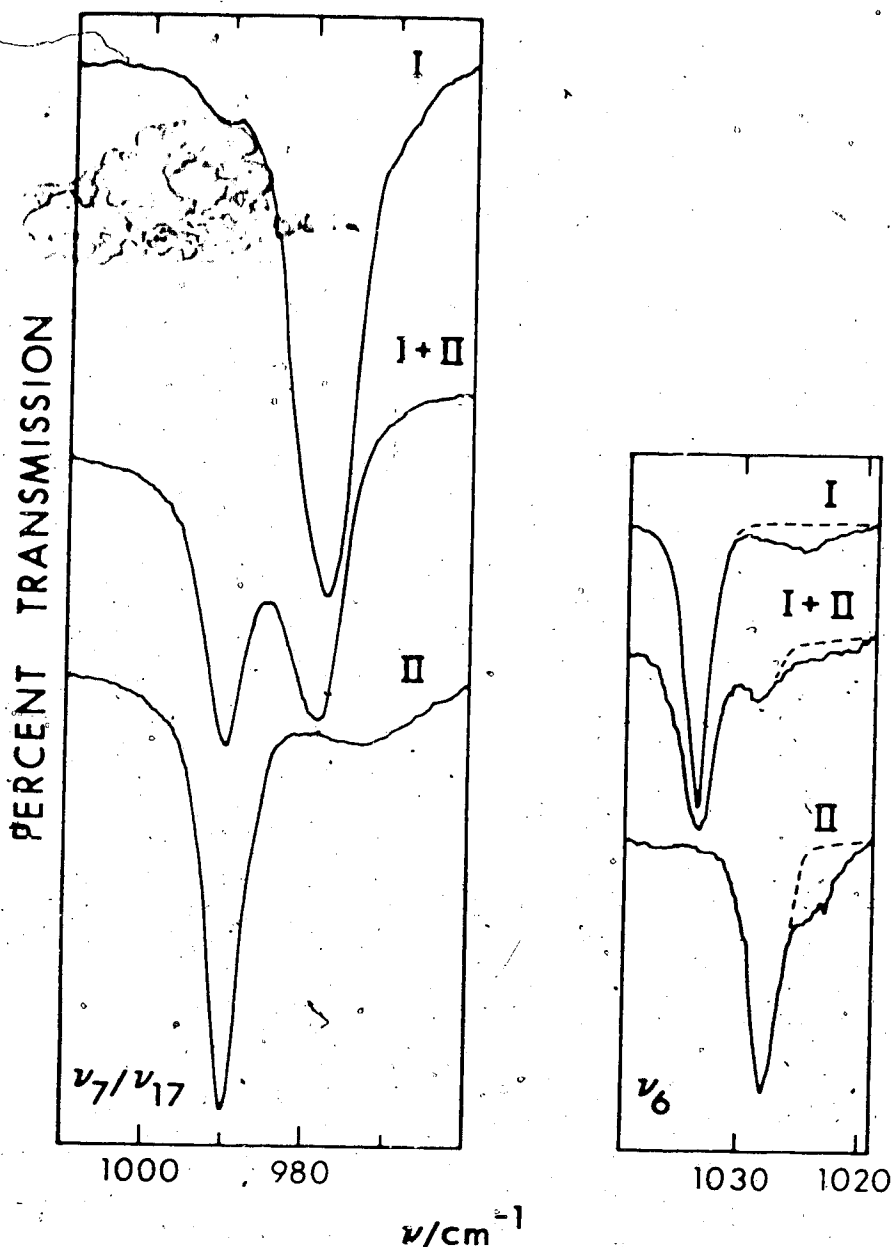


Fig. 4.7. The  $\nu_7/\nu_{17}$  and  $\nu_6$  bands of: (I), structure I trimethylene oxide deuterate in a mull; (I + II), a KBr pellet made from structure II trimethylene oxide deuterate; (II), structure II trimethylene oxide deuterate in a mull; all at 95°K. The maximum and minimum percent transmissions of the bands are: left box- I, 90, 20; I + II, 93, 63; II, 89, 50; right box- I, 88, 63; I + II, 87, 81; II, 77, 64. The dashed lines approximate the true contours of the  $\nu_6$  bands.

frequency band in the middle curve and the band in the bottom curve occur at  $1029.0$  and  $1028.1 \text{ cm}^{-1}$  respectively.

Further evidence of this conversion was sought by subjecting a sample of TMO deuterate II to a typical pellet pressurisation procedure without any potassium bromide. The resultant pellet was ground to a powder and the X-ray powder diffraction photograph and the infrared spectrum of the powder milled with propylene were recorded. Both of these techniques showed that the powder was still unconverted TMO deuterate II. The reason why TMO hydrate and deuterate II convert to the structure I analogues when potassium bromide is present, but do not convert in the absence of potassium bromide, is not clear.

#### 4.4 Powder X-ray Diffraction Pattern of Structure II.

##### Trimethylene Oxide Deuterate

Powder X-ray diffraction photographs were taken of all of the samples of TMO hydrate II and TMO deuterate II to ensure that the correct phase had been obtained and to determine its purity. The two best photographs of different samples of TMO deuterate II were each measured twice to determine the diffraction parameters. These measurements were treated in the same way as those of TMO hydrate I, as described in detail in Section 3.4, to yield four values for the unit cell parameter. These were averaged to yield the value  $17.06 \pm 0.02 \text{ \AA}$ , where  $0.02 \text{ \AA}$  indicates the range of the values obtained.

The powder X-ray diffraction pattern of TMO deuterate II at  $100 \pm 20^\circ\text{K}$  is given in Table 4.2. The calculated intensities were determined from the structure factors of the double hydrate of hydrogen sulphide and tetrahydrofuran at  $-20^\circ\text{C}$  (37), and the observed intensities were measured as peak heights on a microdensitometer trace. The calculated  $2\theta$  and  $d$  values were obtained by supplying the programme 2THETA with the averaged unit cell parameter given above and the wavelength of the  $\text{Cu K}_\alpha$  X-ray radiation (1.5418 Å). The observed  $2\theta$  and  $d$  values are averages of the four sets of values obtained from the photographs.

The intensities of the X-ray diffraction lines of TMO deuterate II are significantly different from those calculated from the structure factors of the double hydrate of tetrahydrofuran and hydrogen sulphide (37). This is to be expected because the strongly scattering sulphur atom contributes to all of the reflections except for 220, 422, 442, 620, 642, 644, 660 and 822 of the double hydrate. The patterns of the two compounds are, however, sufficiently similar to indicate unambiguously that they have the same crystal structure apart from the guest molecules. The calculated  $d$  spacing and  $2\theta$  value of the 311 reflection are outside the standard deviations of the observed values. This is almost certainly due to inaccurate measurements resulting from the poor resolution of this line and that of the strong 222 reflection. The calculated  $d$  spacings and

Table 4.2

Powder X-ray Diffraction Pattern of  
Structure II Trimethylene Oxide  
Deuterate at 100 ± 20°K

Index	Calculated <sup>a</sup>	Calculated <sup>b, d</sup>	Calculated <sup>b, d</sup>	Observed <sup>a, d</sup>	Observed <sup>c, d</sup>	Observed Intensity
	Intensity	d Spacing (Å)	2θ (°)	2θ (°)	d Spacing (Å)	
111	9	9.850	8.98*	8.99 (4)	9.81 (4)	39
220	3	6.032	14.69			
311	3	5.144	17.24	17.09 (5)	5.18 (1)	34
222	15	4.925	18.01	18.02 (7)	4.92 (2)	90
400	24	4.265	20.83	20.80 (8)	4.27 (2)	80
331	17	3.914	22.72	22.68 (6)	3.92 (1)	78
422	38	3.482	25.58	25.56 (6)	3.485 (8)	70
333 } 511 }	100	3.283	27.16	27.12 (6)	3.289 (8)	100
440	42	3.016	29.62	29.56 (6)	3.022 (6)	49
531	95	2.884	31.01	31.00 (6)	2.885 (6)	97
442	5	2.843	31.46			
620	14	2.697	33.21	33.22 (8)	2.697 (7)	22
523	5	2.602	34.47	34.45 (8)	2.603 (6)	17
622	2	2.572	34.88			
444	2	2.462	36.49			
551 } 711 }	2	2.389	37.65	37.65 (7)	2.390 (5)	9
642	0.2	2.280	39.53			
553 } 731 }	6	2.221	40.62			18 <sup>e</sup>
800 <sup>f</sup>	0.5	2.132	42.38	42.35 (3)	2.134 (1)	4
733	10	2.084	43.42	43.45 (3)	2.083 (2)	22
644	0.3	2.069	43.76			
660 } 822 }	33	2.011	45.09	45.09 (3)	2.011 (1)	52
555 } 751 }	11	1.970	46.08	46.08 (3)	1.970 (1)	22
662	0.3	1.957	46.40			
840	5	1.907	47.68	47.57 (2)	1.912 (1)	6
753 } 911 }	11	1.873	48.62	48.70 (5)	1.870 (2)	12

a) Integrated intensity for flat-plate camera, calculated from  $I = [(1 + \cos^2 2\theta) \sin^2 \theta \cos \theta] \cos^2 \theta p F^2$ , where  $p$  is the multiplicity factor and  $F$  is the observed structure factor from reference 37.

b) Calculated from  $a = 17.06$  Å.

c) The average of four measurements. The figure in parenthesis is the standard deviation in the last figure.

d)  $\text{Cu K}_\alpha$  radiation, wavelength = 1.5418 Å.

e) This line was broad and diffuse, so accurate values of  $2\theta$  and  $d$  spacing could not be obtained.

f) Only 2 values for the observed  $2\theta$  and  $d$  spacing were averaged for this line.

20 values of the 840 and 753/911 reflections are also outside the standard deviations of the observed values. In these cases, the reason is probably the poor definition of these broad, diffuse lines.

## Chapter Five. Discussion of the Mid-Infrared Spectra of Structure I and II Trimethylene Oxide Hydrates

### 5.1 General

The absorption by the water molecules of TMO hydrates I and II is discussed in Section 5.2. The assignment was given in Chapters 3 and 4 and needs no further discussion, but the absorption is discussed in relation to the structures of the hydrates and the guest-host interactions. A few comments are made in Section 5.3.2 about the assignment of the trimethylene oxide modes given in Chapters 3 and 4. The differences between the guest frequencies of the two hydrates and those of gaseous trimethylene oxide are discussed in Section 5.3.3 in relation to the interactions between the guest molecule and the two host lattices. Some comments on the temperature dependence of the guest absorptions of the structure I hydrate are also made in Section 5.3.3.

### 5.2 Absorption by the Water Molecules

The absorption by water molecules in the clathrate hydrates and the disordered ice phases at mid-infrared frequencies is not well understood. This has been outlined in Chapter 1 and will be discussed in more detail later. However at this point it should be noted that a contributing factor to the lack of understanding is the coupling between like vibrations of different water molecules. This

occurs between vibrations of different molecules that have the same frequency in the gas phase, for example, between the  $\nu_1$  vibrations in different molecules, because of the dynamic intermolecular forces.

Empirically and theoretically, it is much easier to interpret the bands due to vibrations that do not couple in this way. Such bands are the isolated O-H and O-D stretching bands of HDO molecules isolated among  $D_2O$  and  $H_2O$  molecules, respectively (Section 1.3). Empirically, one sharp band is seen for each O---O bond length in the ordered phases, or a single band with a half-width of less than about  $120 \text{ cm}^{-1}$  is seen for the disordered phases, compared to bands with half-widths of the order of  $300 \text{ cm}^{-1}$  seen for the dynamically coupled vibrations  $\nu_{OH}(H_2O)$  and  $\nu_{OD}(D_2O)$ . Theoretically, the isolated O-H and O-D stretching bands reflect only the static, site effects in the crystal, that is, one absorption frequency occurs for every truly non-equivalent, not diffraction non-equivalent for the disordered phases, O---O bond. Thus the discussion of the water bands will commence with a discussion of the isolated stretching bands.

The isolated O-D stretching band seen in the spectra of mulls of TMO hydrate I is a single band at  $2439 \text{ cm}^{-1}$  with a half-width of  $95 \text{ cm}^{-1}$  at  $95^\circ\text{K}$ . It is believed to be less influenced by anharmonic effects than the  $\nu_{OH}(HDO)$  band of TMO deuterate I, so the following discussion

is based on the  $\nu_{OD}$  (HDO) band as is common practice (48). The isolated O-D stretching band of the structure 'II hydrate is a single band at  $2419 \text{ cm}^{-1}$  with a half-width of  $75 \text{ cm}^{-1}$  at  $95^\circ\text{K}$ . The existence of single, fairly broad bands is consistent with the orientational disorder and the consequent variation in the lengths of diffraction-equivalent O---O bonds that are known to exist in these solids.

The  $\nu_{OD}$  (HDO) band observed for TMO hydrate I is identical, apart from its frequency, with the  $\nu_{OD}$  (HDO) band observed for ethylene oxide, structure I hydrate, so the only effect of the guest molecule on these bands is to shift the frequency. It has been shown previously (48) that an empirical correlation exists between the  $\nu_{OD}$  (HDO) frequency and the weighted mean of the diffraction-determined O---O bond lengths for the various disordered ice phases and ethylene oxide hydrate. For the sake of the present discussion, the partially ordered ice phases, V and VI, will be considered as disordered. The different  $\nu_{OD}$  (HDO) frequencies of the structure I hydrates of trimethylene oxide and ethylene oxide and the different  $\nu_{OD}$  (HDO) frequencies of the structure I and structure II hydrates of trimethylene oxide are probably, therefore, due to the different O---O bond lengths which exist in these compounds.

The diffraction-determined O---O bond lengths in the solids of interest at about  $100^\circ\text{K}$  are presented in Table



5.1, together with their percentage occurrence in the crystal, weighted mean value and the range of the bond lengths. The bond lengths in ices Ih, Ic, V and VI at about 100°K were taken from reference 10. The bond lengths in ethylene oxide hydrate I at -25°C were determined (36) by a single crystal X-ray diffraction study in which the cubic unit cell parameter was found to be 12.03 Å. The bond lengths in the structure I hydrates of trimethylene oxide, ethylene oxide and cyclopropane (see later) at 100°K were obtained from those in ethylene oxide hydrate I at -25°C by scaling, using the values 11.95 (Section 3.4), 11.89 (46) and 11.98 (46) Å, respectively, of the unit cell parameters at about 100°K determined by powder X-ray diffraction. The O---O bond lengths in the double, structure II hydrate of hydrogen sulphide and tetrahydrofuran have been determined at -20°C, at which temperature the cubic unit cell parameter is 17.31 Å (37). The bond lengths in TMO deuterate II at 100°K were found by scaling the bond lengths in reference 37 using the value 17.06 Å found for the unit cell parameter of TMO deuterate II at 100°K from powder X-ray diffraction (Section 4.4).

A plot of the frequencies of the  $\nu_{OD}$  (HDO) bands of ices Ih (32), Ic (27), V (28), VI (20), ethylene oxide hydrate I (48), TMO hydrate I (Table 3.1) and II (Table 4.1) against the weighted mean O---O bond lengths in these phases is shown in Fig. 5.1. Also included are the frequencies

Table 5.1

Structural Data for Ices Ih, Ic, V, VI,  
 Structure I Hydrates of Trimethylene Oxide,  
 Ethylene Oxide and Cyclopropane and the Structure II  
 Hydrate of Trimethylene Oxide at 100°K

Compound	O---O Bond Length <sup>a, b</sup>	Percent Occurrence	Weighted Mean <sup>a</sup>	Range <sup>a, c</sup>
Ice Ih	2.743	100	2.743	0.0
Ice Ic	2.743	100	2.743	0.0
Ice V	2.766	21	2.797	0.021
	2.781	15		
	2.782	15		
	2.798	15		
	2.819	15		
	2.820	15		
Ice VI	2.867	4	2.813	0.022
	2.773	10		
	2.786	10		
	2.801	20		
	2.803	20		
	2.840	40		

Compound	O---O Bond Length <sup>a, b</sup>	Percent Occurrence	Weighted Mean <sup>a</sup>	Range <sup>a, c</sup>
Ethylene Oxide Hydrate	2.735	9	2.761	0.025
	2.745	52		
	2.778	26		
	2.810	13		
TMO hydrate (I)	2.749	9	2.775	0.021
	2.759	52		
	2.792	26		
	2.824	13		
Cyclopropane Hydrate I	2.754	9	2.781	0.023
	2.764	52		
	2.799	26		
	2.832	13		
TMO hydrate (II)	2.727	12	2.748	0.014
	2.736	35		
	2.756	35		
	2.771	18		

a) In A.

b) The values were obtained as described in the text.

c) The range of bond lengths was calculated as the weighted mean of the magnitudes of the deviations from the weighted mean.

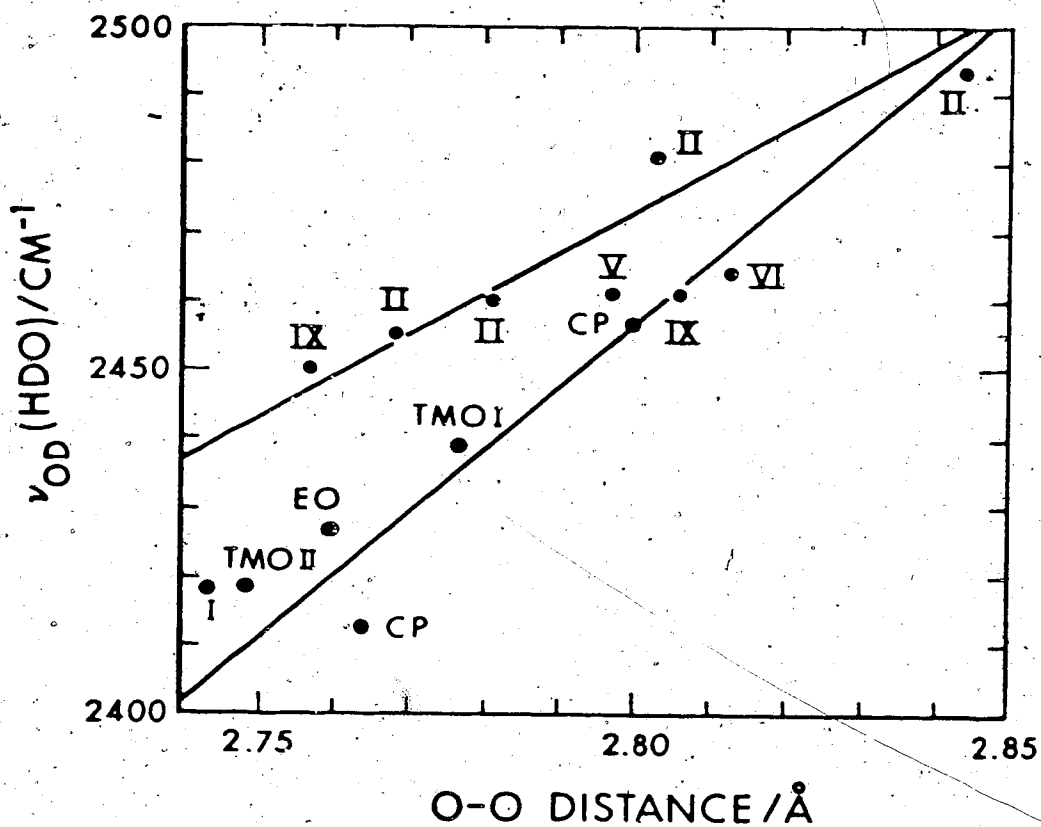


Fig. 5.1. Graph of  $\nu_{OD}(\text{HDO})$  versus the O---O distance for ordered phases and cyclopropane (CP) hydrate or weighted mean O---O distance for the disordered phases. The Roman numerals refer to the ice phases and TMO I, EO and TMO II refer to the structure I hydrates of trimethylene oxide and ethylene oxide, and the structure II hydrate of trimethylene oxide respectively.

of the  $\nu_{OD}$  (HDO) bands of the ordered ices II (28) and IX (28) plotted against the corresponding O---O bond lengths (10). The points for ices Ih and Ic essentially coincide and are simply labelled I in Fig. 5.1. The graph is that given in reference 48 and discussed in Section 1.3, with the data for TMO hydrates I and II (and cyclopropane hydrate I which is discussed below) added.

It is clear that the data for the two hydrates of trimethylene oxide correlate well with those for the other phases formed by orientationally disordered water molecules. Thus the similarity in the frequencies of the  $\nu_{OD}$  (HDO) bands of TMO hydrate II and ice Ih is due to these compounds having the same weighted mean O---O bond length, whereas the large difference in the half-widths of these bands, which are 75 and 20  $\text{cm}^{-1}$  respectively, is due to the large difference in the range of O---O bond lengths in the two compounds. From a comparison of the weighted mean O---O bond lengths of TMO hydrate I, TMO hydrate II and ice Ih (Table 5.1), it can be concluded that the average strength of the hydrogen bonds in TMO hydrate II is very similar to that in ice Ih, whereas the average strength of the hydrogen bonds in TMO hydrate I is smaller. Also it is clear that the different  $\nu_{OD}$  (HDO) frequencies of the structure I hydrates of trimethylene oxide and ethylene oxide are due to the difference in the O---O bond lengths in the two structures. Thus the only detectable effect of changing

the guest molecule from ethylene oxide to trimethylene oxide is the expansion of the 14-hedral structure I cage by the latter molecule. A comparison of the largest van der Waals diameters of ethylene oxide, 5.2 Å, and trimethylene oxide, 6.2 Å, with the mean free diameter of 5.8 Å for the 14-hedral cage (39) allows this expansion to be understood. The 16-hedral cage of the structure II hydrate is not expanded by trimethylene oxide because its mean free diameter is 6.6 Å.

It should be mentioned that a further effect of the guest molecule on the water lattice has been identified from a comparison of the results for the structure I hydrates of ethylene oxide, trimethylene oxide and cyclopropane (30). The  $\nu_{OD}$ (HDO) bands in the spectra of ethylene oxide hydrate (48) and TMO hydrate I (Fig. 3.8) are essentially featureless, whereas the  $\nu_{OD}$ (HDO) absorption by cyclopropane hydrate I (30) consists of two partially resolved peaks at 2457 and 2416  $\text{cm}^{-1}$ , with relative intensities of approximately 1:2. The frequency correlation (Fig. 5.1) and the relative intensities indicate that the more intense band is due to the 52 percent of the O---O bonds that are 2.764 Å long (Table 5.1) and the weaker band is due to the 26 percent of the O---O bonds that are 2.799 Å long. The points marked CP in Fig. 5.1 have been plotted on this basis. Cyclopropane hydrate I is isostructural with TMO hydrate I and its unit cell parameter at

100°K is almost the same as that of TMO hydrate I, so it is clear that steric effects are not the only effect that the guest molecule has on the water lattice.

An obvious difference between cyclopropane and trimethylene oxide is the absence of a permanent dipole moment in cyclopropane. Thus it is possible that the dipole moment of the trimethylene oxide molecule perturbs the O---O bond lengths to an extent sufficient to prevent the  $\nu_{OD}$  (HDO) bands due to the diffraction non-equivalent bond lengths from being resolved. In order to obtain an estimate of this perturbation, a simple calculation was carried out.

A point dipole due to the guest molecule was placed at the center of a 14-hedral cage of the structure I hydrate, collinear with the axis of the O---O bond under consideration, which lies (Section 1.3) on a radial line extending from the center of the cage. The dipole moment of the guest molecule was assumed to interact with the dipole moment of the nearest water molecule in the O---O bond. The dipole moment of this water molecule was taken to be 2.6 Debyes (90) and to be oriented at an angle of 70.5° to the radial line (Section 1.3). The interaction energy between these two dipoles is given by (23),

$$U(r) = \frac{\mu_{H_2O} \cdot \mu_g}{r^3} - \frac{3(\mu_{H_2O} \cdot \underline{r})(\mu_g \cdot \underline{r})}{r^5}$$

where  $U(r)$  is the electrostatic interaction energy in ergs,

$\mu_{H_2O}$  and  $\mu_g$  are the point dipoles of the water and guest molecules in esu cm respectively, and  $r$  is the distance between the point dipoles in cm. The force acting between the two dipoles was found by taking the negative derivative of the interaction energy with respect to the distance between the point dipoles. The extension of the O---O bond resulting from this force was calculated by substituting the values of the force constant for stretching the O---O bond, namely  $0.18 \times 10^5$  dynes per cm (18), and the force into the expression for Hooke's law. The dipole moment of trimethylene oxide is 1.93 Debyes (85) and the distance between the point dipoles was taken to be the mean radius of the 14-hedral cage, 4.3 Å (Table 1.5), and an extension of the O---O bond of about 0.02 Å was calculated. The same value for the extension can be calculated by a quite different approach, which involves the interaction energy between the electric field produced at an O---O bond in the cage wall by the guest dipole and the dipole moment derivative with respect to stretching the O---O bond (91).

These calculations involve some gross approximations, such as the point dipole assumption and the fact that only one O---O bond is considered, but they undoubtedly establish the order of magnitude of the variations in the O---O bond lengths caused by the dipole moment of a guest molecule. The exact length of each bond must depend on the relative orientations of the bond and the guest dipole, so this



effect is expected to broaden the range of the actual lengths of a set of diffraction-equivalent bonds by about  $\pm 0.02$  Å beyond the range which exists, in cyclopropane hydrate I and the disordered ices, due to the orientational disorder of the water molecules.

It is now possible to rationalise the difference between the  $\nu_{OD}$  (HDO) band of cyclopropane hydrate I and those of the structure I hydrates of ethylene oxide and trimethylene oxide. Inspection of Table 5.1 shows that if a range of  $\pm 0.02$  Å is placed on each O---O bond length in ethylene oxide hydrate and TMO hydrate I, a continuous range of O---O bond lengths results, which is compatible with the failure to resolve distinct features on the  $\nu_{OD}$  (HDO) band. It is also possible to rationalise the fact that two bands were observed for the  $\nu_{OD}$  (HDO) absorption of cyclopropane hydrate I. Ice Ih has a single O---O bond length, as determined by X-ray diffraction, and its  $\nu_{OD}$  (HDO) band has a half-width of about  $20 \text{ cm}^{-1}$ . Bertie and Whalley (27) have argued that this half-width is a result of the small range of O---O bond lengths caused by the orientational disorder of the water molecules. Thus the half-width of about  $20 \text{ cm}^{-1}$  observed for this band can be taken as characteristic of a single diffraction-determined O---O bond length perturbed only by the orientational disorder of the water molecules. If a half-width of  $20 \text{ cm}^{-1}$  is associated with each of the two bands

observed for the  $\nu_{OD}$  (HDO) absorption of cyclopropane hydrate I, which are separated by  $41 \text{ cm}^{-1}$ , then the experimental resolution of these features is qualitatively explained.

A single, featureless band was obtained for the  $\nu_{OD}$  (HDO) absorption in the spectrum of TMO hydrate II (Fig. 4.4). Inspection of Table 5.1 shows that the largest separation between O---O bond lengths occurs between the two most abundant O---O bonds and has a value of  $0.022 \text{ \AA}$ , which corresponds to a frequency separation of about  $20 \text{ cm}^{-1}$ . If the influence of the trimethylene oxide dipole moment on the bond lengths is neglected, the band due to each of these O---O bonds is expected to have a half-width of  $20 \text{ cm}^{-1}$  so, even in this case, two bands are not expected to be resolved. The estimated perturbation of the O---O bond lengths by the guest dipole moment is about  $0.01 \text{ \AA}$  for TMO hydrate II, so if this is taken into account, the single featureless band seen for  $\nu_{OD}$  (HDO) of TMO hydrate II can certainly be understood.

Bertie and Othen (48) argued that an approximate correlation exists between the half-width of an unresolved  $\nu_{OD}$  (HDO) band of a disordered phase and the range of O---O bond lengths in the phase. The half-widths of the  $\nu_{OD}$  (HDO) bands of TMO hydrate I, TMO hydrate II and ice Ih are 95, 75 and  $20 \text{ cm}^{-1}$  and the ranges are 0.021, 0.014 and  $0.0 \text{ \AA}$ , respectively, so a rough correlation exists in these cases. However, if an attempt is made to extend the

correlation to ice V, ice VI and ethylene oxide hydrate, whose half-widths are 80, 70 and 80  $\text{cm}^{-1}$  and ranges are 0.021, 0.022 and 0.025  $\text{\AA}$ , respectively, it is seen to meet with only partial success.

A detailed discussion of the bands due to the  $\text{H}_2\text{O}$  and  $\text{D}_2\text{O}$  vibrations of the various disordered ice phases and ethylene oxide hydrate at  $100^\circ\text{K}$  has been given elsewhere (13), and since the corresponding bands of TMO hydrate I and TMO hydrate II are very similar to those already discussed (13), only a brief discussion will be given here.

The disorder in the hydrogen atom positions causes all of the water vibrations of the crystal to be active in both the infrared and Raman spectra. Further, the vibrations of different water molecules interact in the crystal to produce broad bands of vibrational frequencies from each molecular degree of freedom. Consequently, the vibrations of the water molecules in these disordered crystals absorb over the entire mid-infrared frequency range (31). The absorption corresponds to the density of vibrational states curve multiplied by an intensity distribution function which describes the average intensity of absorption by the vibrations at each frequency. Thus the frequencies of maximum absorption need not correspond to the maxima in the density of vibrational states curve and it is not known, at present, to which vibrations they

do correspond. It is evident, therefore, that a detailed assignment of these bands and an interpretation of their differences is impossible at present, so it is only possible to attempt to qualitatively establish the effect of structural differences on the spectrum.

A comparison of the  $\nu_{OH}(H_2O)$  bands in the spectra of ices Ih (27), Ic (27), V (28) and VI (20), ethylene oxide hydrate (48), TMO hydrate I (Fig. 3.6) and TMO hydrate II (Fig. 4.3), all at 100°K, reveals that the frequency of maximum absorption is always between 3200 and 3250  $cm^{-1}$  and that every band has a pronounced high frequency shoulder in the region 3300 to 3450  $cm^{-1}$ . The bands of ices Ih and Ic, the structure I hydrates and TMO hydrate II are strikingly similar because they all also have a pronounced low frequency shoulder near 3100  $cm^{-1}$ . Further, there is an approximate correlation between the frequency of maximum absorption and the weighted mean O---O bond length. The weighted mean O---O bond lengths of ice Ih, ice Ic, TMO hydrate II and ethylene oxide hydrate lie between 2.74 and 2.761 Å (Table 5.1) and the frequencies of their absorption maxima lie between 3220 and 3224  $cm^{-1}$ ; the weighted mean O---O bond length of TMO hydrate I is 2.78 Å and the frequency of its absorption maximum is 3231  $cm^{-1}$  and, finally, the weighted mean O---O bond lengths of ice V and ice VI lie between 2.80 and 2.81 Å and the frequencies of their absorption maxima are 3245 and

3250  $\text{cm}^{-1}$ , respectively, although their precision of measurement is only  $\pm 30$  and  $\pm 15 \text{ cm}^{-1}$  respectively.

The bands due to  $\nu_{\text{OD}}(\text{D}_2\text{O})$  show more detail than those of  $\nu_{\text{OH}}(\text{H}_2\text{O})$  and this is usually attributed to the larger anharmonic effects associated with the  $\text{H}_2\text{O}$  bands than with the  $\text{D}_2\text{O}$  bands (27). The extra detail does show considerable variation with structure. However, for ices Ih and Ic (27), the structure I hydrates of ethylene oxide (48) and trimethylene oxide (Fig. 3.6), and TMO hydrate II (Fig. 4.3), the variations are really only in the relative intensities of the features. All four structures show strong  $\nu_{\text{OD}}(\text{D}_2\text{O})$  features at about 2330, 2425 and 2485  $\text{cm}^{-1}$ , with the middle one being the most intense feature in all cases. The  $\nu_{\text{OD}}(\text{D}_2\text{O})$  bands of TMO hydrate I and ethylene oxide hydrate I are essentially identical and differ from those of ices Ih and Ic only by having the high frequency shoulder more pronounced than the low frequency one, whereas for ices Ih and Ic the reverse is the case and some fine details were resolved between the low frequency shoulder and the peak. For TMO hydrate II (Fig. 4.3), the low frequency feature is resolved as a distinct peak, and the central feature is considerably sharper than in the other phases.

A correlation between the frequency of the band maximum and the weighted mean O---O bond length is only slightly evident for the  $\nu_{\text{OD}}(\text{D}_2\text{O})$  bands. The frequencies are

2428  $\text{cm}^{-1}$  for TMO hydrate I (Table 3.1), 2425  $\text{cm}^{-1}$  for ices Ih and Ic (27) and ethylene oxide hydrate I (48), and 2423  $\text{cm}^{-1}$  for TMO hydrate II (Table 4.1). Thus the band of TMO hydrate I is marginally to high frequency of those of ices Ih and Ic and ethylene oxide hydrate I, whereas the band of TMO hydrate II is marginally to low frequency. The  $\nu_{\text{OD}}(\text{D}_2\text{O})$  bands of ices V and VI are similar to each other (28, 20) in that they both consist of two partially resolved bands, and are quite different from those of the other phases. The frequencies are 2385 and 2525  $\text{cm}^{-1}$  for ice V (28) and 2390 and 2545  $\text{cm}^{-1}$  for ice VI (20), so the frequencies of the centers of the bands are 2455 and 2467  $\text{cm}^{-1}$ . The centers of the bands of the other phases

correspond approximately to the frequencies of maximum absorption cited above, so the longer weighted mean O---O bond lengths in ices V and VI are reflected in the higher frequencies of the centers of their  $\nu_{\text{OD}}(\text{D}_2\text{O})$  absorption.

A comparison of the  $\nu_{\text{R}}(\text{H}_2\text{O})$  bands of ices Ih and Ic (27), TMO hydrate I (Fig. 3.4), ethylene oxide hydrate I (48) and TMO hydrate II (Fig. 4.2) reveals that the intense, high frequency parts of the bands are essentially the same except for the features due to the guest vibrations in the spectra of the hydrates. The  $\nu_{\text{R}}(\text{H}_2\text{O})$  bands are less well defined than the  $\nu_{\text{R}}(\text{D}_2\text{O})$  bands, so the latter will be discussed. The intense high frequency parts of the  $\nu_{\text{R}}(\text{D}_2\text{O})$  bands of ices Ih and Ic (27), TMO hydrate I

(Fig. 3.7), ethylene oxide hydrate I (48) and TMO hydrate II (Fig. 4.2) are identical. The corresponding bands of ices V (28) and VI (20) are very similar to each other in that both have a peak, at 490 and 500  $\text{cm}^{-1}$ , respectively, and a pronounced high frequency shoulder of almost the same intensity as the peak, at 590  $\text{cm}^{-1}$  in both cases; they are, however, very different from the bands of ices Ih and Ic and the hydrates. An approximate correlation between the frequency of maximum absorption and the weighted mean O---O bond lengths also holds for the  $\nu_R(\text{D}_2\text{O})$  bands. The frequencies of maximum absorption of the  $\nu_R(\text{D}_2\text{O})$  bands of ices Ih (27) and Ic (27) and TMO hydrate II (Table 4.1) lie between 630 and 640  $\text{cm}^{-1}$  and the weighted mean O---O bond lengths are essentially equal at 2.745 Å; the corresponding values for ethylene oxide hydrate I are 620  $\text{cm}^{-1}$  (48) and 2.77 Å, for TMO hydrate I 611  $\text{cm}^{-1}$  (Table 3.1) and 2.78 Å, for ice V 540  $\text{cm}^{-1}$  (28) and 2.80 Å, and for ice VI 545  $\text{cm}^{-1}$  (20) and 2.81 Å. The frequencies quoted for ices V and VI are the average of the two, almost equally intense, features.

The correlations between the frequencies of maximum absorption, or the band centers, and the weighted mean O---O bond lengths noted above are, of course, totally consistent with trends long recognised (87) for vibrations of hydrogen-bonded compounds. These are that X-H stretching vibrations of X-H---Y groups decrease their frequency as

X---Y distance decreases and the hydrogen bond becomes stronger while vibrations, like the  $\nu_R$  vibrations, that are pure translations, rotations or hindered rotations in the absence of a hydrogen bond increase their frequency as the hydrogen bond becomes stronger and its length decreases. But the empirical correlations carry further implications for the disordered phases being presently discussed. It is to be expected that the average vibrational frequency in the band due to coupled O-H or O-D stretching vibrations will decrease, and the average  $\nu_R$  frequency will increase, as the hydrogen bond length decreases. However, no such general comments can be made a priori about the shapes of, or frequencies of the maxima

---

in, the density of vibrational states curves for compounds with different crystal structures. The existence of the empirical correlations, and the similar band shapes, discussed above for ice Ih, ice Ic, ethylene oxide hydrate I, TMO hydrate I and TMO hydrate II do, however, strongly indicate that the shapes of the density of vibrational states curves and the intensity distribution functions are insensitive to the number of water molecules per unit cell and also to the number of crystallographically non-equivalent water molecules, since these two parameters vary widely in the structures discussed (13). This perhaps indicates that the vibrations are quite localised, because of the disorder, and are therefore not sensitive to the



long-range structure of the solid. It is particularly noteworthy that it is known from the spectra (27) that the  $\nu_R$  vibrations of normal ice Ih extend from about 1050 to 400  $\text{cm}^{-1}$  and that specific heat data (92, 93) can be represented by assuming a single  $\nu_R$  frequency of 620  $\text{cm}^{-1}$ . Thus, the intense  $\nu_R$  absorption occurs only in the high frequency part of the band in ice Ih (27) and it is clear from the data presented above and the spectra presented in the references that the same situation is true for the other structures, ices Ic (27), V (28), VI (20), ethylene oxide hydrate I (48), trimethylene oxide hydrate I (Fig. 3.4) and trimethylene oxide hydrate II (Fig. 4.2).

---

The bands in the mid-infrared spectrum of ice V are consistently similar to those of ice VI, and quite different from those of ices Ih and Ic and the hydrates. There is also a pronounced structural difference between these phases, in that the O---O---O angles in ice V and VI deviate markedly from the tetrahedral angle, while those in the other phases are much closer to tetrahedral. In ice VI the O---O---O angles range from 75.8 to 128.6° (10) and in ice V they range from 86 to 135° (10), while in ices Ih and Ic they are essentially tetrahedral (10) and in the structure I and II hydrates, the angles are all within 5° of tetrahedral except for 9 percent of them which are 124.3° in the structure I hydrates (36) and 6 percent of them which are 119.9° in the structure II hydrate (37).

The large deviations from the tetrahedral angle in ices V and VI are related to the partial order in the orientations of their water molecules at low temperatures (10) and, although it is not definitely known to be true, the infrared spectra of ices V (28) and VI (20) were presumably of the partially ordered phases, now called V and VI' (10). Thus the differences between the spectra of ices V and VI and those of ices Ih and Ic and the hydrates may arise from the quite different ranges of bond angles in the two sets of phases.

Only the temperature dependence of the absorption by the water molecules remains to be discussed. The bands due to  $\nu_{OD}(D_2O)$ ,  $\nu_R(D_2O)$ ,  $\nu_{OH}(HDO)$  and  $\nu_{OD}(HDO)$  of TMO hydrate I between 175 and 62°K are shown in Figs. 3.15 and 3.16 and the frequencies, half-widths and peak heights are given in Tables 3.3 and 3.4. The general trends which were observed for a decrease in temperature were a decrease in the frequencies of the  $\nu_{OD}(D_2O)$ ,  $\nu_{OH}(HDO)$  and  $\nu_{OD}(HDO)$  bands and an increase in the frequency of the  $\nu_R(D_2O)$  band, a decrease in the half-widths of all of the bands and an increase in the peak heights of all of the bands. Also, all of the bands became less symmetric at lower temperatures due to the increased resolution of shoulders.

Three probable sources of the temperature dependence of the absorption by the water molecules of TMO hydrate I

can be envisaged. Firstly, a reduction in the number of transitions originating in excited vibrational states accompanies a decrease in temperature, due to a decrease in the population of these states. Thus the contributions of hot bands and difference bands to the observed absorption bands decrease with decreasing temperature. Secondly, the contraction of the unit cell with decreasing temperature shifts the vibrational frequencies in the direction favoured by stronger intermolecular forces. Thus, for ice Ih, the lattice modes shift to high frequency (18) and the O-H stretching modes shift to low frequency (32, 94) as the temperature is lowered. Thirdly, it is known from dielectric relaxation and n.m.r. studies (Section 1.3)

---

that the trimethylene oxide molecules in the 14-hedral cages of the structure I hydrate increasingly adopt preferred orientations corresponding to the potential energy minima which exist within the cage, as the temperature is lowered. Thus the perturbation of the O---O bond lengths due to steric effects and to the interaction with the dipole moment of the trimethylene oxide molecule should become more discrete with decreasing temperature.

It should be noted that the first two effects apply to all solids and have the same theoretical basis in the anharmonicity of the intermolecular force field. It is, however, common practice to separate them in the way described, which corresponds to a 'temperature dependent

harmonic force field' approximation, because of the complexity of a fully anharmonic treatment of the absorption by a solid (18, 95). In this approximation, frequency shifts are considered to arise from the second effect and changes in half-width, peak height, and the resolution of the features are considered to arise from the first effect.

The trends observed for TMO hydrate I can clearly be attributed to the first two effects, but it is of interest to see whether any influence of the preferred orientations of the trimethylene oxide molecules in the 14-hedral cages can be detected. It is necessary, therefore, to compare the temperature dependence of the water absorption of TMO hydrate I with that of a phase of ice. The only ice phases whose spectra have been reported as a function of temperature are ice Ih (32) and a phase made by condensing water vapor at  $-180^{\circ}\text{C}$  and annealing the film, which was, without substantiation, called ice Ic (96).

Ford and Falk (32) observed a decrease in the frequency of the  $\nu_{\text{OD}}$ (HDO) band of ice Ih of  $7\text{ cm}^{-1}$  between 175 and  $75^{\circ}\text{K}$ , whereas Hardin and Harvey (96) observed a corresponding decrease of  $11\text{ cm}^{-1}$  for the  $\nu_{\text{OD}}$ (HDO) band of ice Ic. A decrease of  $5\text{ cm}^{-1}$  was found for the frequency of the  $\nu_{\text{OD}}$ (HDO) band of TMO hydrate I (Table 3.4) between 175 and  $80^{\circ}\text{K}$ . The decreases in the half-widths of the  $\nu_{\text{OD}}$ (HDO)

bands in the temperature ranges noted above for ice Ih (32), ice Ic (96) and TMO hydrate I (Table 3.4) were 5, 3 and  $7 \text{ cm}^{-1}$  respectively.

If it is assumed that the change in the weighted mean O---O bond length of TMO hydrate I between 175 and  $80^\circ\text{K}$  is about the same as that for ethylene oxide hydrate, then a value of  $0.006 \text{ \AA}$  is obtained (97). The slope of the line which relates the  $\nu_{\text{OD}}$  (HDO) frequency to O---O distance in different phases (Fig. 5.1) is  $910 \text{ cm}^{-1} \text{ \AA}^{-1}$  for the disordered phases, and Whalley (98) has noted that for ice Ih, the change in frequency per unit change in bond length when the bond is changed by varying the temperature is about twice that found when the bond length is changed by varying the phase. Thus the temperature induced change of  $0.006 \text{ \AA}$  corresponds to a frequency shift of 5.5 to  $11 \text{ cm}^{-1}$  depending on whether Whalley's factor of 2 is applicable to the hydrate. It is clear that the frequency shift observed for TMO hydrate I is sufficiently close to those of ices Ih and Ic, and to that predicted from the assumed change in bond length, to prevent any influence of a preferential orientation of the guest molecules from being inferred.

The change in the half-width of the  $\nu_{\text{OD}}$  of TMO hydrate I is comparable to that of  $\nu_{\text{OD}}$  so no influence of any preferential orientation of the guest molecules can be inferred. The increased resolution of

shoulders seen with decreasing temperature for the  $\nu_{OD}$  (HDO) band of TMO hydrate I must be at least partly due to the diminishing contributions from hot transitions, so it is clearly desirable to draw structural conclusions only from spectra recorded at the lowest possible temperatures, since at higher temperatures the results may be misleading. It is not possible to decide if the increased structure on the band at low temperatures is partly a result of preferential orientation of the guest molecules until results are available of a study of the temperature dependence of the spectrum of a clathrate hydrate, in which no such effect is expected.

---

### 5.3 Absorption by the Guest Molecules

#### 5.3.1 General

The discussion of the assignment of the guest absorption of TMO hydrate I and TMO hydrate II in Section 5.3.2 is based on spectra obtained from samples held at 95°K. In Section 5.3.3, the absorption by the guest molecules of TMO hydrate I and TMO hydrate II at 95°K and as a function of temperature is discussed.

In most cases, the guest absorption bands of TMO hydrate I and TMO deuterate I have the same frequencies (Table 3.1). The same is true for TMO hydrate II and TMO deuterate II for the cases in which the bands can be measured accurately (Table 4.1). This is evidence that the frequencies show essentially no effect of coupling

between the guest and water vibrations, and can be taken as those of a guest molecule in the static environment of the cage. This is consistent with the fairly sharp bands seen for the guest absorptions of the deuterates (Fig. 3.5 and 4.2). Clear evidence of interaction between the guest and host vibrations does exist for those guest vibrations which overlap the  $\nu_{OH}(H_2O)$  and  $\nu_R(H_2O)$  bands, since the corresponding absorptions are reduced from sharp bands in the spectra of the deuterates (Figs. 3.5 and 4.2) to much less intense bands or shoulders in the spectra of the hydrates (Figs. 3.4 and 4.2). Thus in Sections 5.3.2 and 5.3.3, the guest bands in the spectra of the deuterates (Tables 3.1 and 4.1, Figs. 3.5 and 4.2) are discussed, in the approximation that they are characteristic of trimethylene oxide molecules in a static cage environment. The only exception is the  $\nu_{23}(B_2)$  band which was only seen in the spectrum of TMO hydrate I.

The guest bands showed no splittings, even when recorded at  $0.5\text{ cm}^{-1}$  resolution, although occasionally they were accompanied by shoulders. Splittings could have arisen from non-equivalent sites occupied by the guest molecules and from the coupling of the vibrations of neighbouring guest molecules. However the disorder of the water molecules in the hydrate structures leads to a range of fields at crystallographically equivalent sites, which means that although all of the 14- or 16-hedral cages

are crystallographically equivalent, the sites in these cages occupied by the guest molecules are not equivalent, because of the disorder of the water molecules. Thus a continuous range of sites and therefore frequencies for each guest vibration can be expected, rather than a small number of discrete frequencies. Also, in general, the guest molecules are not oriented in an ordered manner with respect to each other, as is the case for the molecules of an ordered solid, so the coupling of the vibrations of nearest neighbour guest molecules should, again, lead to a continuous range of frequencies, rather than the separable frequencies often observed for ordered solids. Thus, on these grounds, the lack of splitting observed

---

for the guest absorptions of TMO hydrates I and II can be understood; however the same arguments apply equally to ethylene oxide hydrate, yet the absorption by the ring breathing mode of the guest is split, for reasons presently unknown, into two components separated by  $2 \text{ cm}^{-1}$  (48). Thus it is not trivial to point out that no such splitting was seen for any of the trimethylene oxide absorptions.

This lack of splitting is even more significant for TMO hydrate I when it is realised that the spectra obtained at  $95^\circ\text{K}$  were of samples that had fully passed through Davidson's ordering transition (Section 1.3.3), which is believed to involve the parallel ordering of the guest dipoles along the  $\bar{4}$  axes of the 14-hedral structure I cages.



The conclusion that these samples had fully passed through the transition was reached in the following way. A time of several weeks, that is a typical time that the samples spent under liquid nitrogen before use, was substituted into Davidson's (54) expression for the time dependence of the dielectric loss of samples quenched to, and held at, liquid nitrogen temperature, and the resulting value for the dielectric loss was essentially equal to the equilibrium value. Clearly the change that occurs on passing through Davidson's transition does not result in the splitting of the absorptions by the vibrations of the guest molecules.

Thus the only information provided by the absorption of the guest molecules of TMO hydrates I and II is the frequencies and half-widths of the bands and their temperature dependences. These properties are discussed in the remainder of this section.

### 5.3.2 Discussion of the Assignment of the Trimethylene Oxide Absorption

In order to interpret the frequencies of the trimethylene oxide vibrations in TMO hydrates I and II, it is necessary to establish the differences between the guest frequencies and those of the gas. Further, the assignments presented in Tables 3.1, 3.2 and 4.1 were obtained by comparing the vibrational frequencies of the guest molecule with those of the gas, liquid and solid

phases of trimethylene oxide, and a few comments are necessary because the comparison was not completely straightforward.

The assignment of  $\nu_1(A_1)$ ,  $\nu_4(A_1)$ ,  $\nu_5(A_1)$ ,  $\nu_6(A_1)$ ,  $\nu_8(A_1)$ ,  $\nu_9(A_2)$ ,  $\nu_{10}(A_2)$ ,  $\nu_{11}(A_2)$ ,  $\nu_{12}(A_2)$ ,  $\nu_{13}(B_1)$ ,  $\nu_{16}(B_1)$ ,  $\nu_{18}(B_1)$ ,  $\nu_{19}(B_2)$ ,  $\nu_{20}(B_2)$ ,  $\nu_{21}(B_2)$  and  $\nu_{22}(B_2)$  is clear from a comparison of the frequencies of the guest molecule (Tables 3.1, 3.2 and 4.1) with those of the gas, liquid and solid phases of trimethylene oxide (Table 1.8).

In Chapter 3, the band at about  $1457\text{ cm}^{-1}$  was assigned to both  $\nu_4(A_1)$  and  $\nu_{14}(B_1)$ . However it is likely to be due solely to  $\nu_4(A_1)$ , because it is probable that  $\nu_{14}(B_1)$  is at about  $1480\text{ cm}^{-1}$  in gaseous trimethylene oxide (80), and was not observed for the guest molecule. The guest absorptions due to  $\nu_3(A_1)$ ,  $\nu_{15}(B_1)$  and  $\nu_{24}(B_2)$  were also not observed. The band due to  $\nu_2(A_1)$  was undoubtedly merged with the intense band due to  $\nu_{13}(B_1)$  in the spectra of the structure I deuterate (Fig. 3.9), however it was observed as a shoulder in the spectra of the structure II deuterate (Fig. 4.5). The assignment of  $\nu_{23}(B_2)$  to a band at  $713.1\text{ cm}^{-1}$  in the spectrum of TMO hydrate I (Fig. 3.4 and Table 3.1) must be considered as uncertain since this mode has been assigned at  $784\text{ cm}^{-1}$  for the gas, and about  $730\text{ cm}^{-1}$  for the liquid and solid (Table 1.8).

The bands observed at  $1008$  and  $999\text{ cm}^{-1}$ ,  $967$  and  $961\text{ cm}^{-1}$ , and  $981\text{ cm}^{-1}$  in the spectra of the gas, solid

and liquid respectively were assigned to the ring deformations,  $\nu_7(A_1)$  and  $\nu_{17}(B_1)$  (Table 1.8). Lafferty (74) assigned  $\nu_7(A_1)$  to high frequency of  $\nu_{17}(B_1)$  in the infrared spectrum of the gas, although this assignment must be considered tentative because of the complicated nature of the band. No attempt was made to individually assign the bands in the spectrum of the solid (76). Thus the two absorptions by the guest between 950 and 1010  $\text{cm}^{-1}$  (Tables 3.1, 3.2 and 4.1) can be assigned to the two fundamentals  $\nu_7$  and  $\nu_{17}$ , but there is no evidence to indicate which has the higher frequency. Further, there appears to be no way to decide the correspondence between the two structure I bands at about 977 and 990  $\text{cm}^{-1}$  and the two structure II bands at about 973 and 990  $\text{cm}^{-1}$ . If this correspondence is based on an intensity relationship, the structure I bands at 976.8 and 989  $\text{cm}^{-1}$  (Fig. 3.11) correspond to the structure II bands at 989.5 and 973.2  $\text{cm}^{-1}$  (Fig. 4.6), in the order given. There are basically two objections to this correspondence. Firstly, the 12.7 and 15.8  $\text{cm}^{-1}$  frequency differences between structures I and II are very large compared to those for all the other guest modes, which are less than 10  $\text{cm}^{-1}$  except for the 21.1  $\text{cm}^{-1}$  shift of  $\nu_{19}(B_2)$  (Tables 3.1, 4.1). Secondly, the frequencies of all of the other guest vibrations of the structure II hydrate are either equal to or less than the corresponding structure I frequencies, in contrast to the

above correspondence which requires that the frequency of a structure II vibration be  $12.7 \text{ cm}^{-1}$  higher than that of the corresponding structure I vibration.

If the correspondence is based on a frequency relationship, then the structure I bands at  $976.8$  and  $989 \text{ cm}^{-1}$ , correspond to the structure II bands at  $973.2$  and  $989.5 \text{ cm}^{-1}$ , in the order given. The obvious objection to this correspondence is the large difference in intensity for the corresponding absorption in the two structures, in contrast to the similar intensities expected in the two structures and seen for the other guest absorptions. There is no obvious solution to this dilemma, so the specific assignments of  $\nu_7(A_1)$  and  $\nu_{17}(B_1)$  in the spectra of both structure I and structure II hydrates must remain uncertain.

A comparison of the fundamental frequencies of trimethylene oxide in the spectra of gaseous trimethylene oxide (Table 1.8), and TMO deuterates I and II (Tables 3.1 and 4.1) at  $95^\circ\text{K}$  is given in Table 5.2. The frequency of  $\nu_{23}(B_2)$  was taken from the spectrum of TMO hydrate I at  $95^\circ\text{K}$  (Table 3.1).

The differences between the vibrational frequencies of engaged and gaseous trimethylene oxide will be discussed in Section 5.3.3 in terms of the intermolecular interactions in the clathrate cages. It is, therefore, necessary to point out the instances of intramolecular Fermi resonance which may contribute to the frequency

Table 5.2

Comparison of the Fundamental Frequencies<sup>a</sup> of

Trimethylene Oxide in the Spectra of Gaseous

Trimethylene Oxide<sup>b</sup> and Structures I and IITrimethylene Oxide Deuterate<sup>c</sup>

Sym. No.	Description	$\nu_{\text{gas}}$	$\nu_{\text{I}}$	$\nu_{\text{II}}$	$\Delta\nu_{\text{I-gas}}$	$\Delta\nu_{\text{II-gas}}$	$\Delta\nu_{\text{I-II}}$
1	$\beta$ -CH <sub>2</sub> sym. str.	2979.0	2984.9 $\pm$ 1	2976.9 $\pm$ 1	+5.9	-2.1	+8.0
2	$\alpha$ -CH <sub>2</sub> sym. str.	2893.9	-	2895 $\pm$ 5	-	0	-
3	$\alpha$ -CH <sub>2</sub> def.	1505.0	-	-	-	-	-
4	$\beta$ -CH <sub>2</sub> def.	1452.0	1457.5 $\pm$ 1	-	+5.5	-	-
5	$\alpha$ -CH <sub>2</sub> wag	1343	1340 $\pm$ 2 <sup>d</sup>	-	-3	-	-
6	ring breathing	1030	1033.6 $\pm$ 0.5	1028.1 $\pm$ 0.5	+4	-2	+5.5
7	ring def.	1008/999	989/976.8	989.5/973.2	-----	uncertain	-----
8	ring def.	908	904.9 $\pm$ 0.5	903.1 $\pm$ 0.5	-3	-5	+1.8

Sym. No.	Description	$\nu_{\text{gas}}$	$\nu_{\text{I}}$	$\nu_{\text{II}}$	$\Delta\nu_{\text{I-gas}}$	$\Delta\nu_{\text{II-gas}}$	$\Delta\nu_{\text{I-II}}$
A <sub>2</sub>	9 $\alpha$ -CH <sub>2</sub> asym. str.	~2940 <sup>e</sup>	2930.9 ±1	2930 ?	-	-	-
	10 $\alpha$ -CH <sub>2</sub> twist	-	1283 ±2	-	-	-	-
	11 $\beta$ -CH <sub>2</sub> twist	-	1201.4 ±1	-	-	-	-
	12 $\alpha$ -CH <sub>2</sub> rock	-	831.2 ±1	-	-	-	-
B <sub>1</sub>	13 $\alpha$ -CH <sub>2</sub> sym. str.	2887.1	2887.7 ±1	2881.2 ±1	+0.6	-5.9	+6.5
	14 $\alpha$ -CH <sub>2</sub> def.	~1480	-	-	-	-	-
	15 $\alpha$ -CH <sub>2</sub> wag	-	-	-	-	-	-
	16 $\beta$ -CH <sub>2</sub> wag	1230	1244.8 ±0.5	1234 ±10	+15.	0	0
	17 ring def.	1008/999	989/976.8	989.5/973.2	-----uncertain-----		
	18 ring def.	940	940.9 ±1 <sup>o</sup>	937 ±5	+1	0	0
	19 $\beta$ -CH <sub>2</sub> asym. str.	3006.0	3018.4 ±1	2997.3 ±1	+12.4	-8.7	+21.1
	20 $\alpha$ -CH <sub>2</sub> asym. str.	2938.3 <sup>f</sup>	2946.1 ±1	2943 ±2	+7.8	+5	+3
B <sub>2</sub>	21 $\alpha$ -CH <sub>2</sub> twist	1136	1137.3 ±0.5	1137 ±5	+1	0	0
	22 $\alpha$ -CH <sub>2</sub> rock	839	846.0 ±1	-	+7	-	-
	23 $\beta$ -CH <sub>2</sub> rock	-	713.1 ±1 <sup>9</sup>	-	-	-	-
	24 ring puckering	53.5	-	-	-	-	-

- a) In cm<sup>-1</sup>.
- b) From Table 1.8.
- c) From Tables 3.1 and 4.1.
- d) From the spectrum of TMO deuterate I in a KBr pellet (Table 3.2).
- e) Estimated from its series of  $\Delta\nu_p = \pm 1$  combinations in the infrared spectrum of gaseous  $\beta$ -d<sub>2</sub> trimethylene oxide, (80).
- f) Estimate of  $\nu_{20}$  (B<sub>2</sub>) frequency unperturbed by Fermi resonance.
- g) Taken from the spectrum of TMO hydrate I (Table 3.1).

differences presented in Table 5.2..

Wieser et al (80) noted that the  $v = 1$  level of the  $\beta$ -CH<sub>2</sub> symmetric stretch,  $\nu_1(A_1)$ , is in Fermi resonance with the  $v = 2$  level of the  $\beta$ -CH<sub>2</sub> deformation,  $\nu_4(A_1)$ . The bands due to  $\nu_1(A_1)$  and  $2\nu_4(A_1)$  appear in the Raman spectrum of the gas at 2979.0 and 2890.3 cm<sup>-1</sup>, respectively, compared with 2904 cm<sup>-1</sup> for the calculated value of  $2\nu_4(A_1)$  ( $2 \times 1452$  cm<sup>-1</sup>). The frequency of  $\nu_4(A_1)$  in TMO deuterate I is 1457 cm<sup>-1</sup> (Tables 3.1 and 3.2), so the unperturbed frequency of the first overtone of the guest vibration is about 10 cm<sup>-1</sup> higher than that of the gas. Thus the Fermi resonance interaction with the unperturbed  $v = 1$  level of  $\nu_1(A_1)$  should be correspondingly larger in the structure I hydrate than in the gas, so the frequency of the  $\nu_1(A_1)$  vibration of the guest molecule may be raised from that of the gas by this intramolecular effect.

The second intramolecular Fermi resonance which may contribute to the frequency difference between the gaseous and encaged trimethylene oxide molecules affects the  $\alpha$ -CH<sub>2</sub> antisymmetric stretch,  $\nu_{20}(B_2)$ , which was observed (80) at 2957.3 cm<sup>-1</sup> in the spectrum of the gas (Table 1.8). Wieser et al (80) noted that  $\nu_{20}(B_2)$  is in Fermi resonance with the combination band  $\nu_2(A_1) + \nu_{24}(B_2)$ , where  $\nu_{24}(B_2)$  is the ring puckering mode. The unperturbed frequency of  $\nu_{20}(B_2)$  in the spectrum of the gas was estimated by Wieser et al (80) to be 2938.3 cm<sup>-1</sup>. Further, a strong band occurs



in the spectrum of liquid trimethylene oxide at  $2934\text{ cm}^{-1}$  which is almost certainly due to  $\nu_{20}(B_2)$ , so the Fermi resonance does not appear to occur in the molecules of the liquid. It is unlikely that the Fermi resonance interaction between  $\nu_{20}(B_2)$  and  $\nu_2(A_1) + \nu_{24}(B_2)$  occurs in the guest molecule in the 14-hedral cages of the structure I hydrate. This is because the guest molecules interact sufficiently strongly with the water molecules of the 14-hedral cages to stretch the cages (Section 5.2), so it is probable that the intermolecular forces perturb the vibrational energy levels of the ring puckering mode, thereby removing the upper state of the  $\nu_2(A_1) + \nu_{24}(B_2)$  transition from the vicinity of the upper state of  $\nu_{20}(B_2)$ . The intermolecular forces should be considerably smaller for a guest molecule in the larger 16-hedral cages of the structure II hydrate, but they may still influence the energy levels of  $\nu_{24}(B_2)$  and, hence, the magnitude of the Fermi resonance interaction.

In order to determine the effect of the intermolecular force on  $\nu_{24}(B_2)$ , an attempt has been made to locate the ring puckering fundamental of TMO hydrates I and II in the far-infrared region. Dr. Steven Jacobs, in this laboratory, has recorded the far-infrared spectra of TMO hydrates I and II at  $4^\circ\text{K}$ , but unfortunately the ring puckering fundamentals were not located. Thus, in the absence of more precise knowledge, the frequencies of the  $\nu_{20}(B_2)$  vibrations of the guests are compared with the unperturbed frequency of the

gas,  $2938.3 \text{ cm}^{-1}$ , since the corresponding vibration in the liquid is close to this frequency.

### 5.3.3 Vibrations of the Trimethylene Oxide Molecules

The absorption by the encaged trimethylene oxide molecules at  $95^\circ\text{K}$  is discussed first, followed by the effect of varying the temperature.

The fundamental frequencies of the guest vibrations of TMO deuterate I and TMO deuterate II at  $95^\circ\text{K}$ , together with those of gaseous trimethylene oxide, are listed in Table 5.2. Two trends are clearly evident from a comparison of these frequencies: firstly, the frequencies of the vibrations of the guest molecule in the 14-hedral cages of the structure I hydrate are higher than those of the gas and secondly, the frequencies of the vibrations of the guest molecule in the 16-hedral cages of the structure II hydrate are lower than those of the gas. In view of the uncertainty in some of the gas phase frequencies (Sections 1.4 and 5.3.2) it is useful to note the corollary of these trends, which is that the frequencies of the vibrations of the guest molecule in the 14-hedral cages are higher than those of the guest molecule in the 16-hedral cages.

The frequency of the ring deformation,  $\nu_8(A_1)$ , is one definite exception to the first trend and, possibly, the frequency of the  $\alpha\text{-CH}_2$  wag,  $\nu_5(A_1)$ , which was only seen in the spectra of pellets, is a second exception. The only

exception to the second trend is the frequency of the  $\alpha$ -CH<sub>2</sub> antisymmetric stretch,  $\nu_{20}^*(B_2)$ , and the appropriate frequency in the gas phase is uncertain for this vibration (Section 5.3.2). There are no exceptions to the corollary. In the following discussion the frequency of a guest vibration minus the frequency of the corresponding vibration in the gas phase is called the  $\Delta\nu$  value. The zero values of  $\Delta\nu$  in Table 5.2 arise from large uncertainties in the frequencies of the guest vibration, and have been excluded from the above trends and will be ignored in the remaining discussion.

The electric and geometric complexity of the clathrate hydrate cages (35) clearly does not permit meaningful, detailed calculations of guest-host interactions such as were made by Barnes (1) for diatomic molecules trapped in low temperature matrices (Section 1.2). It is, however, possible to interpret the observed trends in terms of the 'loose cage - tight cage' ideas of Pimentel and Charles (3), which were discussed in detail in Section 1.2. These are that the potential energy of interaction between the guest molecule and the cage is attractive at large guest-cage distances (Fig. 1.1) and results in negative  $\Delta\nu$  values, that is, the vibrational frequencies of the guest are lower than those of the gas, whereas at very short guest-cage distances (Fig. 1.1) the interaction energy is repulsive, and results in positive  $\Delta\nu$  values. The first situation

is referred to as a loose cage environment and the second as a tight cage environment (Fig. 1.1).

The positive  $\Delta v$  values of the guest vibrations in the 14-hedral cages indicate, therefore, that these vibrations are in a tight cage environment, whereas the negative  $\Delta v$  values for the guest vibrations in the 16-hedral cages indicate a loose cage environment. There is substantial evidence to support these indications and their corollary that the vibrations of a guest molecule in a 14-hedral cage experience a considerably tighter cage environment than those in a 16-hedral cage.

The tightness of fit of a trimethylene oxide molecule in the 14-hedral cage can be estimated by comparing the van der Waals diameters of the guest molecule with the free (Section 1.3) diameters of the cage. The van der Waals diameters of a trimethylene oxide molecule, defined as the distance between the oxygen atom and a  $\beta$ -hydrogen atom and the distance between two  $\alpha$ -hydrogen atoms, are 5.5 and 6.2 Å, respectively. The free diameters of the 14-hedral cage are about 5.03 Å parallel to the  $\bar{4}$  axis between the hexagonal faces, and 6.43  $\pm$  0.2 Å in the equatorial plane perpendicular to this axis; they were determined from the structural parameters of the cages of ethylene oxide hydrate (Fig. 1.2, Table 1.5), and from a knowledge of the ratio of the unit cell parameters of TMO hydrate I (Section 3.4) and ethylene oxide hydrate I.

(46). It is evident, then, that the guest molecule is severely restricted inside the cage, in agreement with the interpretation of the spectroscopic results. The free diameters of the 16-hedral cages are about  $6.53 \pm 0.1 \text{ \AA}$  as determined from the structural parameters of the cages of the double hydrate of hydrogen sulphide and tetrahydrofuran (Fig. 1.2, Table 1.5), appropriately scaled relative to the unit cell parameter of TMO hydrate II (Section 4.4). It is evident in this case that the guest molecule experiences considerable freedom inside the cage, in agreement with the interpretation of the spectroscopic results.

Evidence on the space available to a trimethylene oxide molecule compared to that available to other molecules in the 14- and 16-hedral cages can be obtained by a comparison of the unit cell parameters of TMO hydrate I and II with those of other hydrates. Davidson *et al.* (54) obtained a value of  $12.15 \text{ \AA}$  at  $-30^\circ\text{C}$  for the unit cell parameter of TMO hydrate I and noted that the unit cell parameters of 18 other structure I hydrates near  $0^\circ\text{C}$  range from 11.97 to  $12.14 \text{ \AA}$ . Thus the trimethylene oxide molecule is large enough to slightly expand the normal unit cell parameter. This is also clearly true at about  $100^\circ\text{K}$  (Section 5.2). Sargent and Calvert (55) obtained values of the unit cell parameters at  $135^\circ\text{K}$  of 17.170, 17.166, 17.161, 17.124, 17.118 and  $17.095 \text{ \AA}$  for the structure II

hydrates of tetrahydrofuran, 2,5-dihydrofuran, cyclobutanone, propylene oxide, 1,3-dioxolane and trimethylene oxide respectively. Thus TMO hydrate II has the smallest unit cell parameter which indicates that it fits easily inside the 16-hedral cage.

The degree of freedom experienced by the trimethylene oxide molecules in the 14- and 16-hedral cages is also reflected in the results obtained from dielectric relaxation studies of the guest molecule. Davidson et al (54) noted that the value of  $2.1 \text{ kcal mole}^{-1}$  obtained for the Arrhenius activation energy for the reorientation of the dipole of the trimethylene oxide molecule in the 14-hedral cages is "easily the largest so far found for the reorientation of a guest molecule in a clathrate hydrate". This severe hindrance to the reorientation of the trimethylene oxide molecule by the 14-hedral cage is also reflected in the reorientation rate of the dipole at  $51.5^\circ\text{K}$ , which is 1 kHz and is lower than those of any other guest molecule in a 14-hedral cage. Davidson et al (56) determined values of 0.41, 0.91, 1.02 and 1.44  $\text{kcal mole}^{-1}$  for the Arrhenius activation energies associated with the reorientation of ~~the~~ guest dipoles in the 16-hedral cages of the structure II hydrates of trimethylene oxide, tetrahydrofuran, acetone and cyclobutanone respectively. It is clear from the above values that a trimethylene oxide molecule experiences very little hindrance to reorientation.

in the 16-hedral cages. This is also reflected in the 1 kHz reorientation rate of the trimethylene oxide dipole at 12.1°K which is unusually fast for a guest molecule in the 16-hedral cage. In summary it can be said that there is substantial evidence that a trimethylene oxide molecule is severely restricted in a 14-hedral cage, whereas it experiences considerable freedom in a 16-hedral cage, and that these conclusions agree with the interpretation of the experimental frequency shifts in terms of Pimentel and Charles' (3) loose cage - tight cage ideas.

The interpretation of the experimental results can be extended by considering separately the  $\Delta\nu$  values for the  $\alpha$ -CH<sub>2</sub> and  $\beta$ -CH<sub>2</sub> vibrations of TMO deuterate I. The average of the available  $\Delta\nu$  values of the  $\alpha$ -CH<sub>2</sub> vibrations is +2.7 cm<sup>-1</sup>, whereas that for the  $\beta$ -CH<sub>2</sub> vibrations is +9.7 cm<sup>-1</sup>. These values can be interpreted in terms of Pimentel and Charles' (3) ideas to mean that, on average, a  $\beta$ -CH<sub>2</sub> vibration experiences a tighter cage environment than an  $\alpha$ -CH<sub>2</sub> vibration. This is consistent with the preferential orientation of the trimethylene oxide molecules in the 14-hedral cages proposed by Davidson et al. (54), as shown by the following argument. According to Davidson et al. (54), a trimethylene oxide molecule preferentially orients its dipolar axis along the  $\bar{4}$  axis of the 14-hedral cage, which passes through the middle of the two opposing hexagonal rings (Fig. 1.2). This axis is collinear with the

shortest free diameter of the cage, 5.03 Å. The van der Waals diameter of trimethylene oxide along its dipolar axis is 5.5 Å, so the oxygen atom and the  $\beta$ -CH<sub>2</sub> group must extend into the hexagonal rings to a certain extent. The oxygen atom can enter the hole in the middle of the hexagonal ring, whereas the  $\beta$ -CH<sub>2</sub> group cannot. The  $\beta$ -CH<sub>2</sub> group must, therefore, experience significant repulsive interactions with the cage. The cage diameter perpendicular to the  $\bar{4}$  axis is about 6.4 Å and it must accommodate the 6.2 Å diameter of the trimethylene oxide molecule between its two  $\alpha$ -CH<sub>2</sub> groups. Thus the two  $\alpha$ -CH<sub>2</sub> groups should experience smaller repulsive interactions with the cage than the  $\beta$ -CH<sub>2</sub> group. Thus, the interpretation of the average  $\Delta\nu$  values for the vibrations of the  $\alpha$ - and  $\beta$ -CH<sub>2</sub> groups by the ideas of Pimentel and Charles (3) provides further evidence in support of the preferential orientation proposed by Davidson et al (54). However, this evidence should be used with caution, because  $\Delta\nu$  values are not available for all of the vibrations of the  $\alpha$ - and  $\beta$ -CH<sub>2</sub> groups.

The vibrational frequencies of the structure I hydrate of ethylene oxide at 100°K have been determined by Bertie and Othen (13, 48), so it is of interest to see if they can be interpreted in terms of the ideas of Pimentel and Charles (3). The frequencies of gaseous and encaged ethylene oxide, which were taken from reference 13, are listed in Table 5.3, together with the  $\Delta\nu$  values.



Table 5.3

Comparison of the Fundamental  
Frequencies<sup>a</sup> of Ethylene Oxide in the  
Spectra of Gaseous Ethylene Oxide  
and the Structure I Hydrate of  
Ethylene Oxide

<u>Vibration</u>	<u>Symmetry</u>	<u><math>\nu_{\text{gas}}</math></u>	<u><math>\nu_{\text{hydrate}}</math></u>	<u><math>\Delta\nu^c</math></u>
C-H stretches	A <sub>1</sub>	3018	3008	-10
	A <sub>2</sub>	-	-	-
	B <sub>1</sub>	3005.9	2999	- 7
	B <sub>2</sub>	3065.2	3069	+ 4
	CH <sub>2</sub> deformations	A <sub>1</sub>	1498.4	1491
B <sub>1</sub>		1471.9	1467	- 5
Ring vibrations	A <sub>1</sub>	1270.3	1268 <sup>b</sup>	- 2
	A <sub>1</sub>	876.9	881	+ 4
	B <sub>1</sub>	872	872	0
	CH <sub>2</sub> wags	A <sub>1</sub>	1148	1122
B <sub>1</sub>		1150.8	1147	- 4
CH <sub>2</sub> rocks	A <sub>2</sub>	-	810	-
	B <sub>2</sub>	821.2	807	-14
CH <sub>2</sub> twists	A <sub>2</sub>	-	-	-
	B <sub>2</sub>	1142.0	1147	+ 5

a) In  $\text{cm}^{-1}$ . They were taken from: D. A. Othen, Ph.D thesis, University of Alberta, 1972.

b) The less intense component of this doublet is at  $1270 \text{ cm}^{-1}$ .

c)  $\Delta\nu = \nu_{\text{hydrate}} - \nu_{\text{gas}}$

Nine out of twelve of the  $\Delta\nu$  values are negative with the average value being  $-5.2 \text{ cm}^{-1}$ . This can be interpreted to mean that, on average, the vibrations of an ethylene oxide molecule in a 14-hedral cage are in a loose cage environment and, in particular, in a considerably looser cage environment than the vibrations of a trimethylene oxide molecule in a 14-hedral cage, since the average  $\Delta\nu$  value for the latter is  $+4.5 \text{ cm}^{-1}$ . There is ample evidence to indicate that this interpretation is correct.

The largest van der Waals diameter of ethylene oxide is  $5.2 \text{ \AA}$  between the methylene groups (42), which can be compared to the values of about  $6.3$  and  $4.8 \text{ \AA}$  for the free diameters of the 14-hedral cage of ethylene oxide hydrate. The corresponding comparison for TMO hydrate I was  $6.2 \text{ \AA}$  for the guest diameter compared to  $6.4$  and  $5.0 \text{ \AA}$  for the cage diameters. The unit cell parameters for ethylene oxide hydrate and TMO hydrate I are  $11.89$  (46) and  $11.95$  (Section 3.4)  $\text{\AA}$  respectively. The Arrhenius activation energy associated with the reorientation of the ethylene oxide dipole is  $1.4 \text{ kcal mole}^{-1}$  (99), compared to the value of  $2.1 \text{ kcal mole}^{-1}$  for TMO hydrate I (54), and the temperature at which the ethylene oxide dipole reorients at a rate of  $1 \text{ kHz}$  is  $28.0^\circ\text{K}$  compared to the value of  $51.5^\circ\text{K}$  for TMO hydrate I. All of the above evidence shows that an ethylene oxide molecule experiences much more freedom in a 14-hedral cage than does a trimethylene oxide molecule,

in agreement with the interpretation of the spectroscopic results using Pimentel and Charles' ideas.

It is apparent from the foregoing discussion that the 'loose cage - tight cage' ideas of Pimentel and Charles (3) can successfully interpret the frequencies obtained for trimethylene oxide and ethylene oxide molecules trapped in the cages of the clathrate hydrates. It is likely, therefore, that they can be applied to the guest vibrations in all of the structure I and II clathrate hydrates. It is noteworthy that the frequencies obtained for liquid trimethylene oxide (Table 1.8) and ethylene oxide (13) can be interpreted as reflecting a loose cage environment for the molecules in the liquid phase. Pimentel and Charles (3) noted that it is possible that the "liquid state at normal temperatures is, inherently, always a loose cage", since the thermal agitation will tend to counteract the development of significant repulsive forces. The average  $\Delta\nu$  value of +4.5, -3.1 and -5.2  $\text{cm}^{-1}$  for TMO hydrate I, TMO hydrate II and ethylene oxide hydrate I clearly reflect the general situation that trimethylene oxide molecules in the 14-hedral cages are severely restricted whereas trimethylene oxide molecules in the 16-hedral cages, and ethylene oxide molecules in the 14-hedral cages, are not. However, from the foregoing discussion of the non-spectroscopic evidence, it is clear that trimethylene oxide molecules in the 16-hedral cages experience more freedom.

than ethylene oxide molecules in the 14-hedral cages. The fact that the average  $\Delta\nu$  values are not consistent with this conclusion may be due to the errors associated with the average values or to the insensitivity of the loose cage-tight cage approach to the details of loose cage environments. It is noteworthy that this approach should be much more sensitive to the details of tight cage environments than to those of loose cage environments, since the attractive and repulsive interaction energies have  $r^{-6}$  and  $r^{-12}$  dependences respectively.

The half-widths of the guest bands in the spectra of potassium bromide pellets of TMO hydrate I and TMO deuterate I at 95°K given in Tables 3.5 and 3.6 are essentially the same as the corresponding half-widths in the spectra of mulls (Section 3.2.3). For TMO deuterate I, the half-widths range uniformly from 2.9 to 9.0  $\text{cm}^{-1}$ , apart from the 11.4 and 14.2  $\text{cm}^{-1}$  half-widths of the C-H stretching bands due to  $\nu_1(A_1)$  and  $\nu_{13}(B_1)$  respectively. The measurable half-widths of the guest bands in the spectra of TMO deuterate II (Section 4.2.2) are essentially the same as their structure I counterparts. The half-widths of the guest bands in the spectra of ethylene oxide deuterate I (48) are between 2 and 5  $\text{cm}^{-1}$ , except for the bands at 872 and 3069  $\text{cm}^{-1}$ , which have half-widths of 7 and 8  $\text{cm}^{-1}$  respectively.

The various factors that can contribute to the half-

widths of guest bands of clathrate hydrates can be summarised in the following way. First, the static interactions between the guest and the cage or other guest molecules, due to electrostatic, inductive, dispersive and repulsive forces (Section 1.2), differ from cage to cage because of the disorder and thereby broaden the guest bands. Second, the dynamic interactions due to fluctuations in the forces listed above during the vibrations of the guest and cage molecules cause the vibrations of the guest to couple with those of the water molecules, which broadens the guest bands because there is a continuum of water molecule vibrational frequencies and because of the disorder. Further, the dynamic guest-guest interactions broaden the bands because of the disorder. Third, the rapid, but hindered, reorientation of the guest molecule can cause broadening of the vibrational bands, as is observed in the spectra of liquids (100). Fourth, broadening results from intramolecular anharmonic effects of the guest molecule, and anharmonic coupling between the intramolecular vibrations of the guest molecule and its translational and rotational vibrations in the cage.

One type of dynamic interaction is between the transition dipoles of the guest and water vibrations or between those of the same vibration of different guest molecules. Broadening from this source should increase as the intensity of the guest or water absorption increases. This interaction is probably

responsible for the modification of the guest bands which are superimposed on the intense  $\nu_{OH}(H_2O)$  and  $\nu_R(H_2O)$  bands in the spectra of the hydrates (Figs. 3.4 and 4.2). In the spectra of the deuterates, however, no correlation between the breadth and the intensity of the guest bands is evident (Figs. 3.5 and 4.2), so this interaction cannot be the dominant cause of the breadth of these bands.

Trimethylene oxide experiences larger interactions with the 14-hedral cage than does ethylene oxide because of its larger size. Thus the broadening due to the static and dynamic interactions between the guest and the cage, except for the transition dipole interactions discussed above, should be greater for trimethylene oxide than for ethylene oxide. Thus this interaction can explain the larger half-widths observed for TMO deuterate I than for ethylene oxide deuterate I. However using this argument, the breadths of the guest bands of TMO deuterate II should be smaller than those of TMO deuterate I, and this is not the case. It must be concluded, therefore, that this source of broadening is not the dominant one.

An estimate of the contribution from rotational broadening can be made using the equation, which is based on the uncertainty principle,

$$\Delta\nu \approx \frac{2f}{c}$$

where  $\Delta\nu$  is the half-width due to reorientation in  $\text{cm}^{-1}$ ,  $f$  is the rotational relaxation frequency in Hz and  $c$  is the

speed of light in  $\text{cm sec}^{-1}$ . The rotational broadening contributions are 0.001, 0.2 and  $0.5 \text{ cm}^{-1}$  at about  $95^\circ\text{K}$  for TMO hydrate I, TMO hydrate II and ethylene oxide hydrate I respectively, as calculated from their respective re-orientation rates of  $1.2 \times 10^7$  (54),  $2.7 \times 10^9$  (56) and  $7 \times 10^9$  (99) Hz. Clearly, rotational broadening is not the dominant contribution.

Thus the breadth of the guest bands may be largely due to the fourth effect noted above, the anharmonic effects in the guest molecule and anharmonic interactions between the intramolecular vibrations of the guest and its rotational and translational vibrations in the cage, or may depend on all of the factors listed above in a complicated way.

The remaining discussion deals with the temperature dependence of the frequencies and half-widths of the guest bands of TMO hydrate I and TMO deuterate I between  $175$  and  $62^\circ\text{K}$  (Figs. 3.17 to 3.20, Tables 3.5 and 3.6). It should be noted first that no marked changes were observed in the frequencies, half-widths or band shapes on passing through Davidson's (54) ordering transition. Thus the mid-infrared spectra provide no evidence concerning this transition. With decreasing temperature, three out of four of the absorptions due to the  $\beta\text{-CH}_2$  vibrations shifted to high frequency, while three out of four of the absorptions due to the  $\alpha\text{-CH}_2$  vibrations and three out of four of the absorptions due to the ring vibrations shifted to low

frequency. The half-widths of all of the bands decreased and their peak heights increased on cooling. It is noteworthy that the temperature dependence observed for the clathrate hydrate was much larger than that observed for naphthalene (Section 3.3.1), a solid which may be considered as characteristic of ordered molecular crystals.

The temperature dependence of the frequencies of the guest bands must be due to the temperature dependence of the static and dynamic guest-cage (Section 1.2) and guest-guest interactions and to intramolecular anharmonic effects. Thus it is clear that the origin of the temperature dependence may be very complex. However it is noteworthy that the trends observed for the  $\alpha$ - and  $\beta$ -CH<sub>2</sub> vibrations are consistent with the increased occupancy of preferred orientations with decreasing temperature. The only comment that can be made about the temperature dependence of the half-widths of the guest bands concerns the broadening due to the rapid reorientation of the guest molecule. The reorientation rates of the guest molecule at 175 and 62°K can be calculated, using the Arrhenius rate law, from dielectric measurements (54) below about 90°K to be  $1.9 \times 10^9$  and  $3.2 \times 10^4$  Hz, respectively. The half-widths of the guest bands due to these reorientation rates are 0.13 and  $2.1 \times 10^{-1} \text{ cm}^{-1}$ , respectively, so the reorientation does not contribute significantly to the temperature dependence of the breadth.



## Chapter Six. Vibrational Spectra of Thiophosphoryl Chloride

### 6.1 Introduction

#### 6.1.1 General Introduction

The last chapter of this thesis is concerned with the vibrational spectroscopy of thiophosphoryl chloride,  $\text{SPCl}_3$ . The structure and vibrations of this molecule are presented in Section 6.1, together with a review of the previous studies on thiophosphoryl chloride which are relevant to this work, and a statement of the aims of this study. The experimental techniques which were used to record the mid- and far-infrared spectra and Raman spectra, are covered in Section 6.2. The results of these investigations are presented in Section 6.3. The normal coordinate analysis of Section 6.4 produces a reasonable force field for the molecule, and provides the isotope shifts which are necessary for the assignment of the spectra. The experimental results, together with those predicted by the normal coordinate analysis, are discussed in Section 6.5.

#### 6.1.2 The Structure and Vibrations of Thiophosphoryl Chloride

The molecular structure of gaseous thiophosphoryl chloride has been studied by electron diffraction (101 - 103) and microwave spectroscopy (104). The structural parameters used in this investigation were taken from the microwave results (104):  $r(\text{P}=\overset{\circ}{\text{S}}) = 1.85 \pm 0.02 \text{ \AA}$ ;  
 $r(\text{P}-\overset{\circ}{\text{Cl}}) = 2.02 \pm 0.01 \text{ \AA}$ ;  $\theta(\text{Cl}-\overset{\circ}{\text{P}}-\overset{\circ}{\text{Cl}}) = 100.5 \pm 1^\circ$ ;

$$\theta(\text{S=P-Cl}) = 117.4 \pm 1^\circ.$$

The molecular structure and the designation of the atoms is shown in Fig. 6.1. Only the six most abundant, naturally occurring isotopic forms of the molecule will be considered in this study. They are  $^{32}\text{SP}^{35}\text{Cl}_3$ ,  $^{32}\text{SP}^{35}\text{Cl}_2^{37}\text{Cl}$ ,  $^{32}\text{SP}^{35}\text{Cl}^{37}\text{Cl}_2$ ,  $^{32}\text{SP}^{37}\text{Cl}_3$ ,  $^{34}\text{SP}^{35}\text{Cl}_3$  and  $^{34}\text{SP}^{35}\text{Cl}_2^{37}\text{Cl}$ .

Thiophosphoryl chloride contains five atoms and therefore has nine normal modes of vibration. The molecules  $^{32}\text{SP}^{35}\text{Cl}_3$ ,  $^{32}\text{SP}^{37}\text{Cl}_3$  and  $^{34}\text{SP}^{35}\text{Cl}_3$  belong to the point group  $C_{3v}$  (104), and it can be shown by standard methods (105) that their normal coordinates form the representation:

$$3A_1 + 3E$$

Since vibrations of  $A_1$  and  $E$  symmetry are active in both infrared and Raman spectra under the point group  $C_{3v}$  (105), a total of six fundamental bands is expected. An approximate description of these modes is given in Table 6.1.

The numbering scheme follows Herzberg (106).

The molecules  $^{32}\text{SP}^{35}\text{Cl}_2^{37}\text{Cl}$ ,  $^{32}\text{SP}^{35}\text{Cl}^{37}\text{Cl}_2$  and  $^{34}\text{SP}^{35}\text{Cl}_2^{37}\text{Cl}$  belong to the point group  $C_s$ , and their normal coordinates form the representation:

$$6A' + 3A''$$

All nine vibrations are expected to be active in both infrared and Raman spectra (105). An approximate description of these modes is given in Table 6.2.

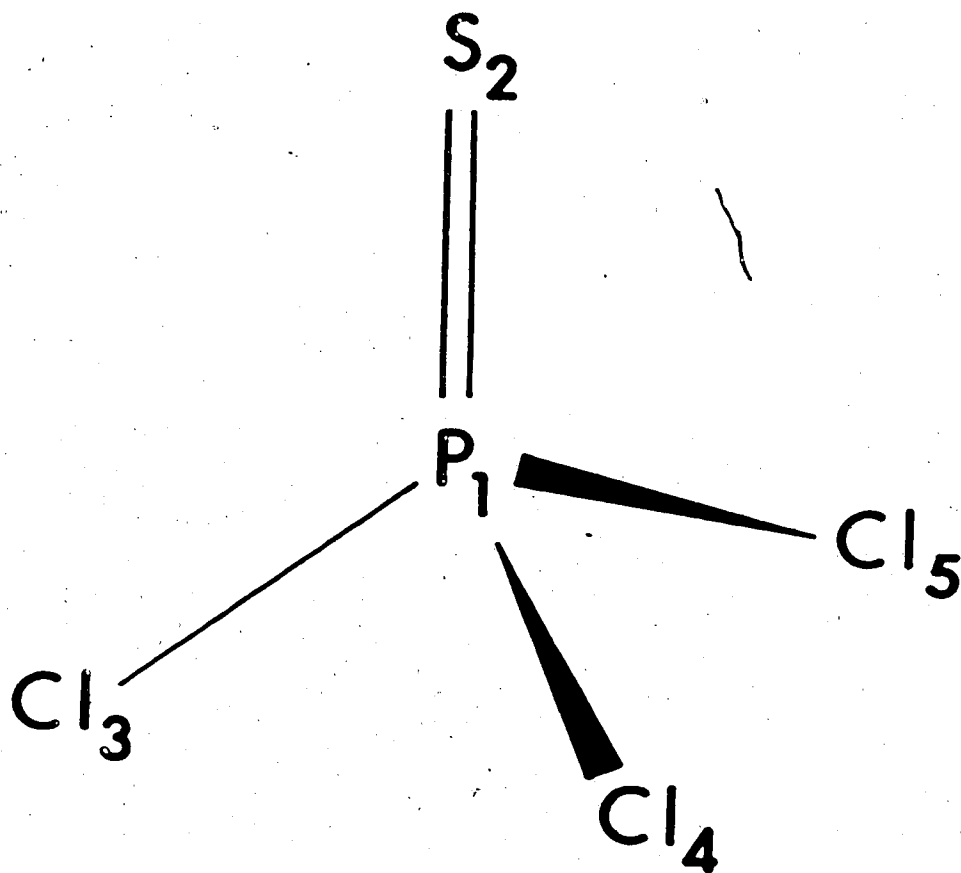


Fig. 6.1. Molecular structure of thiophosphoryl chloride.

Table 6.1

Approximate Description of the Fundamental  
Vibrations of Thiophosphoryl Chloride,  
Point Group  $C_{3v}$

<u>Mode</u> <sup>a</sup>	<u>Approximate Description</u>
$\nu_1(A_1)$	P-S stretch.
$\nu_2(A_1)$	P-Cl stretch
$\nu_3(A_1)$	Cl-P-Cl deformation
$\nu_4(E)$	P-Cl stretch
$\nu_5(E)$	Cl-P-Cl deformation
$\nu_6(E)$	S=P-Cl deformation

a) Numbering scheme follows Herzberg (106).

Table 6.2

Approximate Description of the  
Fundamental Vibrations of Thiophosphoryl  
Chloride, Point Group  $C_s$ .

<u>Mode</u> <sup>a</sup>	<u>Approximate Description</u> <sup>b</sup>
$\nu_1(A')$	P=S stretch
$\nu_2(A')$	antisym. P-Cl stretch
$\nu_3(A')$	sym. P-Cl stretch
$\nu_4(A')$	sym. Cl-P-Cl deformation
$\nu_5(A')$	antisym. Cl-P-Cl deformation
$\nu_6(A')$	S=P-Cl deformation
$\nu_7(A'')$	antisym. P-Cl stretch
$\nu_8(A'')$	antisym. Cl-P-Cl deformation
$\nu_9(A'')$	S=P-Cl deformation

a) Numbering scheme follows Herzberg (106).

b) sym. = symmetric and antisym. = antisymmetric.

### 6.1.3 Previous Studies of the Vibrations of Thiophosphoryl Chloride

The first work on the vibrational spectrum of thiophosphoryl chloride was reported in 1936 by Thatte (107). In this study of the Raman spectrum of the liquid, the frequencies of six fundamental vibrations were given, including one at  $382\text{ cm}^{-1}$ . The P=S stretching vibration was assigned to the band at  $750\text{ cm}^{-1}$ . A year later, in another study of the Raman spectrum of the liquid, Simon and Schulze (108) reported similar frequencies for the fundamental vibrations. Gerding and Westrik (109) re-studied the Raman spectrum of the liquid, after noticing that the correlation from phosphoryl chloride,  $\text{POCl}_3$ , to thiophosphoryl chloride, showed a consistent decrease in the frequency of each fundamental except for the one at  $382\text{ cm}^{-1}$ , which corresponded to the fundamental of phosphoryl chloride at  $337\text{ cm}^{-1}$ . They concluded that the band at  $382\text{ cm}^{-1}$  was not fundamental, but was due to the fundamental at  $435\text{ cm}^{-1}$  excited by a different line of the mercury lamp source. This left only five of the six fundamentals located, which led the authors to suggest that the apparently depolarised band at  $250\text{ cm}^{-1}$  was, in fact, two bands, one polarised and one depolarised. These authors assigned the fundamental frequencies to specific modes of vibration for the first time, and this assignment indicated that the symmetric and antisymmetric Cl-P-Cl deformation

modes,  $\nu_3(A_1)$  and  $\nu_5(E)$  respectively, were the vibrations coincident at  $250\text{ cm}^{-1}$ . This interpretation of the spectrum was accepted by Dewaulle and Francois (110).

The first study of the infrared spectrum of thiophosphoryl chloride was carried out by Cilento, Ramsay and Jones (111). From the infrared spectra of the vapour and liquid in the region  $400 - 1600\text{ cm}^{-1}$ , they were able to assign three fundamentals which were in good agreement with the Raman studies. Durig and Clark (112) re-examined the infrared spectra of the gas and liquid, including the  $250\text{ cm}^{-1}$  region, and the Raman spectrum of the liquid. The spectrum of the gas contained a band near  $250\text{ cm}^{-1}$  which had two sharp features, at  $252\text{ cm}^{-1}$  and  $248\text{ cm}^{-1}$ , and a contour that was not readily attributable to the superposition of bands due to  $\nu_3(A_1)$  and  $\nu_5(E)$ . The assignment of the two sharp features to  $\nu_3(A_1)$  and  $\nu_5(E)$  was, therefore, very tentative. Neither the infrared nor the Raman spectrum of the liquid in this region showed any evidence of the presence of two bands. Goubeau and Kottgen (113) attempted to correlate the P=S stretching frequency with the nature of the substituents in a series of thiophosphoryl compounds, and included a report of the infrared and Raman spectra of thiophosphoryl chloride. However, this work supplied no further evidence on the assignment of the spectrum.

The only work published on solid thiophosphoryl chloride is a study of the infrared spectrum at  $77^\circ\text{K}$  by

Marsault - Hérail and Tartar (114). They assigned a band at  $248.4 \text{ cm}^{-1}$ , with shoulders at  $251.6 \text{ cm}^{-1}$  and  $245.3 \text{ cm}^{-1}$ , to  $\nu_5$ , the antisymmetric Cl-P-Cl deformation, and the bands at  $226 \text{ cm}^{-1}$  and  $222 \text{ cm}^{-1}$  to  $\nu_3$ , the symmetric Cl-P-Cl deformation. They also observed three bands at  $433.5 \text{ cm}^{-1}$ ,  $430.5 \text{ cm}^{-1}$  and  $427.5 \text{ cm}^{-1}$  due to  $\nu_2$ , the symmetric P-Cl stretching mode. They attributed the triplet character of this band to intermolecular coupling and isotopic splitting.

Table 6.3 lists the frequencies from the fore-mentioned studies (107 - 114). None of the above-mentioned authors reported any isotope splitting in spectra of the gas and liquid. A study of the Raman spectrum of gaseous thiophosphoryl chloride at  $185^\circ\text{C}$  by Clark and Rippon (115) was published two years after completion of the work presented in this chapter. The results obtained in that study (115) will be discussed in Section 6.5. The remaining publication (116) on the vibrational spectra of thiophosphoryl chloride contains the work presented in this chapter.

There have been a number of attempts to analyse the normal coordinates of thiophosphoryl chloride, but unfortunately most of them suffer from simplifying assumptions or mistakes. Malants and co-workers (117) performed a normal coordinate calculation assuming all angles to be tetrahedral. The symmetry coordinate which Ziomek and Piotrowski (118) set equal to zero, is only correct if the



Table 3.3

Previous Assignments of the Fundamental Frequencies<sup>a</sup>  
of Gaseous and Liquid Thiophosphoryl Chloride

Thette 107, b Raman Liquid	Simon et al 108, b		Gerding et al 109		Delvaulle et al 110		Cilento et al 111		Durig et al 112		Goubeau et al 113		Zartar et al 114		Assignment
	Raman Liquid	Raman Liquid	Raman Liquid	Raman Liquid	Infrared Gas	Infrared Liquid	Infrared Gas	Infrared Liquid	Raman Gas	Infrared Gas	Raman Liquid	Infrared Liquid	Infrared Liquid	Infrared Liquid	
750	747	753	753	753	769	751	750	750	770	752	747	747	750	750	$\nu_1(A_1)$ , P-B stretch
543	536	542	538	538	550	540	539	539	547	536	539	539	530	530	$\nu_4(E)$ , P-Cl stretch
432	429	435	430	430	433	430	435	431	431	432	432	432	430	430	$\nu_2(A_1)$ , P-Cl stretch
382	382	—	247	247	—	—	250	252	250	250	250	250	250	250	$\nu_3(A_1)$ , Cl-P-Cl bend
246	244	250	247	247	—	—	250	248	250	250	250	250	250	250	$\nu_5(E)$ , Cl-P-Cl bend
171	168	167	172	172	—	—	174	—	174	174	169	169	—	—	$\nu_6(E)$ , S-P-Cl bend

a) In  $\text{cm}^{-1}$ .

b) These authors did not assign the frequencies to specific modes of vibration, except for the  $750 \text{ cm}^{-1}$  frequency of Thette.

angles are tetrahedral. If this coordinate was omitted from the calculation by these workers, their force field must be wrong (119). They (118) also used the wrong value for the Cl-P-Cl angle. Nararajan (120) and Venkateswarlu et al (121) used the band  $382\text{ cm}^{-1}$ , discussed earlier, as the  $\nu_5(E)$  fundamental. In the calculation carried out by Ramaswamy and Rao (122), incorrect values for the angles were used. Cyvin and co-workers (123) calculated force constants, mean amplitudes of vibration, Coriolis coupling constants and thermodynamic functions for thiophosphoryl chloride, using the correct frequencies and molecular parameters. However, these authors used twelve symmetry force constants to explain six observed frequencies. The remaining theoretical work in this field is by Venkateswarlu and Joseph (124), who calculated the centrifugal distortion constants, and Nagarajan (125), who determined the mean amplitudes of vibration, in apparent disagreement with Cyvin et al (123).

#### 6.1.4 Aims of this Study

The primary aim of this study was to attempt to provide strong experimental evidence of the assignment of the Cl-P-Cl deformation vibrations,  $\nu_3(A_1)$  and  $\nu_5(E)$ , of thiophosphoryl chloride. A subsidiary aim was to observe and assign the absorption by the various naturally occurring isotopic forms of the molecule. This required that normal coordinate calculations be carried out to estimate

the separation of the frequencies of these various isotopic forms. If only six frequencies are available as experimental data, a maximum of six force constants can be deduced.

The only calculation in the literature that is free from obvious errors or simplifying assumptions, is that of Cyvin and co-workers (123), and they used twelve symmetry force constants to explain six frequencies. Therefore it was decided to develop a modified valence force field with only six force constants to explain the observed frequencies.

## 6.2 Experimental Techniques

### 6.2.1 Sample Handling and Cells

Thiophosphoryl chloride used in this investigation was initially obtained from Columbia Organic Chemicals. This product was analysed by gas-liquid chromatography using a 10% SE 30 column, 10' x  $\frac{1}{4}$ ". Two impurities, both more volatile than thiophosphoryl chloride, were found, and together these amounted to a 0.5% impurity. About 10 ml of the liquid was put into a glass storage vessel fitted with a stopcock and ground glass ball joint, both lubricated with silicone grease, for connection to a conventional vacuum line. The sample was evaporated in vacuum until two-thirds of its original volume remained and the chromatogram of the remaining fraction showed a 0.3% impurity. Repetition of this procedure reduced the total impurity to 0.2%, which could not be improved by further evaporation. Spectra obtained from the commercial sample and purified fractions showed no differences. The identity of the impurities is unknown, however, from their relative volatilities, as demonstrated by the chromatograms, phosphorus trichloride and phosphoryl chloride are possibilities.

Thiophosphoryl chloride used near the end of this investigation was obtained from Alpha Inorganics. The purity of this product was checked by recording the  $^{31}\text{P}$  n.m.r. spectrum over a wide range of chemical shift,

including the regions where phosphoryl chloride and phosphorus trichloride absorb. The spectrum showed a single resonance at a chemical shift of -26 p.p.m. relative to phosphoric acid, indicating the presence of only thiophosphoryl chloride (126).

Gas samples for mid-infrared spectra, above  $200\text{ cm}^{-1}$ , were contained in a conventional gas cell with a 10 cm optical path. Cesium iodide windows, 50 mm x 6mm, were attached to each end using glyptal cement. The gas cell was evacuated to a pressure of less than 0.01 Torr, measured by an Edwards High Vacuum Speedivac Pirani Gauge, Model B5, and subsequently filled to pressures, measured by a mercury U-tube manometer, varying between 1 and 10 Torr of thiophosphoryl chloride.

Gas samples for far-infrared spectra, below  $300\text{ cm}^{-1}$ , were contained in the stainless steel gas cell shown in Fig. 6.2, which has a 10 cm optical path and was fitted with polyethylene windows. The cell consists of a 5.75" x 5.75" x 0.5" stainless steel top plate, A, in which is embedded a 5.5" diameter O-ring, B, which forms a vacuum tight seal to the sample compartment of the interferometer. A stainless steel cylinder, C, 3" x 1.25" o.d., 1" i.d., is connected through the middle of the plate by a 0.375" o.d. stainless steel tube, D, to a glass stopcock, E, which is attached to a ball-joint for coupling to a vacuum line. A flange, F, 2.3" o.d., at each end of the cylinder,

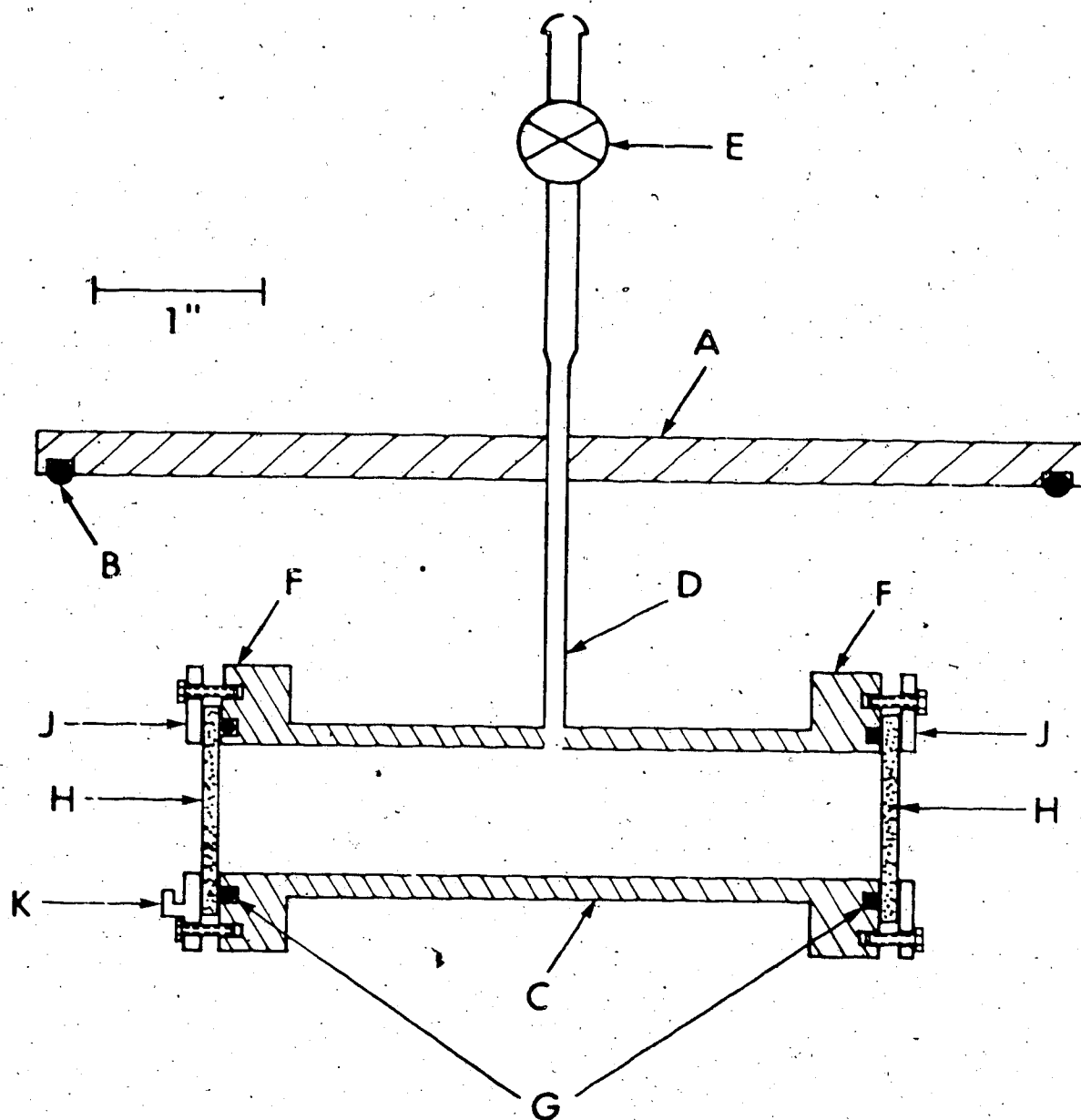


Fig. 6.2. Far-infrared gas cell: A, top plate; B, O-ring; C, cylinder; D, tube; E, stopcock; F, flanges; G, O-rings; H, windows; J, end plates; K, filter holder.

contains a 1.35" diameter O-ring, G, which provides a vacuum tight seal with the polyethylene windows, H. These windows are held in place by the end plates, J. The optical filter holder, K, is attached to one of the end plates. One side of each polyethylene window was conical, double angle  $172.5^\circ$ , to remove interference fringes from the spectra.

Liquid samples for Raman scattering studies were obtained by syringing the commercial thiophosphoryl chloride directly into a 1 mm i.d. capillary tube, and sealing the end with a torch after freezing the sample. Gas-liquid chromatography of the Raman samples after use showed no decrease in purity.

#### 6.2.2 Spectrophotometers

Mid-infrared spectra, above  $200\text{ cm}^{-1}$ , were recorded on the Beckman I. R. 12 Spectrophotometer described in Chapter 2.

Far-infrared spectra, below  $300\text{ cm}^{-1}$ , were obtained using a Beckman - R.I.I.C. F.S.720 Michelson Interferometer. This instrument can be evacuated to less than 0.01 Torr to eliminate the absorption by water vapour. The design, theory and operation of far-infrared interferometers is well documented (127, 128), and only a brief description is given here. The collimated light from the mercury source is split into two beams by one of the five beam splitters, of various thicknesses, available. One of these beams is

reflected by a fixed mirror and the second is reflected by a mirror which is continually moving to provide a continuously changing path difference between the beams. The two beams are recombined by the beam splitter, and pass through a long-wave pass, optical filter and the sample before reaching the Golay detector. The intensities of the light reaching the Golay detector at evenly spaced values of the path difference are transformed to digital voltages and punched onto I.B.M cards. An equal number of points each side of zero path difference are collected. This digitised interferogram is then Fourier transformed using the Fortran programme BOBS IV, which was written in this laboratory. This programme employs the I.B.M. subroutine RHARM to perform a sine plus cosine Fourier transformation, and offers the option of apodization by a triangular function (127). The result of the Fourier transformation is a spectrum which consists of the intensities at evenly spaced wavenumbers from zero to a maximum value,  $(2\Delta x)^{-1}$ , where  $\Delta x$  is the separation of the path difference values at which the intensities were measured. The accuracy of the wavenumbers thus depends on the accuracy of  $\Delta x$ . Calibration spectra using water vapour (129) showed the wavenumbers to be accurate to better than  $0.2 \text{ cm}^{-1}$ . Appropriate choices of the beam splitter, long-wave pass optical filter and  $\Delta x$  permit examination of all regions of the spectrum between 10 and  $380 \text{ cm}^{-1}$  with good



precision.

Sample and reference interferograms were recorded, and Fourier transformed to the corresponding spectra. These were then ratioed and the absorbance was calculated, and the absorbance-versus-wavenumber spectra were plotted by an off-line CALCOMP plotter. Several absorbance spectra may be averaged to increase the signal to noise ratio. The resolution of an unapodized spectrum is equal to the reciprocal of the maximum path difference (128), which was 0.77 cm in this study. This, therefore, gave a resolution of  $1.3 \text{ cm}^{-1}$  which, on apodization, is lowered to  $2.0 \text{ cm}^{-1}$  (130).

The Raman spectrophotometer consisted of a Carson Laboratories model 10SP Ar<sup>+</sup>/Kr<sup>+</sup> laser, a Spex model 1401 double monochromator, a Spex model 1420 sample illuminating chamber, a Spex model 1419 sample module, a cooled FW 130 photomultiplier tube, photon counting electronics and a strip chart recorder. All Raman spectra were excited by the  $4880 \text{ \AA}$  Ar<sup>+</sup> laser line at a power of approximately 80 mW at the sample. Unwanted emission lines were removed by filtering the incident beam. Spectra were obtained using the 90° scattering geometry. The incident light was polarised with the electric vector perpendicular to the direction of scattering, and the polarisation of the scattered light was selected by a polaroid analyser, and subsequently destroyed by a polarisation scrambler in front of the entrance slit. The frequency accuracy of the

monochromator was periodically checked with carbon tetrachloride (131), benzene<sup>c</sup> (106) and indene (132). Each time the spectrophotometer was used, the frequencies were calibrated using the symmetric C-Cl stretching bands of  $C^{35}Cl_4$ ,  $C^{35}Cl_3^{37}Cl$  and  $C^{35}Cl_2^{37}Cl_2$  (131).

### 6.3 Results

#### 6.3.1 General

In this section, the results of the gas phase infrared and liquid phase Raman studies will be presented. This will be followed by an analysis of the effect of impurities produced by the reaction of thiophosphoryl chloride on the window material.

The natural abundance of chlorine isotopes in thiophosphoryl chloride can be calculated using the standard formulae of the theory of combinations (133):

$$f(35) = 0.7553 \text{ (85)} \text{ and } f(37) = 0.2447 \text{ (85)}$$

where  $f(35)$  is the naturally occurring fraction of  $^{35}\text{Cl}$ , and  $f(37)$  is the naturally occurring fraction of  $^{37}\text{Cl}$ , and,

$$f(\text{SP}^{35}\text{Cl}_x^{37}\text{Cl}_{n-x}) = f(35)^x \cdot f(37)^{n-x} \cdot \frac{n!}{x!(n-x)!}$$

where  $n = 3$  and  $x = 0, 1, 2$  or  $3$ .

Thus natural thiophosphoryl chloride is, considering only chlorine isotopes, 43.1% of  $\text{SP}^{35}\text{Cl}_3$ , 41.9% of  $\text{SP}^{35}\text{Cl}_2^{37}\text{Cl}$ , 13.6% of  $\text{SP}^{35}\text{Cl}^{37}\text{Cl}_2$  and 1.5% of  $\text{P}^{37}\text{Cl}_3$ . Therefore the possibility of observing bands due to at least two, and possibly three, isotopic species, must be considered.

Further, 4.22% of each species listed above will contain  $^{34}\text{S}$ , 0.76% will contain  $^{33}\text{S}$  and the remainder will essentially all contain  $^{32}\text{S}$ .

The general features of the gas phase infrared

spectrum and the liquid phase Raman spectrum are well known (112) and will not be repeated here. Rather, a detailed study of the individual bands will be shown, paying particular attention to the Cl-P-Cl deformation region around  $250 \text{ cm}^{-1}$ , and to the occurrence of any isotopic splitting of the fundamental bands. Before presenting the results, it is necessary to briefly discuss the shapes expected for the vibrational-rotational bands of the gas.

Since the molecules of  $C_{3v}$  symmetry are symmetric tops, the gas phase band contours of the  $A_1$  modes are expected to show a well defined PQR structure (106). The band contours of the E modes, however, are strongly dependent on Coriolis coupling, and may vary for different normal vibrations (106, 134). The molecules of  $C_s$  symmetry can be shown, from their moments of inertia, which are given in Table 6.4, to be rotors of Ueda and Shimanouchi's (81) type 40. The A, B and C band contours for this type, all show (81) a strong Q branch flanked by weak P and R branches.

### 6.3.2 Cl-P-Cl Deformation Vibrations

The symmetric and antisymmetric Cl-P-Cl deformation vibrations,  $\nu_3(A_1)$  and  $\nu_5(E)$  respectively, are expected to absorb near  $250 \text{ cm}^{-1}$ . The absorption by these vibrations was studied using the interferometer described earlier.

Curve B of Fig. 6.3 shows the absorbance of about 10 Torr pressure of thiophosphoryl chloride contained

Table 6.4

Principal Moments of Inertia<sup>a</sup> for  
Thiophosphoryl Chloride

	$I_A$	$I_B$	$I_C$
SP <sup>35</sup> Cl <sub>3</sub>	337.51	360.52	360.52
SP <sup>35</sup> Cl <sub>2</sub> <sup>37</sup> Cl	343.52	361.84	367.84
SP <sup>35</sup> Cl <sup>37</sup> Cl <sub>2</sub>	350.02	365.58	372.36
SP <sup>37</sup> Cl <sub>3</sub>	356.79	373.01	373.01

a) In amu Å<sup>2</sup>.

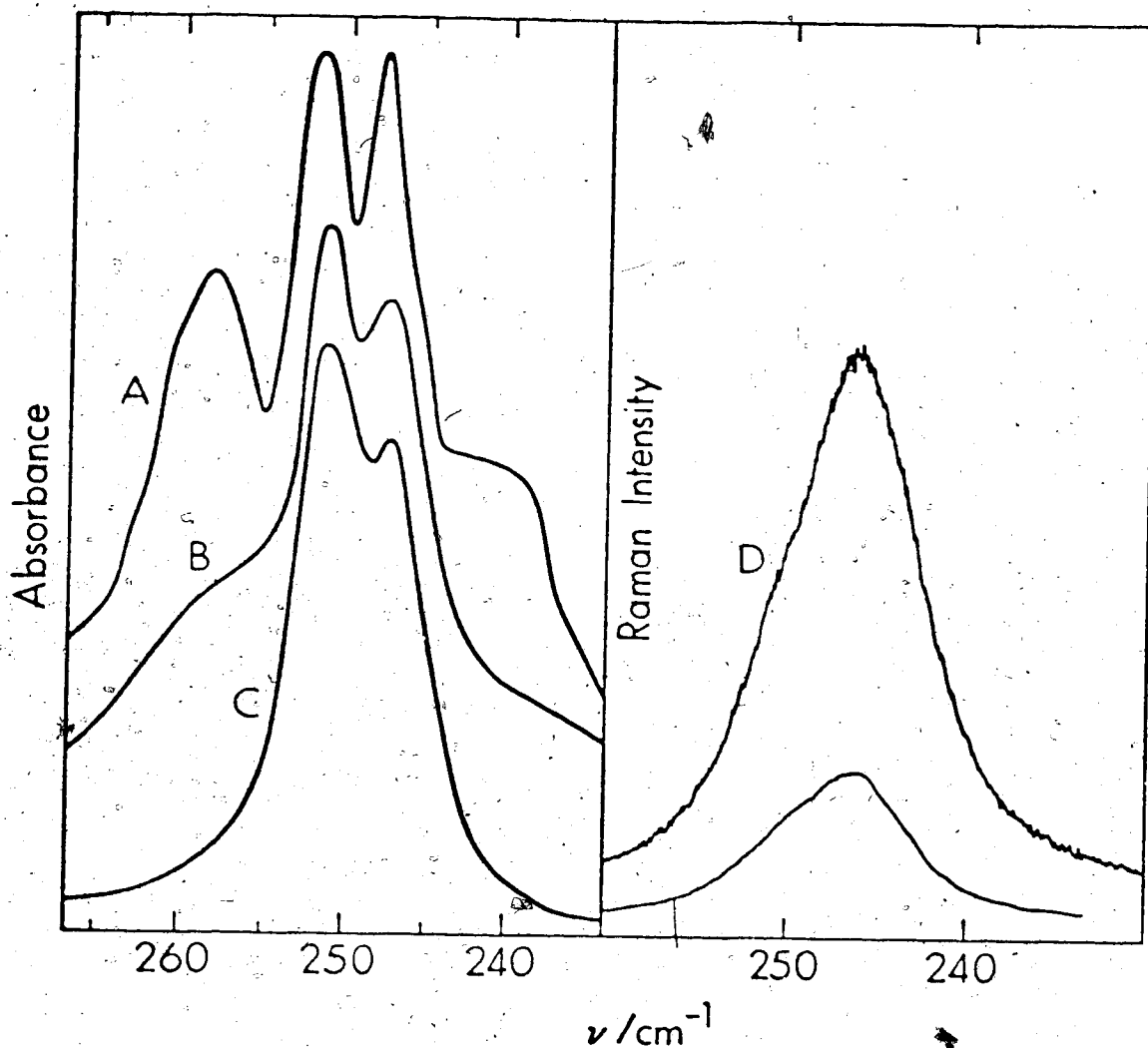


Fig. 6.3. Infrared spectra of gaseous thiophosphoryl chloride between  $235$  and  $265$   $\text{cm}^{-1}$  at  $25^\circ\text{C}$  and  $2$   $\text{cm}^{-1}$  resolution: curve A, gas at  $1$  cm pressure,  $10$  cm path, cesium iodide windows; curve B, gas at  $1$  cm pressure,  $10$  cm path, polyethylene windows; curve C, polyethylene windows with adsorbed thiophosphoryl chloride. Curves D are the Raman spectra of liquid thiophosphoryl chloride in the same region at  $25^\circ\text{C}$  and  $1$   $\text{cm}^{-1}$  resolution using no analyser.

between polyethylene windows. Noise on the wings of this band has been smoothed. The two sharp peaks occur at  $251.4 \text{ cm}^{-1}$  and  $247.7 \text{ cm}^{-1}$ . Curve A of Fig. 6.3 shows the average of three spectra which were run consecutively on the same sample of thiophosphoryl chloride contained between cesium iodide windows. The two central peaks are at the same frequencies as in curve B, and the high frequency band is at  $258.3 \text{ cm}^{-1}$ . Noise on the low frequency shoulder has been smoothed. The origin of the difference between curves A and B can be seen in curve C, which is the spectrum of the evacuated cell with polyethylene windows, after it had been used to record the spectra of several samples of gaseous thiophosphoryl chloride. The doublet at  $251.4 \text{ cm}^{-1}$  and  $247.5 \text{ cm}^{-1}$  in curve C increased in intensity when the windows were further exposed to thiophosphoryl chloride, and decreased in intensity on further evacuation of the cell, or when the windows were left in the air for several days. It is, therefore, necessary to assign this absorption to thiophosphoryl chloride adsorbed on polyethylene. It is well known that small molecules are adsorbed by polyethylene (135, 136).

Curve B of Fig. 6.3 is thus the superposition of absorption by gaseous and adsorbed thiophosphoryl chloride. Thiophosphoryl chloride adsorbed on polyethylene does not undergo quantised rotation, so curve C of Fig. 6.3 does not show the rotational-vibrational band contours of curves

A and B. The appearance of a doublet in curve C therefore indicates that two vibrations do absorb near  $250 \text{ cm}^{-1}$ .

Curves D of Fig. 6.3 show the corresponding Raman band of liquid thiophosphoryl chloride. The band is depolarised and asymmetric, with a peak frequency of  $247 \text{ cm}^{-1} \pm 1 \text{ cm}^{-1}$ , and a high frequency shoulder at about  $251 \text{ cm}^{-1}$ . It is tempting to attribute these features to the two vibrations identified in the far-infrared spectra. However, pronounced high frequency shoulders were also found on the Raman bands due to  $\nu_1(A_1)$  and  $\nu_4(E)$  of liquid thiophosphoryl chloride, as shown in Fig. 6.4.

These results will be discussed, together with those obtained from the normal coordinate analysis, in Section 6.5.

### 6.3.3 P-Cl Symmetric Stretching Vibration

The P-Cl symmetric stretching region was investigated in the infrared spectrum of the gas and the Raman spectrum of the liquid.

Curve A of Fig. 6.5 shows the absorbance due to this mode in the infrared spectrum of the gas. Two sharp Q branches can be seen at  $436.5 \text{ cm}^{-1}$  and  $433.6 \text{ cm}^{-1}$ , together with an R branch at  $440.6 \text{ cm}^{-1}$ . Curves B of Fig. 6.5 show the corresponding region in the Raman spectrum of the liquid. Three bands can be seen at  $433.3 \text{ cm}^{-1}$ ,  $431 \text{ cm}^{-1}$  and  $428 \text{ cm}^{-1}$ .

The two Q branches and the three Raman bands are most logically assigned to the different isotopic species



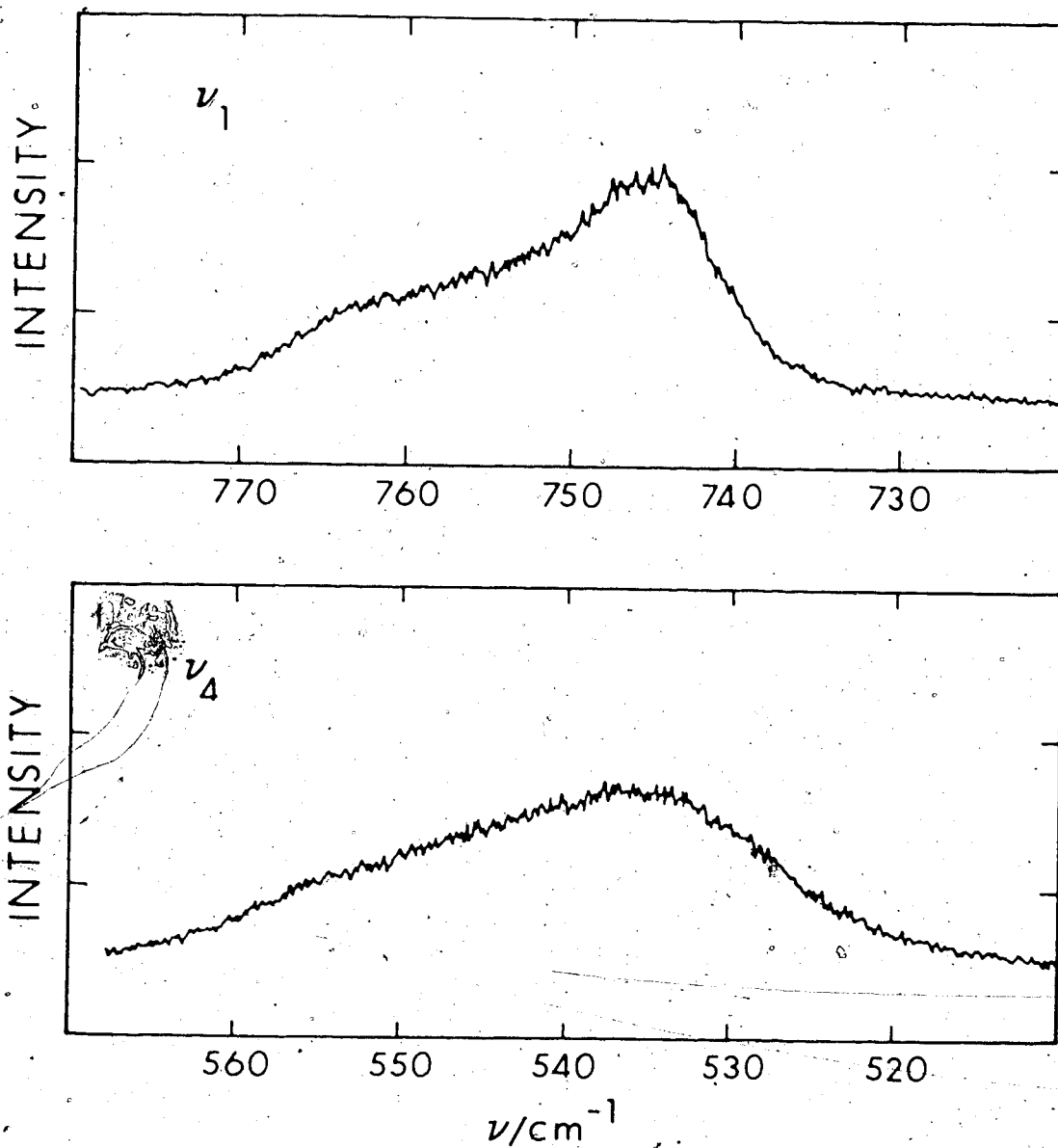


Fig. 6.4. Raman spectra of liquid thiophosphoryl chloride between 720 and 780  $\text{cm}^{-1}$  (upper box) and between 510 and 570  $\text{cm}^{-1}$  (lower box) at 25°C and 1  $\text{cm}^{-1}$  resolution using no analyser.

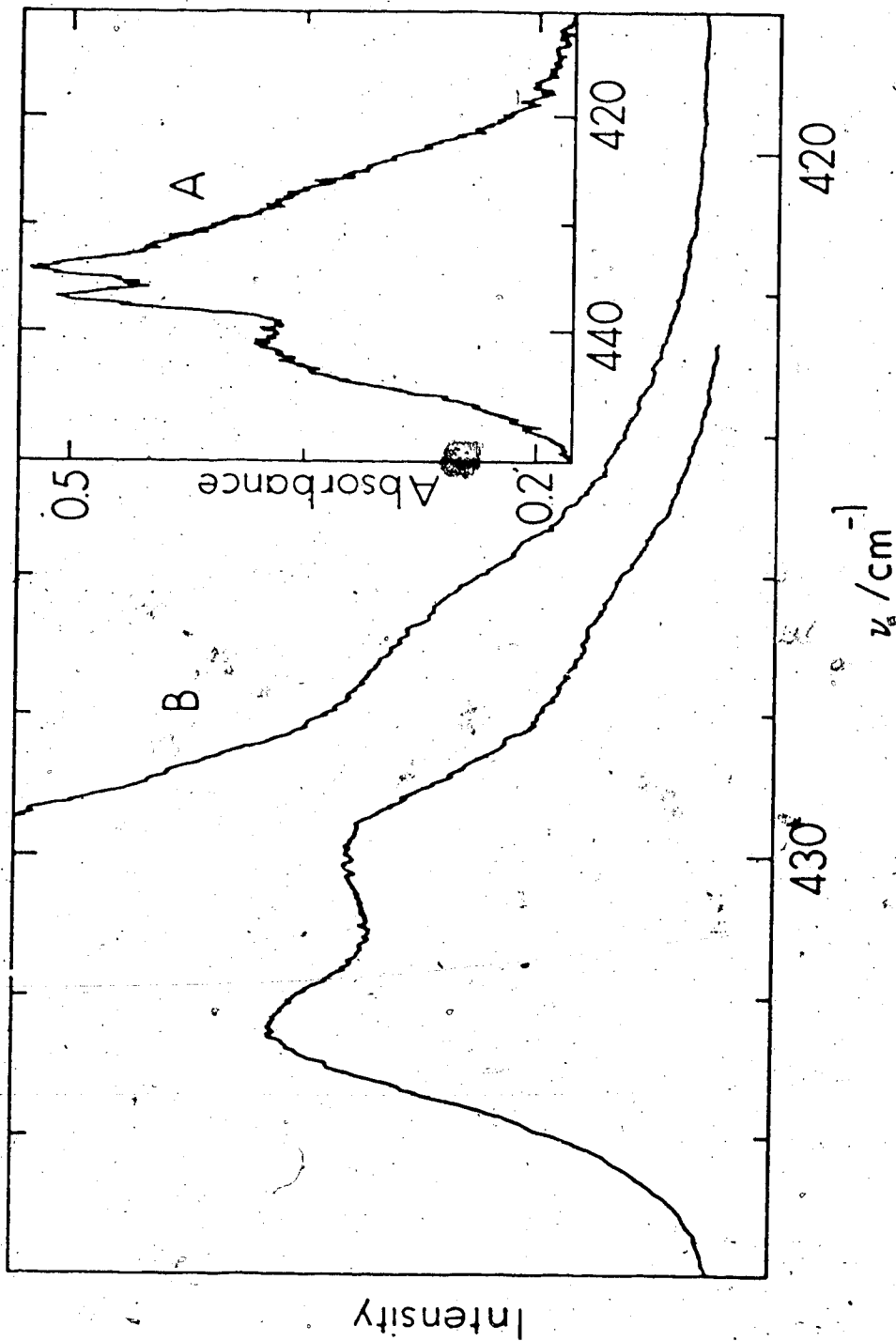


Fig. 6.5. Box A: infrared spectrum between 410 and 450  $\text{cm}^{-1}$  at 2  $\text{cm}^{-1}$  resolution of gaseous thiophosphoryl chloride at 25°C; 0.7 cm path, 10° cm path, cesium iodide windows. Box B: Raman spectrum between 420 and 435  $\text{cm}^{-1}$  at 0.5  $\text{cm}^{-1}$  resolution of liquid thiophosphoryl chloride at 25°C using no analyser.

present. The consistency of this assignment, with the results of the normal coordinate analysis, will be discussed in Section 6.5.

#### 6.3.4 Other Fundamental Vibrations

The remaining fundamentals are the P=S stretching mode,  $\nu_1(A_1)$ , the antisymmetric P-Cl stretching mode,  $\nu_4(E)$ , and the S=P-Cl deformation mode,  $\nu_6(E)$ .

The absorption by the P=S stretching mode of gaseous thiophosphoryl chloride is shown in Fig. 6.6. This band shows the well defined PQR pattern which is expected (Section 6.3.1). The frequencies of the P, Q and R branches are 772.8  $\text{cm}^{-1}$ , 769.6  $\text{cm}^{-1}$  and 775.5  $\text{cm}^{-1}$  respectively. As well as the main Q branch at 769.6  $\text{cm}^{-1}$ , a second weak branch appears at 763.1  $\text{cm}^{-1}$ .

The absorption by the antisymmetric P-Cl stretching mode of gaseous thiophosphoryl chloride, shown in Fig. 6.6, is split into a doublet with peak frequencies of 550.5  $\text{cm}^{-1}$  and 547.7  $\text{cm}^{-1}$ . The band contour of this mode is largely determined by Coriolis coupling effects.

The last fundamental to be considered is the S=P-Cl deformation mode,  $\nu_6(E)$ . The band due to this vibration was not seen in the infrared spectrum of the gas, which indicates that its dipole moment derivative is very small. However, the change in polarisability during this vibration is large enough to produce the symmetric, depolarised band shown in Fig. 6.6 at 171.5  $\text{cm}^{-1}$ . The results for  $\nu_1(A_1)$

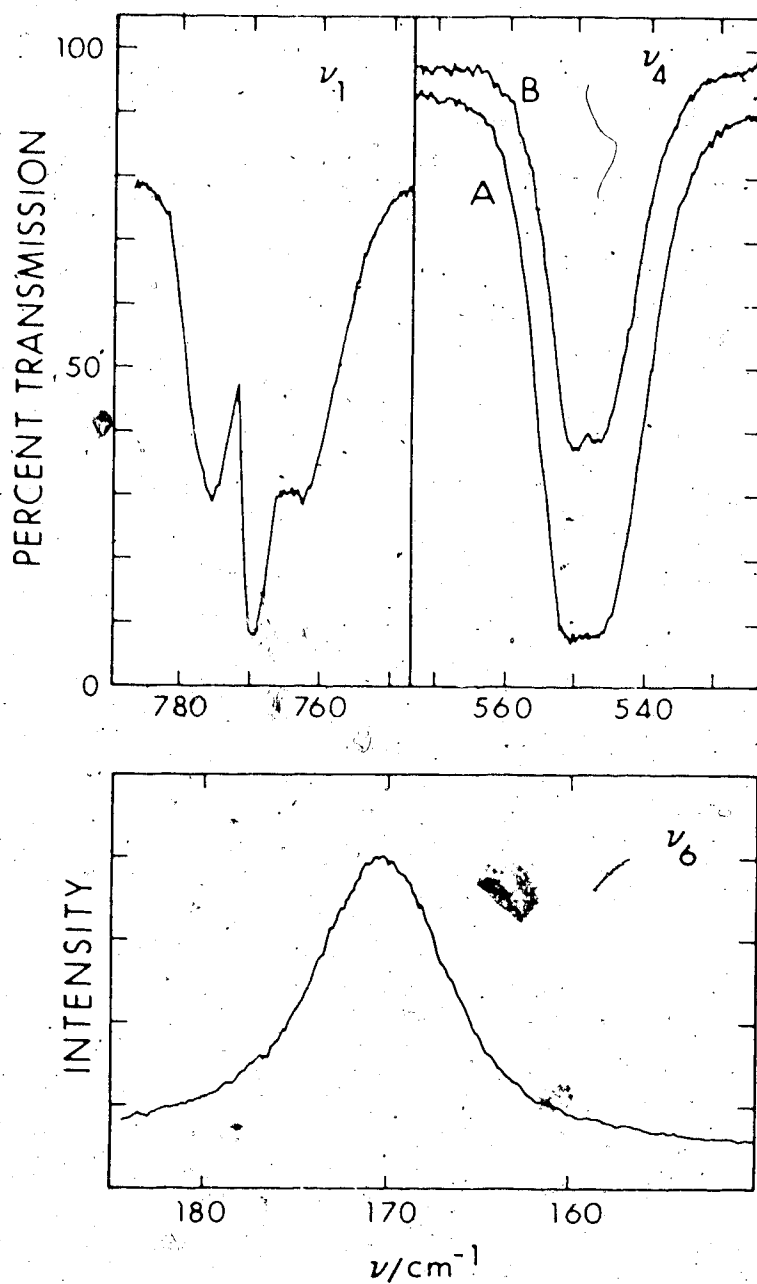


Fig. 6.6. Infrared spectra at 1 cm<sup>-1</sup> resolution between 750 and 790 cm<sup>-1</sup> (left upper box) and at 2 cm<sup>-1</sup> resolution between 530 and 570 cm<sup>-1</sup> (right upper box) of gaseous thiophosphoryl chloride at 25°C, cesium iodide windows. Raman spectrum of liquid thiophosphoryl chloride between 150 and 180 cm<sup>-1</sup> at 25°C and 1 cm<sup>-1</sup> resolution (lower box) using no analyser.

and  $\nu_4(E)$  will be discussed in Section 6.5.2, whereas those for  $\nu_6(E)$  are included for completeness.

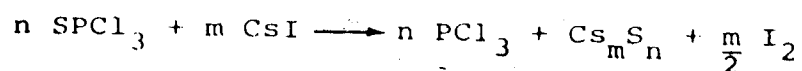
### 6.3.5 Impurities

The purity of commercial thiophosphoryl chloride has already been discussed in Section 6.2.1. In this section, the effect of impurities which result from the reaction of thiophosphoryl chloride with cesium iodide windows will be discussed.

Thiophosphoryl chloride reacts with the cesium iodide windows, turning them yellow, then brown, then deep red-brown. In order to identify the reaction products and determine the effect these would have on the spectrum, the gaseous products from a reaction between powdered cesium iodide and thiophosphoryl chloride were analysed by  $^{31}\text{P}$  n.m.r. spectroscopy and infrared spectroscopy. In the  $^{31}\text{P}$  n.m.r. spectrum, a resonance at -217 p.p.m., relative to phosphoric acid, was observed, in addition to the resonance at -219 p.p.m., relative to phosphoric acid, due to (126) thiophosphoryl chloride. The low field chemical shift can be compared to the chemical shift of -219 p.p.m., relative to phosphoric acid, of the phosphorus atom in phosphorus trichloride. The infrared spectrum of the gaseous reaction products showed, in addition to the thiophosphoryl chloride peaks, a new strong band at  $508\text{ cm}^{-1}$  and a sharpening of the absorption at  $260\text{ cm}^{-1}$ . The frequencies of these peaks agree well with those reported

by Frankiss and Miller (137) for the two strongest bands in the infrared spectrum of phosphorus trichloride.

The presence of phosphorus trichloride can be rationalised by the following reaction,



where  $m = 2$  and  $n = 1, 2, 3$  or  $6$ ; or  $m = 1$  and  $n = 4$ .

The colours of the cesium sulphides are white, yellow, red and brown, which explains the colour of the windows after the reaction with thiophosphoryl chloride. Also a violet colour formed immediately on mixing the powdered cesium iodide with thiophosphoryl chloride, which is consistent with the presence of iodine.

The only bands in the infrared spectrum of thiophosphoryl chloride which could be affected by the presence of phosphorus trichloride are the Cl-P-Cl deformations. The three spectra which were averaged to give curve A of Fig. 6.3 were run over a period of six hours, and the only change noticed was a slight decrease in the intensity of the  $251.4 \text{ cm}^{-1}$  peak relative to that of the  $247.7 \text{ cm}^{-1}$  peak.

## 6.4 Normal Coordinate Analysis

### 6.4.1 General

A normal coordinate analysis of thiophosphoryl chloride was necessary primarily to differentiate between bands due to the same vibration in different isotopic species, and bands due to different vibrations of the same isotopic species.

Previous normal coordinate calculations on thiophosphoryl chloride have already been discussed in Section 6.1.3, where it was concluded that only one study (123) was free from obvious mistakes or invalid assumptions concerning the molecular geometry. However, this note (123) gave no details of the development of the force field, which contained more force constants than the number of experimental data available. Further the note (123) offered no information concerning the average error (hereafter called the fit) between observed and calculated frequencies, and did not show the distribution of the potential energy of each vibration between the various force constants, which is one of the standard criteria for assigning frequencies to specific modes of motion.

It was, therefore, necessary to develop a modified valence force field for thiophosphoryl chloride.

### 6.4.2 Theory of Normal Vibrations

The theory of normal vibrations is well known (105) and only a brief statement will be given here, in order to

describe the computer programmes used.

The vibrational potential energy,  $V$ , of a molecule is assumed to be adequately described by the harmonic approximation,

$$V = \frac{1}{2} \underline{R}^t \underline{F} \underline{R},$$

where  $\underline{F}$  is the matrix of the force constants,  $f_{ij}$ , which are diagonal force constants when  $i = j$  and interaction force constants when  $i \neq j$ ;  $\underline{R}$  is the column vector of the internal displacement coordinates,  $R_i$ , (changes in the bond lengths and inter-bond angles) and  $\underline{R}^t$  is the transpose of  $\underline{R}$ . The vibrational kinetic energy,  $T$ , in the harmonic approximation, is given by,

$$T = \frac{1}{2} \underline{R}^t \underline{G}^{-1} \dot{\underline{R}}$$

where  $\underline{G}^{-1}$  is the kinetic energy matrix and  $\dot{\underline{R}}$  is the derivative of  $\underline{R}$  with respect to time. Under these assumptions, the roots,  $\lambda_k$ , of the vibrational secular equation, are proportional to the square of the frequencies of the normal vibrations. The vibrational secular equation is given by,

$$\left| \underline{G} \underline{F} - \underline{E} \underline{\lambda} \right| = 0$$

where  $\underline{G}$  is the inverse of  $\underline{G}^{-1}$ ,  $\underline{E}$  is the unit matrix, and  $\underline{\lambda}$  is the diagonal matrix of the roots  $\lambda_k$ . The substitution of the individual roots,  $\lambda_k$ , into the secular equation gives, after normalisation with respect to the potential



energy, the eigenvectors,  $l_{ik}$ , whose matrix  $L$  is defined by,

$$R = \sqrt{L} Q,$$

where  $Q$  is the column vector of the normal coordinates,  $Q_k$ .

The harmonic potential and kinetic energy expressions in terms of the normal coordinates are,

$$V = \sum_k \frac{1}{2} \lambda_k Q_k^2 \quad \text{and} \quad T = \sum_k \frac{1}{2} \dot{Q}_k^2,$$

where  $\dot{Q}_k$  is the derivative of  $Q_k$  with respect to time.

The set of eigenvectors for a given normal coordinate provide a description for that coordinate, in terms of the internal displacement coordinates.

An alternative description of a normal vibration is provided by the contributions to the potential energy of that normal vibration by the various force constants,  $f_{ij}$ . These contributions, for the  $k$ th normal vibration, are given by,

$$\frac{f_{ij} l_{ik} l_{jk}}{\lambda_k} (2 - \delta_{ij}) \times 100\%$$

where  $\delta_{ij} = 0$  for  $i \neq j$  and  $\delta_{ij} = 1$  for  $i = j$ .

#### 6.4.3 Computer Programmes

Four computer programmes written by J. H. Schachtschneider (138) were used to set up and solve the vibrational secular equation. The programmes were written in FORTRAN IV, and modified, in this laboratory, for use on an I B M.

computer.

The programme CART calculates the Cartesian coordinates of each atom in the molecule with respect to pre-selected axes from the bond lengths and inter-bond angles supplied to it. The moments of inertia, presented in Table 6.4, were also calculated by CART, using supplied atomic weights.

The programme GMAT uses the Cartesian coordinates and masses of the atoms to calculate Wilson's (105) inverse kinetic energy matrix  $\underline{G}$ . The relationship between the internal coordinate matrix,  $\underline{R}$ , and the Cartesian coordinate matrix,  $\underline{X}$ , is

$$\underline{R} = \underline{B} \underline{X},$$

where  $\underline{B}$  is the transformation matrix. The inverse kinetic energy matrix,  $\underline{G}$ , is related to  $\underline{B}$  by (105)

$$\underline{G} = \underline{B} \underline{M}^{-1} \underline{B}^t,$$

where  $\underline{B}^t$  is the transpose of  $\underline{B}$  and  $\underline{M}^{-1}$  is the diagonal matrix of the reciprocal masses.

The final step is the solution of the vibrational secular equation using the programme VSEC or FPRT. These programmes take the force constant matrix,  $\underline{F}$ , and the inverse kinetic energy matrix,  $\underline{G}$ , and find the eigenvalues,  $\lambda_k$ , and the eigenvectors,  $l_{ik}$ , of the product matrix,  $\underline{G.F}$ . This is mathematically equivalent to solving the secular equation. FPRT then compares the calculated and

observed frequencies, modifies the  $F$  matrix and recalculates the frequencies, iterating this procedure until the best least-squares fit between observed and calculated frequencies is obtained. Both programmes, VSEC and FPRT, can also calculate the potential energy distributions for the normal coordinates and VSEC can give the Coriolis coupling constants between the normal coordinates.

Symmetry may be used in both programmes to factorise the  $F$  and  $G$  matrices, thus reducing the size of the secular equations to be solved. When this is done, linear combinations of the internal displacement coordinates,  $R_i$ , are constructed (105), which transform under the irreducible representations of the point group of the molecule. These linear combinations are the symmetry coordinates,  $S_i$ , and are defined by,

$$\underline{S} = \underline{U} \underline{R},$$

where  $\underline{U}$  is the transformation matrix. Similarly the  $F$  and  $G$  matrices are transformed to their symmetrised equivalents by,

$$\underline{F}_S = \underline{U} \underline{F} \underline{U}^t \quad \text{and} \quad \underline{G}_S = \underline{U} \underline{G} \underline{U}^t.$$

$\underline{S}$ ,  $\underline{S}^t$ ,  $\underline{S}_i$ ,  $\underline{G}_S$ ,  $\underline{G}_S^{-1}$ , and  $\underline{F}_S$  then replace  $\underline{R}$ ,  $\underline{R}^t$ ,  $\underline{R}_i$ ,  $\underline{G}$ ,  $\underline{G}^{-1}$  and  $\underline{F}$  in the equations given earlier in this section, except in those describing the construction of  $\underline{G}$ .

#### 6.4.4 Vibrational Coordinates and Force Field Development

The internal coordinates for thiophosphoryl chloride

are defined in Table 6.5 in terms of bond stretching and inter-bond angle bending displacements. Tables 6.6 and 6.7 define the symmetry coordinates for molecules of  $C_{3v}$  and  $C_s$  symmetry, respectively. For the molecules of  $C_s$  symmetry, the unique isotopic atom is taken to be  $Cl_4$  of Fig. 6.1. It is necessary to use ten internal coordinates to describe the nine normal modes of vibration. Thus one redundant coordinate is included, which will result in one root of the secular equation being equal to zero.

The G matrices for  $^{32}SP^{35}Cl_3$ ,  $^{32}SP^{35}Cl_2^{37}Cl$ ,  $^{32}SP^{35}Cl^{37}Cl_2$ ,  $^{32}SP^{37}Cl_3$ ,  $^{34}SP^{35}Cl_3$  and  $^{34}SP^{35}Cl_2^{37}Cl$ , with respect to the internal coordinates defined in Table 6.5, are given in Appendix I.

The experimental data used in the initial calculations consisted of the frequency of  $\nu_6(E)$  in the Raman spectrum of the liquid, and the frequencies of the remaining bands, attributed to  $^{32}SP^{35}Cl_3$  (Section 6.3), in the infrared spectra of the gas. It was assumed that the peaks at 251.4 and 247.7  $cm^{-1}$  were due to  $\nu_3(A_1)$  and  $\nu_5(E)$ , respectively. Other possibilities were considered later. The six available frequencies are insufficient to determine the sixteen force constants of the general valence force field of thiophosphoryl chloride, and so it was necessary to develop a modified valence force field containing, at most, six force constants. The philosophy followed in

Table 6.5

Internal Coordinates of  
Thiophosphoryl Chloride

<u>Number</u>	<u>Designation</u>	<u>Description</u> <sup>a</sup>
1	$R_1$	$\nu(P_1-Cl_3)$
2	$R_2$	$\nu(P_1-Cl_4)$
3	$R_3$	$\nu(P_1-Cl_5)$
4	$R_4$	$\nu(P_1-S_2)$
5	$\alpha_1$	$\delta(Cl_3-P_1-Cl_4)$
6	$\alpha_2$	$\delta(Cl_4-P_1-Cl_5)$
7	$\alpha_3$	$\delta(Cl_5-P_1-Cl_3)$
8	$\beta_1$	$\delta(S_2-P_1-Cl_3)$
9	$\beta_2$	$\delta(S_2-P_1-Cl_4)$
10	$\beta_3$	$\delta(S_2-P_1-Cl_5)$

a)  $\nu$  and  $\delta$  indicate bond stretching and valence angle bending displacements respectively. The atom-numbers are defined in Fig.6.1.

Table 6.6

Symmetry Coordinates for

 $^{32}\text{SP}^{35}\text{Cl}_3$ ,  $^{32}\text{SP}^{37}\text{Cl}_3$  and  $^{34}\text{SP}^{35}\text{Cl}_3$ , Point Group  $C_{3v}$ .

<u>Number</u>	<u>Description</u>	<u>Symmetry</u>
$S_1$	$\frac{1}{\sqrt{3}} \{ R_1 + R_2 + R_3 \}$	$A_1$
$S_2$	$R_4$	$A_1$
$S_3$	$\frac{1}{\sqrt{6}} \{ \alpha_1 + \alpha_2 + \alpha_3 - \beta_1 - \beta_2 - \beta_3 \}$	$A_1$
$S_4$	$\frac{1}{\sqrt{6}} \{ \alpha_1 + \alpha_2 + \alpha_3 + \beta_1 + \beta_2 + \beta_3 \}$	$A_1$
$S_5$	$\frac{1}{\sqrt{6}} \{ 2R_1 - R_2 - R_3 \}$	$E_a$
$S_6$	$\frac{1}{\sqrt{6}} \{ 2\alpha_2 - \alpha_3 - \alpha_1 \}$	$E_a$
$S_7$	$\frac{1}{\sqrt{6}} \{ 2\beta_1 - \beta_2 - \beta_3 \}$	$E_a$
$S_8$	$\frac{1}{\sqrt{2}} \{ R_2 - R_3 \}$	$E_b$
$S_9$	$\frac{1}{\sqrt{2}} \{ \alpha_3 - \alpha_1 \}$	$E_b$
$S_{10}$	$\frac{1}{\sqrt{2}} \{ \beta_2 - \beta_3 \}$	$E_b$

Table 6.7

Symmetry Coordinates for  $^{32}\text{SP}^{35}\text{Cl}_2$ ,  $^{37}\text{Cl}$ ,  $^{32}\text{SP}^{35}\text{Cl}$ ,  $^{37}\text{Cl}_2$  and  $^{34}\text{SP}^{35}\text{Cl}_2$ ,  $^{37}\text{Cl}$ , Point Group  $C_s$

<u>Number</u>	<u>Description</u>	<u>Symmetry</u>
S <sub>1</sub>	$\frac{1}{\sqrt{2}} \{ R_1 + R_3 \}$	A'
S <sub>2</sub>	R <sub>2</sub>	A'
S <sub>3</sub>	R <sub>4</sub>	A'
S <sub>4</sub>	$\frac{1}{\sqrt{2}} \{ \alpha_1 + \alpha_2 \}$	A'
S <sub>5</sub>	$\alpha_3$	A'
S <sub>6</sub>	$\frac{1}{\sqrt{2}} \{ \beta_1 + \beta_3 \}$	A'
S <sub>7</sub>	$\beta_2$	A'
S <sub>8</sub>	$\frac{1}{\sqrt{2}} \{ R_1 - R_3 \}$	A''
S <sub>9</sub>	$\frac{1}{\sqrt{2}} \{ \alpha_1 - \alpha_2 \}$	A''
S <sub>10</sub>	$\frac{1}{\sqrt{2}} \{ \beta_1 - \beta_3 \}$	A''

selecting the force constants to be included was the following one. The diagonal force constants must always be included, since they are expected to make the dominant contribution to the force field. The most significant off-diagonal, or interaction, force constants must then be determined. Those selected should give an optimal improvement of the fit, while remaining small in value and contributing only minimally to the potential energy distribution.

The force fields which developed at various stages of the calculations, are numbered consecutively and listed in Table 6.8. The frequencies calculated from these force fields for  $^{32}\text{S}^{35}\text{Cl}_3$  are listed in Table 6.9, together with the observed frequencies.

The initial values for the diagonal force constants, force field 1, were obtained by simple, manual calculations which involved solving secular equations for the appropriate, isolated part of the molecule. The programme VSEC used these force constants to calculate the frequencies shown under force field 1 in Table 6.8. There was an average error between observed and calculated frequencies of  $43\text{ cm}^{-1}$  of 16%. A reduction in this error required that the P-Cl stretching, Cl-P-Cl deformation and the S=P-Cl deformation force constants be raised, and that the P=S stretching force constant be lowered. These adjustments resulted in force field 2 of Tables 6.8 and 6.9, which



Table 6.8

Force Field Development  
for Thiophosphoryl Chloride<sup>a</sup>

Force <sup>b</sup> Constant	Force Fields					
	1	2	3	4	5	Final
f(P-Cl)	2.276	2.576	2.576	2.576	2.770	2.780
f(P=S)	5.163	4.000	3.950	3.950	3.557	3.557
f(Cl-P-Cl)	0.919	1.459	1.500	1.750	1.859	1.812
f(S=P-Cl)	0.350	0.600	0.600	0.600	0.570	0.570
f( $\begin{matrix} \text{P-Cl}' \\ \text{P-Cl}'' \end{matrix}$ )	—	—	0.350	0.450	0.585	0.580
f( $\begin{matrix} \text{P=S}' \\ \text{P-Cl}'' \end{matrix}$ )	—	—	0.120	0.120	—	—
f( $\begin{matrix} \text{Cl-P-Cl}' \\ \text{Cl}'\text{-P-Cl}'' \end{matrix}$ )	—	—	—	-0.100	-0.129	-0.105

a) The units are: mdyne Å<sup>-1</sup> for bond stretching force constants, and mdyne Å for angle deformation force constants.

b) All force constants that are equivalent under C<sub>3v</sub> symmetry were given the same value under C<sub>s</sub> symmetry.

Table 6.9

Experimental Frequencies and Assignment for  
Gaseous  $^{32}\text{S}^{35}\text{Cl}_3$ , and Calculated Frequencies  
from Various Force Fields

Mode	Empirical Assignment	Frequencies <sup>b</sup> from Force Fields <sup>b</sup>					Final Experimental
		1	2	3	4	5	
$\nu_1(A_1)$	P=S stretch	803.2	750.7	750.6	757.9	769.6	769.6
$\nu_2(A_1)$	P-Cl stretch	374.6	386.3	430.2	438.7	436.2	436.5
$\nu_3(A_1)$	Cl-P-Cl def.	195.6	241.4	245.2	248.6	251.4	251.4
$\nu_4(E)$	P-Cl stretch	531.4	578.1	544.3	541.1	548.8	548.8
$\nu_5(E)$	Cl-P-Cl def.	179.0	222.3	223.1	243.4	251.4	247.7 <sup>c</sup>
$\nu_6(E)$	S=P-Cl def.	134.8	175.0	174.6	174.8	171.0	171.0

a) Frequencies in  $\text{cm}^{-1}$

b) The force fields are defined in Table 6.8.

c) Force field 5 was developed using 251.4  $\text{cm}^{-1}$  for  $\nu_5(E)$  instead of 247.7  $\text{cm}^{-1}$ .

gave a fit of  $24 \text{ cm}^{-1}$  or 6%.

It was then necessary to add an interaction constant,  $f(\text{PCl}, \text{PCl}')$ , between the P-Cl stretching displacements, since the frequency calculated for the symmetric P-Cl stretching vibration was about  $50 \text{ cm}^{-1}$  too low and the value for the antisymmetric P-Cl stretching vibration was about  $30 \text{ cm}^{-1}$  too high. This interaction constant,  $f(\text{PCl}, \text{PCl}')$  was equal to  $0.25 \text{ mdyne } \text{Å}^{-1}$ , and this improved the fit to  $14 \text{ cm}^{-1}$  or 4%. Improvements were made by increasing  $f(\text{PCl}, \text{PCl}')$  to  $0.35 \text{ mdyne } \text{Å}^{-1}$ , and introducing an interaction constant between the P=S and P-Cl stretching displacements,  $f(\text{PS}, \text{PCl})$ , of  $0.12 \text{ mdyne } \text{Å}^{-1}$ , which gave a fit of  $10 \text{ cm}^{-1}$  or 3%. This is force field 3 of Tables 6.8 and 6.9.

The next stage of the refinement concentrated on the deformation vibrations. Under force field 3, the calculated frequency for the antisymmetric Cl-P-Cl deformation vibration was about  $20 \text{ cm}^{-1}$  too low, and the value for the S=P-Cl deformation vibration was slightly high (Table 6.9). Therefore interaction constants between the S=P-Cl and the Cl-P-Cl deformation displacements were each separately added to the force field. However, these interaction constants did not improve the fit, so they were set equal to zero and an interaction constant between the Cl-P-Cl deformation displacements,  $f(\text{ClPCl}', \text{Cl}'\text{PCl}'')$  was added. A value of  $-0.100 \text{ mdyne } \text{Å}$  lowered the symmetric Cl-P-Cl deformation

vibration and raised the antisymmetric Cl-P-Cl deformation vibration to about the same frequency. Since this was about  $20 \text{ cm}^{-1}$  below the observed frequencies, the diagonal Cl-P-Cl deformation force constant,  $f(\text{ClP-Cl})$ , was raised to  $1.75 \text{ mdyne } \text{\AA}^{\circ}$ , and the Cl-P-Cl deformation vibrations were then fitted to within  $3 \text{ cm}^{-1}$ . At this point, the frequencies for the symmetric and antisymmetric P-Cl stretching vibrations were slightly low and slightly high, at  $430$  and  $551 \text{ cm}^{-1}$ , respectively, so  $f(\text{P-Cl}, \text{P-Cl}')$  was raised slightly to  $0.45 \text{ mdyne } \text{\AA}^{\circ-1}$ , giving a fit of  $4.5 \text{ cm}^{-1}$  or 1.3%. This is force field 4 of Tables 6.8 and 6.9.

The programme VSEC had been used for the calculations up to this point. The manual control of force field modification is useful in the initial stages of a calculation, however, once a reasonable force field has been developed, the programme FPERT should quickly refine this to an optimum solution. Therefore force field 4 was used as input to a calculation using FPERT. This force field used seven force constants to calculate six frequencies for  $^{32}\text{SP}^{35}\text{Cl}_3$ , thus introducing an interdependence among the force constants. This was tolerated in the hope that FPERT would refine one of the interaction constants to the point where it could be set equal to zero. Further, essentially all of the force fields had calculated the separation between the symmetric P-Cl stretching frequencies of  $^{32}\text{SP}^{35}\text{Cl}_3$  and  $^{32}\text{SP}^{35}\text{Cl}_2^{37}\text{Cl}$  to be  $2.3$  to  $2.5 \text{ cm}^{-1}$ . This was taken as confirmation that

the second Q branch at  $433.6 \text{ cm}^{-1}$  in the spectrum of the gas (Fig. 6.5) is due to  $^{32}\text{SP}^{35}\text{Cl}_2^{37}\text{Cl}$ . This frequency was therefore added to the six frequencies of  $^{32}\text{SP}^{35}\text{Cl}_3$  as input data to FPERT.

The first FPERT calculation produced a fit of  $0.7 \text{ cm}^{-1}$  or 0.23% after two adjustments of the force constants. The only significant change in the force field was a 50% reduction of  $f(\text{PS}, \text{PCl})$  to a value of  $0.062 \text{ mdyne } \text{Å}^{-1}$ , which suggested that it could be set equal to zero, leaving  $f(\text{PCl}, \text{PCl}')$  and  $f(\text{ClPCl}', \text{Cl}'\text{PCl}'')$  as the only interaction constants. Before doing so, a second FPERT calculation was performed in which  $f(\text{PCl}, \text{PCl}')$  was set equal to zero, leaving only the interaction constants  $f(\text{PS}, \text{PCl})$  and  $f(\text{ClPCl}', \text{Cl}'\text{PCl}'')$ . Although a fit of  $0.8 \text{ cm}^{-1}$  was achieved,  $f(\text{PS}, \text{PCl})$  was refined to a value of  $1.075 \text{ mdyne } \text{Å}^{-1}$ , and contributed more than 55% to the potential energy of one normal vibration. Such a large contribution from an interaction constant is not consistent with our physical model of the forces which exist between atoms in a molecule. Therefore, it was decided to set  $f(\text{PS}, \text{PCl})$  equal to zero in the force field obtained from the first FPERT calculation.

Two subsequent calculations were performed using this force field. First  $\nu_3(\text{A}_1)$  and  $\nu_5(\text{E})$  were both assigned at  $251.4 \text{ cm}^{-1}$ , to calculate the isotopic splitting for this possible assignment. Four force constant adjustments were needed to obtain a fit of  $0.1 \text{ cm}^{-1}$  or 0.02%. The

resulting force field is force field 5 of Tables 6.8 and 6.9. The frequencies calculated for the six isotopic forms of thiophosphoryl chloride, from force field 5, are given in Table 6.10. Second,  $\nu_3(A_1)$  and  $\nu_5(E)$  were placed at 251.4 and 247.7  $\text{cm}^{-1}$ , respectively. A fit of 0.10  $\text{cm}^{-1}$  or 0.02% was obtained after four force constant adjustments. This gave the final force field of Tables 6.8 and 6.9.

The calculated frequencies for the six isotopic forms of thiophosphoryl chloride for this force field are given in Table 6.11. The justification for calling this the final force field will be discussed in Section 6.5. The eigenvectors from this force field are listed in Appendix II.

The potential energy distributions for the normal vibrations can be described with respect to both the force constants for the internal coordinates and those for the symmetry coordinates, that is, with respect to the elements of  $F$  and those of  $F_s$ . Conventionally, vibrations are qualitatively described by the symmetry coordinates which most closely approximate the normal coordinates. For this reason, the potential energy distributions will be given in terms of the symmetrised force constants. Tables 6.12 and 6.13 give the potential energy distributions for the two most abundant molecules,  $^{32}\text{SP}^{35}\text{Cl}_3$  and  $^{32}\text{SP}^{35}\text{Cl}_2^{37}\text{Cl}$ , while those for  $^{32}\text{SP}^{35}\text{Cl}^{37}\text{Cl}_2$ ,  $^{32}\text{SP}^{37}\text{Cl}_3$ ,  $^{34}\text{SP}^{35}\text{Cl}_3$  and  $^{34}\text{SP}^{35}\text{Cl}_2^{37}\text{Cl}$  are listed in Appendix III. These potential energy distributions show that the normal coordinate

Table 6.10

Calculated Frequencies for Six Isotopic Forms of Thiophosphoryl Chloride from Force Field 5<sup>a,b</sup>

C <sub>3v</sub> Mode	<sup>32</sup> SP <sup>35</sup> Cl <sub>3</sub>	<sup>32</sup> SP <sup>35</sup> Cl <sub>2</sub> <sup>37</sup> Cl	<sup>52</sup> SP <sup>35</sup> Cl <sup>37</sup> Cl <sub>2</sub>	<sup>32</sup> SP <sup>37</sup> Cl <sub>3</sub>	<sup>34</sup> SP <sup>35</sup> Cl <sub>3</sub>	<sup>34</sup> SP <sup>35</sup> Cl <sub>2</sub> <sup>37</sup> Cl	C <sub>s</sub> Mode
$\nu_1(A_1)$	769.6	768.8	767.9	767.0	766.0	765.1	$\nu_1(A')$
$\nu_2(A_1)$	436.2	433.8	431.5	429.2	430.8	428.5	$\nu_3(A')$
$\nu_3(A_1)$	251.4	251.2	249.2	246.8	249.6	250.5	$\nu_4(A')$
$\nu_4(E)$	548.8	546.1	547.2	544.4	548.8	546.1	$\nu_2(A')$
$\nu_5(E)$	251.4	248.2	245.7	244.7	251.4	247.2	$\nu_5(A')$
$\nu_6(E)$	171.0	170.9	170.2	168.7	168.9	167.3	$\nu_6(A')$
		170.9	168.7	168.8	168.8	168.8	$\nu_9(A'')$
						248.8	$\nu_8(A'')$
						548.2	$\nu_7(A'')$

a) Of Tables 6.8 and 5.9.

b) Frequencies in cm<sup>-1</sup>.

Table 6.11

Calculated Frequencies for Six Isotopic Forms of

Thiophosphoryl Chloride from the Final Force Field <sup>a,b</sup>

<sup>C<sub>3v</sub></sup> Mode	<sup>32</sup> SP <sup>35</sup> Cl <sub>3</sub>	<sup>32</sup> SP <sup>35</sup> Cl <sub>2</sub> <sup>37</sup> Cl	<sup>32</sup> SP <sup>37</sup> Cl <sup>37</sup> Cl <sub>2</sub>	<sup>32</sup> SP <sup>37</sup> Cl <sub>3</sub>	<sup>34</sup> SP <sup>35</sup> Cl <sub>3</sub>	<sup>34</sup> SP <sup>35</sup> Cl <sub>2</sub> <sup>37</sup> Cl	<sup>C<sub>s</sub></sup> Mode
$\nu_1(A_1)$	769.6	768.8	767.9	767.0	766.0	765.1	$\nu_1(A')$
$\nu_2(A_1)$	436.2	433.8	431.5	429.2	430.8	428.5	$\nu_3(A')$
$\nu_3(A_1)$	251.4	250.4	248.7	246.8	249.5	248.8	$\nu_4(A')$
$\nu_4(E)$	548.8	546.1	547.2	544.3	548.8	546.0	$\nu_2(A')$
$\nu_5(E)$	247.7	245.4	242.5	241.2	247.7	245.2	$\nu_5(A')$
$\nu_6(E)$	171.0	169.5	170.2	168.7	168.9	167.3	$\nu_6(A')$
		170.9	168.7			168.8	$\nu_9(A'')$
			243.8			245.1	$\nu_8(A'')$

a) Of Tables 6.8 and 6.9.

b) Frequencies in  $\text{cm}^{-1}$ .



Table 6.12

Potential Energy Distribution<sup>a</sup> between the Diagonal Elements of the Symmetrised Force Constant Matrix<sup>b</sup> for  $^{32}\text{SP}^{35}\text{Cl}_3$

(i)  $A_1$  Vibrations

Mode	Frequency <sup>c</sup>	Contribution from force constant			
		$f(S_1)$	$f(S_2)$	$f(S_3)$	$f(S_4)$
$\nu_1$	769.6	36.07	50.64	11.91	0.14
$\nu_2$	436.2	58.56	41.43	0.00	0.00
$\nu_3$	251.4	5.37	7.92	77.67	0.94

## (ii) E Vibrations

Mode	Frequency <sup>c</sup>	Contribution from force constant		
		$f(S_5)$	$f(S_6)$	$f(S_7)$
$\nu_4$	548.8	79.11	14.10	6.79
$\nu_5$	247.7	15.48	84.49	0.03
$\nu_6$	171.0	5.42	1.41	93.18

a). As percentages.

b)  $\underline{F}_S = \underline{U}\underline{F}\underline{U}^t$  where  $\underline{U}$  is defined by the symmetry coordinates in Table 6.6.

c) Calculated frequency in  $\text{cm}^{-1}$  from final force field.

Table 6.13

Potential Energy Distribution<sup>a</sup> between the  
Diagonal Elements of the Symmetrised Force  
Constant Matrix<sup>b</sup> for  $^{32}\text{S}^{35}\text{Cl}_2^{37}\text{Cl}$

(i) A' Vibrations

Mode	Frequency <sup>c</sup>	Contribution from force constant						
		f(S <sub>1</sub> )	f(S <sub>2</sub> )	f(S <sub>3</sub> )	f(S <sub>4</sub> )	f(S <sub>5</sub> )	f(S <sub>6</sub> )	f(S <sub>7</sub> )
v <sub>1</sub>	768.8	20.73	8.04	50.98	7.66	4.14	1.65	0.84
v <sub>2</sub>	546.1	41.33	65.08	0.03	4.45	8.93	2.37	4.58
v <sub>3</sub>	433.8	32.12	14.89	41.22	0.01	0.01	0.00	0.01
v <sub>4</sub>	250.4	6.41	0.00	7.08	26.49	51.75	9.73	4.84
v <sub>5</sub>	245.4	4.38	14.99	0.69	48.39	28.05	1.24	0.36
v <sub>6</sub>	169.5	2.79	4.77	0.00	0.47	0.81	30.76	62.25

(ii) A'' Vibrations

Mode	Frequency <sup>c</sup>	Contribution from force constant		
		f(S <sub>8</sub> )	f(S <sub>9</sub> )	f(S <sub>10</sub> )
v <sub>7</sub>	548.6	79.25	13.95	6.80
v <sub>8</sub>	245.1	15.42	84.52	0.06
v <sub>9</sub>	170.9	5.33	1.53	93.14

a) As percentages.

b)  $F_s = UFU^t$  where U is defined by the symmetry coordinates in Table 6.7.c) Calculated frequency in  $\text{cm}^{-1}$  from final force field.

calculation reproduces the experimental assignment well, although some mixing of symmetry coordinates does occur in the normal coordinates. For example, for  $^{32}\text{S}^{35}\text{Cl}_3$  (Table 6.12), the P=S stretching vibration,  $\nu_1(A_1)$ , and the symmetric P-Cl stretching vibration,  $\nu_2(A_1)$ , are both heavily dependent on the force constants for the P=S and symmetric P-Cl stretching displacements, with  $\nu_1(A_1)$  being more dependent on the P=S stretching displacement and  $\nu_2(A_1)$  being more dependent on the P-Cl stretching displacement. Thus,  $\nu_1(A_1)$  is predominantly the P=S stretching vibration, and  $\nu_2(A_1)$  is predominantly the P-Cl stretching vibration, as they were assigned by Gerding and Westrik (109). For the other vibrations, the potential energy distributions indicate that at least 75% of their potential energy is derived from the symmetry coordinate used in the empirical assignment.

## 6.5 Discussion

### 6.5.1 Cl-P-Cl Deformation Vibrations

The experimental results of Section 6.3 clearly demonstrated that at least two vibrations of thiophosphoryl chloride absorb near  $250 \text{ cm}^{-1}$ . These two vibrations could be the symmetric and antisymmetric Cl-P-Cl deformation vibrations, or they could be just one of these vibrations in two isotopic molecules. The results are interpreted below to indicate rather clearly that the symmetric and antisymmetric Cl-P-Cl deformation vibrations both absorb near  $250 \text{ cm}^{-1}$ . The individual steps in the interpretation are not definitive, most of the facts being capable of alternative interpretation, but taken together they indicate that this interpretation is by far the most probable.

The natural abundances of  $^{32}\text{SP}^{35}\text{Cl}_3$ ,  $^{32}\text{SP}^{35}\text{Cl}_2^{37}\text{Cl}$  and  $^{32}\text{SP}^{35}\text{Cl}^{37}\text{Cl}_2$  are in the approximate ratio 3:3:1. Thus the symmetric Cl-P-Cl deformation vibrations,  $\nu_3(A_1)$  of  $^{32}\text{SP}^{35}\text{Cl}_3$  and  $\nu_4(A')$  of  $^{32}\text{SP}^{35}\text{Cl}_2^{37}\text{Cl}$  can be expected to yield bands of approximately the same integrated intensities, since the presence of the  $^{37}\text{Cl}$  atom is not expected to change the dipole moment derivative with respect to the normal coordinate greatly. Further, both of these bands should be about three times as intense as the band from  $\nu_4(A')$  of  $\text{SP}^{35}\text{Cl}^{37}\text{Cl}_2$ . A similar result holds for the antisymmetric Cl-P-Cl deformation vibrations. The degenerate

pair of vibrations  $\nu_5(E)$  of  $^{32}\text{SP}^{35}\text{Cl}_3$  should yield about the same integrated intensity as the combined bands due to  $\nu_5(A')$  and  $\nu_8(A'')$  of  $^{32}\text{SP}^{35}\text{Cl}_2^{37}\text{Cl}$ , and should be about three times more intense than the combined bands due to  $\nu_5(A')$  and  $\nu_8(A'')$  of  $^{32}\text{SP}^{35}\text{Cl}^{37}\text{Cl}_2$ . Thus to interpret the doublet seen in the spectrum of thiophosphoryl chloride adsorbed on polyethylene (Fig. 6.3, curve C), only the vibrations of  $\text{SP}^{35}\text{Cl}_3$  and  $\text{SP}^{35}\text{Cl}_2^{37}\text{Cl}$  need be considered.

The frequencies calculated for these molecules, under two assumptions concerning the relative frequencies of  $\nu_3(A_1)$  and  $\nu_5(E)$  of  $\text{SP}^{35}\text{Cl}_3$ , are shown in Tables 6.10 and 6.11. Further evidence is provided in Table 6.14 which shows the frequencies calculated from a diagonal force field, force field 2 of Tables 6.8 and 6.9, and those calculated from force field 6, which placed  $\nu_3(A_1)$  at  $247.7 \text{ cm}^{-1}$  and  $\nu_5(E)$  at  $251.4 \text{ cm}^{-1}$ , the reverse of the assignment used for the final force field of Section 6.4. In no case did the frequency difference between  $\nu_3(A_1)$  of  $^{32}\text{SP}^{35}\text{Cl}_3$  and  $\nu_4(A')$  of  $^{32}\text{SP}^{35}\text{Cl}_2^{37}\text{Cl}$  exceed  $2.1 \text{ cm}^{-1}$ , so it is extremely improbable that the observed doublet (Fig. 6.3, curve C) split by  $3.7 \text{ cm}^{-1}$  is due to these two vibrations. The accuracy of the observed  $3.7 \text{ cm}^{-1}$  separation is  $\pm 0.2 \text{ cm}^{-1}$ , and the fact that so many varied force fields all gave a splitting of about 50% or less of the observed value is good, but not absolutely definitive, evidence for this conclusion. With slightly less confidence,

Table 6.14

Calculated Frequencies<sup>a</sup> for  $^{32}\text{SP}^{35}\text{Cl}_3$  and  
 $^{32}\text{SP}^{35}\text{Cl}_2^{37}\text{Cl}$  using Force Fields 2<sup>b</sup> and 6

$C_{3v}$ Mode	Force Field 2		Force Field 6		$C_s$ Mode
	$^{32}\text{SP}^{35}\text{Cl}_3$	$^{32}\text{SP}^{35}\text{Cl}_2^{37}\text{Cl}$	$^{32}\text{SP}^{35}\text{Cl}_3$	$^{32}\text{SP}^{35}\text{Cl}_2^{37}\text{Cl}$	
$\nu_1(A_1)$	750.7	750.3	769.6	768.8	$\nu_1(A')$
$\nu_2(A_1)$	386.3	384.2	436.2	433.8	$\nu_3(A')$
$\nu_3(A_1)$	241.4	239.9	247.7	250.1	$\nu_4(A')$
		574.8		546.1	$\nu_2(A')$
$\nu_4(E)$	578.1		548.8		
		578.0		548.6	$\nu_7(A'')$
		220.8		245.6	$\nu_5(A')$
$\nu_5(E)$	222.3		251.4		
		220.1		248.8	$\nu_8(A'')$
		173.5		169.5	$\nu_6(A')$
$\nu_6(E)$	175.0		171.0		
		174.9		170.9	$\nu_9(A'')$

a) In  $\text{cm}^{-1}$ .

b) Of Table 6.8.

the same arguments indicate that the doublet is not due to the antisymmetric Cl-P-Cl deformation vibration,  $\nu_5(E)$ , of  $^{32}\text{SP}^{35}\text{Cl}_3$  and the unresolved pair,  $\nu_5(A')$  and  $\nu_8(A'')$ , of  $^{32}\text{SP}^{35}\text{Cl}_2^{37}\text{Cl}$ . The largest separation calculated for this case was  $2.8 \text{ cm}^{-1}$ , obtained using the assumption that  $\nu_3(A_1)$  and  $\nu_5(E)$  are accidentally degenerate at  $251.4 \text{ cm}^{-1}$ . This is still nearly 30% below the observed separation, making it improbable that the antisymmetric stretching mode alone can be responsible for the doublet. Thus it is concluded that the symmetric and the antisymmetric Cl-P-Cl deformation modes most probably both contribute to the doublet seen for thiophosphoryl chloride adsorbed on polyethylene.

In the infrared spectrum of the gas, the Q branch at  $251.4 \text{ cm}^{-1}$  and the peak of the R branch at  $258.3 \text{ cm}^{-1}$  are separated by  $6.9 \text{ cm}^{-1}$ . If it is assumed that the upper and lower state rotational constants for  $\nu_3(A_1)$  are the same, then the value calculated (139), from the moments of inertia given in Table 6.4, for the separation is  $6.2 \text{ cm}^{-1}$ . This value is in reasonably good agreement with the observed Q to R separation of  $5.9 \text{ cm}^{-1}$  for  $\nu_1(A_1)$ , and an average value of  $5.7 \text{ cm}^{-1}$  for  $\nu_2(A_1)$  of  $^{32}\text{SP}^{35}\text{Cl}_3$  and  $\nu_3(A')$  of  $^{32}\text{SP}^{35}\text{Cl}_2^{37}\text{Cl}$ . Thus it is most probable that the Q and R branches at  $251.4$  and  $258.3 \text{ cm}^{-1}$  are due to the symmetric Cl-P-Cl deformation vibration,  $\nu_3(A_1)$  of  $^{32}\text{SP}^{35}\text{Cl}_3$ .

Further,  $\nu_4(A')$  of  $^{32}\text{SP}^{35}\text{Cl}_2^{37}\text{Cl}$  is expected to yield a PQR band contour, and all of the calculations from force fields containing six force constants indicate that it lies within  $1.2\text{ cm}^{-1}$  of  $\nu_3(A_1)$  of  $^{32}\text{SP}^{35}\text{Cl}_3$ , which would make its Q branch merge with that of  $\nu_3(A_1)$ . The Q-R separation expected for  $\nu_4(A')$  of  $^{32}\text{SP}^{35}\text{Cl}_2^{37}\text{Cl}$  is about  $6.5\text{ cm}^{-1}$ , so that its R branch also coincides with that of  $\nu_3(A_1)$ . Thus, this most probable assignment is completely consistent with the spectra.

The second Q branch at  $247.7\text{ cm}^{-1}$  in the infrared spectrum of the gas (Fig. 6.3, curve A) must also be explained. It can be assigned to  $\nu_5(A')$  and  $\nu_8(A'')$  of  $\text{SP}^{35}\text{Cl}_2^{37}\text{Cl}$  by the following argument. The final force field places these two vibrations within  $0.3\text{ cm}^{-1}$  of each other, about  $2.5\text{ cm}^{-1}$  to low frequency of  $\nu_5(E)$  of  $^{32}\text{SP}^{35}\text{Cl}_3$ , and each of them should yield a PQR structured absorption band. They will, therefore, give a single PQR band contour whose integrated intensity should be about equal to that of the band due to  $\nu_5(E)$  of  $^{32}\text{SP}^{35}\text{Cl}_3$ . The Coriolis coupling constant for  $\nu_5(E)$  was calculated from the final force field to be  $-0.9$ , and this value was used in a computer programme written and described by Faniran and Shurvell (140) to calculate the contour of the band due to  $\nu_5(E)$ . The band was calculated to be broad, with a half-width of about  $33\text{ cm}^{-1}$ , and to show very weakly defined PQR structure on the top. Thus, the band due to  $\nu_5(E)$  of  $^{32}\text{SP}^{35}\text{Cl}_3$



should have a much lower peak absorbance than the Q branch of the band due to  $\nu_5(A')$  and  $\nu_8(A'')$  of  $^{32}\text{SP}^{35}\text{Cl}_2^{37}\text{Cl}$ , since the same integrated intensity is spread out into a broad band with little structure in the former and is concentrated in well defined P, Q and R branches in the latter. Therefore the Q branch at  $247.7\text{ cm}^{-1}$  in the absorption spectrum of gaseous thiophosphoryl chloride is logically assigned to  $\nu_5(A')$  combined with  $\nu_8(A'')$  of  $^{32}\text{SP}^{35}\text{Cl}_2^{37}\text{Cl}$ , and  $\nu_5(E)$  of  $^{32}\text{SP}^{35}\text{Cl}_3$  is sufficiently broad and less intense that it does not contribute to the profile of the band. The calculations indicate that  $\nu_5(E)$  of  $\text{SP}^{35}\text{Cl}_3$  must be at about  $250\text{ cm}^{-1}$  if  $\nu_5(A')$  and  $\nu_8(A'')$  of  $\text{SP}^{35}\text{Cl}_2^{37}\text{Cl}$  are at  $247.7\text{ cm}^{-1}$ .

This assignment of the infrared spectrum of the gas is, unfortunately, not definitive, because the Q and R branches at  $251.4$  and  $258.3\text{ cm}^{-1}$  could arise from  $\nu_5(A')$  and  $\nu_8(A'')$  of  $^{32}\text{SP}^{35}\text{Cl}_2^{37}\text{Cl}$ , with the lower frequency Q branch arising from  $\nu_3(A_1)$  of  $^{32}\text{SP}^{35}\text{Cl}_3$ . This alternative assignment is considered less likely because a strong R branch is not expected (81) from the bands due to  $\nu_5(A')$  and  $\nu_8(A'')$  in a first approximation. Although this argument by itself is not strong, it does combine with the evidence to be presented from the Raman spectra to make the first assignment presented above by far the most probable.

The Raman spectrum of the liquid shows a depolarised

band at  $247 \text{ cm}^{-1}$ . In general, this could arise from a totally symmetric or a non-totally symmetric mode, but for a molecule that has symmetry as high as  $C_{3v}$ , it is more likely to arise from a non-totally symmetric mode, in this case  $\nu_5(E)$  of  $^{32}\text{SP}^{35}\text{Cl}_3$ . The band must also contain the scattering by  $\nu_5(A')$  and  $\nu_8(A'')$  of  $^{32}\text{SP}^{35}\text{Cl}_2^{37}\text{Cl}$  since it was not observed separately. This interpretation implies that the scattering by the totally symmetric vibration,  $\nu_5(A')$ , is insufficiently polarised to cause the observed band to be partly polarised. It is more likely that a totally symmetric vibration of a molecule of  $C_s$  symmetry would yield a weakly polarised band than an  $A_1$  vibration of a molecule of  $C_{3v}$  symmetry. This interpretation also implies that the symmetric deformation vibrations,  $\nu_3(A_1)$  of  $^{32}\text{SP}^{35}\text{Cl}_3$  and  $\nu_4(A')$  of  $^{32}\text{SP}^{35}\text{Cl}_2^{37}\text{Cl}$  are too weak to be seen in the Raman effect.

The Raman spectrum of gaseous thiophosphoryl chloride at  $185^\circ\text{C}$  has been reported by Clark and Rippon (115), and Dr. M. V. Falk, of this laboratory, has obtained the Raman spectrum of the gas at  $25^\circ\text{C}$ . Falk observed bands with contours very similar to those reported at  $246.0$  and  $167.3 \text{ cm}^{-1}$  by Clark and Rippon. The contours of these two bands are very similar, both consisting of a Q branch flanked by strong side branches, and both bands are depolarised. The main difference between the two bands is the separation of the P and R peaks, which is about  $12 \text{ cm}^{-1}$  for the band

at  $246.0 \text{ cm}^{-1}$  and about  $17 \text{ cm}^{-1}$  for the band at  $167.3 \text{ cm}^{-1}$ . Clark and Rippon noted that the P-R separations are usually highly variable for E modes of the same molecule. The band at  $167.3 \text{ cm}^{-1}$  must be assigned to  $\nu_6(\text{E})$  of  $^{32}\text{SP}^{35}\text{Cl}_3$ , and  $\nu_6(\text{A}')$  and  $\nu_9(\text{A}'')$  of  $^{32}\text{SP}^{35}\text{Cl}_2^{37}\text{Cl}$ , so the band at  $246.0 \text{ cm}^{-1}$  is most logically assigned to  $\nu_5(\text{E})$  of  $^{32}\text{SP}^{35}\text{Cl}_3$ , and  $\nu_5(\text{A}')$  and  $\nu_8(\text{A}'')$  of  $^{32}\text{SP}^{35}\text{Cl}_2^{37}\text{Cl}$ . At  $25^\circ\text{C}$ , the Q branch of the latter band was found at  $247.1 \pm 0.4 \text{ cm}^{-1}$ , in agreement with the  $247.7 \pm 0.3 \text{ cm}^{-1}$  in the infrared spectrum. Thus the Raman spectra of both the gas phase and liquid phase are consistent with the assignment proposed previously from the infrared spectra. Thus  $\nu_3(\text{A}_1)$  of  $^{32}\text{SP}^{35}\text{Cl}_3$  and  $\nu_4(\text{A}')$  of  $^{32}\text{SP}^{35}\text{Cl}_2^{37}\text{Cl}$  are assigned at  $251.4 \text{ cm}^{-1}$ , and  $\nu_5(\text{A}')$  and  $\nu_8(\text{A}'')$  of  $^{32}\text{SP}^{35}\text{Cl}_2^{37}\text{Cl}$  are assigned at  $247.7 \text{ cm}^{-1}$  in the infrared spectrum of the gas at  $25^\circ\text{C}$ . The remaining fundamental,  $\nu_5(\text{E})$  of  $^{32}\text{SP}^{35}\text{Cl}_3$ , is expected (Table 6.11) to be about  $2.5 \text{ cm}^{-1}$  above the frequency for the unresolved pair  $\nu_5(\text{A}')$  and  $\nu_8(\text{A}'')$ , so it should yield a broad band centered at approximately  $250 \text{ cm}^{-1}$ .

In contrast to the above assignment, Clark and Rippon (115) assigned the depolarised band at  $246.0 \text{ cm}^{-1}$  in the Raman spectrum of the gas to  $\nu_3(\text{A}_1)$ . The basis for this assignment was their inability to reproduce the observed band contour under the assumption that the fundamental, with its associated rotational branches, was  $\nu_5(\text{E})$ . They noted that the P-R, O-P and R-S observed separations are

consistent with those expected for an  $A_1$  mode of thiophosphoryl chloride at 185°C. They also noted that the fact that the 246.0  $\text{cm}^{-1}$  band is depolarised is not definitive evidence for its assignment to a non-totally symmetric vibration, since totally symmetric bending modes of two other  $XYZ_3$  symmetric top molecules that they studied (115) had depolarisation ratios very close to 0.75. However, the totally symmetric bending modes of the six remaining  $XYZ_3$  symmetric top molecules studied by Clark and co-workers (115, 141) have depolarisation ratios considerably below 0.75.

Clark and Rippon's failure to reproduce the observed band contour at 246.0  $\text{cm}^{-1}$ , under the assumption that the band was due to  $\nu_5(E)$ , is understandable since they neglected the bands due to the equally abundant  $^{32}\text{P}^{35}\text{Cl}_2^{37}\text{Cl}$  species. The following evidence strongly suggests that bands due to  $^{32}\text{P}^{35}\text{Cl}_2^{37}\text{Cl}$  do contribute to the observed band contours. Clark and Rippon (115) did not reproduce by calculation the observed band contour for  $\nu_6(E)$  of thiophosphoryl chloride, and they attributed this to an insufficiency of detail in the band contour for an accurate analysis. However, they did successfully calculate the nearly identical band contour of  $\nu_6(E)$  of phosphorus oxytrifluoride, where complications due to naturally abundant isotopic modifications are absent. This strongly suggests that the neglect of such isotopic modifications in the thiophosphoryl chloride case, was the reason for

failure.

With this very plausible reason for the failure of the band contour calculation, the assignment of  $\nu_3(A_1)$  to the band at  $246.0 \text{ cm}^{-1}$  becomes very suspect for the following reasons. First, the depolarised band at  $167.3 \text{ cm}^{-1}$  must be due to  $\nu_6(E)$  of  $^{32}\text{SP}^{35}\text{Cl}_3$ , and  $\nu_6(A')$  and  $\nu_9(A'')$  of  $^{32}\text{SP}^{35}\text{Cl}_2^{37}\text{Cl}$ , and so the very similarly contoured, depolarised band at  $246.0 \text{ cm}^{-1}$  is most logically assigned to  $\nu_5(E)$  of  $^{32}\text{SP}^{35}\text{Cl}_3$ , and  $\nu_5(A')$  and  $\nu_8(A'')$  of  $^{32}\text{SP}^{35}\text{Cl}_2^{37}\text{Cl}$ . Second, Clark and Rippon (115) report the band contours for 18  $A_1$  modes of six symmetric top molecules, and everyone, except the one assigned by them at  $246.0 \text{ cm}^{-1}$  for thiophosphoryl chloride, has a strong or very strong Q branch relative to its side branches even in cases where the depolarisation ratio is close to 0.75. This observation very strongly suggests that a non-totally symmetric mode is located at  $246.0 \text{ cm}^{-1}$ .

In summary, the most logical assignment from the evidence presented is that  $\nu_3(A_1)$  of  $^{32}\text{SP}^{35}\text{Cl}_3$  and  $\nu_4(A')$  of  $^{32}\text{SP}^{35}\text{Cl}_2^{37}\text{Cl}$  lie within  $1 \text{ cm}^{-1}$  of each other at  $251.4 \text{ cm}^{-1}$ , and that  $\nu_5(A')$  and  $\nu_8(A'')$  of  $^{32}\text{SP}^{35}\text{Cl}_2^{37}\text{Cl}$  lie within  $0.25 \text{ cm}^{-1}$  of each other at  $247.7 \text{ cm}^{-1}$ . The results of the normal coordinate calculation then place  $\nu_5(E)$  of  $^{32}\text{SP}^{35}\text{Cl}_3$  at about  $250 \text{ cm}^{-1}$ .

#### 6.5.2 Other Fundamental Vibrations

In Section 6.3.3, the structure seen on the absorption

band of gaseous thiophosphoryl chloride (Fig. 6.5, curve A), and on the Raman band of liquid thiophosphoryl chloride (Fig. 6.5, curve B), due to the symmetric P-Cl stretching mode, was assigned to the different isotopic species present. The separation of the Q branches in the spectrum of the gas (Fig. 6.5, curve A) is  $2.9 \text{ cm}^{-1}$ , which can be compared to the value of  $2.4 \text{ cm}^{-1}$  (Table 6.11), calculated for the separation of the bands due to  $^{32}\text{SP}^{35}\text{Cl}_3$  and  $^{32}\text{SP}^{35}\text{Cl}_2^{37}\text{Cl}$  from the final force field of Table 6.8. The accuracy of the measured  $2.9 \text{ cm}^{-1}$  difference is  $\pm 0.2 \text{ cm}^{-1}$  so the calculations clearly support the assignment of the two Q branches to the symmetric P-Cl stretching vibrations of  $^{32}\text{SP}^{35}\text{Cl}_3$  and  $^{32}\text{SP}^{35}\text{Cl}_2^{37}\text{Cl}$ . The calculated decreases in frequency of  $2.4$  and  $2.3 \text{ cm}^{-1}$  with each substitution of a  $^{37}\text{Cl}$  atom (Table 6.11) can be compared to the observed decreases of  $2.3 \pm 0.5 \text{ cm}^{-1}$  and  $3 \pm 0.5 \text{ cm}^{-1}$  in the Raman spectrum of the liquid (Fig. 6.5, curve B). Further, the relative intensities of the bands at  $433.3$ ,  $431$  and  $428 \text{ cm}^{-1}$  in the Raman spectrum of the liquid are in approximate agreement with the ratio 3:3:1 of the natural abundances of  $\text{SP}^{35}\text{Cl}_3$ ,  $\text{SP}^{35}\text{Cl}_2^{37}\text{Cl}$  and  $\text{SP}^{35}\text{Cl}^{37}\text{Cl}_2$ . Thus these bands can surely be assigned to the symmetric P-Cl stretching vibrations of  $^{32}\text{SP}^{35}\text{Cl}_3$ ,  $^{32}\text{SP}^{35}\text{Cl}_2^{37}\text{Cl}$  and  $^{32}\text{SP}^{35}\text{Cl}^{37}\text{Cl}_2$  respectively.

Another feature which may reflect an isotopic splitting is a weak Q-branch at  $763.71 \text{ cm}^{-1}$  in the spectrum

of gaseous thiophosphoryl chloride (Fig. 6.6),  $6.5 \text{ cm}^{-1}$  lower than the main Q branch. The calculations from the final force field (Table 6.11) indicate an isotopic splitting for  $\nu_1(A_1)$ , the P=S stretching vibration, of  $3.6 \text{ cm}^{-1}$  for  $^{34}\text{SP}^{35}\text{Cl}_3$ ,  $4.5 \text{ cm}^{-1}$  for  $^{34}\text{SP}^{35}\text{Cl}_2^{37}\text{Cl}$ ,  $0.8 \text{ cm}^{-1}$  for  $^{32}\text{SP}^{35}\text{Cl}_2^{37}\text{Cl}$  and  $1.7 \text{ cm}^{-1}$  for  $^{32}\text{SP}^{35}\text{Cl}^{37}\text{Cl}_2$ , with respect to  $^{32}\text{SP}^{35}\text{Cl}_3$ . It is therefore probable that the weak Q branch is due to a hot band, and not to isotopic splitting. The  $0.8 \text{ cm}^{-1}$  calculated difference between  $\nu_1(A')$  of  $^{32}\text{SP}^{35}\text{Cl}_2^{37}\text{Cl}$  is consistent with the observed unresolved superposition of the PQR band contours for these two modes, since the observed Q branch has a half width of about  $2 \text{ cm}^{-1}$ .

The observed band contour for the antisymmetric P-Cl stretching mode,  $\nu_4(E)$ , is shown in Fig. 6.6. A poorly resolved doublet split by  $2.8 \text{ cm}^{-1} \pm 0.2 \text{ cm}^{-1}$ , is seen in the weakly absorbing sample and a definite indication of a doublet is seen in the strongly absorbing sample. The calculations predict that  $\nu_4(E)$  of  $^{32}\text{SP}^{35}\text{Cl}_3$  and  $\nu_7(A'')$  of  $^{32}\text{SP}^{35}\text{Cl}_2^{37}\text{Cl}$  will be within  $0.2 \text{ cm}^{-1}$  of each other, with  $\nu_2(A')$  of  $^{32}\text{SP}^{35}\text{Cl}_2^{37}\text{Cl}$   $2.5 \text{ cm}^{-1}$  to low frequency of  $\nu_7(A'')$ . An approximate band contour calculation (140) was performed for  $\nu_4(E)$  of  $^{32}\text{SP}^{35}\text{Cl}_3$ , using a Coriolis constant, which was calculated from the final force field, of 0.8, which is close to Cyvin's (123) value of 0.73. A broad band with a half-width of about  $15 \text{ cm}^{-1}$  and very

poorly resolved PQR structure resulted. The band contours expected (81) for  $\nu_2(A')$  and  $\nu_7(A'')$  of  $^{32}\text{S}^{35}\text{Cl}_2^{37}\text{Cl}$  show a well defined PQR structure (81), and each should have an integrated intensity equal to one half of that of  $\nu_5(E)$ . Thus the bands at 550.5 and 547.7  $\text{cm}^{-1}$  are most reasonably assigned to  $\nu_7(A'')$  and  $\nu_2(A')$  of  $^{32}\text{S}^{35}\text{Cl}_2^{37}\text{Cl}$ , respectively. The half-width observed for the band was about 15  $\text{cm}^{-1}$ , in excellent agreement with the predicted value, and this breadth must be mainly due to  $\nu_4(E)$  of  $^{32}\text{S}^{35}\text{Cl}_3$  which, from the normal coordinate calculations, should be centered at about 551  $\text{cm}^{-1}$ .

Table 6.15 gives the assignment of the fundamental vibrations in the infrared spectrum of gaseous thiophosphoryl chloride and the Raman spectrum of liquid thiophosphoryl chloride. The percentage contributions to the potential energy of the vibrations by the various symmetrised force constants, taken from Tables 6.12 and 6.13, have been quoted to the nearest 5%, and only those contributions greater than 20% have been included. The mid-infrared frequencies are believed to be accurate to  $\pm 0.5 \text{ cm}^{-1}$ , and the far-infrared frequencies to  $\pm 0.3 \text{ cm}^{-1}$ . The Raman frequencies are believed to be accurate to  $\pm 1 \text{ cm}^{-1}$ , with the exception of the bands at 747 and 537  $\text{cm}^{-1}$ , where the broad, asymmetric contours of the bands makes it difficult to estimate the peak frequency.



Table 6.15  
Assignment of the Fundamental  
Vibrations of Thiophosphoryl Chloride

Mode <sup>b</sup>	Frequencies <sup>a</sup>		Assignment
	Raman <sup>c</sup> Liquid	Infrared <sup>c,d</sup> Gas	
$\nu_1(A_1) \left\{ \begin{matrix} 32 \\ 35 \end{matrix} \right. SP-Cl_3$	747 pol., w	775.5 R 769.6 Q s 762.8 P	50% P-S stretch 35% P-Cl stretch
$\nu_4(E) \left\{ \begin{matrix} 32 \\ 35 \end{matrix} \right. Cl_3$	537 depol., w	551 br	P-Cl stretch
$\nu_7(A^*) \left\{ \begin{matrix} 32 \\ 35 \end{matrix} \right. Cl_2 \left\{ \begin{matrix} 37 \\ 37 \end{matrix} \right. Cl$		550.5 Q s	antisym P-Cl stretch
$\nu_2(A^*) \left\{ \begin{matrix} 32 \\ 35 \end{matrix} \right. SP-Cl_2 \left\{ \begin{matrix} 37 \\ 37 \end{matrix} \right. Cl$		547.7 Q s	antisym. P-Cl stretch
$\nu_2(A_1) \left\{ \begin{matrix} 32 \\ 35 \end{matrix} \right. SP-Cl_3$	433.3 pol., s	440.6 R	$\left\{ \begin{matrix} 60\% \text{ P-Cl stretch} \\ 40\% \text{ P-S stretch} \\ 50\% \text{ sym. P-Cl stretch} \\ 40\% \text{ P-S stretch} \\ 50\% \text{ sym. P-Cl stretch} \\ 40\% \text{ P-S stretch} \end{matrix} \right.$
$\nu_3(A^*) \left\{ \begin{matrix} 32 \\ 35 \end{matrix} \right. SP-Cl_2 \left\{ \begin{matrix} 37 \\ 37 \end{matrix} \right. Cl$	431.0 pol., s	436.5 Q m	
$\nu_3(A^*) \left\{ \begin{matrix} 32 \\ 35 \end{matrix} \right. SP-Cl \left\{ \begin{matrix} 37 \\ 37 \end{matrix} \right. Cl_2$	428 pol., sh	433.6 Q m	
$\nu_3(A_1) \left\{ \begin{matrix} 32 \\ 35 \end{matrix} \right. SP-Cl_3$		258.3 R	$\left\{ \begin{matrix} Cl-P-Cl \text{ deformation} \\ Cl-P-Cl \text{ deformation} \end{matrix} \right.$
$\nu_5(E) \left\{ \begin{matrix} 32 \\ 35 \end{matrix} \right. SP-Cl_3$	247 depol., m	251.4 Q w	
$\nu_5(A^*) \left\{ \begin{matrix} 32 \\ 35 \end{matrix} \right. SP-Cl_2 \left\{ \begin{matrix} 37 \\ 37 \end{matrix} \right. Cl$		250 br	$\left\{ \begin{matrix} antisym. Cl-P-Cl \text{ deformation} \\ antisym. Cl-P-Cl \text{ deformation} \end{matrix} \right.$
$\nu_8(A^*) \left\{ \begin{matrix} 32 \\ 35 \end{matrix} \right. SP-Cl_2 \left\{ \begin{matrix} 37 \\ 37 \end{matrix} \right. Cl$		247.7 Q w	
$\nu_6(E) \left\{ \begin{matrix} 32 \\ 35 \end{matrix} \right. SP-Cl_3$	171.5 depol., m	—	S-P-Cl deformation

a) In  $cm^{-1}$

b) For conciseness, a band with unresolved isotopic components is assigned to  $32Sp35Cl_3$ .

c) Pol. = polarised; depol. = depolarised; s = strong; m = medium; w = weak; sh = shoulder.

d) P = P branch; Q = Q branch; R = R branch; br. = broad.

### References

1. A. J. Barnes in *Vibrational Spectroscopy of Trapped Species*, edited by H. E. Hallam, John Wiley & Sons 1973, Chapter 4.
2. A. D. Buckingham, *Proc. Roy. Soc. (London)*, A248, 169 (1958).
3. G. C. Pimentel and S. W. Charles, *Pure Appl. Chem.*, 7, 111 (1963).
4. C. B. Murchison and J. Overend, *Spectrochim. Acta*, 27A, 1509 (1971).
5. M. Allavena, R. Rysnik, D. White, V. Calder and D. E. Mann, *J. Chem. Phys.*, 50, 3399 (1969).
- ~~6. C. M. King and E. R. Nixon, *J. Chem. Phys.*, 48, 1685 (1968).~~
7. D. E. Palin and H. M. Powell, *J. Chem. Soc.*, 1947, 208 (1947).
8. W. C. Child jun., *Quart. Rev. Chem. Soc.*, 18, 321 (1964).
9. K. D. Cleaver, J. E. D. Davies and W. J. Wood, *J. Mol. Struct.*, 25, 222 (1975).
10. B. Kamb in *Physics and Chemistry of Ice*, edited by E. Whalley, S. J. Jones and L. W. Gold, Royal Society of Canada 1973, p. 28.
11. D. Eisenberg and W. Kauzmann, *The Structure and Properties of Water*, Oxford University Press, 1969.
12. E. Whalley in *Physics and Chemistry of Ice*, edited by

- E. Whalley, S. J. Jones and L. W. Gold, Royal Society of Canada 1973, p. 73, 87 and 93.
13. D. A. Othén, Ph.D thesis, University of Alberta, 1972.
  14. M. Solinas, Ph.D thesis, University of Alberta, 1973.
  15. E. Whalley in Developments in Applied Spectroscopy, edited by W. K. Bauer, A. J. Perkins and E. L. Grove, Plenum Press, New York 1968, 6, 277 (1967).
  16. J. E. Bertie, Appl. Spectrosc., 22, 634 (1968).
  17. H. Engelhardt and E. Whalley, J. Chem. Phys., 56, 2678 (1972).
  18. J. E. Bertie and E. Whalley, J. Chem. Phys., 46, 1271 (1967).
  19. J. E. Bertie, H. J. Labbé and E. Whalley, J. Chem. Phys., 49, 775 (1968).
  20. J. E. Bertie, H. J. Labbé and E. Whalley, J. Chem. Phys., 49, 2141 (1968).
  21. E. Whalley and J. E. Bertie, J. Chem. Phys., 46, 1264 (1967).
  22. G. Turrell, Infrared and Raman Spectra of Crystals, Academic Press, 1972.
  23. C. Kittel, Introduction to Solid State Physics, John Wiley & Sons, Inc., 1971, 4th edition.
  24. K. E. Larson and U. Dahlborg, J. Nucl. Energy Pt. A, B 16, 81 (1962).
  25. R. L. Stearns, H. R. Muether and H. Palevsky, Bull. Am. Phys. Soc., 6, 71 (1961).

26. A. B. D. Woods, B. N. Brockhouse, M. Sakamoto and R. N. Sinclair, Inelastic Scattering Neutrons Solids Liquids, Proc. Symp. Vienna, Austria, 1960, 487 (1961).
27. J. E. Bertie and E. Whalley, J. Chem. Phys., 40, 1637 (1964).
28. J. E. Bertie and E. Whalley, J. Chem. Phys., 40, 1646 (1964).
29. C. Haas and D. F. Hornig, J. Chem. Phys., 32, 1763 (1960).
30. F. E. Bates, Private communication.
31. J. E. Bertie, H. J. Labbé and E. Whalley, J. Chem. Phys., 50, 4501 (1969).
32. T. A. Ford and M. Falk, Can. J. Chem., 46, 3579 (1968)

---

33. D. F. Hornig, H. F. White and F. P. Reding, Spectrochim. Acta, 12, 338 (1958).
34. N. Ockman, Advan. Phys., 7, 199 (1958).
35. D. W. Davidson in Water, A Comprehensive Treatise, Vol. 2, edited by F. Franks, Plenum Press 1973, p. 119.
36. R. K. McMullan and G. A. Jeffrey, J. Chem. Phys., 42, 2725 (1965).
37. T. C. W. Mak and R. K. McMullan, J. Chem. Phys., 42, 2732 (1965).
38. Reference 35, p. 129.
39. Reference 35, p. 130.
40. Reference 35, p. 128.
41. Reference 35, p. 172.

42. Reference 35, p. 131.
43. J. E. Bertie and D. A. Othen, *Can. J. Chem.*, 50, 3443 (1972).
44. D. D. Klug and E. Whalley, *Can. J. Chem.*, 51, 4062 (1973).
45. R. E. Hawkins and D. W. Davidson, *J. Phys. Chem.*, 70, 1889 (1966).
46. J. E. Bertie, F. E. Bates and D. K. Hendricksen, *Can. J. Chem.*, 53, 71 (1975).
47. J. E. Bertie and M. Solinas, *Can. J. Chem.*, 53, 2642 (1975).
48. J. E. Bertie and D. A. Othen, *Can. J. Chem.*, 51, 1159 (1973).

---

49. J. E. Bertie and M. Solinas, *Can. J. Chem.*, 53, 2624 (1975).
50. Reference 35, p. 210.
51. W. H. Orrtung and J. A. Meyers, *J. Phys. Chem.*, 67, 1905 (1963).
52. J. A. Greenhouse and H. L. Strauss, *J. Chem. Phys.*, 50, 124 (1969).
53. J. C. Rosso and L. Carbonnel, *Compt. Rend. Acad. Sci. (Paris)*, 274C, 1108 (1972).
54. S. R. Gough, S. K. Garg and D. W. Davidson, *Chem. Phys.*, 3, 239 (1974).
55. D. F. Sargent and L. D. Calvert, *J. Phys. Chem.*, 70, 2689 (1966).

56. S. R. Gough, R. E. Hawkins, B. Morris and D. W. Davidson, *J. Phys. Chem.*, 77, 2969 (1973).
57. S. K. Garg and D. W. Davidson in *Physics and Chemistry of Ice*, edited by E. Whalley, S. J. Jones and L. W. Gold, Royal Society of Canada 1973, p. 56.
58. S. K. Garg and D. W. Davidson, *Chem. Phys. Letters*, 13, 73 (1972).
59. A. Danti, W. J. Lafferty and R. C. Lord, *J. Chem. Phys.*, 33, 294 (1960).
60. S. I. Chan, J. Zinn and W. D. Gwinn, *J. Chem. Phys.*, 33, 295 (1960).
61. S. I. Chan, T. R. Borgers, J. W. Russell, H. L. Strauss and W. D. Gwinn, *J. Chem. Phys.*, 44, 1103 (1966).

---

62. H. Wieser, M. Danyluk and R. A. Kydd, *J. Mol. Spectrosc.*, 43, 382 (1972).
63. R. A. Kydd, H. Wieser and M. Danyluk, *J. Mol. Spectrosc.*, 44, 14 (1972).
64. J. Jokisaari and J. Kauppinen, *J. Chem. Phys.*, 59, 2260 (1973).
65. W. Kiefer, H. J. Bernstein, M. Danyluk and H. Wieser, *Chem. Phys. Letters*, 12, 605 (1972).
66. W. Kiefer, H. J. Bernstein, H. Wieser and M. Danyluk, *J. Mol. Spectrosc.*, 43, 393
67. J. Fernandez, R. J. Meyer and W. D. Gwinn, *J. Chem. Phys.*, 23, 758 (1955).

68. S. I. Chan, J. Zinn, J. Fernandez and W. D. Gwinn, J. Chem. Phys., 33, 1643 (1960).
69. S. I. Chan, J. Zinn and W. D. Gwinn, J. Chem. Phys., 34, 1319 (1961).
70. K. W. F. Kohlrausch and A. W. Reitz, Z. Physik. Chem., 45B, 249 (1939).
71. G. M. Barrow and S. Searles, J. Am. Chem. Soc., 75, 1175 (1953).
72. R. F. Zürcher and Hs. H. Günthard, Helv. Chim. Acta, 38, 849 (1955).
73. R. F. Zürcher and Hs. H. Günthard, Helv. Chim. Acta, 40, 89 (1957).
74. W. J. Lafferty, Ph.D thesis, Massachusetts Institute of Technology, 1960.

---

75. T. Ueda and T. Shimanouchi, J. Chem. Phys., 47, 5018 (1967).
76. J. Le Brumant, Compt. Rend. Acad. Sci. (Paris), 267B, 946 (1968).
77. W. H. Green, J. Chem. Phys., 52, 2156 (1970).
78. H. Wieser and M. Danyluk, Can. J. Chem., 50, 2761 (1972).
79. H. Wieser, M. Danyluk, W. Kiefer and H. J. Bernstein, Can. J. Chem., 50, 2771 (1972).
80. H. Wieser, M. Danyluk, R. A. Kydd, W. Kiefer and H. J. Bernstein, J. Chem. Phys., 61, 4380 (1974).

81. T. Ueda and T. Shimanouchi, *J. Mol Spectrosc.*, 28, 350 (1968).
  82. R. Brille and A. Tippe, *Acta Cryst.*, 23, 343 (1967).
  83. J. E. Bertie and E. Whalley, *Spectrochim. Acta*, 20, 1349 (1964).
  84. I. U. P. A. C. Tables of Wavenumbers for the Calibration of Infrared Spectrometers, Butterworths, London, 1961.
  85. R. C. Weast, editor, *Handbook of Chemistry and Physics* 51 st. edition, The Chemical Rubber Co., 1970.
  86. F. A. Jenkins and H. E. White, *Fundamentals of Optics*, p. 469, McGraw-Hill Book Company Inc., 1957, 3rd. edition.
- 
87. G. C. Pimentel and A. L. McClellan, *The Hydrogen Bond*, W. H. Freeman and Company, 1960.
  88. H. E. Hallam in *Vibrational Spectroscopy of Trapped Species*, edited by H. E. Hallam, John Wiley & Sons 1973, Chapter 2.
  89. K. Simpson, Ph.D thesis, University of Alberta, 1973.
  90. C. A. Coulson and D. Eisenberg, *Proc. Roy. Soc.*, A291, 445 (1966).
  91. E. Whalley, Private communication.
  92. R. W. Blue, *J. Chem. Phys.*, 22, 280 (1954).
  93. P. Flubacher, A. J. Leadbetter and J. A. Morrison, *J. Chem. Phys.*, 33, 1751 (1960).



94. A. H. Hardin and K. B. Harvey, *Spectrochim. Acta*, 29A, 1139 (1973).
95. G. Leibfried and W. Ludwig, *Solid State Phys.*, 12, 275 (1961).
96. A. H. Hardin, Ph.D thesis, University of British Columbia, 1970.
97. J. A. McIntyre and D. R. Petersen, *J. Chem. Phys.*, 47, 3850 (1967).
98. E. Whalley, Private communication.
99. S. K. Garg, B. Morris and D. W. Davidson, *J. Chem. Soc. Farad. Trans. II*, 68, 481 (1972).
100. S. Sunder, Ph. D. thesis, University of Alberta, 1972.
101. J. X. Beach and D. P. Stevenson, *J. Chem. Phys.*, 6, 75 (1938).

---

102. L. V. Vilkov, L. S. Khaikin, A. F. Vasil'ev and T. F. Tulyakova, *Zh. Strukt. Khim.*, 9, 1071 (1968).
103. T. Moritani, K. Kuchitsu and Y. Morino, *Inorg. Chem.*, 10, 344 (1971).
104. Q. Williams, J. Sheridan, and W. Gordy, *J. Chem. Phys.*, 20, 164 (1952).
105. E. B. Wilson, J. C. Decius and P. C. Cross, *Molecular Vibrations*, McGraw-Hill Book Company, New York, 1955.
106. G. Herzberg, *Infrared and Raman Spectra of Polyatomic Molecules*, Van Nostrand, Princeton, 1945.
107. V. N. Thatte, *Nature*, 138, 468 (1936).
108. A. Simon and G. Schulze, *Naturwissen*, 25, 669 (1937).

109. H. Gerding and R. Westrik, *Rec. Trav. Chim.*, 61, 842 (1942).
110. M. Delwaulle and F. Francois, *Compt. Rend. Acad. Sci. (Paris)*, 224, 1422 (1947); M. Delwaulle and F. Francois, *J. Chim. Phys.*, 46, 87 (1949).
111. G. Cilento, D. A. Ramsay and R. N. Jones, *J. Am. Chem. Soc.*, 71, 2753 (1949).
112. J. R. Durig and J. W. Clark, *J. Chem. Phys.*, 46, 3057 (1967).
113. J. Goubeau and D. Köttgen, *Z. Anorg. Allgemein. Chem.*, 360, 182 (1968).
114. F. Marsault - Hérail and N. Tartar, *Compt. Rend. Acad. Sci. (Paris)*, 267B, 270 (1968).
- 
- ~~115. R. J. H. Clark and D. M. Rippon, *Mol. Phys.*, 28, 305 (1974).~~
116. J. E. Bertie and P. G. Wright, *J. Chem. Phys.*, 61, 2167 (1974).
117. L. S. Maiants, E. M. Popov and M. I. Kabachnik, *Optics and Spect.*, VI, 384 (1959).
118. J. S. Ziomek and E. A. Piotrowski, *J. Chem., Phys.*, 34, 1087 (1961).
119. J. E. Bertie, R. J. Andersen and P. G. Wright, *Can. J. Spectrosc.*, 19, 153 (1974).
120. G. Nagarajan, *J. Sci. Industr. Res.*, 21B, 356 (1962).
121. K. Venkateswarlu and R. Thanalakshmi, *Acta Physica Polon.*, XXII, 423 (1962).

122. K. Ramaswamy and B. K. Rao, *Z. Phys. Chem. (Leipzig)*, 240, 127 (1969).
123. S. J. Cyvin, B. Vizi, A. Müller and B. Krebs, *J. Mol. Struct.*, 3, 173 (1969).
124. K. Venkateswarlu and P. A. Joseph, *Indian J. Pure Appl. Phys.*, 9, 235 (1971).
125. G. Nagarajan, *Z. Phys. Chem. (Leipzig)*, 237, 297 (1968).
126. A. Müller, E. Niecke and B. Krebs, *Mol. Phys.*, 14, 591 (1968).
127. G. Horlick, *Appl. Spectrosc.*, 22, 617 (1968).
128. A. E. Martin, *Infrared Instrumentation and Techniques*, Elsevier, New York, 1966.
- 
- ~~129. K. N. Rao, C. J. Humphries and D. H. Rank, *Wavelength Standards in the Infrared*, Academic Press, New York, 1966.~~
130. A. Filler, *J. Opt. Soc. Am.*, 54, 762 (1964).
131. D. H. Rank and J. A. van Horn, *J. Opt. Soc. Am.*, 36, 454 (1946).
132. J. Loader, *Basic Laser Raman Spectroscopy*, Heyden and Son Ltd., 1970.
133. H. Margenau and G. M. Murphy, *The Mathematics of Physics and Chemistry*, D. van Nostrand Company Inc., Princeton, New Jersey, 1956.
134. W. F. Edgell and R. F. Moynihan, *J. Chem. Phys.*, 45, 1205 (1966).

135. J. Brasch and R. Jakobsen, *Spectrochim. Acta*, 20, 1644 (1964).
136. W. Rothschild, *Spectrochim. Acta*, 21, 852 (1965).
137. S. Frankiss and F. Miller, *Spectrochim. Acta*, 21, 1235 (1965).
138. J. H. Schachtschneider, *Vibrational Analysis of Polyatomic Molecules V and VI*, Project no. 31450, Technical Report no. 57 - 65 and 231 - 64, Shell Development Co., Emeryville, California.
139. S. L. Gerhard and D. M. Dennison, *Phys. Rev.*, 43, 197 (1933).
140. J. A. Faniran and H. F. Shurvell, *Spectrochim. Acta*, 26A, 1459 (1970).
141. R. J. H. Clark and O. H. Ellestad, *J. Mol. Spectrosc.*, 56, 386 (1975).

Appendix I

G Matrices<sup>a</sup> for  $^{32}\text{SP}^{35}\text{Cl}_3$ ,  $^{32}\text{SP}^{35}\text{Cl}_2^{37}\text{Cl}$ ,  
 $^{32}\text{SP}^{35}\text{Cl}^{37}\text{Cl}_2$ ,  $^{32}\text{SP}^{37}\text{Cl}_3$ ,  $^{34}\text{SP}^{35}\text{Cl}_3$  and  $^{34}\text{SP}^{35}\text{Cl}_2^{37}\text{Cl}$ .

(i)  $^{32}\text{SP}^{35}\text{Cl}_3$

ROW 1	0.0609	-0.0059	-0.0059	-0.0149	-0.0157	0.0070	-0.0157	-0.0155	0.0175	0.0175
ROW 2	-0.0059	0.0609	-0.0059	-0.0149	-0.0157	-0.0157	0.0070	0.0175	-0.0155	0.0175
ROW 3	-0.0059	-0.0059	0.0609	-0.0149	0.0070	-0.0157	-0.0157	0.0175	0.0175	-0.0155
ROW 4	-0.0149	-0.0149	-0.0149	0.0635	0.0377	0.0177	0.0177	-0.0142	-0.0142	-0.0142
ROW 5	-0.0157	-0.0157	0.0070	0.0177	0.0327	0.0036	0.0036	-0.0056	-0.0056	-0.0209
ROW 6	0.0070	-0.0157	-0.0157	0.0177	0.0036	0.0327	0.0036	-0.0209	-0.0056	-0.0056
ROW 7	-0.0157	0.0070	-0.0157	0.0177	0.0036	0.0036	0.0327	-0.0056	-0.0209	-0.0056
ROW 8	-0.0155	0.0175	0.0175	-0.0142	-0.0056	-0.0209	-0.0056	0.0414	-0.0079	-0.0079
ROW 9	0.0175	-0.0155	0.0175	-0.0142	-0.0056	-0.0056	-0.0209	-0.0079	0.0414	-0.0079
ROW 10	0.0175	0.0175	-0.0155	-0.0142	-0.0209	-0.0056	-0.0056	-0.0079	-0.0079	0.0414

(ii)  $^{32}\text{SP}^{35}\text{Cl}_2^{37}\text{Cl}$

ROW 1	0.0609	-0.0059	-0.0059	-0.0149	-0.0157	0.0070	-0.0157	-0.0155	0.0175	0.0175
ROW 2	-0.0059	0.0593	-0.0059	-0.0149	-0.0157	-0.0157	0.0070	0.0175	-0.0155	0.0175
ROW 3	-0.0059	-0.0059	0.0609	-0.0149	0.0070	-0.0157	-0.0157	0.0175	0.0175	-0.0155
ROW 4	-0.0149	-0.0149	-0.0149	0.0635	0.0177	0.0177	0.0177	-0.0142	-0.0142	-0.0142
ROW 5	-0.0157	-0.0157	0.0070	0.0177	0.0323	0.0037	0.0036	-0.0056	-0.0054	-0.0209
ROW 6	0.0070	-0.0157	-0.0157	0.0177	0.0037	0.0323	0.0036	-0.0209	-0.0054	-0.0056
ROW 7	-0.0157	0.0070	-0.0157	0.0177	0.0036	0.0036	0.0327	-0.0056	-0.0209	-0.0056
ROW 8	-0.0155	0.0175	0.0175	-0.0142	-0.0056	-0.0209	-0.0056	0.0414	-0.0079	-0.0079
ROW 9	0.0175	-0.0155	0.0175	-0.0142	-0.0054	-0.0054	-0.0209	-0.0079	0.0411	-0.0079
ROW 10	0.0175	0.0175	-0.0155	-0.0142	-0.0209	-0.0056	-0.0056	-0.0079	-0.0079	0.0414

(iii)  $^{32}\text{S}^{35}\text{Cl}^{37}\text{Cl}_2$ 

ROW 1	0.0593	-0.0059	-0.0059	-0.0149	-0.0157	0.0070	-0.0157	-0.0155	0.0175	0.0175
ROW 2	-0.0059	0.0609	-0.0059	-0.0149	-0.0157	-0.0157	0.0070	0.0175	-0.0155	0.0175
ROW 3	-0.0059	-0.0059	0.0593	-0.0149	0.0070	-0.0157	-0.0157	0.0175	0.0175	-0.0155
ROW 4	-0.0149	-0.0149	-0.0149	0.0635	0.0177	0.0177	0.0177	-0.0142	-0.0142	-0.0142
ROW 5	-0.0157	-0.0157	0.0070	0.0177	0.0323	0.0036	0.0037	-0.0054	-0.0056	-0.0209
ROW 6	0.0070	-0.0157	-0.0157	0.0177	0.0036	0.0323	0.0037	-0.0209	-0.0056	-0.0054
ROW 7	-0.0157	0.0070	-0.0157	0.0177	0.0037	0.0320	0.0320	-0.0054	-0.0209	-0.0054
ROW 8	-0.0155	0.0175	0.0175	-0.0142	-0.0054	-0.0209	-0.0054	0.0411	-0.0079	-0.0079
ROW 9	0.0175	-0.0155	0.0175	-0.0142	-0.0056	-0.0056	-0.0209	-0.0079	0.0414	-0.0079
ROW 10	0.0175	0.0175	-0.0155	-0.0142	-0.0209	-0.0054	-0.0054	-0.0079	-0.0079	0.0411

(iv)  $^{32}\text{S}^{37}\text{Cl}_3$ 

ROW 1	0.0593	-0.0059	-0.0059	-0.0149	-0.0157	0.0070	-0.0157	-0.0155	0.0175	0.0175
ROW 2	-0.0059	0.0593	-0.0059	-0.0149	-0.0157	-0.0157	0.0070	0.0175	-0.0155	0.0175
ROW 3	-0.0059	-0.0059	0.0593	-0.0149	0.0070	-0.0157	-0.0157	0.0175	0.0175	-0.0155
ROW 4	-0.0149	-0.0149	-0.0149	0.0635	0.0177	0.0177	0.0177	-0.0142	-0.0142	-0.0142
ROW 5	-0.0157	-0.0157	0.0070	0.0177	0.0320	0.0037	0.0037	-0.0054	-0.0054	-0.0209
ROW 6	0.0070	-0.0157	-0.0157	0.0177	0.0037	0.0320	0.0037	-0.0209	-0.0054	-0.0054
ROW 7	-0.0157	0.0070	-0.0157	0.0177	0.0037	0.0037	0.0320	-0.0054	-0.0209	-0.0054
ROW 8	-0.0155	0.0175	0.0175	-0.0142	-0.0054	-0.0209	-0.0054	0.0411	-0.0079	-0.0079
ROW 9	0.0175	-0.0155	0.0175	-0.0142	-0.0054	-0.0054	-0.0209	-0.0079	0.0411	-0.0079
ROW 10	0.0175	0.0175	-0.0155	-0.0142	-0.0209	-0.0054	-0.0054	-0.0079	-0.0079	0.0411

(v)  $^{34}\text{SP}^{35}\text{Cl}_3$ 

ROW 1	0.0609	-0.0059	-0.0059	-0.0149	-0.0157	0.0070	-0.0157	-0.0155	0.0175	0.0175
ROW 2	-0.0059	0.0609	-0.0059	-0.0149	-0.0157	-0.0157	0.0070	0.0175	-0.0155	0.0175
ROW 3	-0.0059	-0.0059	0.0609	-0.0149	0.0070	-0.0157	-0.0157	0.0175	0.0175	-0.0155
ROW 4	-0.0149	-0.0149	-0.0149	0.0617	0.0177	0.0177	0.0177	-0.0142	-0.0142	-0.0142
ROW 5	-0.0157	-0.0157	0.0070	0.0177	0.0327	0.0036	0.0036	-0.0056	-0.0056	-0.0209
ROW 6	0.0070	-0.0157	-0.0157	0.0177	0.0036	0.0327	0.0036	-0.0209	-0.0056	-0.0056
ROW 7	-0.0157	0.0070	-0.0157	0.0177	0.0036	0.0036	0.0327	-0.0056	-0.0209	-0.0056
ROW 8	-0.0155	0.0175	0.0175	-0.0142	-0.0056	-0.0209	-0.0056	0.0409	-0.0076	0.0076
ROW 9	0.0175	-0.0155	0.0175	-0.0142	-0.0056	-0.0056	-0.0209	-0.0076	0.0409	-0.0076
ROW 10	0.0175	0.0175	-0.0155	-0.0142	-0.0209	-0.0056	-0.0056	-0.0076	-0.0076	0.0409

(vi)  $^{34}\text{SP}^{35}\text{Cl}_2^{37}\text{Cl}$ 

ROW 1	0.0609	-0.0059	-0.0059	-0.0149	-0.0157	0.0070	-0.0157	-0.0155	0.0175	0.0175
ROW 2	-0.0059	0.0593	-0.0059	-0.0149	-0.0157	-0.0157	0.0070	0.0175	-0.0155	0.0175
ROW 3	-0.0059	-0.0059	0.0609	-0.0149	0.0070	-0.0157	-0.0157	0.0175	0.0175	-0.0155
ROW 4	-0.0149	-0.0149	-0.0149	0.0617	0.0177	0.0177	0.0177	-0.0142	-0.0142	-0.0142
ROW 5	-0.0157	-0.0157	0.0070	0.0177	0.0323	0.0037	0.0036	-0.0056	-0.0054	-0.0209
ROW 6	0.0070	-0.0157	-0.0157	0.0177	0.0037	0.0323	0.0036	-0.0209	-0.0054	-0.0056
ROW 7	-0.0157	0.0070	-0.0157	0.0177	0.0036	0.0036	0.0327	-0.0056	-0.0209	-0.0056
ROW 8	-0.0155	0.0175	0.0175	-0.0142	-0.0056	-0.0209	-0.0056	0.0409	-0.0076	-0.0076
ROW 9	0.0175	-0.0155	0.0175	-0.0142	-0.0054	-0.0054	-0.0209	-0.0076	0.0405	-0.0076
ROW 10	0.0175	0.0175	-0.0155	-0.0142	-0.0209	-0.0056	-0.0056	-0.0076	-0.0076	0.0409

a) With respect to the internal coordinates defined in Table 6.5,

Appendix II

Eigenvectors<sup>a, b</sup> for  ${}^{32}\text{SP}^{35}\text{Cl}_3$ ,  ${}^{32}\text{SP}^{35}\text{Cl}_2$ ,  ${}^{37}\text{Cl}$ ,  
 ${}^{32}\text{SP}^{35}\text{Cl}$ ,  ${}^{37}\text{Cl}_2$ ,  ${}^{32}\text{SP}^{37}\text{Cl}_3$ ,  ${}^{34}\text{SP}^{35}\text{Cl}_3$ ,  ${}^{34}\text{SP}^{35}\text{Cl}_2$ ,  ${}^{37}\text{Cl}$ .

(i)  ${}^{32}\text{SP}^{35}\text{Cl}_3$

FREQUENCY = 769.6 CM-1										
0.1032	0.1032	0.1032	-0.2228	-0.0886	-0.0886	-0.0886	0.0711	0.0711	0.0711	
FREQUENCY = 436.2 CM-1										
0.0745	0.0745	0.0745	0.1142	0.0006	0.0006	0.0006	-0.0005	-0.0005	-0.0005	
FREQUENCY = 251.4 CM-1										
0.0130	0.0130	0.0130	-0.0288	0.0739	0.0739	0.0739	-0.0593	-0.0593	-0.0593	
FREQUENCY = 0.0 CM-1										
0.0	0.0	0.0	0.0	0.0	0.0	0.0	0.0	0.0	0.0	
FREQUENCY = 548.8 CM-1										
0.2052	-0.1031	-0.1031	0.0	-0.0466	0.0933	-0.0466	-0.1187	0.0593	0.0593	
FREQUENCY = 247.7 CM-1										
-0.0412	0.0206	0.0206	0.0	-0.0515	0.1030	-0.0515	-0.0037	0.0019	0.0019	
FREQUENCY = 171.0 CM-1										
0.0168	-0.0084	-0.0084	0.0	-0.0046	0.0092	-0.0046	0.1370	-0.0685	-0.0685	
FREQUENCY = 548.8 CM-1										
0.0	0.1786	-0.1786	0.0	-0.0808	0.0	0.0808	0.0	-0.1028	0.1028	
FREQUENCY = 247.7 CM-1										
0.0	-0.0357	0.0357	0.0	-0.0892	0.0	0.0892	0.0	-0.0032	0.0032	
FREQUENCY = 171.0 CM-1										
0.0	0.0146	-0.0146	0.0	-0.0080	0.0	0.0080	0.0	0.1186	-0.1186	

(ii)  ${}^{32}\text{SP}^{35}\text{Cl}_2$ ,  ${}^{37}\text{Cl}$

FREQUENCY = 768.8 CM-1										
0.1036	0.1003	0.1036	-0.2233	-0.0884	-0.0884	-0.0891	0.0709	0.0715	0.0709	
FREQUENCY = 546.1 CM-1										
-0.1039	0.2028	-0.1039	-0.0041	-0.0478	-0.0478	0.0930	0.0604	-0.1187	0.0604	
FREQUENCY = 433.8 CM-1										
0.0728	0.0770	0.0728	0.1133	-0.0018	-0.0018	0.0029	0.0020	-0.0034	0.0020	
FREQUENCY = 250.4 CM-1										
0.0188	-0.0004	0.0188	-0.0271	0.0535	0.0535	0.1027	-0.0561	-0.0560	0.0561	
FREQUENCY = 245.4 CM-1										
0.0152	-0.0437	0.0152	0.0083	-0.0709	-0.0709	0.0741	0.0196	0.0150	0.0196	
FREQUENCY = 169.5 CM-1										
0.0084	-0.0170	0.0084	-0.0002	0.0048	0.0048	-0.0087	0.0676	-0.1359	0.0676	
FREQUENCY = 0.0 CM-1										
0.0	0.0	0.0	0.0	0.0	0.0	0.0	0.0	0.0	0.0	
FREQUENCY = 548.6 CM-1										
0.1787	0.0	-0.1787	0.0	-0.0803	0.0803	0.0	-0.1028	0.0	0.1028	
FREQUENCY = 245.1 CM-1										
0.0352	0.0	-0.0352	0.0	0.0883	-0.0883	0.0	0.0042	0.0	-0.0042	
FREQUENCY = 170.9 CM-1										
0.0144	0.0	-0.0144	0.0	-0.0083	0.0083	0.0	0.1186	0.0	-0.1186	



(iii)  $^{32}\text{SP}^{35}\text{Cl}^{37}\text{Cl}_2$ 

FREQUENCY = 767.9 CM-1									
0.1008	0.1041	0.1008	-0.2238	-0.0889	-0.0889	-0.0881	0.0713	0.0707	0.0713
FREQUENCY = 547.2 CM-1									
-0.1011	0.2071	-0.1011	0.0040	-0.0455	-0.0455	0.0936	0.0589	-0.1198	0.0589
FREQUENCY = 431.5 CM-1									
0.0753	0.0712	0.0753	0.1125	0.0004	0.0004	-0.0041	-0.0009	0.0044	-0.0009
FREQUENCY = 248.7 CM-1									
-0.0079	-0.0226	-0.0079	0.0272	-0.0837	-0.0837	-0.0452	0.0569	0.0567	0.0569
FREQUENCY = 242.5 CM-1									
0.0232	-0.0357	0.0232	-0.0063	-0.0313	-0.0313	0.1152	-0.0115	-0.0192	-0.0115
FREQUENCY = 170.2 CM-1									
-0.0084	0.0166	-0.0084	-0.0002	-0.0045	-0.0045	0.0100	-0.0684	0.1359	-0.0684
FREQUENCY = 0.0 CM-1									
0.0	0.0	0.0	0.0	0.0	0.0	0.0	0.0	0.0	0.0
FREQUENCY = 544.5 CM-1									
0.1764	0.0	-0.1764	0.0	-0.0814	0.0814	0.0	-0.1039	0.0	0.1039
FREQUENCY = 243.8 CM-1									
0.0356	0.0	-0.0356	0.0	0.0876	-0.0876	0.0	0.0026	0.0	-0.0026
FREQUENCY = 168.7 CM-1									
0.0147	0.0	-0.0147	0.0	-0.0079	0.0079	0.0	0.1169	0.0	-0.1169

(iv)  $^{32}\text{SP}^{37}\text{Cl}_3$ 

FREQUENCY = 767.0 CM-1									
0.1012	0.1012	0.1012	-0.2243	-0.0886	-0.0886	-0.0886	0.0711	0.0711	0.0711
FREQUENCY = 429.2 CM-1									
0.0736	0.0736	0.0736	0.1117	-0.0019	-0.0019	-0.0019	0.0015	0.0015	0.0015
FREQUENCY = 246.8 CM-1									
0.0134	0.0134	0.0134	-0.0274	0.0725	0.0725	0.0725	-0.0582	-0.0582	-0.0582
FREQUENCY = 0.0 CM-1									
0.0	0.0	0.0	0.0	0.0	0.0	0.0	0.0	0.0	0.0
FREQUENCY = 544.3 CM-1									
0.2038	-0.1019	-0.1019	0.0	-0.0467	0.0935	-0.0467	-0.1200	0.0600	0.0600
FREQUENCY = 241.2 CM-1									
-0.0406	0.0203	0.0203	0.0	-0.0500	0.1000	-0.0500	-0.0042	0.0021	0.0021
FREQUENCY = 168.7 CM-1									
0.0168	-0.0084	-0.0084	0.0	-0.0048	0.0095	-0.0048	0.1349	-0.0674	-0.0674
FREQUENCY = 544.3 CM-1									
0.0	0.1765	-0.1765	0.0	-0.0809	0.0	0.0809	0.0	-0.1039	0.1039
FREQUENCY = 241.2 CM-1									
0.0	-0.0352	0.0352	0.0	-0.0866	0.0	0.0866	0.0	-0.0036	0.0036
FREQUENCY = 168.7 CM-1									
0.0	0.0145	-0.0145	0.0	-0.0082	0.0	0.0082	0.0	0.1168	-0.1168

(v)  $^{34}\text{SP}^{35}\text{Cl}_3$ 

FREQUENCY = 766.0 CM-1									
0.1042	0.1042	0.1042	-0.2189	-0.0891	-0.0891	-0.0891	0.0715	0.0715	0.0715
FREQUENCY = 430.8 CM-1									
0.0732	0.0732	0.0732	0.1136	0.0033	0.0033	0.0033	-0.0026	-0.0026	-0.0026
FREQUENCY = 249.6 CM-1									
0.0124	0.0124	0.0124	-0.0300	0.0732	0.0732	0.0732	-0.0588	-0.0588	-0.0588
FREQUENCY = 0.0 CM-1									
0.0	0.0	0.0	0.0	0.0	0.0	0.0	0.0	0.0	0.0
FREQUENCY = 548.8 CM-1									
0.2062	-0.1031	-0.1031	0.0	-0.0466	0.0933	-0.0466	-0.1184	0.0592	0.0592
FREQUENCY = 247.7 CM-1									
-0.0412	0.0206	0.0206	0.0	-0.0515	0.1030	-0.0515	-0.0036	0.0018	0.0018
FREQUENCY = 168.9 CM-1									
0.0166	-0.0083	-0.0083	0.0	-0.0045	0.0090	-0.0045	0.1353	-0.0676	-0.0676
FREQUENCY = 548.8 CM-1									
0.0	0.1786	-0.1786	0.0	-0.0808	0.0	0.0808	0.0	-0.1025	0.1025
FREQUENCY = 247.7 CM-1									
0.0	-0.0356	0.0356	0.0	-0.0892	0.0	0.0892	0.0	-0.0032	0.0032
FREQUENCY = 168.9 CM-1									
0.0	0.0143	-0.0143	0.0	-0.0078	0.0	0.0078	0.0	0.1172	-0.1172

(vi)  $^{34}\text{SP}^{35}\text{Cl}_2^{37}\text{Cl}$ 

FREQUENCY = 765.1 CM-1									
0.1046	0.1013	0.1046	-0.2194	-0.0889	-0.0889	-0.0897	0.0713	0.0719	0.0713
FREQUENCY = 546.0 CM-1									
-0.1038	0.2029	-0.1038	-0.0040	-0.0479	-0.0479	0.0930	0.0603	-0.1184	0.0603
FREQUENCY = 428.5 CM-1									
0.0716	0.0755	0.0716	0.1127	0.0009	0.0009	0.0055	-0.0002	-0.0054	-0.0002
FREQUENCY = 248.8 CM-1									
0.0202	-0.0074	0.0202	-0.0267	0.0420	0.0420	0.1118	-0.0522	-0.0526	-0.0522
FREQUENCY = 245.2 CM-1									
0.0126	-0.0429	0.0126	0.0127	-0.0777	-0.0777	0.0586	0.0274	0.0229	0.0274
FREQUENCY = 167.3 CM-1									
0.0083	-0.0168	0.0083	-0.0003	0.0048	0.0048	-0.0085	0.0667	-0.1342	0.0667
FREQUENCY = 0.0 CM-1									
0.0	0.0	0.0	0.0	0.0	0.0	0.0	0.0	0.0	0.0
FREQUENCY = 548.6 CM-1									
0.1787	0.0	-0.1787	0.0	-0.0803	0.0803	0.0	-0.1025	0.0	0.1025
FREQUENCY = 245.1 CM-1									
0.0352	0.0	-0.0352	0.0	0.0883	-0.0883	0.0	0.0041	0.0	-0.0041
FREQUENCY = 168.8 CM-1									
0.0142	0.0	-0.0142	0.0	-0.0081	0.0081	0.0	0.1171	0.0	-0.1171

- a) Obtained from the final force field of Table 6.8.  
 b) Entries under each frequency are listed in the order of the internal coordinates of Table 6.5.

Appendix III

Potential Energy Distributions<sup>a, b</sup> for  $^{32}\text{SP}^{35}\text{Cl}^{37}\text{Cl}_2$ ,  
 $^{32}\text{SP}^{37}\text{Cl}_3$ ,  $^{34}\text{SP}^{35}\text{Cl}_3$  and  $^{34}\text{SP}^{35}\text{Cl}_2^{37}\text{Cl}$ .

(i)  $^{32}\text{SP}^{35}\text{Cl}^{37}\text{Cl}_2$

FREQUENCY = 767.9 CM-1									
0.1965	0.0867	0.5131	0.0776	0.0405	0.0167	0.0082	0.0	0.0	0.0
FREQUENCY = 547.2 CM-1									
0.3894	0.6766	0.0003	0.0401	0.0901	0.0224	0.0464	0.0	0.0	0.0
FREQUENCY = 431.5 CM-1									
0.3475	0.1284	0.4104	0.0000	0.0003	0.0000	0.0001	0.0	0.0	0.0
FREQUENCY = 248.7 CM-1									
0.0116	0.0389	0.0721	0.6563	0.1017	0.1015	0.0503	0.0	0.0	0.0
FREQUENCY = 242.5 CM-1									
0.1047	0.1023	0.0040	0.0967	0.6936	0.0043	0.0060	0.0	0.0	0.0
FREQUENCY = 170.2 CM-1									
0.0279	0.0448	0.0000	0.0040	0.0107	0.3127	0.6178	0.0	0.0	0.0
FREQUENCY = 544.5 CM-1									
0.0	0.0	0.0	0.0	0.0	0.0	0.0	0.7840	0.1455	0.0704
FREQUENCY = 243.8 CM-1									
0.0	0.0	0.0	0.0	0.0	0.0	0.0	0.1596	0.8402	0.0002
FREQUENCY = 168.7 CM-1									
0.0	0.0	0.0	0.0	0.0	0.0	0.0	0.0564	0.0142	0.9293

(ii)  $^{32}\text{SP}^{37}\text{Cl}_3$

FREQUENCY = 767.0 CM-1									
0.3495	0.5166	0.1199	0.0014	0.0	0.0	0.0	0.0	0.0	0.0
FREQUENCY = 429.2 CM-1									
0.5909	0.4089	0.0002	0.0000	0.0	0.0	0.0	0.0	0.0	0.0
FREQUENCY = 246.8 CM-1									
0.0596	0.0745	0.7757	0.0093	0.0	0.0	0.0	0.0	0.0	0.0
FREQUENCY = 544.3 CM-1									
0.0	0.0	0.0	0.0	0.7855	0.1440	0.0705	0.0	0.0	0.0
FREQUENCY = 241.2 CM-1									
0.0	0.0	0.0	0.0	0.1590	0.8405	0.0004	0.0	0.0	0.0
FREQUENCY = 168.7 CM-1									
0.0	0.0	0.0	0.0	0.0555	0.0155	0.9290	0.0	0.0	0.0
FREQUENCY = 544.3 CM-1									
0.0	0.0	0.0	0.0	0.0	0.0	0.0	0.7855	0.1440	0.0705
FREQUENCY = 241.2 CM-1									
0.0	0.0	0.0	0.0	0.0	0.0	0.0	0.1590	0.8405	0.0004
FREQUENCY = 168.7 CM-1									
0.0	0.0	0.0	0.0	0.0	0.0	0.0	0.0555	0.0155	0.9290

(iii)  $^{34}\text{SP}^{35}\text{Cl}_3$ 

FREQUENCY = 766.0 CM-1									
0.3211	0.4931	0.1216	0.0015	0.0	0.0	0.0	0.0	0.0	0.0
FREQUENCY = 430.8 CM-1									
0.5797	0.4197	0.0005	0.0000	0.0	0.0	0.0	0.0	0.0	0.0
FREQUENCY = 249.6 CM-1									
0.0492	0.0871	0.7737	0.0093	0.0	0.0	0.0	0.0	0.0	0.0
FREQUENCY = 548.8 CM-1									
0.0	0.0	0.0	0.0	0.7914	0.1411	0.0676	0.0	0.0	0.0
FREQUENCY = 247.7 CM-1									
0.0	0.0	0.0	0.0	0.1547	0.8450	0.0003	0.0	0.0	0.0
FREQUENCY = 168.9 CM-1									
0.0	0.0	0.0	0.0	0.0540	0.0139	0.9321	0.0	0.0	0.0
FREQUENCY = 548.8 CM-1									
0.0	0.0	0.0	0.0	0.0	0.0	0.0	0.7914	0.1411	0.0676
FREQUENCY = 247.7 CM-1									
0.0	0.0	0.0	0.0	0.0	0.0	0.0	0.1547	0.8450	0.0003
FREQUENCY = 168.9 CM-1									
0.0	0.0	0.0	0.0	0.0	0.0	0.0	0.0539	0.0139	0.9321

(iv)  $^{34}\text{SP}^{35}\text{Cl}_2^{37}\text{Cl}$ 

FREQUENCY = 765.1 CM-1									
0.2134	0.0827	0.4965	0.0782	0.0422	0.0168	0.0085	0.0	0.0	0.0
FREQUENCY = 546.0 CM-1									
0.4124	0.6520	0.0003	0.0446	0.0892	0.0236	0.0455	0.0	0.0	0.0
FREQUENCY = 428.5 CM-1									
0.3188	0.1468	0.4177	0.0000	0.0005	0.0000	0.0002	0.0	0.0	0.0
FREQUENCY = 248.8 CM-1									
0.0752	0.0041	0.0694	0.1651	0.6212	0.0853	0.0433	0.0	0.0	0.0
FREQUENCY = 245.2 CM-1									
0.0300	0.1446	0.0161	0.5821	0.1758	0.0242	0.0084	0.0	0.0	0.0
FREQUENCY = 167.3 CM-1									
0.0277	0.0474	0.0000	0.0047	0.0080	0.3077	0.6229	0.0	0.0	0.0
FREQUENCY = 548.6 CM-1									
0.0	0.0	0.0	0.0	0.0	0.0	0.0	0.7928	0.1396	0.0677
FREQUENCY = 245.1 CM-1									
0.0	0.0	0.0	0.0	0.0	0.0	0.0	0.1541	0.8453	0.0005
FREQUENCY = 168.8 CM-1									
0.0	0.0	0.0	0.0	0.0	0.0	0.0	0.0531	0.0151	0.9318

- a) Obtained from the final force field of Table 6.8.  
 b) Entries under each frequency are listed in the order of the symmetry coordinates in Tables 6.6 and 6.7 for the molecules of  $C_{3v}$  and  $C_s$  symmetry, respectively.